



Provided by the author(s) and University of Galway in accordance with publisher policies. Please cite the published version when available.

Title	Modelling the mechanical and fatigue behaviour of superelastic NiTi: analysing the role of microstructural phase and crystallographic texture
Author(s)	Weafer, Fiona
Publication Date	2015-08-26
Item record	http://hdl.handle.net/10379/5457

Downloaded 2024-05-14T03:51:28Z

Some rights reserved. For more information, please see the item record link above.



Modelling the Mechanical and Fatigue Behaviour of Superelastic
NiTi: Analysing the Role of Microstructural Phase and
Crystallographic Texture

by

Fiona M. Weafer

A thesis submitted to the National University of Ireland as fulfilment
of the requirements for the Degree of Doctor of Philosophy



Discipline of Biomedical Engineering
National University of Ireland, Galway

2015

Supervisor of Research: Prof. M. S. Bruzzi

Abstract

Superelastic NiTi self-expanding stents push the boundaries of our current understanding of material behaviour which ultimately influences the design of biomedical devices. In particular, the influence of microstructure on NiTi's behaviour is not well understood. Therefore, the objective of this thesis is to computationally investigate the impact of the two major influences on NiTi's fundamental mechanical and fatigue behaviour, namely, microstructural phase and crystallographic texture.

Employing the Finite Element Analysis (FEA) platform ABAQUS™, the influence of microstructural phase and crystallographic texture is first examined under quasi-static tension-compression conditions as a potential indicator of superelastic NiTi's fatigue performance. Subsequently, the fatigue behaviour of superelastic NiTi's is investigated using fatigue modelling methods incorporating the microstructural effects of both microstructural phase and crystallographic texture, respectively.

Firstly, through the individual examination of the mechanical behaviour of both the austenitic and martensitic microstructural phases of NiTi, it is confirmed there exists a strong association between the stress-induced martensitic (SIM) phase and the observed unusual fatigue behaviour of superelastic NiTi. It is proposed that superelastic NiTi's unique trait of increasing fatigue performance with increasing mean strain can be attributed to the shift from austenitic to martensitic NiTi fatigue behaviour, i.e. through stress-induced martensite transformation (SIMT).

Secondly, grain orientation distribution (crystallographic texture) is determined to cause significant deviation of the fundamental mechanical and fatigue behaviour of polycrystalline superelastic NiTi specimens from that of their predicted continuum behaviour. It is suggested that the use of homogenous bulk material properties, as is standard practice in the computational design process of biomedical devices, are inadequate to fully describe the complex material behaviour of superelastic NiTi. It is proposed current material models should be amended to include such microstructural effects for the continued safe use of NiTi for commercial applications and products.

Table of Contents

List of Figures.....	vii
List of Tables	xvii
List of Publications.....	xviii
Acknowledgements	xix
Introduction.....	20
1.1 Background and Motivation	21
1.1.1 <i>A Brief History of NiTi</i>	21
1.1.2 <i>Biomedical Application of NiTi: Endovascular Stents</i>	22
1.1.3 <i>Unique Mechanics of NiTi: Shape memory and Superelasticity</i>	25
1.1.4 <i>Microstructural Phases of NiTi</i>	28
1.1.5 <i>Crystallographic Texture of NiTi</i>	29
1.2 Objectives of Thesis	31
1.3 Thesis Structure	32
1.4 References	34
Literature Review	40
2.1 Introduction	41
2.2 Fatigue Behaviour Characterisation	42
2.2.1 <i>A Brief History of Fatigue</i>	42
2.2.2 <i>Fracture Mechanics Approach to Fatigue Analysis</i>	44
2.3 Fatigue Crack Behaviour Characterisation.....	45
2.3.1 <i>Linear Elastic Fracture Mechanics</i>	45
2.3.2 <i>Small Fatigue Crack Behaviour</i>	48
2.3.3 <i>Fatigue Crack Closure</i>	49
2.3.4 <i>Elastic-Plastic Fracture Mechanics</i>	50
2.4 Fatigue Testing of NiTi Biomedical Stents	53
2.4.1 <i>Effect of Thermal Processing</i>	54
2.4.2 <i>Effect of Test Temperature</i>	56
2.4.3 <i>Effect of Specimen Configuration</i>	58
2.4.4 <i>Effect of Loading Conditions</i>	59
2.5 Influence of Microstructure	62

2.5.1	<i>NiTi Composition and Microstructural Phases</i>	63
2.5.2	<i>Crystallographic Texture</i>	64
2.5.3	<i>Precipitate Fraction, Size and Location</i>	66
2.6	Micro-Macro NiTi Fatigue Investigations.....	67
2.7	Conclusions	69
2.8	References	72
Material Characterisation		89
3.1	Introduction	90
3.2	‘V-strut’ Stent Subcomponent.....	91
3.2.1	<i>Uniaxial Material Behaviour</i>	92
3.2.2	<i>Transformational Behaviour</i>	93
3.2.3	<i>Microstructural Imaging</i>	95
3.3	Micro-Dogbone Specimen.....	96
3.3.1	<i>Uniaxial Material Behaviour</i>	96
3.3.2	<i>Transformational Behaviour</i>	98
3.3.3	<i>Microstructural Imaging</i>	98
3.3.4	<i>Texture Characterisation</i>	99
3.3.5	<i>Grain Orientation Behaviour</i>	100
3.4	Summary of Results	102
3.5	References	104
Effect of Microstructural Phase on the Tensile Behaviour of NiTi		119
4.1	Introduction	120
4.2	Computational Background.....	121
4.3	Computational Investigation.....	124
4.3.1	<i>Finite Element Model Development</i>	124
4.3.2	<i>Finite Element Model Inputs</i>	126
4.3.3	<i>Finite Element Model Results</i>	127
4.3.4	<i>Computational Model Validation</i>	128
4.4	Discussion.....	129
4.5	References	132
Effect of Crystallographic Texture on the Tensile Behaviour of NiTi		141
5.1	Introduction	142

5.2	Computational Background.....	143
5.3	Computational Investigation.....	146
5.3.1	<i>Finite Element Model Development</i>	146
5.3.2	<i>Finite Element Model Inputs</i>	150
5.3.3	<i>Finite Element Model Results</i>	151
5.3.4	<i>Finite Element Model Validation</i>	155
5.4	Experimental Investigation.....	156
5.5	Discussion.....	157
5.6	References	160
Effect of Microstructural Phase on the Fatigue Behaviour of NiTi		171
6.1	Introduction	172
6.2	Fatigue Modelling Methodology	174
6.3	Fatigue Model Inputs.....	177
6.3.1	<i>J-integral</i>	177
6.3.2	<i>Ramberg-Osgood Parameters</i>	179
6.3.3	<i>R-curves</i>	180
6.3.4	<i>Fatigue Crack Growth Rate Behaviour</i>	183
6.4	Predicted Fatigue Behaviour	184
6.4.1	<i>Small Crack Behaviour</i>	184
6.4.2	<i>Predicted Stable Austenitic and Martensitic Fatigue Behaviour</i>	185
6.4.3	<i>Predicted Superelastic NiTi Fatigue Behaviour</i>	186
6.4.4	<i>Comparison to Experimental Data</i>	187
6.5	Discussion.....	189
6.6	References	193
Effect of Crystallographic Texture on the Fatigue Behaviour of NiTi.....		206
7.1	Introduction	207
7.2	Incorporation of Texture.....	208
7.2.1	<i>J-integral</i>	208
7.2.2	<i>R-curves</i>	210
7.3	Predicted Fatigue Behaviour	212
7.3.1	<i>Small Fatigue Behaviour</i>	212
7.3.2	<i>Effect of Grain Orientation at Crack Tip</i>	214

7.3.3	<i>Predicted Endurance Limits</i>	216
7.3.4	<i>Predicted Constant Life Diagram</i>	217
7.4	Discussion	218
7.5	References	220
Summary of Results and Concluding Remarks		229
8.1	Objectives of Thesis	230
8.2	Tensile Modelling	231
8.2.1	<i>Tensile Modelling Approach</i>	231
8.2.2	<i>Effect of Microstructural Phase on NiTi's Tensile Behaviour</i>	231
8.2.3	<i>Effect of Crystallographic Texture on NiTi's Tensile Behaviour</i>	232
8.3	Fatigue Modelling	233
8.3.1	<i>Fatigue Modelling Approach</i>	233
8.3.2	<i>Effect of Microstructural Phase on NiTi's Fatigue Behaviour</i>	234
8.3.3	<i>Effect of Crystallographic Texture on NiTi's Fatigue Behaviour</i>	236
8.4	Concluding Remarks	238
8.5	References	241
Appendix A		242
Appendix B		249
Appendix C		255

List of Figures

- Figure 1.1:** Schematic of a balloon expandable stenting procedure in an artery of a patient suffering from arterial stenosis.....38
- Figure 1.2:** Schematic of uniaxial stress-strain curve of superelastic NiTi showing loading and unloading curves. Also displayed are the *in vivo* chronic outward force (COF) exerted by the stent on the artery in retaining it open and the stent's radial resistive force (RRF) in resisting stent collapse.....38
- Figure 1.3:** Shape memory effect: From the austenitic phase, lowering of the temperature below M_f , without the addition of stress, causes a phase transformation to twinned martensite. Upon loading, de-twinning occurs until fully deformed martensite remains. Upon unloading, martensite elastically recovers but retains some permanent deformation. Full recovery, to its original shape and austenite phase, is achieved upon heating from the austenite start to finish temperatures (A_s to A_f).....39
- Figure 1.4:** (a) Portion of a twinned martensite specimen composed of self-accommodating variants of martensite and (b) reorientation to one preferential direction upon loading resulting in a deformed martensite structure.....39
- Figure 2.1:** Schematic of an example S-N curve (stress-fatigue life curve) for a typical engineering metallic material, also displayed is the endurance limit for the given metallic specimen.....83
- Figure 2.2:** Schematic of fatigue crack growth behaviour: Small crack growth behaviour is shown in regime 'A'; Paris law long crack growth behaviour is shown in regime 'B'; rapid long crack growth behaviour to failure is shown in regime 'C'.....83
- Figure 2.3:** Schematic of a constant life diagram for a typical engineering metallic material following the Goodman approach to fatigue failure.....84

Figure 2.4: Influence of test temperature on the uniaxial tensile behaviour of a NiTi specimen with an A_s temperature of -22°C and an A_f temperature of 11°C . Adapted from [Pelton <i>et al.</i> , 2000].....	85
Figure 2.5: Experimental established constant life diagram of superelastic NiTi for a -4% to $+6\%$ mean strain range. Adapted from [Pelton <i>et al.</i> , 2003].....	86
Figure 2.6: Experimental established constant life diagram of superelastic NiTi for $+1\%$ to $+9\%$ mean strain range. Adapted from [Pelton <i>et al.</i> , 2008].....	86
Figure 2.7: Stable martensitic NiTi specimen displaying a higher threshold for fatigue crack initiation when compared to both stable austenitic and superelastic NiTi specimens for a load ratio of $R=0.1$. Adapted from [McKelvey and Ritchie, 2001].....	87
Figure 2.8: Microstructure of a NiTi specimen annealed to be in the (a) stable austenitic, (b) stable martensitic and (c) superelastic phase [Dauskardt <i>et al.</i> , 1989].....	88
Figure 3.1: SEM micrograph of the superelastic NiTi ‘v-strut’ stent subcomponent specimen, strut width identified as approximately $85\mu\text{m}$	110
Figure 3.2: SEM micrograph of the superelastic NiTi ‘v-strut’ stent subcomponent specimen, total specimen length identified as $3260\mu\text{m}$	110
Figure 3.3: Schematic of the linear support strut test specimen (from the ‘v-strut’ stent subcomponent specimen) used in this work. All dimensions are in mm...111	111
Figure 3.4: Schematic of micro-dogbone specimen used in this work. All dimensions are in mm.....111	111
Figure 3.5: Experimental set-up of the EnduraTEC ELF/3200 with environmental chamber used in the uniaxial tension-compression testing of the linear support strut NiTi specimen.....	112

Figure 3.6: Experimental uniaxial tensile stress-strain response of the linear support strut specimen to 6% strain. Displayed are the extracted inputs for the computational modelling.....	112
Figure 3.7: Resulting experimental DSC curve of the linear support strut specimen with all transformation temperatures labelled.....	113
Figure 3.8: SEM micrograph of microstructure identified in the linear support strut of the ‘v-strut’ stent subcomponent specimen.....	113
Figure 3.9: Experimental set-up of the Deben micro-stage tester used in the <i>in situ</i> SEM tensile test of the micro-dogbone NiTi specimen.....	114
Figure 3.10: Experimental uniaxial stress-strain curve of the micro-dogbone specimen; loading to 5% strain, followed by unloading and subsequently loaded to 10% strain.....	114
Figure 3.11: Experimental uniaxial tensile stress-strain response of the micro-dogbone specimen used in this work under 5% strain reversed loading displaying the extracted inputs for computational modelling.....	115
Figure 3.12: Resulting experimental DSC curve of the micro-dogbone specimen with all transformation temperatures labelled.....	115
Figure 3.13: Schematic of dogbone specimen highlighting location of testing with corresponding SEM micrograph of the microstructure present in specimen.....	116
Figure 3.14: (a) Unlabeled and (b) labelled Kikuchi patterns for a (111) orientated grain identified under electron backscatter diffraction (EBSD) analysis in the test region of the micro-dogbone specimen.....	116
Figure 3.15: Grain orientation distribution map generated for the chosen test area of the micro-dogbone specimen using results from EBSD analysis. All crystallographic orientation with respect to loading direction.....	117

Figure 3.16: Sample nano-indentation unloading curves for (100), (110) and (111) orientated grain targeted in the chosen test area of the micro-dogbone specimen.....	118
Figure 4.1: Calibration of material properties from uniaxial tension-compression testing curves for input into the in-built UMAT/Nitinol subroutine.....	135
Figure 4.2: The homogenous 3-D FEA model of the ‘v-strut’ stent subcomponent specimen used in this work.....	136
Figure 4.3: Figure 4.3: Max. nodal principal strain in the 3-D ‘v-strut’ FEA model for various levels of axial displacement imposed, for the range of 6% to -4% strain levels.....	136
Figure 4.4: Maximum strain experienced in ‘v-strut’ stent subcomponent FEA model under (a) compressive loading and (b) tensile loading. Highlighting importance of correct loading procedure for physiologically relevant computational analysis.....	137
Figure 4.5: Contour plots of the 3-D ‘v-strut’ stent subcomponent FEA model displaying the volume fraction of SIM (‘SDV21’) present in the ‘v-strut’ geometry under (a) 2.5%, (b) 4% and (c) 6% compressive loading.....	138
Figure 4.6: The percentage volume fraction of SIM extracted from the node exhibiting maximum tensile stress, located on the outer apex of the 3-D ‘v-strut’ FEA model, plotted against the imposed mean strain levels of -4% to +6%. Dotted line represents the predicted volume fraction of SIM up to levels of 10% mean strain.....	139
Figure 4.7: Experimental established constant life diagram of superelastic NiTi from the combined works of [Pelton <i>et al.</i> , 2003] and [Pelton <i>et al.</i> , 2008].....	139
Figure 4.8: Validation of the UMAT/Nitinol subroutine used in this work through the comparison of generated results from a 3-D single element FEA model	

against the experimentally established stress-strain response of the linear support strut specimen.....140

Figure 4.9: Validation of the 3-D ‘v-strut’ FEA model, employing the UMAT/Nitinol subroutine, through comparing the generated load-displacement curve against the experimentally established load-displacement curve of the ‘v-strut’ specimen.....140

Figure 5.1: (a) SEM micrograph of the selected test area of the micro-dogbone NiTi specimen, and (b) the generated FEA micro-mechanical model based on the microstructure present in the micrograph with crystallographic grain orientations with respect to the loading direction included.....164

Figure 5.2: (a) SEM micrograph of the linear support strut of the ‘v-strut’ subcomponent specimen, and the two generated FEA micro-mechanical models based on the microstructure present in the micrograph using (b) Voronoi tessellation, and (c) idealised hexagonal unit cells.....164

Figure 5.3: Rectangular FEA micro-mechanical model used in this work with an idealised representation of the specimen’s granular structure employing hexagonal unit cells, also displaying boundary conditions used.....165

Figure 5.4: ‘V-strut’ FEA micro-mechanical model used in this work with an idealised representation of the specimen’s granular structure employing hexagonal unit cells, also displaying boundary conditions used.....165

Figure 5.5: (a) Max. principal strain and (b) volume fraction of SIM (‘SDV21’) under a maximum of 2.5% and 5% localised tensile strain in the realistic FEA model.....166

Figure 5.6: Max. principal strain evolution and uniaxial macroscopic material response due to varying textures, (a) and (b), in the idealised FEA model.....166

Figure 5.7: Distribution of grain orientations within the micro-mechanical models, based on experimental textural results of [Robertson and Ritchie, 2007].....	167
Figure 5.8: Resulting localised maximum principal strain evolution under 2.5% compressive strain in the ‘v-strut’ FEA micro-mechanical model with (a) a (100) orientated grain and (b) a (110) orientated grain, and (c) a (111) orientated grain at the critical location of peak tensile stress located on the outer apex of the ‘v-strut’	168
Figure 5.9: Validation of the UMAT/Nitinol subroutine used in this work through direct comparison of the generated results from the FEA micro-mechanical model, incorporating a realistic granular structure, against the experimentally established uniaxial stress-strain response of the micro-dogbone specimen.....	169
Figure 5.10: Micrographs of the micro-dogbone specimen under (a) 0% strain and (b) 10% strain taken during the <i>in situ</i> SEM tensile testing procedure.....	169
Figure 5.11: SEM micrograph of the micro-dogbone specimen used in this work which displays the presence of inherent martensite plates in the austenitic specimen.....	170
Figure 6.1: Flowchart detailing the main steps taken in the crack-closure based fatigue modelling procedure in this work.....	176
Figure 6.2: Uniaxial stress-strain behaviour of the stable austenitic, stable martensitic and superelastic NiTi materials used as input to the FEA model, adapted from [McKelvey and Ritchie, 2001].....	197
Figure 6.3: <i>J</i> -integral calculated through FEA modelling of the crack tip, <i>J</i> -integral extracted from the model upon loading to a maximum applied tensile stress.....	197

Figure 6.4: <i>J</i> -integral data extracted from the FEA model with an initial defect size, a_0 , of $5\mu\text{m}$ using stable austenitic, stable martensitic and superelastic NiTi material data, respectively.....	198
Figure 6.5: Crack growth resistance curves, R-curves, for stable austenitic NiTi for load ratios, $R=-1$ to $R=0.5$. Data adapted from [McKelvey and Ritchie, 2001], [Holtz <i>et al.</i> , 1999] and [Robertson and Ritchie, 2007].....	198
Figure 6.6: Crack growth resistance curves, R-curves, for stable martensitic NiTi for load ratios, $R=-1$ to $R=0.5$. Data adapted from [McKelvey and Ritchie, 2001], [Holtz <i>et al.</i> , 1999] and [Robertson and Ritchie, 2007].....	199
Figure 6.7: Flowchart detailing the main inputs for superelastic NiTi in the fatigue modelling procedure in this work.....	182
Figure 6.8: Fatigue crack growth rate behaviour for stable martensitic NiTi with load ratio, $R=0.1$. Tested at -65°C . Adapted from [McKelvey and Ritchie, 2001].....	199
Figure 6.9: Fatigue crack growth rate behaviour for stable austenitic NiTi (a) neglecting, and (b) including crack closure, with load ratio, $R=0.1, 0.5$ and 0.7 . Tested at 120°C . Adapted from [McKelvey and Ritchie, 2001].....	200
Figure 6.10: Fatigue crack growth rate behaviour for superelastic NiTi (a) neglecting, and (b) including crack closure, with load ratio, $R=0.1, 0.5$ and 0.7 . Tested at 37°C . Adapted from [McKelvey and Ritchie, 2001].....	201
Figure 6.11: Predicted fatigue crack growth rate behaviour of a stable austenitic NiTi specimen with an initial defect size, a_0 , of $5\mu\text{m}$ for various applied maximum stress values.....	202
Figure 6.12: Predicted fatigue crack growth rate behaviour of a superelastic NiTi specimen with an initial defect size, a_0 , of $5\mu\text{m}$ for various applied maximum stress values.....	202

Figure 6.13: Predicted S-N curves for stable austenitic and stable martensitic NiTi specimens with initial defect size $a_0=5\mu\text{m}$ and load ratio $R=0.1$	203
Figure 6.14: Predicted constant life diagram for stable austenitic and stable martensitic NiTi specimens with initial defect size $a_0=5\mu\text{m}$	203
Figure 6.15: Predicted constant life diagram for stable austenitic, stable martensitic and superelastic NiTi specimens with initial defect size $a_0=5\mu\text{m}$	204
Figure 6.16: Predicted S-N curve for a stable austenitic specimen with initial defect size $a_0=5\mu\text{m}$ and load ratio $R=0$ compared against experimental S-N data taken from [Miyazaki <i>et al.</i> , 1988].....	204
Figure 6.17: Predicted S-N curve for a stable martensitic specimen with initial defect size $a_0=5\mu\text{m}$ and load ratio $R=-1$ compared against experimental S-N data taken from [Melton and Mercier, 1979].....	205
Figure 6.18: Comparison of the predicted constant life diagram to the experimental works of [Pelton <i>et al.</i> , 2003] and [Pelton <i>et al.</i> , 2008] for NiTi specimens with initial defect sizes, a_0 , of 5, 10, 15 and $25\mu\text{m}$	205
Figure 7.1: J -integral calculated through FEA modelling of the crack tip using a realistic representation of the specimen's microstructure. J -integral extracted from the model upon loading to a maximum applied tensile stress.....	222
Figure 7.2: J -integral calculated through FEA modelling of the crack tip using an idealised representation of the specimen's microstructure. J -integral extracted from the model upon loading to a maximum applied tensile stress.....	222
Figure 7.3: Predicted stress-strain response of a NiTi specimen generated by FEA models using a realistic and idealised representation microstructure compared against the predicted response using a continuum model.....	223

Figure 7.4: Maximum stress experienced by the crack tip along the crack length extracted from the FEA model incorporating an idealised representation of the specimen’s microstructure and a (100) orientated grain located at the crack tip with an applied far-field stress of 600MPa.....223

Figure 7.5: Altering R-ratio with crack extension due to shifting maximum stress experienced by the crack tip along the crack path path in the textured model for a specimen with initial defect size 5µm and an applied far field stress of 600MPa.....224

Figure 7.6: R-ratio with added legacy effect to account for the stress overload effects experienced by the crack tip in the textured model along the crack path for a specimen with initial defect size 5µm and an applied far field stress of 600MPa.....224

Figure 7.7: Crack growth resistance curve, R-curve, for a superelastic NiTi specimen with an applied load ratio R=0.1. Displaying altering stress intensity range, ΔK , with crack extension due to the shifting maximum stress experienced by the crack tip along the crack path in the textured model.....225

Figure 7.8: Predicted small crack fatigue growth rate behaviour generated from FEA models with, and without, textural effects. Both models having an initial defect size $a_0=5\mu\text{m}$, load ratio R=0.1 and 600MPa applied far-field stress.....225

Figure 7.9: Altering material response with varying grain orientation along the crack path: (a) the grain orientations present in first 350µm of the crack path displaying a (100) orientated grain at the crack tip, (b) contour plot displaying the non-uniform evolution of the maximum stress (σ_{22}) in the FEA model, and (c) the maximum stress (σ_{22}) extracted along the crack path of the FEA model.....226

Figure 7.10: Predicted small fatigue crack growth rate behaviour generated from FEA model with varying grain orientations at the crack tip. All models have an initial defect size $a_0=5\mu\text{m}$, load ratio $R=0.1$ and 600MPa applied far-field stress.....	227
Figure 7.11: Predicted S-N curves generated from FEA models with a (100), (110) and (111) orientated grain at the crack tip, respectively, compared against the predicted S-N curve generated using a continuum model.....	227
Figure 7.12: Predicted constant life diagram of a superelastic NiTi specimen with an initial defect size $a_0=25\mu\text{m}$, with and without the incorporation of textural effects, compared against the experimental works of [Pelton <i>et al.</i> , 2003] and [Pelton <i>et al.</i> , 2008].....	228
Figure A.1: Identification of Case 1 loading condition (Austenite).....	242
Figure A.2: Identification of Case 2 loading condition (Austenite-to-Plateau).....	243
Figure A.3: Identification of Case 3 loading condition (Plateau).....	244
Figure A.4: Identification of Case 4 loading condition (Plateau).....	245
Figure A.5: Identification of Case 5 loading condition (Plateau-to-Martensite).....	246
Figure A.6: Identification of Case 6 loading condition (Martensite).....	247
Figure A.7: Identification of Case 7 loading condition (Austenite-to-Martensite)...	248

List of Tables

Table 3.1: Material properties extracted from the experimental uniaxial tensile testing procedure completed on the linear support strut specimen.....	107
Table 3.2: Material properties extracted from experimental uniaxial tensile testing procedure completed on the micro-dogbone specimen.....	108
Table 3.3: Material properties extracted from experimental tensile testing curves of NiTi single crystals with varying crystallographic orientation with respect to the loading direction [Gall <i>et al.</i> , 1998].....	109
Table 6.1: Material properties extracted from the experimental uniaxial tensile testing procedure completed on the superelastic NiTi round-bar tensile specimens reported in literature [McKelvey and Ritchie, 2001].....	196
Table A.1: Identification of Case 1 loading condition (Austenite).....	242
Table A.2: Identification of Case 2 loading condition (Austenite-to-Plateau).....	243
Table A.3: Identification of Case 3 loading condition (Plateau).....	244
Table A.4: Identification of Case 4 loading condition (Plateau).....	245
Table A.5: Identification of Case 5 loading condition (Plateau-to-Martensite).....	246
Table A.6: Identification of Case 6 loading condition (Martensite).....	247
Table A.7: Identification of Case 7 loading condition (Austenite-to-Martensite)....	248

List of Publications

Chapter 4:

Weafer F.M. and Bruzzi M.S., 'The Micro-Macroscale Correlation of NiTi Mechanical Behavior: A Finite Element Analysis', *WIT Transactions on Engineering Sciences*, 2013, **77**, p 17-30.

Weafer F.M. and Bruzzi M.S., 'Influence of Microstructure on the Performance of Nitinol: A Computational Analysis', *Journal of Material Engineering and Performance*, 2014, **23(7)**, p 2539-2544.

Chapter 5:

Weafer F.M., Guo Y. and Bruzzi M.S., 'Effect of Crystallographic Texture on Stress-induced Martensitic Transformation in NiTi: An in-situ SEM Study', *Journal of the Mechanical Behavior of Biomedical Materials*, 2015, **53**, p 210-217

Chapter 6:

Weafer F.M. and Bruzzi M.S., 'Crack-closure based Method for Modelling the Fatigue Behavior of Superelastic Nitinol', *International Journal of Fatigue*, 2016, **82**, p 730-736.

Chapter 7:

Weafer F.M. and Bruzzi M.S., 'Micromechanical Investigation into the Effect of Texture on the Fatigue Behaviour of Superelastic Nitinol', *International Journal of Fatigue*, 2016, Under Review.

Acknowledgements

First of all, I would like to offer my sincere appreciation to my academic advisor Prof. Mark Bruzzi for giving me the opportunity to work in the exciting field of NiTi research. This thesis would not have been possible without his continuous support and encouragement.

I would also like to express my gratitude to all affiliated with the Disciplines of Mechanical and Biomedical Engineering at the National University of Ireland, Galway who have guided and supported me, both as an undergraduate and postgraduate student, over the better part of the last decade.

I would like to offer my particular thanks to Mr. Patrick Kelly for his invaluable advice during the experimental phase of this thesis. His gracious assistance undoubtedly aided in the smooth completion of my research. I also owe a huge debt of gratitude to Dr. Barry O'Brien who generously offered his valuable time in patiently answering all of my NiTi-related questions.

Recognitions must also be given to my good friends at home and in Galway. In particular I must mention my childhood partner in crime, Lorraine, and the man-child that has always kept me smiling, Oisín. Both have undeniably proven themselves as vital resources in the maintenance of my sanity throughout the course of my postgraduate studies.

Most importantly, however, I would like to thank my parents for their unconditional love and support during my undergraduate and postgraduate studies, and always. Thanks also to my brother, Paul, and my sister, Sarah, for putting up with me in my not-so-gracious times.

Finally, I would like to acknowledge Science Foundation Ireland for funding this research project. Sincere thanks must also go to the University of California for funding my stay at UC Santa Barbara under its Education Abroad Program.

Chapter 1

Introduction

1.1 Background and Motivation

1.1.1 A Brief History of NiTi

Certain materials are favoured by the biomedical industry due to their particular beneficial properties and characteristics. One such material is the near equi-atomic nickel-titanium alloy, NiTi. William J. Buehler, along with Frederick Wang, discovered the unique properties of NiTi in 1962 while carrying out research at the U.S. Naval Ordnance Laboratory (NOL) [Buehler *et al.*, 1963] [Wang *et al.*, 1965]. The chemical composition of this alloy, along with the location in which its properties were first discovered, gives rise to its commercial name: 'NiTiNOL'. The two researchers were engaged in the design of an improved missile nose cone which would have the ability to resist fatigue, high temperatures and the immense force of impact. They discovered that a 1:1 alloy of nickel and titanium offered the greatest potential and subsequently presented their findings to colleagues at a laboratory management meeting. A specimen of this NiTi alloy, which was folded in a zig-zag shape, was circulated and flexed by the participants. It was noted that the ability of the specimen to elastically deform was much greater than with other engineering materials; this characteristic was termed 'superelastic' behaviour. One of the men present applied heat from his pipe lighter to the specimen and, to everyone's surprise, the NiTi strip recoiled to return to its original zig-zag shape. In this way, he had inadvertently demonstrated the 'shape-memory' characteristic of the NiTi material.

While the potential applications for NiTi were appreciated immediately, efforts to realise the practical and commercial use of the alloy did not take place until a decade later. The early historical development of NiTi was reviewed by [Kauffman and Mayo, 1997]. They attribute much of the delay in development to the extraordinary difficulties associated with the melting, processing and machining of the NiTi alloy. These early efforts in development also encountered financial challenges which were not overcome until the 1990s. Therefore, despite its discovery in the 1960s, the bulk of research on the material behaviour of NiTi only spans the last 25 years as these practical difficulties began to be resolved. In particular, research into the benefits of

NiTi's superelastic behaviour has become a rapidly expanding research field. However, many unknowns still remain in the understanding of NiTi's fundamental behaviour. This is highlighted in a paper by [Duerig, 2006] which discusses the local microstructural effects on the global mechanical response of superelastic NiTi which are still not properly understood. As a result, more comprehensive research is therefore required as a priority in this field for the continued safe use of NiTi in commercial applications and products.

1.1.2 Biomedical Application of NiTi: Endovascular Stents

In the 1980s, an American physician, Dr. Richard Schatz conceived the idea to prop open blocked human arteries with a spring-like metal device known as a 'stent' and in doing so he created a product which revolutionised the medical device industry. The balloon-expandable stent has become the most widely used commercial stent device. Such stents are typically manufactured from stainless steel due to its excellent biocompatibility. A schematic illustrating a typical balloon-expandable stenting procedure in a human artery suffering from stenosis can be seen in Figure 1.1. As the name suggests, a balloon-expandable stent is deployed into an artery suffering from stenosis when the balloon, on which it is mounted, is inflated. The extent to which the stent is deployed is dependent on the inflation pressure of the balloon. Many surgeons expand the stents to a diameter greater than that required in order to account for elastic recoil of the device [Costa *et al.*, 2000]. However, due to the stress imposed on the soft muscle tissue of the vessel in which the stent is placed, restenosis of the vessel occurs in the order of 20-30% of reported clinical cases [Togni *et al.*, 2004] [Maier *et al.*, 2001]. Restenosis of vessels is generally attributed to the hyperplastic response of the target vessel to the stent-induced injury (caused by the over-expansion of the stent) on the vessel's most inner layers, namely, the endothelium and the intima layers [Hoffmann *et al.*, 2002]. Inflammation associated with this injury can cause cell growth, reducing the diameter of the lumen once again and thus considerably reducing the effectiveness of the original procedure.

An emerging alternative to the balloon-expandable stent is the innovative self-expanding stent which, as the names suggests, eliminates the need for a balloon. NiTi demonstrates many properties which make it suitable for use in self-expanding stent devices including its characteristic superelasticity, biocompatibility, flexibility, and compatibility with magnetic resonance imaging (MRI) procedures. An ideal superelastic stress-strain curve of superelastic NiTi, showing long and elevated plateaus following an initial elastic loading regime is shown in Figure 1.2. Large recoverable strains are required for both deployment and *in vivo* crush resistance in self-expanding stents, the stent is therefore designed to remain within the superelastic range inside the delivery catheter. It may also enter the superelastic range after deployment if sufficient deformation occurs due to vessel interaction or external forces. In this way, the superelastic NiTi stent can withstand the large levels of strains caused by the muscular movement associated with the anatomy in which it is placed, in addition to the physiological movement from the cardiac systolic-diastolic cycle, with limited changes to the imposed stress on the device which ultimately increases its resistance to fatigue (cyclic) failure.

In vivo crush resistance is also of paramount importance for consideration during the manufacture of self-expanding NiTi stents. Upon removal of an imposed load, NiTi's superelastic stress recovers at a lower stress level to that at which it was induced, i.e. along a hysteresis curve, as shown in Figure 1.2. These stress levels are identified as the loading and unloading plateau stresses, respectively. This associated hysteresis is a valuable feature in superelastic stent design since it allows the stent to provide a very low chronic outward force (COF) against a vessel wall, minimising the remodelling of the vessel, while still maintaining a high level of crush resistance through its radial resistance force (RFF) as identified in Figure 1.2. In this way, any 'crushing' of the vessel will further load the stent material along the austenitic modulus until it reaches the higher loading transformation plateau; this behaviour is termed 'biased stiffness'. One of the first to research such theoretical advantages of superelastic NiTi in the design of endovascular self-expanding stents was [Duerig *et al.*, 2000]. This biased stiffness of superelastic NiTi is, however, subject to much

debate. There are arguments in favour of a significant hysteresis to generate resistance to compression and to minimise elastic recoil after deployment. On the other hand, the absence of a hysteresis leads to vessel compliance in terms of crushability and recoverability similar to the behaviour of natural healthy vessels which may minimise tissue damage, i.e. to avoid restenosis of target vessels. Therefore, it can be said, there still remain many unknowns associated with the optimum design of NiTi self-expanding devices.

Nevertheless, commercial self-expanding NiTi biomedical endovascular stents have proven effective in the treatment of coronary artery disease (CAD) and peripheral artery disease (PAD) including in the superficial femoral, carotid, and renal arteries. To highlight their growing importance, every year approximately 600,000 Americans [Auerbach *et al.*, 2012] and 800,000 Europeans undergo cardiac stenting procedures for CAD [Market Report, 2010]; thus making medical devices and diagnostics (MD&D) a €342 billion global industry [Market Report, 2015]. However, there have been an alarming number of self-expanding NiTi stent failures reported in the literature. In two studies, carried out by [Schlager *et al.*, 2005] and [Scheinert *et al.*, 2005], fracture rates of up to 28% and 37.2% were reported, respectively, in such stents used to treat PAD in the superior femoral artery. Many of these failures have been attributed to cumulative fatigue damage due to the tortuous anatomy in which they are placed as the superior femoral artery inflicts a variety of non-uniaxial motion on the device including high levels of flexion and torsion. The lack of understanding into NiTi's fundamental mechanical and fatigue behaviour is exposed by such statistics.

Unforeseen failures in medical devices highlight the concerns with current testing protocols for superelastic NiTi materials. Characteristic uniaxial tension-compression material properties, extracted for use in the design of self-expanding NiTi stents, are evaluated using the ASTM standard F2516-14 [ASTM, 2014]. This standard specifies a method for testing the loading and unloading plateau stresses, tensile strength and elongation of a superelastic NiTi material through uniaxial tensile-compressive testing at a given test temperature. However, no reference is made to

include non-uniaxial testing which ultimately is shown to severely affect the *in vivo* service (fatigue) life of a stent. The ASTM standard for the fatigue analysis of superelastic NiTi devices, through hydrodynamic pulsation, is specified in the ASTM standard F2477-07 [ASTM, 2013]. This method involves placing complete devices into mock arteries and subjecting them to 400 million cycles of internal pressure pulsation, forcing them to radially expand and contract in each cycle. The acceptance criterion of a device is a simple pass/fail, in that no fracture of the stent can occur during these *in vitro* tests for success. Under this ‘test-to-success’ criterion, the solitary concern is the *in vivo* performance of the stent, this therefore does not promote investigation into fundamental microstructural failure mechanisms of NiTi. As a result the underlying microscopic mechanisms relating to NiTi’s macroscopic behaviour, which ultimately determines its fatigue life, are still not well understood. However, understanding local microstructural effects on the global mechanical response can lead to a much fuller appreciation towards the deviation of the mechanical response from predictions and thus the unforeseen fracture observed in NiTi biomedical self-expanding stent devices. In 2006, the FDA and ASTM committees started to investigate methods to improve the current durability assessment of biomedical stent devices. An alternative method that has since been adopted by many researchers is a ‘test-to-failure’ criterion approach. This methodology involves a combination of Finite Element Analysis (FEA) modelling and *in vitro* testing to assess the durability of stent devices through established fracture mechanics techniques. However, these testing guidelines are still under development.

1.1.3 Unique Mechanics of NiTi: Shape memory and Superelasticity

As mentioned in Section 1.1.1, shape-memory refers to the ability of a NiTi specimen to ‘remember’ its shape upon heating following an imposed external deformation. This behaviour has many benefits and is attributed to a first-order transformation from a parent austenite to daughter martensite microstructural phase. This phase transformation can be induced by a change in temperature or stress whereby martensite forms upon cooling below the characteristic martensite start, M_s ,

temperature or via the application of an external stress. The phenomenon of shape-memory utilises the temperature effects on NiTi's phase transformation; as demonstrated in the plot of Figure 1.3. From the austenitic microstructural phase, the material is cooled to its martensite start, M_s , temperature and subsequently cooled to below its martensite finish, M_f , temperature such that the stable phase is in a (twinned) martensitic phase. If the material is mechanically loaded in this martensitic phase, upon removal of the stress, the martensitic NiTi has the ability to elastically recover but still retains some permanent deformation. The addition of heat to above the austenite finish, A_f , temperature fully returns the material to its original shape and austenite phase [Duerig *et al.*, 1990]. An example of the application of this unique thermo-mechanical property is the Simon vena cava filter which is manufactured by BARD Peripheral Vascular™. This device is cooled to below its martensite finish, M_f , temperature, collapsed into a chilled saline catheter, and tortuously inserted into the vena cava; at which point the human body temperature is sufficiently above the austenite finish, A_f , temperature of the device to cause expansion of the filter into its pre-determined shape [O'Brien and Bruzzi, 2011].

NiTi self-expanding stents, on the other hand, are specifically designed to exploit NiTi's advantageous superelastic behaviour. Superelasticity is the ability to elastically deform to higher than normal strain levels when subject to mechanical loading. As mentioned, it is the phase transformation from an austenitic to martensitic microstructural phase which gives rise to NiTi's advantageous behaviour. Where an external stress is applied to induce the phase transformation, as opposed to a temperature change, a stress-induced martensite (SIM) is formed. The research discussed in this thesis considers only SIM for analysis as this is the most relevant form of martensite in the context of biomedical stent devices. In a crystallographic context, stress-induced martensite transformation (SIMT) occurs upon loading through the rearrangement of atomic planes with the release of latent heat due to the exothermic nature of the transformation process [Bhattacharya, 2003]. Lattice-distortive strains, known as Bain strains, are the strains necessary to transform the simple cubic crystal structure of austenitic NiTi into the more complex body-centred tetragonal crystal

structure of martensitic NiTi [Bain, 1924]. The deformation describing the Bain strain is given by:

$$B = \begin{pmatrix} \varepsilon_0 & 0 & 0 \\ 0 & \varepsilon_0 & 0 \\ 0 & 0 & \varepsilon'_0 \end{pmatrix} \quad \text{EQ. 1.1}$$

$$\varepsilon_0 = \frac{\sqrt{2}\alpha_{mar} - \alpha_{aus}}{\alpha_{aus}}, \quad \varepsilon'_0 = \frac{\alpha_{mar} - \alpha_{aus}}{\alpha_{aus}} \quad \text{EQ. 1.2, 1.3}$$

where α_{aus} and α_{mar} are the lattice parameters of austenite and martensite, respectively. The austenite-to-martensite transformation is diffusionless with no associated breaking of atomic bonds. Therefore, no macroscopic change is associated with the transformation which can be attributed to the self-accommodating nature of twinned martensite variants. However, it should be noted that a slight contraction is experienced during the forward austenite-to-martensite transformation in the form of a transformational volume strain change of approximately -0.39% as experimentally determined by [Holtz *et al.*, 1999]. Following EQ. 1.1, this contraction will be experienced along the [001] axis of the transforming structure.

When the material is deformed in the twinned martensite phase, the twin boundaries readily shift such that the twins are predominantly oriented in one preferential direction while still maintaining a martensite crystal structure [Duerig *et al.*, 1990]. This process is known as ‘de-twinning’ and gives rise to NiTi’s superelastic behaviour. By this microstructural process, NiTi can typically withstand 8-11% strain without permanent deformation. This ability to accommodate such significant strains is highly desirable in stent device design for stent deliverability, durability, and conformance. The microstructural process of de-twinning has been a topic of research for many researchers including [Abeyaratne *et al.*, 1994], [Vivet and LExcellent, 1998] and [Waltz *et al.*, 2004]. The formation of variants of martensite can be explained by a simple two dimensional approach considering the geometrical change associated with the transformation from the cubic austenitic NiTi, B2, to monoclinic martensitic NiTi, B19’, crystal structure. This distortion can occur in one of four ways depending

on the direction of shear. As a result, up to 12 different variants of martensite can be formed upon phase transformation. Due to the aforementioned self-accommodating nature of martensite, the four monoclinic variants tend to group together in equal portions in the specimen, as shown in Figure 1.4. Once a particular orientation is formed, it can only return to its cubic parent by means of inverse shear. In this way SIMT is reversible, in that, upon removal of the stress the martensite plates undergo ‘backwards shear’ and return to their original austenite condition.

Under certain circumstances, however, an undesired intermediate rhombohedral phase known as the ‘R-phase’ may appear resulting in a two-stage transformation. This can be induced due to microstructural defects in the material such as those introduced through annealing, ageing heat treatments, chemical alloying elements or natural defects such as precipitates. The R-phase is undesirable in commercial NiTi self-expanding stents since recoverable strains associated with the R-phase are in the order of approximately 0.5% [Uchil *et al.*, 2001], as compared to up to 11% [Duerig *et al.*, 1999] [Duerig *et al.*, 2000] in the twinned monoclinic martensite phase. From this alone, it is clear that a precise knowledge of the influence of microstructural composition and processing techniques must be known to optimise the advantageous properties of superelastic NiTi material in the manufacture of biomedical devices. In this thesis, the R-phase will not be considered in the FEA computational models due to its inherent complex nature and the lack of knowledge in the published literature on appropriate modelling approaches to capture its material behaviour.

1.1.4 Microstructural Phases of NiTi

Austenitic NiTi is a hard, stiff material whereas martensitic NiTi is a softer, more ductile material with a lower yield stress [Van Humbeeck and Stalmans, 1998]. Such vast differences in material properties can be explained by the varying microstructural crystallographic structures of the two material microstructural phases. As mentioned, the austenitic NiTi phase has an ordered cubic B2 structure while the martensitic NiTi has a more complex twinned monoclinic B19’ structure. The stress-induced phase transformation from austenitic to martensitic NiTi, as described in Section 1.1.3, can

only occur within the temperature range between the austenite finish, A_f , and the martensite deformation, M_d , temperature. In this way, if temperatures exceed the martensite deformation M_d , temperature the energy (in the form of applied external stress) required to form martensite exceeds the energy to plastically deform the austenite via dislocation mobility, thereby making the structure a stable, non-transforming austenite phase. In a similar manner, at temperatures below the martensite finish, M_f , temperature the martensite is stable and a transformation to austenite cannot occur by the addition of an external stress. The fundamental fatigue behaviour of both microstructural phases will be discussed in Section 2.5.1.

1.1.5 Crystallographic Texture of NiTi

At a microstructural level, all metals are composed of individual grains. The grain size varies considerably depending on product form and processing techniques. Deformations within grains are attributed to slip in defined directions on defined planes. Therefore, the deformation behaviour of a grain in a given direction is dependent upon the global loading direction with respect to the grain orientation. As grains are randomly orientated within a metal, known as crystallographic texture, each grain deforms to a different extent at a local level when the structure is subject to an externally applied mechanical load. For most metal components, the grain size is so small relative to the size of the component that its effect on component performance is negligible, in that, no deformation within a single grain resulting from a preferential slip orientation dominates the overall component behaviour. For this reason, design engineers generally consider a component to be composed of a continuum material and hence are assumed to exhibit isotropic material behaviour. Associated design calculations, in particular in computational methods such as FEA, reflect this assumption in the use of bulk homogenous material properties to fully describe material behaviour.

However, when the grain size is of the order of the component size, for example in a biomedical stent strut, a different approach must be taken. When the grain size and specimen size are of the same order, the orientation of individual grains has a

significant effect on component behaviour. The resulting deviation from the expected homogenous isotropic material behaviour due to the grain to component size ratio is called the 'size effect'. A series of tensile tests carried out by [Murphy *et al.*, 2003] on electro-polished 316L stainless steel stent struts established that a size effect exists when the strut width is less than 500 μ m. Above this strut width it was determined that bulk properties are sufficient to fully describe the 316L stainless steel. The size effect was shown to reduce the strain to failure with decreasing specimen size. In the computational investigation of [Donnelly, 2012] it was concluded that the size effect could be attributed to a reduction in the level of constraint experienced by the individual grains and a consequent increase in granular compliance to external applied loading. It was also noted that there was a less uniform distribution of plastic strain and peak tensile stress associated with the decrease of stent strut dimensions which may lead to unexpected material behaviour. Designers of micro-sized products, such as endovascular stents with typically strut widths of approximately 100 μ m, should therefore be aware of such microstructural effects on a device's macroscopic behaviour for the prevention of unforeseen in vivo failures.

The existence of a size effect under tensile loading for materials such as 316L stainless steel raises the question as to whether a similar effect exists for NiTi under conditions of tensile and fatigue loading at a similar size scale. In the literature available to date, this size effect has not yet been studied with respect to NiTi materials. Again, this is directly applicable to a medical device such as a biomedical stent which undergoes an initial compressive and tensile loading upon crimping into the catheter and subsequent deployment, followed by continuous cyclic loading at a given mean and strain amplitude for the service life of the device of 400 million cycles [ASTM, 2013]. Due to the strut versus grain size ratio in a NiTi biomedical self-expanding stent, the deviating transformational behaviour of individual grains within the superelastic NiTi material may cause localised variations in the stress-strain response of the device resulting in an altered global anisotropic material response. Should such a microstructural effect exist, standard fatigue behaviour prediction tools such as characteristic constant life diagrams could potentially produce non-conservative

estimates of the safe working conditions. This may lead to reduced device performance and, in worst-case-scenario, may lead to unanticipated *in vivo* device failure with potential injury or even death to the patient.

1.2 Objectives of Thesis

NiTi self-expanding stents have proven beneficial in the medical device industry as they eliminate the need for a balloon, thus reducing the complexity of the *in vivo* deployment procedure. In addition, the ability of NiTi self-expanding stents to accommodate significant strains, through the advantageous trait of superelasticity, is highly desirable in stent design for stent flexibility, durability and conformance when placed within the human body. The use of superelastic NiTi in minimally invasive technologies, however, poses new challenges and demands a new set of design requirements. Implicit in the design of a successful biomedical device is a complete understanding of the problem to be addressed; first among these is the understanding of the mechanical and fatigue behaviour of the material from which the device will be made. There are several microstructural factors which influence the superelastic characteristics in NiTi which therefore must be thoroughly understood to ensure the safe design of biomedical endovascular self-expanding NiTi stent devices. These include, for example, the processing techniques and thermomechanical treatments, the volume fraction of SIM present in the material, the influence of grain orientation distribution (crystallographic texture) and inherent precipitate size and density. However, the influence of such microstructural effects on the fatigue behaviour of NiTi is not well understood in the published literature available to date.

Therefore, the objective of this PhD thesis is to computationally investigate the effect of microstructural phase and crystallographic texture on NiTi's fundamental mechanical behaviour and, thus, on its overall fatigue performance. This is achieved employing the commercially available FEA platform ABAQUS™, in addition to an in-built material subroutine UMAT/Nitinol, using geometrically relevant specimens and physiologically applicable stresses and strains. The influences of the individual microstructural phases of NiTi, in particular SIM, in addition to its crystallographic

texture, are first examined under quasi-static tensile-compression conditions as a potential indicator of its fatigue performance. Secondly, the fatigue behaviour of NiTi is explicitly examined using fatigue modelling methodologies which are capable of incorporating the micro-mechanical effects of varying microstructural phases and crystallographic textures. This thesis aims to highlight concerns with the current design procedures and protocols, which utilise homogenised material models, through the comparison of the results generated from standard continuum models against those generated from models which incorporate the effects of microstructure.

1.3 Thesis Structure

Chapter 1 of this thesis offers an introductory background knowledge to the major topics discussed in the investigations of this thesis. Subsequently Chapter 2, in the form of a literature review, discusses previously published literature on these topics in order to give context to the work undertaken as part of the thesis.

A concise summary of all experimental work completed is given in Chapter 3. Material characterisation procedures and techniques are performed in order to characterise the material behaviour of the NiTi specimens, namely a ‘v-strut’ stent subcomponent specimen and a micro-dogbone specimen, for extracting input data for the tensile computational models employed in Chapters 4 and 5, and the fatigue computational models employed in Chapters 6 and 7 of this thesis.

The investigation into the influence of microstructural phase on the uniaxial mechanical behaviour of NiTi is discussed in Chapter 4, while the investigation into the influence of crystallographic texture is discussed in Chapter 5. A background to the computational modelling methodology employed in these two chapters is presented in the introduction of Chapter 4.

The investigation into the effect of microstructural phase on fatigue behaviour of NiTi is discussed in Chapter 6, while the investigation into the influence of crystallographic texture is discussed in Chapter 7. As before, a background to the

computational modelling methodology employed in these two chapters is presented in the introduction of Chapter 6.

Finally, Chapter 8 offers a summary of the computational modelling methodologies employed in this thesis, accompanied by the results generated for each of the computational studies performed. Concluding remarks are subsequently offered on the novelty of this work in the field of NiTi computational research.

1.4 References

Abeyaratne R., Chu C. and James R.D., Kinetics and Hysteresis in Martensitic Single Crystals, *American Society of Mechanical Engineers, Applied Mechanics Division*, 1994, **189**, p. 85-98.

ASTM International Standards, ASTM F2477-07 Standard Test Methods for in vitro Pulsatile Durability Testing of Vascular Stents, 2013.

ASTM International Standards, ASTM F2516-14 Test Method for Tension Testing of Nickel-Titanium Superelastic Materials, 2014.

Auerbach D., Maeda J. and Steiner C., Hospital Stays with Cardiac Stents, 2009, *HCUP Statistical Brief #128*, Agency for Healthcare Research and Quality, 2012, Available at: <http://www.hcup.us.ahrq.gov/reports/statbriefs/sb128.pdf>.

Bain E.C., The Nature of Martensite, *Transactions of the American Institute of Mining and Metallurgical Engineers*, 1924, **70**, p 25-46.

Bhattacharya K., Microstructure of Martensite - How it Forms and how it gives rise to the Shape-memory Effect, *Oxford University Press Inc.*, New York, USA, 2003.

Buehler W.J., Gilfrich J.W., Wiley R.C., Effects of Low-Temperature Phase Changes on the Mechanical Properties of Alloys Near Composition TiNi, *Journal of Applied Physics*, 1963, **34(5)**, p 1475–1477.

Costa M.A., Sabate M., Kay I.P. and de Feyter F., Three-dimensional Intravascular Ultrasonic Volumetric Quantification of Stent Recoil and Neointimal Formation of Two New Generation Tubular Stents, *American Journal of Cardiology*, 2000, **85**, p 135-139.

Donnelly E., Ph.D Thesis, *Mechanical and Biomedical Engineering, National University of Ireland, Galway, Ireland*, 2012.

Duerig T., Some Unresolved Aspects of NiTi, *Materials Science and Engineering A*, 2006, **438-440**, p 69-74.

Duerig T., Melton K.N., Stockel D., Wayman C.M., Engineering Aspects of Shape Memory Alloys. London: Butterworth-Heinemann Ltd., 1990.

Duerig T., Pelton A. and Stockel D., An Overview of Nitinol Medical Applications, *Materials Science and Engineering A*, 1999, **273-275**, p 149-160.

Duerig T., Tolomeo D.E. and Wholey M., An Overview of Superelastic Stent Design, *Minimally Invasive Therapy & Allied Technologies*, 2000, **9(3/4)**, p 235-246.

Hane K. F. and Shield T.W., Microstructure in the Cubic to Monoclinic Transition in Ti-Ni Shape Memory Alloys, *Acta Materialia*, 1999, **9**, p 2603-2617.

Holtz R.L., Sadananda K. and Imam M.A., Fatigue Thresholds of Ni-Ti alloys near the Shape Memory Transition Temperatures, *International Journal of Fatigue*, 1999, **21**, p 137-145.

Hoffmann R., Mintz G.S., Haager P.K., Bozoglu T., Grube E., Gross M., Beythien C., Mudra H., vom Dahl J. and Hanrath P., Relation of Stent Design and Stent Surface Material to Subsequent in-stent Intimal Hyperplasia in Coronary Arteries Determined by Intravascular Ultrasound, *American Journal of Cardiology*, 2002, **89(12)**, p 1360-1364.

Kauffman G.B. and Mayo I., The Story of Nitinol: The Serendipitous Discovery of the Memory Metal and its Applications, *The Chemical Educator*, 1997, **1(2)**, p 1–21.

Liang Y., Taya M. and Mori T., Micromechanics of Stress-induced Martensitic Transformation in Mono- and Polycrystalline Shape Memory Alloys: Ni-Ti, *Proceeding of the Advanced Materials for the 21st Century: The 1999 Julia R. Weertman Symposium*, 1999, p 385-396.

Maier W., Windecker S., Lablanche J.M., Muhlberger V., Wijns W. and Meier B., The European Registry of Cardiac Catheter Interventions 1996, *European Heart Journal*, 2001, **22**, p 373 – 377.

Market Report, 2015 Opportunities in Global Medical Devices and Diagnostics, *Life Science Institute*, Huntington Beach, CA, USA, 2015. Available at: <https://www.lifescienceintelligence.com/market-reports-page.php?id=HRI-258>

Market Report, European Markets for Percutaneous Transluminal Coronary Angioplasty and Coronary Stenting Procedures, *Life Science Institute*, Huntington Beach, CA, USA, 2010. Available at: <http://www.lifescienceintelligence.com/market-reports-page.php?id=a-244>

McKelvey A.L. and Ritchie R.O., Fatigue-Crack Growth Behavior in the Superelastic and Shape-Memory Alloy Nitinol, *Metallurgical and Material Transactions A*, 2001, **32**, p 731-743.

Melton K.N., Mercier O., Fatigue of NiTi Thermoelastic Martensites, *Acta Metallurgica*, 1979, **27**, p 137-144

Miyazaki S., Sugaya Y. and Otsuka K., Effects of Various Factors on Fatigue Life of Ti-Ni Alloys, *Proceeding of the International Meeting on Advanced Materials*, 1988, **9**, p 251-256.

Murphy B.P., Savage P., McHugh P.E. and Quinn D.F., The Stress-strain Behaviour of Coronary Stent Struts is Size Dependent, *Annals of Biomedical Engineering*, 2003, **31**, p 686-691.

O'Brien B. and Bruzzi M.S., Shape Memory Alloys for Use in Medicine, *Comprehensive Biomaterials*, 2011, **1**, p 49–72.

Pieczyska E.A. and Tobushi H., Temperature Evolution in Shape Memory Alloy during Loading in various Conditions, *Proceedings of the International Conference on Quantitative InfraRed Thermography*, 2010, **10**, p 1-6.

Schlager O., Dick P., Sabeti S., Amighi J., Mlekusch W., Minar E. and Schillinger M., Long-segment SFA Stenting - The dark sides: In-stent Restenosis, Clinical Deterioration, and Stent Fractures, *Journal of Endovascular Therapy*, 2005, **12**, p 676-684.

Scheinert D., Scheinert S., Sax. J., Piorkowski C., Braunlich S., Ulrich M., Biamino G. and Schmidt A., Prevalence and Clinical Impact of Stent Fractures after Femoropopliteal Stenting. *Journal of the American College of Cardiology*, 2005, **45**, p 312–315.

Togni M., Balmer F., Pfiffner D., Maier W., Zeiher A.M. and Meier B., Percutaneous Coronary Interventions in Europe 1992-2001, *European Heart Journal*, 2004, **25**, p 1208-1213.

Uchil J., Mahesh K.K. and Ganesh Kumara K., Calorimetric Study of the Effect of Linear Strain on the Shape Memory Properties of Nitinol, *Physica B: Condensed Matter*, 2001. **305(1)**, p 1-9.

Van Humbeeck J. and Stalmans R., Characteristics of Shape Memory Alloys, *Shape Memory Materials*, Cambridge University Press, Cambridge, UK, 1998, p 149–183.

Vivet A. and LExcellent C., Observations and Analysis of Martensitic Phase Transformation on CuZnAl Single Crystals, *Journal de Physique IV*, 1998, **9**, p 411-418.

Waltz T., Kaztkhanov V. and Karnthaler H.P., Martensitic Phase Transformations in Nanocrystalline NiTi Studied by TEM, *Acta Materialia*, 2004, **52(1)**, p 137-147.

Wang F.E., Buehler W.J., Pickart S. J., Crystal Structure and a Unique Martensitic Transition of TiNi, *Journal of Applied Physics*, 1965, **36(10)**, p 3232–3239.

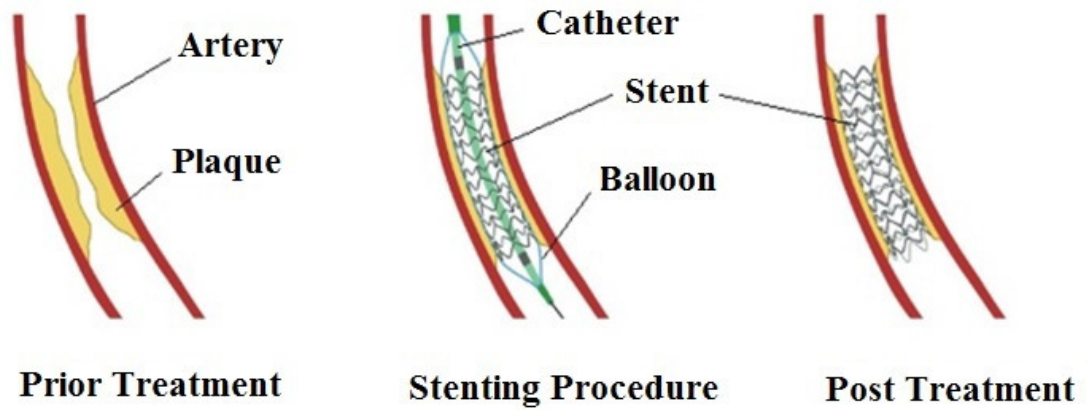


Figure 1.1: Schematic of a balloon expandable stenting procedure in an artery of a patient suffering from arterial stenosis.

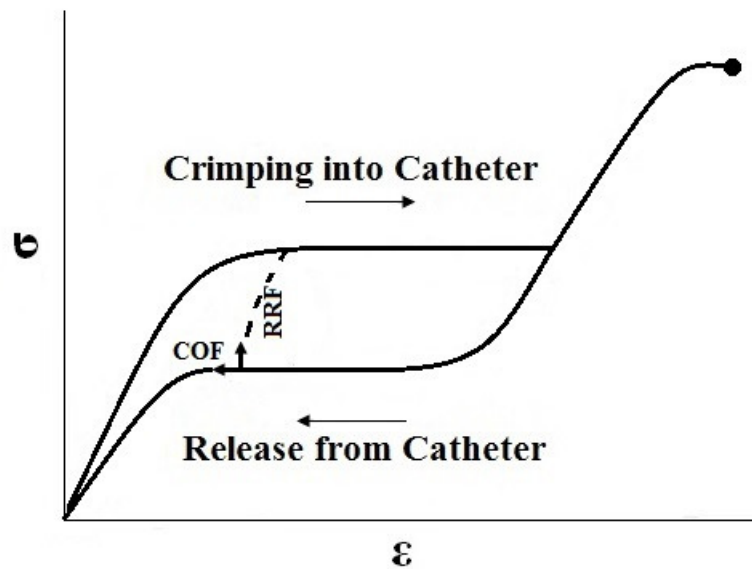


Figure 1.2: Schematic of uniaxial stress-strain curve of superelastic NiTi showing loading and unloading curves. Also displayed are the *in vivo* chronic outward force (COF) exerted by the stent on the artery in retaining it open and the stent's radial resistive force (RRF) in resisting stent collapse.

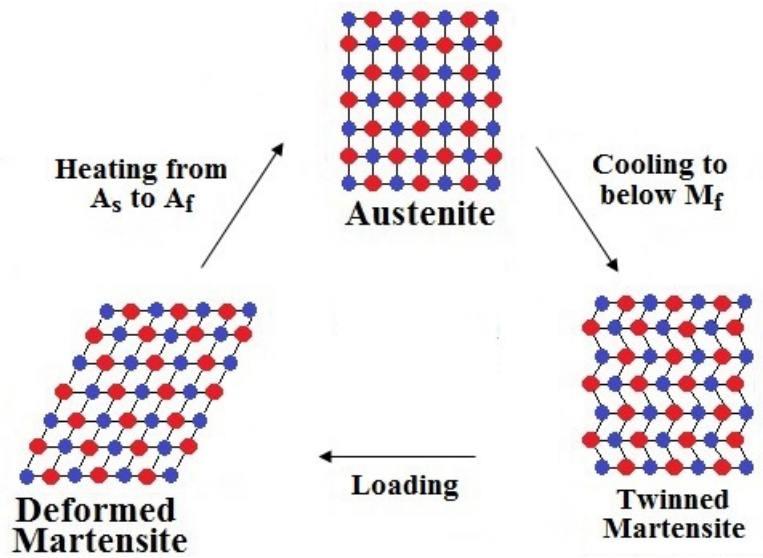


Figure 1.3: Shape memory effect: From the austenitic phase, lowering of the temperature below M_f , without the addition of stress, causes a phase transformation to twinned martensite. Upon loading, de-twinning occurs until fully deformed martensite remains. Upon unloading, martensite elastically recovers but retains some permanent deformation. Full recovery, to its original shape and austenite phase, is achieved upon heating from the austenite start to finish temperatures (A_s to A_f).

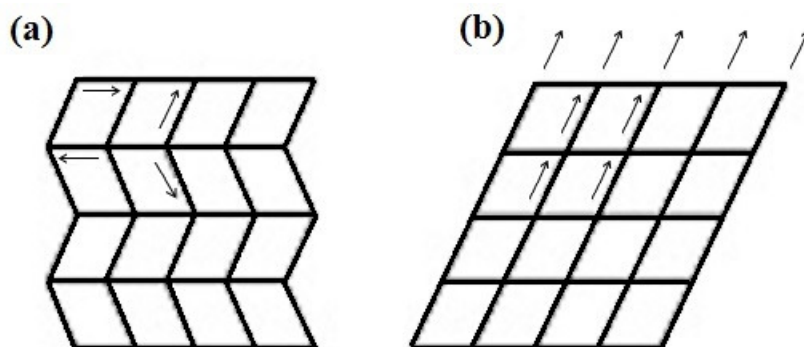


Figure 1.4: (a) Portion of a twinned martensite specimen composed of self-accommodating variants of martensite and (b) reorientation to one preferential direction upon loading resulting in a deformed martensite structure.

Chapter 2

Literature Review

2.1 Introduction

The main focus of this thesis is the computational examination into the effect of microstructure, namely, individual microstructural phases and crystallographic texture, on NiTi's mechanical and fatigue behaviour with application to NiTi biomedical stent devices. The purpose of this chapter is to review published literature in the field of NiTi research in order to provide context for the work of this thesis. Firstly, in Section 2.2, a brief history of the fatigue characterisation of metallic materials is given with a short discussion on various fatigue analysis methodologies employed by researchers. Following this, details of the chosen approach of fracture mechanics is given in Section 2.3 which delve into the presented theories behind both linear elastic fracture mechanics (LEFM) and elastic-plastic fracture mechanics (EPFM). An introduction to 'small' crack behaviour is given in this section describing the 'short crack problem' associated with the fracture mechanics analysis of devices such as biomedical stents due to the micro-scale component size. Finally, an overview of the concept of 'fatigue crack closure' is offered which has been used by researchers in explaining the 'actual' driving force for both long and small fatigue crack behaviour using the framework of fracture mechanics.

A review of relevant experimental studies is presented in Section 2.4 which specifically offers a further insight into the fatigue behaviour of superelastic NiTi stent devices. This section begins by presenting a brief outline of early NiTi fatigue studies and a discussion is offered with respect to the associated issue of thermal processing of the test specimens. Modern mechanical and fatigue testing of NiTi stent devices are subsequently discussed with respect to the effect of test temperature, sample configuration and selected loading modes. Section 2.5 offers a discussion on previous experimental investigations into the effect of microstructure on the uniaxial tension-compression mechanical behaviour and fatigue behaviour of NiTi with respect to microstructural composition and phase, crystallographic texture, and precipitate fraction, size and location. Finally, Section 2.6 offers a review of uniaxial tensile experimental studies which aim to capture both the micro- and macro-mechanical

behaviour of NiTi simultaneously. To end this chapter, a brief conclusion is given in Section 2.7 which summarises the main concepts discussed in this chapter and offers a context to the work of this thesis with respect to the published literature in the NiTi research field.

2.2 Fatigue Behaviour Characterisation

2.2.1 A Brief History of Fatigue

Fatigue is the term given to the progressive and localised accumulation of structural damage which leads to the weakening of a metallic material subjected to cyclic loading. If the loads are above a certain threshold, microscopic cracks will begin to form at stress concentrators located on or within the material. With continued cyclic loading, a dominant fatigue crack will propagate until it reaches a critical length for component failure to occur. This mechanism of failure in metallic components through cyclic loading is known as ‘mechanical fatigue’. This first arose as an issue of concern during the industrial revolution in Europe (1760-1830) when metallic components began to replace those made from natural materials. As the industrial revolution progressed, machines with metal frames and components became commonplace and the intense demands imposed on these ensured that they experienced a sufficient number of load cycles for fatigue failure to occur. Before the 1760s, metal was worked on manually using basic hand tools such as hammers, files, scrapers, saws and chisels. Consequently, the use of metal was kept to a minimum and relatively little was known about its fatigue behaviour before this time.

The term ‘fatigue’ was first coined by Englishman F. Braithwaite in the early 1850s [Braithwaite, 1854]. He employed the term exclusively to refer to the cracking of metallic components under continued cyclic loading. In subsequent years, a German engineer named A. Wöhler carried out extensive work (1858-1870) characterising the ‘fatigue life’ of railway axles. He observed that the strength of steel axles subjected to cyclic loading was noticeably lower than its static strength [Wöhler, 1867]. His pioneering work in this field led to the characterisation of fatigue behaviour in terms

of stress amplitude versus fatigue life (S-N curves) and to the concept of the endurance limit. An example S-N curve is given in Figure 2.1 which displays the concept of the endurance limit for a typical engineering metallic material. The experimental works of [Ewing and Rosenhain, 1900] and [Ewing and Humfrey, 1903] were the first to produce optical micrographs which explicitly display fatigue-induced slip bands on the surface of polished polycrystalline metallic specimens. These slip bands were observed to deepen following repeated cycling, in that, intrusions and extrusions were formed with repeated loading. The experimental work of [Thompson *et al.*, 1956] demonstrated that these slip bands persistently reappeared at the same locations during cyclic loading, even after some of the material was removed near the surface, and termed them 'persistent slip bands'. Fatigue cracks were found to initiate from these surface intrusions and extrusions, i.e. at locations of stress concentrators in the material, with subsequent propagation of the crack to a critical length for failure under continued loading. In this way, an understanding of the fundamental mechanisms contributing to fatigue failure had been developed; it was widely accepted that fatigue was governed by two distinct and separate mechanisms: (1) the initiation of a fatigue crack, and (2) the propagation of that single dominant fatigue crack to failure.

Up to the early 1900s research into the fatigue of metals dealt exclusively with mechanical fatigue, i.e. component failure under the application of cyclic loads. Since the 1900s researchers have become aware that, depending on the type of loading applied, there are many other types of fatigue which exist in metallic materials such as creep fatigue, thermo-mechanical fatigue, corrosion fatigue and fretting fatigue. By 1920, fatigue had evolved into a major field of study and the pace of developments in this area accelerated. For example, damage accumulation in metallic specimens was investigated by [Palmgren, 1924] and [Miner, 1945], while statistical theories of the strength of material were proposed by [Weibull, 1939]. Notch effects were examined by [Neuber, 1946] in which it was identified that the shape of a specimen significantly affects the fatigue behaviour. It was reported that square holes or sharp corners lead to elevated local stress concentrations where fatigue cracks can initiate, while round holes and smooth transitions or fillets increase the fatigue strength of a specimen. Since the

fatigue of biomedical stent components refers to the repeatedly applied variations in external stresses/strains imposed on the stent by the vessel anatomy in which it is placed, mechanical fatigue will therefore be the only type of fatigue failure analysis considered in the computational investigations of this thesis.

2.2.2 Fracture Mechanics Approach to Fatigue Analysis

One of the main goals of fatigue analysis is to develop reliable relationships and parameters for the characterisation of the fatigue crack growth rate behaviour of materials which form a basis for the safe design of commercial products and components. In this way, it aims to quantify the intrinsic resistance of a given material to fatigue crack growth for different combinations of applied stress, specimen and crack geometry. Although the fatigue failure of metallic materials was experimentally identified by the development of slip bands in the early 1900s, the mathematical framework for characterising such behaviour was not yet available at that time. The stress analysis of [Inglis, 1913] and the energy concepts of [Griffith, 1921] only provided the mathematical tools for characterising fracture in brittle materials. It was the work of [Irwin, 1957] on crack tip stress singularities which extended this field of fracture analysis to cover metallic materials. This new field, of linear elastic fracture mechanics (LEFM), related Irwin's stress intensity factor, K , to the increment of cyclic crack growth per cycle, da/dN . The American mathematician P.C. Paris made further important contributions to this field through the suggestion that, for an initiated crack, the increment of cyclic crack growth, da/dN , could be related to the stress intensity factor range, ΔK [Paris *et al.*, 1961] [Paris and Erdogan, 1963]. In this way, the 'Paris law' provides a relationship between crack size and the remaining number of cycles before failure. The Paris law has since become the established method for quantifying fatigue crack propagation in metallic materials; this will be discussed in Section 2.3.1.

With the application of fracture mechanics concepts to characterise fatigue failure mechanisms, increasingly more attention was given by researchers to sub-critical crack growth. As a result, it was concluded that all metallic materials are inherently flawed and therefore a 'defect tolerant approach' to fatigue analysis should

be taken. This approach assumes the useful fatigue life of a component under cyclic loading is defined as the number of cycles to propagate a dominant flaw in the material to a critical size for failure. This is in contrast to the classical ‘total life approach’ in which the total number of cycles to failure for a component under cyclic loading is assumed to comprise of both the initiation of a fatigue crack and the propagation of this crack to failure. However, this over-estimates the useful fatigue life of the component since this approach assumes it necessary to also include the number of cycles to initiate a crack. As a result, with respect to the fatigue investigations described in Chapters 6 and 7 of this thesis, only aspects relating to a defect tolerant approach to the mechanical fatigue failure of NiTi will be considered.

2.3 Fatigue Crack Behaviour Characterisation

2.3.1 Linear Elastic Fracture Mechanics

As previously stated, the fatigue life of a cyclically loaded metallic component is defined as the number of cycles to propagate a dominant flaw in the material to a critical size for failure when using a defect tolerant approach to fatigue analysis. The prediction of such crack growth rates relies on empirical crack growth laws based on fracture mechanics. The rate of growth of a fatigue crack subjected to constant amplitude of stress reversals is expressed in terms of the crack length increment per cycle, da/dN . In the early 1960s, [Paris *et al.*, 1961] and [Paris and Erdogan, 1963] proposed that the linear elastic fracture mechanics (LEFM) characterisation of the rate of fatigue crack growth for an applied cyclic stress should be based on the stress intensity factor range:

$$\Delta K = K_{max} - K_{min}, \quad \text{EQ. 2.1}$$

where K_{max} and K_{min} are the maximum and minimum values, respectively, of the stress intensity factor during a fatigue stress cycle and are defined as:

$$K_{max} = Y \sigma_{max} \sqrt{\pi a}; \quad K_{min} = Y \sigma_{min} \sqrt{\pi a}, \quad \text{EQ. 2.2}$$

where Y is defined as the collective geometry term, σ_{max} and σ_{min} are the maximum and minimum values, respectively, of the imposed fatigue stress cycle and a is the crack length.

For an edge cracked metallic specimen under cyclic loading, as will be the condition examined in the computational fatigue investigations of Chapters 6 and 7 of this thesis, the stress intensity factor range, ΔK , is given by:

$$\Delta K = Y \Delta\sigma \sqrt{\pi a}, \quad \text{EQ. 2.3}$$

where Y has a value of 1.2. [Paris *et al.*, 1961] and [Paris and Erdogan, 1963] showed that the fatigue crack growth rate per cycle for a fatigue crack can be related to the stress intensity factor range by the power law relationship, the Paris law, which is given by:

$$\frac{da}{dN} = C(\Delta K)^m, \quad \text{EQ. 2.4}$$

where C and m are scaling constants. The Paris law for characterisation of fatigue crack growth, however, only holds true for a fixed material microstructure, environment and load ratio (R-ratio) within the fatigue crack growth regime labelled 'B' in Figure 2.2; this will be discussed further in Section 2.3.2.

Over the past two decades, a considerable amount of data has been gathered in relation to the fatigue crack growth rate behaviour of superelastic NiTi. In two separate experimental studies on this topic, disk-shaped 50Ni-50Ti at. % NiTi compact-tension samples were used by [McKelvey and Ritchie, 2001] in one, while square-shaped compact-tension 50.8Ni-49.2Ti at. % NiTi samples were used by [Robertson and Ritchie, 2007] in the other. An induced austenite finish, A_f , temperature of slightly less than 37°C was achieved in the specimens through heat treatment procedures by both researchers. In this way, the specimens would exhibit the characteristic superelastic behaviour when tested at 37°C. In both studies, fatigue crack growth rate behaviour of the superelastic NiTi specimens were shown to display a clear dependence on load

ratio (R-ratio). Specifically, both studies reported an increasing crack growth rate and decreasing fatigue thresholds being measured with increasing positive R-ratio. Where the load ratio, R , is defined by:

$$R = \frac{\sigma_{min}}{\sigma_{max}} = \frac{K_{min}}{K_{max}}. \quad \text{EQ. 2.5}$$

For the appropriate application of LEFM to cyclic loading, it should be noted, an assumption is made that the zone of plastic deformation ahead of the advancing fatigue crack is relatively small in an otherwise elastic field. The extent of the plastic zone, r_p , ahead of the crack tip for an applied mode I monotonic stress under plane strain conditions was approximated by [Irwin, 1960] as:

$$r_p = \frac{1}{3\pi} \left(\frac{K_I}{\sigma_y} \right)^2, \quad \text{EQ. 2.6}$$

where σ_y is the yield stress of the material. For cyclic loading, there also exists a region of reversed flow at the crack tip. This is called the cyclic plastic zone, r_c , and is derived by replacing K_I by ΔK_I and σ_y by $2\sigma_y$ in the aforementioned approximation of the plastic zone in EQ. 2.6, such that the cyclic plastic zone for plane strain conditions was approximated by [Rice, 1967] as:

$$r_c = \frac{1}{3\pi} \left(\frac{\Delta K_I}{2\sigma_y} \right)^2. \quad \text{EQ. 2.7}$$

The use of LEFM has undoubtedly proven itself as being extremely useful for characterising the crack growth rate behaviour of fatigue cracks. However, the use of ΔK as an actual driving force for crack extension limits itself to characterising fatigue crack growth rates which are independent of crack length and follow the traditional Paris law. Yet, ‘small’ fatigue cracks exist which do not obey such laws and a different approach must therefore be taken to analysis their behaviour.

2.3.2 Small Fatigue Crack Behaviour

Thus far, fatigue cracks referred to in this chapter allude to ‘long’ fatigue cracks which are typically of several millimetres or more in length. The crack growth rates for such cracks are independent of the crack length and, as described in Section 2.3.1, they follow the classic Paris law of a linear variation in the log of the increment of cyclic crack growth, da/dN , with the log of the stress intensity factor range, ΔK . This behaviour is displayed in the regime labelled ‘B’ in Figure 2.2 of the typical fatigue crack growth rate behaviour of a standard metallic material. However, as shown in this schematic, three distinct regimes of crack growth can be identified. At extreme values of ΔK , both above and below the Paris regime, there is an increase in crack growth rate with increasing ΔK . In Figure 2.2, regime ‘A’ is specifically associated with the growth of ‘small’ cracks, while regime ‘C’ is associated with the rapid increase of long crack growth rates causing catastrophic failure. As illustrated in regime ‘A’, small cracks have the ability to grow at stress intensities lower than the experimentally measured stress intensities threshold for long cracks, ΔK_{th} [Pearson, 1975]. In addition, as identified in regime ‘A’, crack growth rates of small cracks are shown to exceed those of long cracks at theoretically equivalent stress intensity ranges, ΔK [Suresh and Ritchie, 1984] [Lankford *et al.*, 1982]. Such crack growth rates for small cracks at thresholds below ΔK_{th} have therefore been associated with the absence of crack closure.

As a result biomedical stent struts, which have dimensions comparable to the microstructural size scale, will exhibit an initial accelerated crack growth rate due to the presence of an initial small crack; these effects will subsequently diminish with the increase in crack length to that of a long crack. Therefore, small cracks are intrinsically significant to consider during the early stages of fatigue crack growth rate behaviour for the most accurate prediction of fatigue life. However, such crack growth behaviour has not been satisfactorily analysed in terms of available theories in fracture mechanics and has been termed the ‘short crack problem’ [Ritchie and Lankford, 1986]. In applying the fracture mechanics Paris law, this small crack growth rate behaviour is

neglected as this methodology only considers long crack growth rate behaviour. However, if small crack behaviour in a stent strut is neglected, there is a very minimal period of long crack growth before the critical size for failure is reached due to the small cross-sections in biomedical devices. In this way, conventional fracture mechanics has proven to be unsuitable for analysing the fatigue life of small components such as biomedical stents. As a result, an alternative elastic-plastic fracture mechanics (EPFM) approach must be taken which allows for the incorporation of this small crack growth rate behaviour through employing the concept of fatigue crack closure.

2.3.3 Fatigue Crack Closure

Conditions exist in which the local stress intensity factor range at the crack tip varies significantly from the nominally applied stress intensity factor range. This local 'effective' stress intensity factor range, ΔK_{eff} , represents the 'actual' driving force for fatigue crack growth. The main mechanism which is accepted to be responsible for this difference, between the apparent and actual driving force for fatigue crack growth, is termed 'fatigue crack closure'. This mechanism describes the premature closure of the opposing crack faces of a fatigue crack during cyclic loading. An important contribution in this field came from the aforementioned experimental works of [Elber, 1970] and [Elber, 1971] (Section 2.2.1). From these studies it was found that the opposing fracture surfaces came into contact in the wake of the advancing crack tip. Furthermore, it was reported that fatigue cracks could remain closed even when subjected to cyclic tensile loads. Elber argued that a zone of residual tensile deformation is left in the wake of a fatigue crack tip which can be characterised using the maximum applied stress intensity, K_{max} (EQ. 2.2). As the crack advances, through fatigue crack growth, this permanently deformed zone is left in the wake of the advancing crack tip. This plastic zone manifests itself as a region of dilated material on the crack fracture surfaces. This 'plasticity-induced crack closure' may result in the crack faces coming into contact during unloading, before the applied far-field stress has fully unloaded, such that the crack tip experiences only part of the applied stress

range. In this way, the process of crack closure has been shown to lead to an apparent retardation of the fatigue crack growth. Hence, during testing of experimental specimens, the test material's resistance to fatigue crack growth is observed to be enhanced. In contrast, small fatigue cracks do not experience the effects of crack closure and therefore will grow at relatively faster rates than long cracks.

In the 1980s, Suresh pioneered the field of fatigue crack closure research and experimentally established that, in addition to plasticity-induced crack closure (PICC), other types of crack closure phenomena exist which are induced by a variety of mechanical, microstructural and environmental factors [Suresh and Ritchie, 1981] [Suresh and Ritchie, 1982] [Suresh and Ritchie, 1984]. It was also recognised by [Pineau and Pelloux, 1974] and [Hornbogen, 1978] that the phase transformation mechanism at the crack tip can also lead to crack closure effects in stress-induced phase transforming materials such as superelastic NiTi. This phenomenon of 'transformation-induced plasticity' (TRIP) is characterised by the phase change at the crack tip leading to a net increase in the volume of the transforming region in the wake of the advancing crack [Iacoviello *et al.*, 2012]. As the enlarged material in the transformed zone is left in the wake of the advancing fatigue crack tip, a net reduction in the crack opening displacement ensues. With reference to fatigue crack closure, crack tip phase transformation is analogous to crack tip plasticity in the sense that compressive residual stresses are also induced during cyclic tensile loading. Furthermore, in both cases, the residual displacements left in the wake of the extending fatigue crack act to close the crack prematurely at a far-field tensile stress.

2.3.4 Elastic-Plastic Fracture Mechanics

As discussed in Section 2.3.2, the use of the linear elastic fracture mechanics (LEFM) parameter ΔK can lead to serious non-conservative estimations of crack growth rates with respect to small fatigue cracks. This can be attributed to the fact that the plastic zone ahead of the crack tip can no longer be assumed to be negligible. For situations where the LEFM condition does not hold, elastic-plastic fracture mechanics (EPFM) provides a means for characterising fatigue crack growth. Many researchers,

such as [Dowling and Begley, 1976] and [Dowling, 1977], employed a cyclic form of the EPFM parameter J -integral, ΔJ , to characterise fatigue fracture at room and elevated temperatures. The experimental documentation of the reasonably good characterisation of fatigue crack growth under elastic-plastic conditions from such studies was the main justification made by [Suresh, 1998] for the acceptance of the application of the J -integral to characterise fatigue crack growth under cyclic loading. In addition, the use of ΔJ for cyclic loading conditions has also been deemed satisfactory in arguments made in the theoretical papers by [Lamba, 1975], [Wuthrich, 1982] and [Kumar *et al.*, 1981]. A large number of ΔJ solutions and estimation schemes for the numerical modelling of elastic-plastic fracture analysis problems have since become readily available to characterise the fatigue crack driving force for fatigue crack growth behaviour for many different materials and geometries, as summarised in the paper by [McClung and Sehitoglu, 1988].

At present, ΔJ appears to be the parameter of choice for the characterisation of elastic-plastic fatigue crack growth. It has been confirmed that ΔJ represents, with sufficient accuracy, the ‘actual’ driving force for crack extension. In this way, its use can be justified to characterise the sub-threshold fatigue crack growth of small cracks in metallic materials. The parameter ΔJ has been successfully used by dozens of researchers and engineers during the last three decades to correlate actual fatigue crack growth data. Following from such studies, [Lamba, 1975] and others, such as [Wuthrich, 1982] and [Kumar, 1981], it has been agreed that the correct estimate of ΔJ parameter is made up for the monotonic J expression of [McClung, 1997]:

$$J = \frac{K^2}{E'} \left\{ 1 + \frac{Y^2}{c_2} \left(\frac{n-1}{n+1} \right) \left[\frac{(\sigma_\infty/\sigma_0)^2}{1 + (\sigma_\infty/\sigma_0)^2} \right] \right\} + \alpha \sigma_0 \varepsilon_0 a h_1 \left(\frac{\sigma_\infty}{\sigma_0} \right)^{n+1}, \quad \text{EQ. 2.8}$$

with the single values of K and σ replaced with their range ΔK and $\Delta \sigma$ in the EPFM parameter ΔJ . In addition to the plastic term being modified to approximately correct for the effects of reversed deformation, thus giving:

$$\Delta J = \frac{\Delta K^2}{E'} \left\{ 1 + \frac{Y^2}{c_2} \left(\frac{n-1}{n+1} \right) \left[\frac{(\sigma_\infty^{max}/\sigma_0)^2}{1 + (\sigma_\infty^{max}/\sigma_0)^2} \right] \right\} + 4\alpha \sigma_0 \varepsilon_0 a h_1 \left(\frac{\Delta \sigma_\infty}{2\sigma_0} \right)^{n+1}, \quad \text{EQ. 2.9}$$

where σ_∞ is the nominally applied far-field stress, C_2 for plane strain is 6 and Y has a value of 1.2 and is defined as the collective geometry term in the elastic K expression: $K = Y\sigma_\infty^{max}\sqrt{\pi a}$. The Ramberg-Osgood coefficients α , ε_0 and σ_0 , and the strain hardening exponent n are fit to an experimental true tensile stress–logarithmic strain curve for the given metallic material under investigation.

Therefore, for a given initial small crack length and a nominally applied stress amplitude the effective range of the J -integral, ΔJ_{eff} , which incorporates the effects of fatigue crack closure provides a means of characterising the crack tip conditions which is often given by [McClung *et al.*, 1997]:

$$\Delta J_{eff} = \frac{(U\Delta K)^2}{E'} \left\{ 1 + \frac{Y^2}{C_2} \left(\frac{n-1}{n+1} \right) \left[\frac{\left(\frac{\sigma_\infty^{max}}{\sigma_0} \right)^2}{1 + \left(\frac{\sigma_\infty^{max}}{\sigma_0} \right)^2} \right] \right\} + 4\alpha\sigma_0\varepsilon_0 ah_1 U \left(\frac{\Delta\sigma_\infty}{2\sigma_0} \right)^{n+1}, \quad \text{EQ.2.10}$$

where U is the effective stress range ratio due to crack closure given by:

$$U = \frac{\sigma_{max} - \sigma_{open}}{\sigma_{max} - \sigma_{min}} = \frac{\Delta K_{eff}}{\Delta K}, \quad \text{EQ.2.11}$$

and σ_{open} is the stress at which the crack surfaces become completely separated.

In the fatigue modelling methodology used to describe the fatigue behaviour of superelastic NiTi in Chapters 6 and 7 of this thesis, ΔK_{eff} (as identified in regime ‘A’ in the schematic of Figure 2.2 displaying small fatigue crack growth behaviour) is used to characterise the long crack growth behaviour and the initial growth of small cracks in place of the nominally applied stress intensity factor range, ΔK . However, as the near-tip plastic zone size for small cracks can no longer be assumed to be negligible the correlating parameter, ΔJ_{eff} , is used to provide a means of characterising the crack tip conditions [McClung *et al.*, 1997]. The principal of adopting the closure-corrected EPFM parameter ΔJ_{eff} was confirmed as the most suitable approach for small cracks in the experimental work of [Richie *et al.*, 1986] and [Pineau, 1986]. This approach was also employed in the computational work of [Bruzzi and McHugh, 2002] in the fatigue modelling of particulate reinforced metal matrix composites. This work, in

relation to the modelling methodology adapted for use in the computational fatigue analysis of this thesis, will be discussed in greater detail in Section 6.2.

2.4 Fatigue Testing of NiTi Biomedical Stents

The fatigue behaviour of engineering materials is typically studied by either an initiation dominated approach, using either the stress- or strain-life approach, or alternatively by the conventional fracture mechanics-based fatigue crack growth methodology. However, as discussed in Section 2.3.2 of this review, the traditional fracture mechanics approach only considers long crack behaviour and therefore would not be applicable to fully characterise failure in the micro-scaled size NiTi biomedical stent devices due to the size scale of the device. The stress- and strain-life approaches to fatigue analysis are based on the observation that the response of the metallic material in critical locations is either stress, or strain dependent. The unique non-linear shape of uniaxial tension-compression curve for superelastic NiTi (Figure 1.2), lends itself to strain-control experimental tests as the stress-induced phase transformation will be in progress at non-unique stress values. Therefore, the strain-life approach is widely accepted to be the most applicable when performing experimental fatigue testing of superelastic NiTi stent specimens. As a result, the review of this section will mainly focus on experimental investigations into the fatigue behaviour of superelastic NiTi stents components which employ the strain-life approach to fatigue analysis.

NiTi specimens capable of representing the fatigue behaviour of stent subcomponents is a relatively new research topic since the use of NiTi as a medical implant device has only become viable since the early 1990s. The ASTM standard F2516-14 [ASTM, 2014] and ASTM standard F2477-07 [ASTM, 2013] describe the current tensile and fatigue testing procedures for superelastic NiTi, respectively. These standards, previously discussed in greater detail in Section 1.1.2, highlight several complexities associated with testing NiTi due to its characteristic superelastic properties. Following ASTM standard 2477-07, stent devices are required to be mechanically fatigue tested at various physiologically relevant conditions to a total fatigue life of 400 million cycles. Employing the fail/no-fail approach to the results

gathered, a constant life diagram is constructed from which the safe design of NiTi biomedical stents is based. An example constant life diagram, also known as the ‘Goodman diagram’ is shown in Figure 2.3 for a typical engineering metallic material. As demonstrated in this figure, it follows a conventional linear decrease in fatigue performance with increasing mean strain, i.e. the ‘Goodman approach’ to fatigue failure. However, a number of factors may influence the accuracy of results from the experimental testing of NiTi which will be discussed in this section, namely, influence of thermal processing on the NiTi specimen (Section 2.4.1), the test temperature (Section 2.4.2), specimen configuration (Section 2.4.3) and chosen loading modes during testing (Section 2.4.4).

2.4.1 Effect of Thermal Processing

Over a decade after its discovery, the work of [Melton and Mercier, 1979] pioneered the field of NiTi mechanical fatigue research. Beginning in the mid-1980s, [Miyazaki, 1988] and [Miyazaki and Otsuka, 1989] also made significant initial contributions to the field with their novel experimental investigations into the fatigue properties of superelastic NiTi. However, a number of issues arise when discussing early investigations into the fatigue behaviour of superelastic NiTi. These include the aforementioned different initiation dominated methods by which to experimentally evaluate the fatigue behaviour of NiTi, namely, the stress- or strain-life approach. Therefore, data obtained by one test method may not provide enough understanding of the results obtained from another test method due to the characteristic stress plateau of superelastic NiTi in which large strain changes occur in the material at non-unique stress values. However, most importantly, early fatigue studies employed experimental specimens that were typically tested in the annealed condition; this will be discussed in greater detail in this section. Nevertheless, the significant work carried out by the early researchers had set the foundations on which the unique behaviour of NiTi was identified. In particular, [Melton and Mercier, 1979] documented several important trends which sparked much interest within the research field:

- Superelastic NiTi provides a longer life and greater endurance limits than thermal martensite subjected to stress-controlled fatigue.
- The fatigue life of thermal martensite, however, is superior to superelastic NiTi subjected to strain-controlled fatigue.
- Repeated stress-controlled cyclic loading of superelastic NiTi leads to an increase in strain at constant stress amplitude, implying there is an accumulation of plasticity with cycling.
- Repeated strain-controlled cyclic displacement, at constant strain amplitude, was shown to lead to cyclic hardening of superelastic NiTi.

However, the effect of the thermo-mechanical annealing of these early test specimens should not be neglected. To ensure NiTi self-expanding stents expand and recover to the designed shape after deployment, thermo-mechanical treatments are applied to the final product to shape-set and optimise the superelastic properties at the body temperature. Thermo-mechanical processes have been shown to significantly affect NiTi's microstructure and, depending on the time and temperature scale used, can lead to marked changes in its transformational behaviour and therefore in the material's mechanical properties. The effects of thermo-mechanical treatments on the martensitic transformation behaviour of superelastic NiTi has been extensively studied and characterised by a number of researchers, including [Huang and Liu, 2001], [Gall and Maier, 2002], [Wang *et al.*, 2004], [Li *et al.*, 2005], and [Nurveren and Akdogan, 2008]. In a recent study by [Liu *et al.*, 2008], efforts were made to identify the effects of heat treatments on the transformational temperatures and corresponding mechanical properties of superelastic NiTi thin wires. The experimental results show that the shape-setting results were stable when wires were constrain-treated at 500°C and 550°C and the ageing times were longer than 10 minutes. Austenite finish, A_f , temperatures of the wires increased with ageing time and decreased with ageing temperature after an initial increase. As NiTi self-expanding stents are designed to exploit their superelasticity upon deployment into a target vessel, this study demonstrates the necessity of a design engineer to thoroughly understand and appreciate the effect of heat treatments on the transition temperatures and

characteristic superelastic plateaus which will be subsequently exhibited by the device material.

The effects of thermo-mechanical treatments on NiTi's microstructure with respect to its mechanical and fatigue properties has been extensively studied and characterised by a number of researchers, including [Khalil-allafi *et al.*, 2002], [Gall *et al.*, 2008], [Sergueeva *et al.*, 2003], [Robertson *et al.*, 2006] [Stankiewicz *et al.*, 2006], [Liu *et al.*, 2008] and [Paryab *et al.*, 2010]. In a study by [Robertson *et al.*, 2004] an attempt was made to correlate the effect of heat treatments on the fatigue behaviour of superelastic NiTi. Three different heat treatments were performed on tubular specimens in order to vary grain size and Ni-rich precipitates densities. It was revealed that increasing the annealing time and temperature resulted in improved fatigue lifetimes. Specifically, annealing at 500°C for 90 minutes produced endurance strength of approximately 0.8%, compared to endurance strength of only approximately 0.2% for shorter annealing treatments for 41 and 37 minutes. It is clear that processing plays a key role in the fatigue behaviour of superelastic NiTi and thus in NiTi self-expanding biomedical stent devices. Despite the quantity of research, knowledge of the heat treatment parameters appropriate for medical applications is still far from sufficient. It can be concluded, however, that it is essential for test specimens to be subjected to similar processing and heat treatments as stent devices to accurately represent the behaviour of the stent to achieve the most accurate fatigue life estimates for optimal device design.

2.4.2 Effect of Test Temperature

The effect of test temperature on the mechanical behaviour of NiTi wire was demonstrated in a comprehensive study carried out by [Pelton *et al.*, 2000]. A systematic increase in the loading and unloading plateau stresses with increasing test temperature was observed, as shown in Figure 2.4. As discussed in Section 1.1.4 of Chapter 1, below the martensite finish, M_f , temperature (i.e. 0°C in this study) the structure is in the stable martensitic microstructural phase and above the martensite deformation, M_d , temperature (i.e. 150°C in this study) the material exhibits the

conventional deformation of the stable austenitic microstructural phase. Intermediate temperatures all show classic transformational superelasticity of the NiTi material. Accordingly, it can be deduced that there exists an optimum temperature for the material to demonstrate its advantageous superelastic behaviour, namely, just above the austenite finish, A_f , temperature. At increasing temperatures above the A_f temperature, the austenitic microstructural phase is shown to become more thermodynamically stable such that higher stresses are required to transform the austenite to the martensite phase [Pelton *et al.*, 2000]. Therefore during the production of a NiTi self-expanding stent, the A_f temperature is specifically tuned to remain below body temperature, i.e. 37°C, for optimum *in vivo* performance.

From this study alone it has been clearly demonstrated that the material properties of superelastic NiTi are highly temperature-dependent. As a result, fatigue testing of biomedical stent devices should be carried out at body temperature, i.e. 37°C, to simulate *in vivo* conditions experienced by the device. During testing, the martensite phase is stress-induced upon loading with the release of latent heat. Therefore the exothermic phase transformation, and endothermic reverse transformation, may also have a significant influence on the uniaxial stress-strain response of the highly temperature-dependent superelastic NiTi material. This effect has been studied using superelastic NiTi dogbone specimens by [Gadaj *et al.*, 1999], and more recently by [Pieczyska and Tobushi, 2010], under tensile loading. In both studies, the temperature changes were measured in a contactless way by recording the infra-red radiation emitted by the surface of the specimen. Both studies report complimentary results such that the temperature distribution on the surface of the tensile specimen was uniform during straining below the austenite start, A_s , temperature, while bands of higher temperature were reported which corresponded to localised SIMT in the specimen above the austenite finish, A_f , temperature. In the study by [Gadaj *et al.*, 1999], the temperature change was demonstrated to increase with increasing test temperature.

The effect of the exothermic/endothermic phase transformation was also studied by [Yin and Sun, 2012] this time under cyclic loading employing both computational

and experimental methods. Reported results confirm that temperature oscillations occur primarily due to the release/absorption of latent heat during cyclic phase transformation. Therefore, to ensure accuracy of data, test temperature must be strictly controlled during tensile and fatigue testing to promote heat exchange between the NiTi specimen and the ambient environment. This is typically achieved experimentally using a fan-controlled environmental chamber. This hypothesis was investigated by [Johe, 2009] whereby NiTi specimens were tested in both static air and in a fan-circulated environment. It was demonstrated that a significant improvement in heat exchange was displayed when a fan was employed, leading to more accurate and repeatable results. Improved heat exchange also allows higher strain rates to be used due to the faster dissipation of heat from the specimen, and therefore reducing the overall testing time required. This concept will be addressed again in Chapter 3 during the discussion of the tensile testing procedure of the NiTi specimens used in this thesis.

2.4.3 Effect of Specimen Configuration

Early researchers employed various experimental specimen shapes such as bars, rods, wires, and plates when attempting to characterise the fundamental tensile and fatigue behaviour of superelastic NiTi. However, biomedical endovascular stent devices present an entirely different deformation profile than those studied by early investigators and therefore a different approach is required. In order to accurately represent the mechanical response of a biomedical stent device, a suitable specimen configuration must be selected [Robertson *et al.*, 2006] [Duerig *et al.*, 2000]. This can be attributed to the micro-size scale of the stent struts in the device which could introduce stress and strain gradients which would vary dramatically from a bulk material test specimen. It is common practice, therefore, to employ a stent subcomponent specimen during tensile and fatigue testing procedures of stent materials for the generation of the most accurate results. In this way, the effect of cyclic fatigue loading on a stent device can be successfully analysed employing a less complex configuration and thus eliminating the need for complete device testing.

A commonly used configuration to represent stent geometry is the ‘diamond’ stent subcomponent specimen. The diamond configuration, often cut directly from a stent, is used to examine the varying deformation profiles and potential locations of failure in the hinged joints of the device. In experimental fatigue testing studies carried out by researchers such as [Tolomeo *et al.*, 2000], [Pelton and Gong, 2002], [Pelton *et al.*, 2003] and [Pelton *et al.*, 2008], the diamond subcomponents were successfully employed. In a paper by [Perry *et al.*, 2002], diamond shaped specimens are also used to determine the factor of safety in the design process for a superelastic NiTi self-expanding stent. The ‘v-strut’ stent subcomponent specimen configuration has also been employed by many researchers such as [Tolomeo *et al.*, 2000], [Pelton *et al.*, 2008], [Harrison and Lin, 2000] and [Dordoni *et al.*, 2015] in the computational and experimental fatigue analysis of NiTi self-expanding stents. The ‘v-strut’ subcomponent specimen is representative of the single hinged connection of a strut in an endovascular stent device. Details of all fatigue investigations cited in this section will be discussed in greater detail in Section 2.4.4 below.

2.4.4 Effect of Loading Conditions

NiTi self-expanding stents are crimped to fit within a catheter to allow *in vivo* deployment. This process exerts a significant single compressive strain overload, typically 8-12%, on the hinged struts of the NiTi stent geometry [Duerig *et al.*, 2000] [Pelton *et al.*, 2008]. Upon deployment from the crimped condition into the target vessel the superelastic stent begins to expand at body temperature, i.e. 37°C. However, as it is slightly oversized by design with respect to the vessel diameter it experiences an ‘interference fit’. This interference fit produces an *in vivo* compressive mean strain on the NiTi stent device. Furthermore, the physiological movement within the vessel, attributed to the cardiac systolic-diastolic cycle, exerts strain amplitudes on the stent structure. The ability to predict the fatigue life of superelastic NiTi subjected to cyclic motion is therefore critical for the safe design of NiTi biomedical endovascular stents. When investigating the fatigue behaviour of stent materials it is therefore essential to

simulate the *in vivo* loading conditions, with respect to the imposed compressive mean strains and strain amplitudes, for an accurate prediction of fatigue life.

The effect of mean strain on the fatigue behaviour of NiTi was first explored by [Tabanli *et al.*, 1999] and [Tabanli *et al.*, 2001]. Cyclic loading of superelastic NiTi hypo-tubing was performed at room temperature for various levels of mean strain. However, the specimens were not subjected to stent-like processing and were not tested at 37°C, i.e. body temperature. The key issue of concern, however, lies in the tensile loading modes used rather than the correct compressive loading modes. As a result, maximum strain fields were experienced on the inside of the stent strut, while *in vivo* failure would occur on the outside of the hinged joint [Gong *et al.*, 2003]. The fatigue behaviour of NiTi was investigated using diamond shaped specimens at 37°C by [Pelton and Gong, 2002]. However, as a zero mean strain was employed during testing, this does not accurately represent the conditions experienced by the stent *in vivo* as a stent will always experience a compressive mean strain in retaining the vessel wall open following deployment. While the results from such investigations are certainly insightful, it must be noted that these approaches do not represent the intended physiological applications of the stent material and therefore they cannot be used to fully characterise superelastic NiTi stent device behaviour.

In a study investigating the effect of mean strain and strain amplitude on the fatigue life of fully processed NiTi stent subcomponents in the diamond configuration at 37°C by [Tolomeo *et al.*, 2000], the results demonstrated an initial decrease and, remarkably, a subsequent increase in the endurance limit with increasing mean strain. It was noted, for a given strain amplitude, specimens that were subjected to 3% mean strain resulted in longest lives. They were amongst the first to publish such extraordinary results which suggested an increase in fatigue life is observed with an increasing mean strain and lowering strain amplitude in superelastic NiTi specimens. A subsequent study, carried out by [Perry *et al.*, 2002], investigated the effect of mean strain on the endurance limit of diamond specimens which were laser cut from fully processed NiTi tubing at 37°C. Similar results were reported with respect to the

improvement of the material's fatigue resistance with increasing mean strain levels. This behaviour is in stark contrast to typical engineering materials in which a decrease in fatigue performance is expected with increasing mean strain. The work of [Harrison and Lin, 2000] and [Morgan *et al.*, 2003] also confirmed the hypothesis of increasing fatigue life in superelastic NiTi with increasing mean strain and low strain amplitudes using superelastic NiTi stent subcomponent and thin wire specimens, respectively.

Two inter-connected studies were undertaken by [Pelton *et al.*, 2003] and [Pelton *et al.*, 2008] which systematically addressed the issue of tensile versus compressive loading modes and the accuracy of fatigue results. Fully processed diamond shaped specimens were subjected to various combinations of mean strain and strain amplitudes at 37°C in the work of [Pelton *et al.*, 2003]. In this way, a full range of varying loading conditions was explored for the first time. From these investigations, as seen in Figure 2.5, compressive mean strains were shown to be beneficial while tensile mean strains were shown to be detrimental up to strain levels of approximately 1.5%. It can therefore be concluded that the chosen loading conditions employed during testing greatly affect the relevancy of the resulting data which must be taken into account when creating a fatigue testing protocol for NiTi stent specimens. Interestingly, above this 1.5% mean strain level, a gradual improvement in fatigue life was reported. Indeed, as with the previous studies mentioned, with increasing mean strain between 1.5-6% an overall trend of increasing fatigue life was reported following the initial decrease. This behaviour was also captured in the more recent study by [Pelton *et al.*, 2008], as seen in Figure 2.6, which employed NiTi dogbone specimens for testing of the higher mean strain ranges examined. Furthermore, in both studies, specimens that were subjected to a 4% mean strain level resulted in longest fatigue lives.

When comparing the generated constant life diagrams to the uniaxial stress-strain curves of the NiTi specimens of [Pelton *et al.*, 2003] and [Pelton *et al.*, 2008] it can be identified that, following an initial decrease of fatigue performance, the improvement in fatigue behaviour is observed at 1.5% mean strain which corresponds

with the initiation of the SIM microstructural phase. This concept will be discussed further in Section 4.4 and throughout this thesis. Investigations into the effect of strain amplitude are also central to the understanding of superelastic NiTi's fatigue behaviour as, even with a relatively low strain amplitude SIMT may occur if the mean strain is sufficiently high. This is significant as cycling in the mixed austenite/martensite phase regime has been experimentally shown to be detrimental to the fatigue life of NiTi when compared to cycling in a single-phase regime [Tabanlı *et al.*, 1999]. This behaviour can be identified in the constant life diagrams shown in Figure 2.5 and Figure 2.6, from the experimental works of [Pelton *et al.*, 2003] and [Pelton *et al.*, 2008], in which an overall lower endurance limit can be observed in the range of approximately 1.5-6% mean strain. This mean strain range corresponds to the characteristic SIMT plateau (i.e. the mixed phase regime) of the NiTi fatigue specimens. It is clear that further investigations are required in the research field of fatigue analysis of superelastic NiTi in order to fully characterise the optimisation of the fatigue performance and safety of NiTi biomedical devices.

2.5 Influence of Microstructure

The objective of this thesis is to computationally investigate the effect of the microstructural phases of NiTi, namely, austenite and SIM, and crystallographic texture on NiTi's fundamental mechanical and fatigue behaviour with respect to NiTi stent devices. This is achieved through the computational modelling of suitable superelastic NiTi specimens which requires the input of precise details of the specimen's material behaviour. In this way, an in-depth understanding of NiTi's microstructural phases and crystallographic texture are therefore essential for the successful creation of the micro-mechanical models in this thesis. Experimental investigations which target the effect of microstructure on NiTi's macroscopic material response, specifically of the two main topics of microstructural phase and crystallographic texture, are discussed in Section 2.5.1 and Section 2.5.2. Also included is a brief discussion on the associated effect of thermal processing and

resulting precipitate fraction, size and location in NiTi microstructure in Section 2.5.3 which will also be included in the micro-mechanical models of Chapter 5.

2.5.1 NiTi Composition and Microstructural Phases

As far back as the earliest work of [Melton and Mercier, 1979] it was known that differing compositions of the NiTi alloys can significantly affect transformational temperatures. This, in turn, can affect the materials suitability in certain NiTi devices such as self-expanding stents since the material may not exhibit its characteristic superelastic behaviour at body temperature. Many researchers, such as [Yoneyama *et al.*, 1992] and [Bujoreanu *et al.*, 2010], have studied the importance of material purity and elemental microstructural composition to highlight its fundamental importance in determining NiTi's macroscopic uniaxial behaviour. This concept was experimentally investigated by [Wu, 2001], and it was found that shifting to a Ni-rich composition by only 1.0% can decrease transformation temperatures by as much as 100°C and thus render them unsuitable as stent materials. Therefore, it is of extreme importance that the initial material composition must be as close to an equi-atomic ratio as possible in order to avail of NiTi's advantageous stress-induced transformation from the austenite to martensite microstructural phase.

Few studies directly investigate the fatigue behaviour of stable austenitic and stable martensitic NiTi microstructural phases due to the fact that the superelastic NiTi behaviour is of greatest importance for commercial application. However, in addition to the superelastic NiTi crack growth data discussed in Section 2.3.1 of [McKelvey and Ritchie, 2001], this study also investigated the fatigue crack growth rate behaviour of both stable austenitic and stable martensitic NiTi. Each microstructural phase was targeted by a method of controlling the test temperature; at temperatures less than the martensite finish, M_f , temperature stable martensite was achieved (i.e. -65°C) and at temperatures above the martensite deformation, M_d , temperature stable austenite was achieved (i.e. 120°C). Under these strain-controlled testing procedures, martensitic NiTi is documented as having a higher threshold for fatigue crack initiation when compared to both austenitic and superelastic NiTi; as shown in Figure 2.7. In this way,

theoretically, stable martensite should be more tolerant of stress concentrators such as surface defects or internal inherent flaws before crack propagation will occur.

This behaviour was also reported in the early studies of [Melton and Mercier, 1979] and [Miyazaki *et al.*, 1988] in which the strain-life and stress-life behaviour (S-N curves) of stable austenite and stable martensite were investigated. Both studies utilise heat treatment to vary the austenite finish, A_f , temperature of the specimens as a method of targeting the individual material phases at a given test temperature. Despite the lack of data on this topic, the significant outcome to be taken from such investigations is the dominance of martensitic NiTi as the superior phase in terms of fatigue performance when compared to austenitic and superelastic NiTi when tested under strain-controlled conditions. The microstructural features of a specimen annealed to be in the stable austenitic, stable martensitic and superelastic phase can be compared in Figure 2.8 [Dauskaradt *et al.*, 1989]. The vast difference in fatigue behaviour between austenitic and martensitic microstructural phases of NiTi may offer a possible explanation for the unusual fatigue behaviour of superelastic NiTi. This concept will be discussed again during the tensile modelling investigations of Chapter 4 and during the fatigue investigations of Chapter 6.

2.5.2 Crystallographic Texture

NiTi derives its unique mechanical behaviour from the coordinated atomic movements manifesting in the phase transformations from the cubic austenite to monoclinic martensite microstructural phase. Therefore, any significant alignment of the atomic planes attributed to crystallographic grain orientation distribution (i.e. crystallographic texture) in the polycrystalline material can have a marked influence on the mechanical response of the material. This can be physically presented by either a limitation or promotion of the SIMT. In a study carried out by [Robertson *et al.*, 2006], the processing techniques employed to form NiTi materials were investigated in order to determine the connection between differing product forms and the resulting microstructural textures; varying experimental specimens such as rods, sheets and tubes were used in this study. Reported results confirmed that the texture in

superelastic NiTi can be significantly different depending on which product form is used. Upon investigation, these varying textures were subsequently verified to cause marked differences in resulting mechanical properties by [Lin *et al.*, 1994] [Liu *et al.*, 1999] [Robertson *et al.*, 2006] [Fonte and Saigal, 2010]. Such studies confirm there are underlying microstructural mechanisms occurring which are ultimately dependent on the processing techniques used and product form selected.

In the study carried out by [Liu *et al.*, 1999], variations in mechanical behaviour were observed between ‘rolled’ direction and ‘transverse’ direction of cold-drawn NiTi sheet materials. However, they do not delve into the microstructural explanations for this finding as it was not the main focus of the investigation. The underlying microstructural explanations for these observations may be found in an earlier study carried out by [Lin *et al.*, 1994] in which tensile tests were also performed on cold-drawn NiTi sheets. In this study, it was demonstrated that the self-accommodating nature of the martensite and the martensitic reorientation process was suppressed when loaded in the ‘transverse’ direction. This was attributed to the hindrance of deformed martensite structures and defects in the specimen due to texture. This in turn, led to differing dominant de-twinning and reorientation modes and dislocation densities depending on the direction of loading. When the specimen was loaded in the ‘rolled’ direction, the strengthening effect induced by cold-rolling was shown to significantly improve its superelastic properties by raising the critical shear stress for slip.

Similar results were also reported in a more recent investigation into the influence of texture on the mechanical behaviour of superelastic NiTi performed by [Fonte and Saigal, 2010]. In this study it was also observed that crystallographic texture anisotropies occur when single crystal specimens were compressed in different crystallographic alignment directions. Different recovery strains and strength levels were displayed for varying directions which were dependent on texture. They concluded that the compression strength of polycrystalline NiTi is stronger when tested in the longitudinal direction, which has a [111] texture, compared to a specimen tested in the transverse direction with a [110] texture. Ultimately, it can be concluded

that different microstructural textures have a marked influence on NiTi's macroscopic material response. In order to achieve the optimum design for a biomedical stent device, the effect of processing and product form on resulting textures should therefore be taken into account during the manufacturing stage of stent production in addition to the fatigue analysis stage.

2.5.3 Precipitate Fraction, Size and Location

As mentioned in Section 1.1.5, with reference to a study completed on 316L stainless steel, the 'size effect' comes into play when discussing specimens with dimensions less than 500 μ m. Therefore, due to this associated 'size effect' in biomedical stent struts, precipitates may act as initial flaws in the material itself and thus may have a potentially detrimental effect on the performance of the device. The presence of precipitates may also lead to a significant reduction in fatigue life of the device due to the introduction of the undesired R-phase and, if not taken into account during fatigue analysis, would result in non-conservative approximations of fatigue life. The method of processing has been shown to be highly significant in minimising precipitates and their size. Many processing techniques are used in the manufacture of NiTi alloys, some of which are described in a detailed paper by [Wu *et al.*, 2001]. One such technique is powder metallurgy (PM) in which NiTi materials are sintered from elemental powders which result in highly porous materials and which may contain other intermetallic phases such as Ti₂Ni and TiNi₃. Secondary processing, such as re-melt or extrusion, may be required to achieve improved microstructures with minimal precipitate population. In this way, a thorough knowledge of the effects of processing is essential in producing the desired macroscopic behaviour of NiTi stent devices.

The influence of precipitates on the mechanical behaviour of NiTi has been a dominant topic of interest for researchers in recent years, including [Sehitoglu *et al.*, 2000], [Gall and Maier, 2002], [Khalil-allafi *et al.*, 2002], [Michutta and Somsen, 2006], [Shabalovskaya *et al.*, 2008] and [Holec *et al.*, 2008]. In an experimental study performed by [Sehitoglu *et al.*, 2000], an attempt was made to correlate the effect of the size of Ti₃Ni₄ precipitates and the stress-induced martensitic transformational

(SIMT) behaviour in superelastic NiTi specimens. It was observed that deformation patterns around the precipitates were non-uniform which resulted in local untransformed areas of the austenitic material; these areas were shown to gradually transform to martensite with increasing stress levels. The evolution of NiTi's microstructure during stress-free and stress-assisted ageing in terms of Ni₄Ti₃ precipitate size, volume fraction, inter-particle spacing and distribution of precipitates in the microstructure was investigated by [Khalil-allafi *et al.*, 2002]. In this study, the correlation between the presence of precipitates and SIMT behaviour of superelastic NiTi was investigated. The martensitic transformation temperatures of the specimens were characterised using Differential Scanning Calorimetry (DSC); details of this experimental procedure will be discussed in Chapter 3. It was observed, upon short to intermediate term ageing treatments, the presence of precipitates affected transformation in that a two-step transformation was observed due to the presence of the undesired R-phase. A resulting heterogeneous microstructure was reported in which precipitates were mainly found around grain boundaries while grain interiors exhibit precipitate-free zones. However, as precipitates grow to large sizes during long term stress-free ageing, it was found that the inter-particle spacing became so large that SIMT is no longer affected by the presence of precipitates. Accordingly, it was concluded that characteristics of the martensitic transformation are directly related to the precipitate fraction, size and location.

2.6 Micro-Macro NiTi Fatigue Investigations

Experimental NiTi investigations incorporating simultaneous *in situ* mechanical loading and optical microscopy is seldom found in literature. Yet these experiments can offer a rich understanding of NiTi's fundamental material response as they address both micro- and macro-mechanical behaviour. Work by Miyazaki and co-workers [Miyazaki *et al.*, 1982], [Miyazaki, 1988] and [Miyazaki and Otsuka, 1989] systematically examined the crystallography and mechanical behaviour of single and polycrystalline NiTi specimens. *In situ* optical micrographic observations were performed to investigate microstructural phenomena such as the self-accommodating

nature of the twinned martensite during transformation. In addition, the martensite variant reorientation to form the most favourable variant, i.e. de-twinning of the martensite, was also investigated. Similar work was carried out by [Jiang *et al.*, 1997] into the martensitic transformation and variant reorientation on the microscopic scale in polycrystalline NiTi materials. In the study carried out by [Liu *et al.*, 1999], discussed previously in Section 2.5.2 of this review, an attempt was made to link the macroscopic stress-strain response of NiTi cold-drawn sheets with microstructure; variations in mechanical behaviour were found between the examined ‘rolled’ and ‘transverse’ direction. This anisotropic behaviour can be attributed to differing dominant de-twinning and reorientation modes and dislocation densities with varying textures. As an exciting step forward, these studies were among the first to attempt to correlate microscopic mechanisms in NiTi’s microstructure and the overall macroscopic material response.

Standard and thermal cameras were used by [Shaw and Kyriakides, 1995] and [Shaw and Kyriakides, 1997] to capture the macro-transformation state of NiTi in conjunction with the thermal signatures of SIMT upon loading. Using the thermal camera, it was confirmed that martensitic transformation was occurring due to the release of latent heat associated with the first-order transformation. In a similar study, high-speed and infra-red cameras were used by [Feng and Sun, 2006] to observe the complete transformation process, from nucleation to growth and to the eventual vanishing of the martensitic phase, under reversed displacement-controlled loading. However, focus is simply placed on a single stress-induced macroscopic deformation domain in the tubular specimens, with no microstructural investigation being performed in the study. In a more comprehensive study by [Brinson, 2004], the correlation between the microstructure of superelastic NiTi, in particular martensitic variants, and the macro-mechanical response of the material was investigated. The primary focus of this investigation was the relationship between variant formation, macroscopic Lüder-like bands and localised permanent deformation. In this study, as with the previous papers discussed, focus is placed on the macroscopic behaviour of the material rather than delving into the underlying microscopic phenomena taking

place. Nevertheless, key results of the experiments on the NiTi include observation of localised plastic deformation after only a few cycles and a refined definition of ‘full transformation’ for polycrystalline NiTi materials. In this way, even when ‘full transformation’ of the specimen occurs according to the macroscopic stress-strain curve, their results show that the polycrystalline NiTi material is approximately only 70% martensitic microscopically. This has been attributed to the sequenced transformation of grains within the specimen influencing the local stress states such that variants become ‘trapped’ and grains are unable to transform. This concept of ‘trapped martensite’ will be discussed in greater detail in the experimental work of this thesis in Section 5.4.

2.7 Conclusions

The effect of microstructure on NiTi’s mechanical and fatigue behaviour is the main focus of this thesis with respect to the safe design of NiTi self-expanding stents. The purpose of this chapter was to review published literature in the field of NiTi research in order to give context to this work. Firstly, a brief history of the fatigue characterisation of metallic materials was given in Section 2.2. The fundamental mechanisms of mechanical fatigue were discussed in addition to the application of fracture mechanics by researchers to characterise fatigue failure mechanisms. The proposed theories behind linear elastic fracture mechanics (LEFM) and elastic-plastic fracture mechanics (EPFM) approaches to fatigue analysis were discussed in detail in Section 2.3. Also included in this section was an introduction to ‘small’ fatigue cracks and the concept of ‘fatigue crack closure’. Small cracks were confirmed to be intrinsically significant to be included in the fatigue analysis of stent devices for the most accurate prediction of fatigue life due to the micro-scale size such devices. It was concluded that an EPFM approach should be employed in the computational analysis of this thesis as it allows for the incorporation of small crack behaviour through the use of fatigue crack closure.

It was established in Section 2.4 that superelastic NiTi fatigue test specimens must undergo similar thermo-mechanical heat treatments to that of NiTi self-

expanding stent devices in order to produce appropriate microstructures and mechanical properties for accurate testing. Suitable test specimen must also be designed to correctly simulate the compressive stresses and strains experienced by the microscale-sized device. Furthermore, it was confirmed that the test set-up and procedure, particularly the test temperature and the selected loadings modes, must represent *in vivo* conditions experienced by the biomedical stent device in order to achieve the most accurate fatigue life predictions. In this way, the knowledge gathered from previous experimental investigations in this research field is used in the construction of the experimental tests conducted as part of this thesis. Details of the experimental set-up will be discussed in greater detail in Chapter 3 of this thesis.

Experimental studies into the effect of mean strain and strain amplitudes have proven to be an interesting research topic. The effect of mean strain on NiTi's fatigue behaviour appears to be different to that of common engineering materials. It has been experimentally demonstrated by multiple researchers that superelastic NiTi exhibits the unusual behaviour of increasing fatigue performance with increasing mean strain between approximately 1.5-6% mean strain range. This has proven to be an extremely important finding that is contrary to logical engineering rational and has been directly attributed to the SIMT associated with superelastic NiTi. However, investigations into NiTi's fatigue behaviour is an on-going research topic as researchers have yet to provide a coherent insight into the mechanisms for all observed phenomena of NiTi's unique behaviour. This thesis, therefore, is dedicated to providing a potential microstructural explanation towards the unusual fatigue behaviour of superelastic NiTi which aims to advance the knowledge and understanding of this advantageous material.

In order to achieve the objectives of this thesis, a thorough understanding of NiTi's microstructure must be appreciated in order to construct computational models which accurately simulate superelastic NiTi's material behaviour. Therefore a review of key experimental investigations into NiTi composition, microstructural phases, crystallographic texture, and precipitate fraction, size and location was given in

Section 2.5. It was confirmed that the two microstructural phases of NiTi, namely austenite and martensite, have vastly differing mechanical and fatigue properties. In this way, this alteration in fatigue behaviour between the two microstructural phases may present a possible explanation towards the unusual fatigue behaviour of the phase-transforming superelastic NiTi. Furthermore, it was confirmed that varying crystallographic textures in a polycrystalline NiTi material can also have a marked influence on the mechanical and fatigue behaviour of NiTi specimens. As a result, the influence of microstructural phase and crystallographic texture have been targeted as the main focus of investigation in this thesis with the objective of providing a comprehensive understanding of NiTi's fundamental mechanical and fatigue behaviour for the safe design of NiTi biomedical stent devices.

As a final observation on the published literature, Section 2.6 offers a review of experimental investigations which were designed to examine the micro- and macro-mechanical behaviour of the NiTi specimen simultaneously. Collectively, these innovative experimental investigations demonstrate the existence of several underlying micro-mechanical mechanisms in the superelastic NiTi material which generally remain over-looked when employing standard macro-scale material testing procedures. As an exciting step forward, these studies begin to correlate NiTi's microstructure and its overall macroscopic material behaviour. Following this novel approach to superelastic NiTi's material behaviour research, an *in situ* Scanning Electron Microscopy (SEM) tensile test is performed as part of the research in this thesis. In this way, the microstructure of the superelastic NiTi specimen can be simultaneously investigated during the uniaxial loading and unloading experimental procedure. Overall, it can be concluded that detailed investigations, such as those described in this review, are essential in the quest to advance our understanding of the unique behaviour of superelastic NiTi.

2.8 References

ASTM International Standards, ASTM F2477-07 Standard Test Methods for *in vitro* Pulsatile Durability Testing of Vascular Stents, 2013.

ASTM International Standards, ASTM F2516-14 Test Method for Tension Testing of Nickel-Titanium Superelastic Materials, 2014.

Braithwaite F., On the Fatigue and Consequent Fracture of Metals, *Minutes of Proceedings at the Institution of Civil Engineers*, 1854, p 463-474.

Brinson L., Stress-Induced Transformation Behavior of a Polycrystalline NiTi Shape Memory Alloy: Micro and Macromechanical Investigations via In-Situ Optical Microscopy. *Journal of the Mechanics and Physics of Solids*, 2004, **52(7)**, p 1549–1571.

Bruzzi M.S. and McHugh P.E., Methodology for Modelling the Small Crack Fatigue Behaviour of Aluminium Alloys, *International Journal of Fatigue*, 2002, **24**, p 1071–1078.

Bujoreanu L.-G., Young M.L., Gollerthan S., Somsen C. and Eggeler G., Influence of Heat Treatment and Microstructure on the Tensile Pseudoelastic Response of an Ni-rich NiTi Shape Memory Alloy, *International Journal of Materials Research*, 2010, **101(5)**, p 1-8.

Dauskardt R.H., Duerig T.W., Ritchie R.O., Effects of *in situ* Phase Transformation on Fatigue-Crack Propagation in Titanium Nickel Shape Memory Alloys, *MRS Shape Memory Materials*, 1989, **9**, p 243-429.

Dordoni, E., Petrini L., Wu W., Migliavacca F., Dubini G. and Pennati G., Computational Modeling to Predict Fatigue Behavior of NiTi Stents: What do we need?, *Journal of Functional Biomaterials*, 2015, **6(2)**, p 299-317.

Dowling N.E., Crack Growth During Low-cycle Fatigue of Smooth Axial Specimens, *American Society for Testing and Materials*, 1977, Special Technical Publication **637**, p 97-121.

Dowling N.E. and Begley J.A., Fatigue Crack Growth during Gross Plasticity and the new J-integral, *Mechanics of Crack Growth*, 1976, Special Technical Publications **590**, p 82-103.

Duerig T., Tolomeo D.E. and Wholey M., An Overview of Superelastic Stent Design, *Minimally Invasive Therapy & Allied Technologies*, 2000, **9(3/4)**, p 235-246.

Elber W., Fatigue Crack Closure under Cyclic Tension, *Engineering Fracture Mechanics*, 1970, **2**, p 37-45.

Elber W., The Significance of Fatigue Crack Closure, *Damage Tolerance in Aircraft Structures*, 1971, Special Technical Publication **486**, p 230-242.

Ewing J.A., Humfrey J.C., The Fracture of Metals under Rapid Alterations of Stress, *Philosophical Transactions of the Royal Society, London*, 1903, **A200**, p 241-250.

Ewing J.A., Rosenhain W., Experiments in Micro-metallurgy: Effects of Strain, *Philosophical Transactions of the Royal Society, London*, 1900, **A199**, p 85-90.

Feng P. and Sun Q.P., Experimental Investigation on Macroscopic Domain Formation and Evolution in Polycrystalline NiTi Microtubing under Mechanical Force, *Journal of the Mechanics and Physics of Solids*, 2006, **54**, p 1568–1603.

Fonte M. and Saigal A., Effects of Crystallographic Texture Directionality on the Compressive Stress–Strain Response of Shape Recovered Polycrystalline Nitinol, *Scripta Materialia*, 2010, **63**, p 320–323.

Gadaj S.P. Nowacki W.K. and Tobushi H., Temperature Evolution during Tensile Test of TiNi Shape Memory Alloy, *Archives of Mechanics*, 1999, **51(6)**, p 649-663.

Gall K. and Maier H.J., Cyclic Deformation Mechanisms in Precipitated NiTi Shape Memory Alloys, *Acta Materialia*, 2002, **50**, p 4643-4657.

Gall K., Tyber J., Wilkesanders G., Robertson S.W., Ritchie R.O., Maier H.J., Effect of Microstructure on the Fatigue of Hot-rolled and Cold-drawn NiTi Shape Memory Alloys, *Materials Science and Engineering A*, 2008, **486**, p 389–403.

Gong X.-Y., Pelton A.R., Duerig T.W., Rebelo N. and Perry K., Finite Element Analysis and Experimental Evaluation of Superelastic Nitinol Stent, *Proceedings of the International Conference on Shape Memory and Superelastic Technologies*, 2003, p 1-10.

Griffith A.A., The Phenomenon of Rupture and Flow in Solids, *Philosophical Transactions of the Royal Society, London*, 1921, **A221**, p 163-197.

Harrison W.J. and Lin Z.C., The Study of Nitinol Bending Fatigue, *Proceedings of the International Conference on Shape Memory and Superelastic Technologies*, 2000, p 391-396.

Holec D., Bojda O. and Dlouhy A., Ni₄Ti₃ Precipitate Structures in Ni-rich Shape Memory Alloys, *Materials Science and Engineering A*, 2008, **481**, p. 462-465.

Hornbogen E., Martensitic Transformation at a Propagating Crack, *Acta Metallurgica*, 1978, **26**, p 147-152.

Huang X. and Liu Y., Effect of Annealing on the Transformation Behavior and Superelasticity of NiTi Shape Memory Alloy, *Scripta Materialia*, 2001, **45**, p 153-160.

Iacoviello, F., Di Cocco V., Natali S. and Maletta C., Microstructural Influences on Crack Initiation and Growth in an Equiatomic NiTi PE Alloy, *Proceeding of the International Conference on Crack Paths*, 2012, **4**, p 319-326.

Inglis C.E., Stresses in a Plate due to the Presence of Cracks and Sharp Corners, *Transactions of the Institute of Naval Architects*, 1913, **55**, p 219-241.

Irwin G.R., Analysis of Stresses and Strains near the end of a Crack Traversing a Plate. *Journal of Applied Mechanics*, 1957, **24**, p 361-364.

Irwin G.R., Plastic zone near a Crack and Fracture Toughness. *Proceedings of the Seventh Sagamore Ordnance Materials Conference*, Syracuse University, New York, USA, 1960, **2**, p 289-305.

Jiang X., Hida M., Takemoto Y., Sakakibara A., Yasuda H. and Mori H., In-situ Observation of Stress-induced Martensitic Transformation and Plastic Deformation in TiNi alloy, *Materials Science and Engineering A*, 1997, **238**, p 303–308.

Johe R., Tensile Testing of Nitinol Tubes and Wires with Higher Strain Rates, *Journal of Materials Engineering and Performance*, 2009, **18(5-6)**, p 836-842.

Khalil-allafi J., Dlouhy A. and Eggeler G., Ni₄Ti₃-precipitation during Aging of NiTi Shape Memory Alloys and its Influence on Martensitic Phase Transformations, *Acta Materialia*, 2002, **50**, p 4255–4274.

Kumar V., German M.D. and Shih C.F., An Engineering Approach for Elastic-Plastic Fracture Analysis, *Electric Power Research Institute*, 1981, Report NP-1931.

Lamba H.S., The J-integral Applied to Cyclic Loading, *Engineering Fracture Mechanics*, 1975, **7**, p 693-703.

Lankford J., The Growth of Small Fatigue Cracks in 7075-T6 Aluminium, *Fatigue and Fracture of Engineering Materials and Structures*, 1982, **5**, p 233–248.

Li Z., Cheng X. and ShangGuan Q., Effects of Heat Treatment and ECAE Process on Transformation Behaviors of TiNi Shape Memory Alloy, *Materials Letters*, 2005, **59**, p 705-709.

Lin H.C., Wu S.K. and Lin J.C., The Martensitic Transformation in Ti-rich TiNi Shape Memory Alloys, *Materials Chemistry and Physics*, 1994, **37(2)**, p184-190.

Liu Y., Xie Z.L., Van Humbeeck J. and Delaey L., Effect of Texture Orientation on the Martensite Deformation of NiTi Shape Memory Alloy Sheet, *Acta Materialia*, 1999, **47**, p 645-660.

Liu X., Wang Y., Yang D. and Qi M., The Effect of Ageing Treatment on Shape-setting and Superelasticity of a Nitinol Stent, *Material Characterization*, 2008, **59(4)**, p 402-406.

McClung R.C., Chell G.G., Russel D.A. and Orient G.E., A Practical Methodology for Elastic-Plastic Fatigue Crack Growth, *Fatigue and Fracture Mechanics*, 1997, **27**, p 317-337.

McClung R.C. and Sehitoglu H., On the Finite Element Analysis of Fatigue Crack Closure, *Engineering Fracture Mechanics*, 1988, **33**, p 237-272.

McKelvey A.L. and Ritchie R.O., Fatigue-Crack Growth Behavior in the Superelastic and Shape-Memory Alloy Nitinol, *Metallurgical and Material Transactions A*, 2001, **32**, p 731-743.

Melton K.N., Mercier O., Fatigue of NiTi Thermoelastic Martensites, *Acta Metallurgica*, 1979, **27**, p 137-144.

Michutta J. and Somsen C., Elementary Martensitic Transformation Processes in Ni-rich NiTi Single Crystals with Ni₄Ti₃ Precipitates, *Acta Materialia*, 2006, **54**, p 3525-3542.

Miner M.A., Cumulative Damage in Fatigue, *Journal of Applied Mechanics*, 1945, **12(3)**, p 159-164.

Miyazaki S., Kawai T. and Otsuka K., On the Origin of Intergranular Fracture in β Phase Shape Memory Alloys, *Scripta Metallurgica*, 1982, **16**, p 431-436.

Miyazaki S., Sugaya Y., Otsuka K., Effects of Various Factors on Fatigue Life of Ti-Ni Alloys, *Proceeding of the International Meeting on Advanced Materials*, 1988, **9**, p 251-256.

Miyazaki S. and Otsuka K., Development of Shape Memory Alloys, *International Journal of the Iron and Steel Institute of Japan*, 1989, **29**, p 353-377.

Morgan N.B., Painter J. and Moffat A., Mean Strain Effects and Microstructural Observations during *in-vitro* Fatigue Testing of NiTi, *Proceedings of the International Conference on Shape Memory and Superelastic Technologies*, 2003, p 1-8.

Neuber H., Theory of Notch Stresses, Kerbspannungslehre, 2nd edition, Berlin, Germany, 1946, translated by Edwards Brothers Michigan, USA.

Nurveren K. and Akdogan A., Evolution of Transformation Characteristics with Heating/Cooling rate in NiTi Shape Memory Alloys, *Journal of Materials Processing Technology*, 2008, **196**, p 129-134.

Palmgren A., Die Lebensdauer von Kugellagern (The Service Life of Ball Bearings), *Zeitschrift des Vereines DeutscherIngenieure*, 1924, **68(14)**, p. 339-341.

Paris P.C. and Erdogan F., A Critical Analysis of Crack Propagation Laws, *Journal of Basic Engineering*, 1963, **85(4)**, p 528-533.

Paris P.C., Gomez M.P. and Anderson W.P., A Rational Analytical Theory of Fatigue, *The Trend in Engineering*, 1961, **13**, p 9-14.

Paryab M., Nasr A., Bayat O., Abouei, V. and Eshraghi A., Effect of Heat Treatment on the Microstructural and Superelastic Behavior of NiTi Alloy with 58.5wt% Ni, *Mediterranean Journal of Mathematics*, 2010, **16(2)**, p 123-131.

Pearson S., Initiation of Fatigue Cracks in Commercial Aluminium Alloys and the Subsequent Propagation of very Short Cracks, *Engineering Fracture Mechanics*, 1975, **7**, p 235-247.

Pelton A.R., DiCello J. and Miyazaki S., Optimization of Processing and Properties of Medical-Grade Nitinol Wire, *Proceedings of the International Conference on Shape Memory and Superelastic Technologies*, 2000, p 361-374.

Gong X.-Y. and Pelton A.R., Finite Element Analysis on Nitinol Medical Applications, *Proceedings of the International Conference of Shape Memory and Superelastic Technologies*, 2002, p 443–451.

Pelton A.R., Gong X.-Y. and Duerig T., Fatigue Testing of Diamond-Shaped Specimens, *Proceedings of the Materials and Processes for Medical Devices Conference*, 2003, p 199-204.

Pelton A.R., Schroder V., Mitchell M.R., Gong X.-Y., Barney M. and Robertson S.W., Fatigue and Durability of Nitinol Stents, *Journal of the Mechanical Behavior of Biomedical Materials*, 2008, **1**, p 153–164.

Perry M., Oktay S. and Muskivitch J.C., Finite Element Analysis and Fatigue of Stents, *Minimally Invasive Therapy and Allied Technologies*, 2002 **11(4)**, p 165-171.

Pieczyska E.A. and Tobushi H., Temperature Evolution in Shape Memory Alloy during Loading in various Conditions, *Proceedings of the International Conference on Quantitative InfraRed Thermography*, 2010, **10**, p 1-6.

Pineau, A.G. and Pelloux R.M., Influence of Strain-induced Martensitic Transformations on Fatigue Crack Growth Rates in Stainless Steels, *Metallurgical Transactions*, 1974, **5(5)**, p 1103-1112.

Pineau, A.G., Small Fatigue Cracks, *Metallurgical Society of AIME*, Warrendale, PA, USA, 1986, p. 191.

Rice J.R., Mechanics of Crack-Tip Deformation and Extension by Fatigue, Fatigue Crack Propagation, *American Society for Testing and Materials*, 1967, Special Technical Publication **415**, p 247-309.

Ritchie R.O. and Lankford J., Small Fatigue Cracks: A Statement of the Problem and Potential Solutions, *Material Science and Engineering*, 1986, **84**, p 11-16.

Robertson S.W., Gong X.-Y. and Ritchie R.O., Effect of Product Form and Heat Treatment on the Crystallographic Texture of Austenitic Nitinol, *Journal of Materials Science*, 2006, **41**, p 621-630.

Robertson S.W. and Ritchie R.O., In-vitro Fatigue–Crack Growth and Fracture Toughness Behavior of Thin-Walled Superelastic Nitinol Tube for Endovascular Stents: A Basis for Defining the Effect of Crack-like Defects, *Biomaterials*, 2007, **28**, p 700–709.

Robertson S.W., Stankiewicz J., Gong X.-Y. and Ritchie R.O., Cyclic Fatigue of Nitinol. *Proceedings of the International Conference of Shape Memory and Superelastic Technologies*, 2004, p 79–88.

Sehitoglu H., Karaman I., Anderson R., Zhang X., Gall K., Maier H.J. and Chumlyakov Y., Compressive Response of NiTi Single Crystals, *Acta Materialia*, 2000, **48**, p 3311-3326.

Sergueeva A.V., Song C., Valiev R.Z. and Mukherjee A.K., Structure and Properties of Amorphous and Nanocrystalline NiTi Prepared by Severe Plastic Deformation and Annealing, *Materials Science and Engineering A*, 2003, **339**, p 159-165.

Shabalovskaya S., Anderegg J. and Van Humbeeck J., Recent Observations of Particulates in Nitinol, *Materials Science and Engineering A*, 2008, **481-482**, p 431-436.

Shaw J.A. and Kyriakides S., Thermomechanical Aspects of NiTi, *Journal of the Mechanics and Physics of Solids*, 1995, **43(8)**, p 1243-1281.

Shaw J.A. and Kyriakides S., Initiation and Propagation of Localized Deformation in Elasto-Plastic Strips Under Uniaxial Tension, *International Journal of Plasticity*, 1997, **13(10)**, p 837-871.

Stankiewicz J.M., Robertson S.W. and Ritchie R.O., Fatigue-crack Growth Properties of Thin-Walled Superelastic Austenitic Nitinol tube for Endovascular Stents, *Journal of Biomedical Research Part A*, 2006, p 685-691.

Suresh S. and Ritchie R.O., On the Influence of Fatigue Underloads on Cyclic Crack Growth at Low Stress Intensities, *Material Science and Engineering*, 1981, **51**, p 61-69.

Suresh S. and Ritchie R.O., A Geometric Model for Fatigue Crack Closure Induced by Fracture Surface Morphology, *Metallurgical Transactions*, 1982, **13A**, p 1627-1631.

Suresh S. and Ritchie R.O., Near-threshold Fatigue Crack Propagation: A Perspective on the Role of Crack Closure, *Fatigue Crack Growth Threshold Concepts*, 1984, p 227-261.

Suresh S., Fatigue of Materials, *Cambridge University Press, Cambridge, UK*, 1998.

Tabanlı R.M., Simha N.K. and Berg B.T., Mean Stress Effects on Fatigue of NiTi, *Materials Science and Engineering A*, 1999, **275**, p 644-648.

Tabanlı R.M., Simha N.K. and Berg B.T., Mean Stress Effects on the Fatigue Properties of Superelastic NiTi, *Metallurgical Material Transactions*, 2001, **2(7)**, p 1866-1869.

Thompson N., Wadsworth N.J. and Louat N., The Origin of Fatigue Fracture in Copper, *Philosophical Magazine*, 1956, **1**, p 113-126.

Tolomeo D., Davidson S. and Santinoranout M., Cyclic Properties of Superelastic Nitinol: Design Implications, *Proceedings of the International Conference of Shape Memory and Superelastic Technologies*, 2000, p 409–417.

Wang Z.G., Zu X.T., Feng X.D., Zhu S., Zhou J.M. and Wang L.M., Annealing-induced Evolution of Transformation Characteristics in TiNi Shape Memory Alloys, *Physica B: Condensed Matter*, 2004, **353**, p 9-14.

Weibull W., A Statically Theory of the Strength of Material, *Ingeniörs Vetenskaps Akademiens Handlingar*, 1939, **151**, Generalstabens Litografisky Anstalts Förlag, Stockholm, Sweden.

Wöhler A., Wöhler's Experiments on the Strength of Metals, *Engineering*, 1867, **4**, p 160–161.

Wu M.H., Fabrication of Nitinol Materials and Components, *Proceedings of the International Conference of Shape Memory and Superelastic Technologies*, 2001, p 285–292.

Wuthrich C., The Extension of the J-integral to Fatigue Cracks, *International Journal of Fracture*, 1982, **20**, p 35-37.

Yin H. and Sun Q., Temperature Variation in NiTi Shape Memory Alloy During Cyclic Phase Transition, *Journal of Materials Engineering and Performance*, 2012, **12**, p 2505-2508.

Yoneyama T., Doi H. and Hamanaka H., Influence of Composition and Purity on Tensile Properties of Ni-Ti Alloy Castings, *Dental Materials Journal*, 1992, **11(2)**, p 157-64.

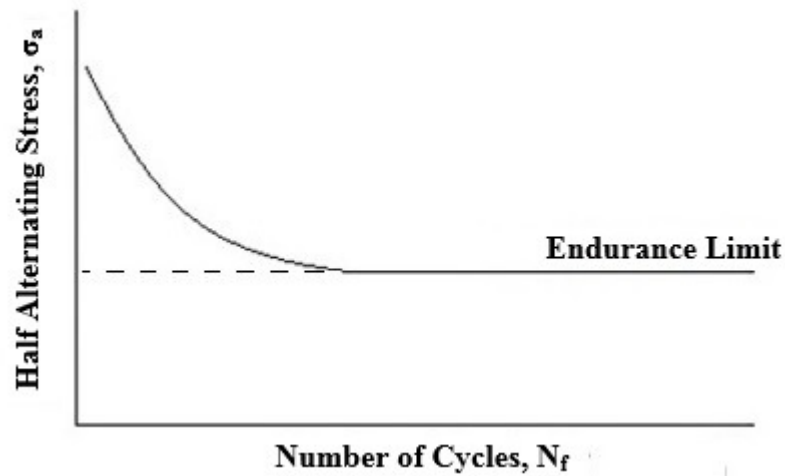


Figure 2.1: Schematic of an example S-N curve (stress-fatigue life curve) for a typical engineering metallic material, also displayed is the endurance limit for the given metallic specimen.

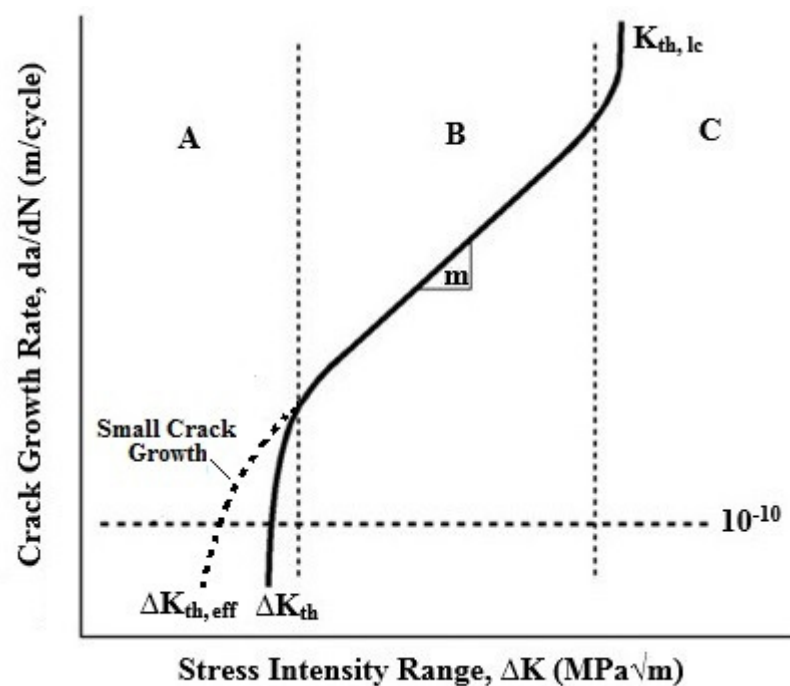


Figure 2.2: Schematic of fatigue crack growth behaviour: Small crack growth behaviour is shown in regime 'A'; Paris law long crack growth behaviour is shown in regime 'B'; rapid long crack growth behaviour to failure is shown in regime 'C'.

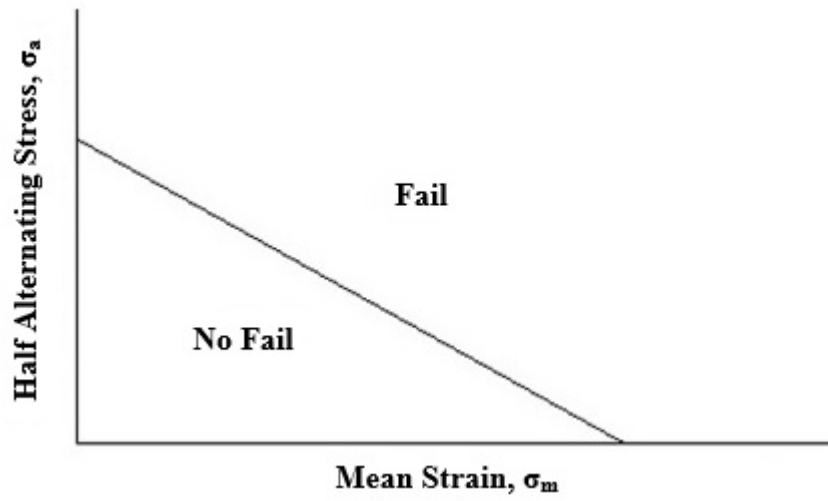


Figure 2.3: Schematic of a constant life diagram for a typical engineering metallic material following the Goodman approach to fatigue failure.

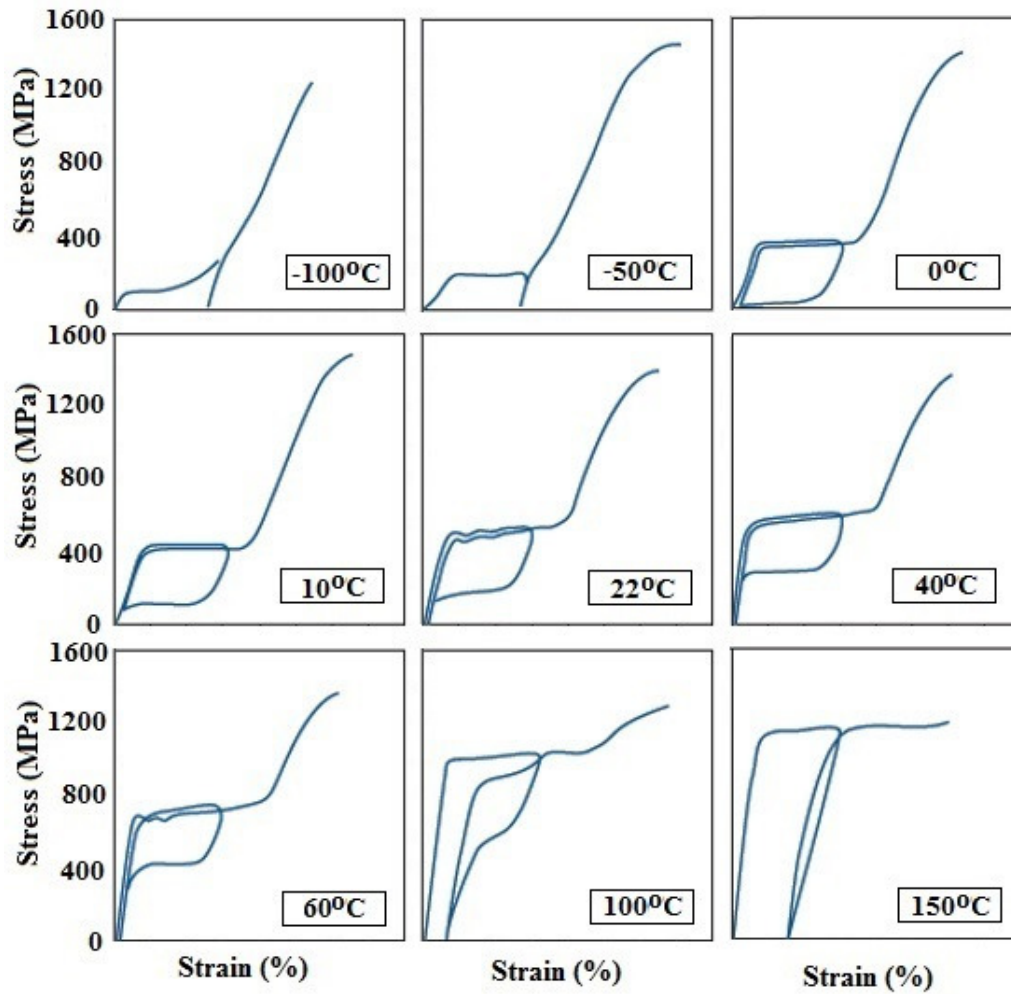


Figure 2.4: Influence of test temperature on the uniaxial tensile behaviour of a NiTi specimen with an A_s temperature of -22°C and an A_f temperature of 11°C . Adapted from [Pelton *et al.*, 2000].

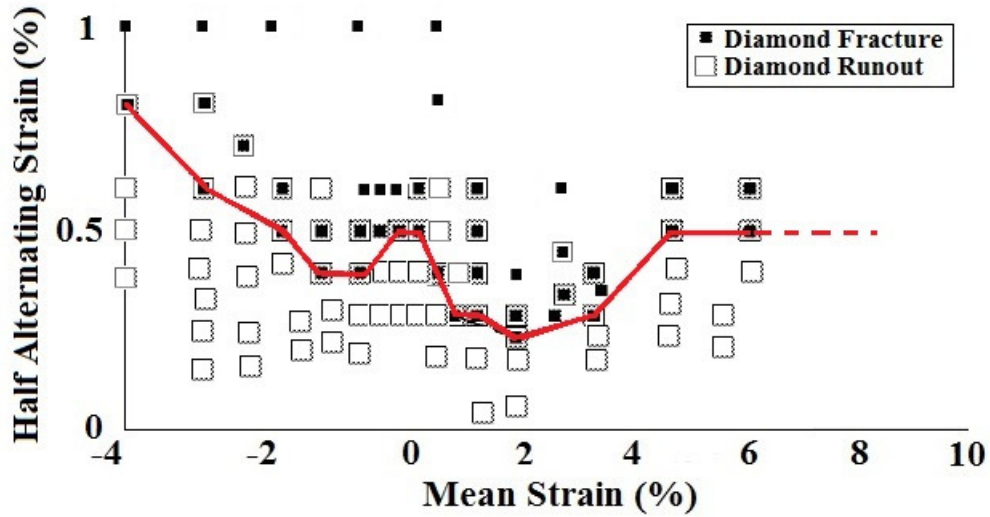


Figure 2.5: Experimental established constant life diagram of superelastic NiTi for a -4% to +6% mean strain range. Adapted from [Pelton *et al.*, 2003].

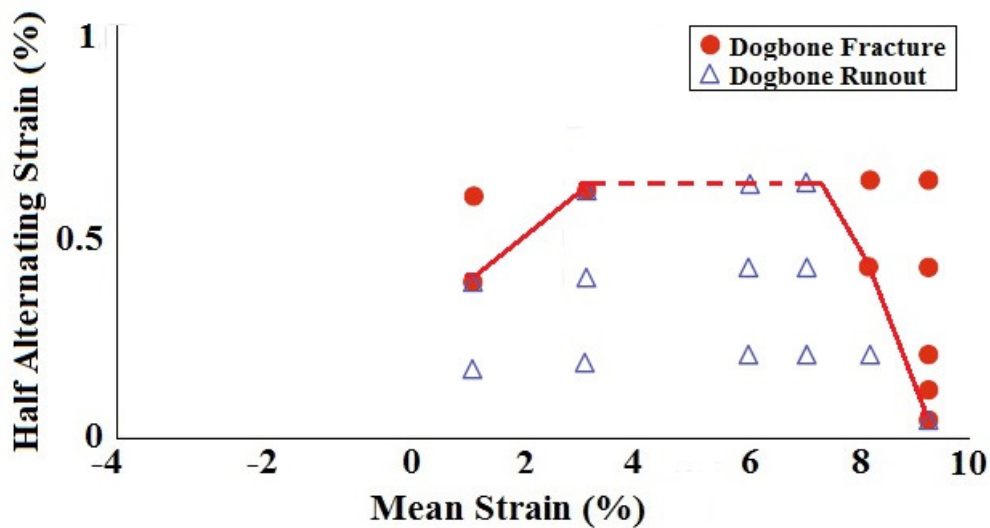


Figure 2.6: Experimental established constant life diagram of superelastic NiTi for a +1% to +9% mean strain range. Adapted from [Pelton *et al.*, 2008].

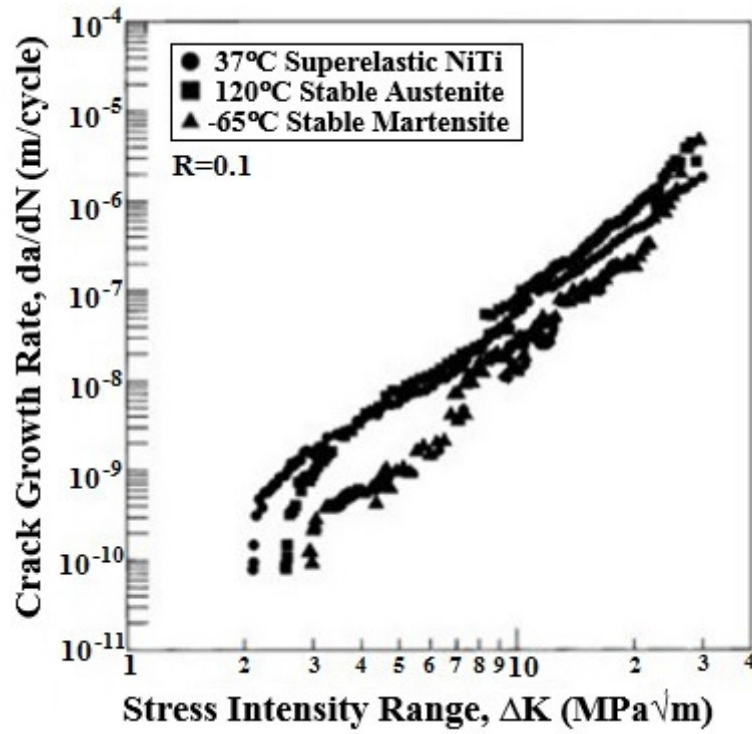


Figure 2.7: Stable martensitic NiTi specimen displaying a higher threshold for fatigue crack initiation when compared to both stable austenitic and superelastic NiTi specimens for a load ratio of $R=0.1$. Adapted from [McKelvey and Ritchie, 2001].

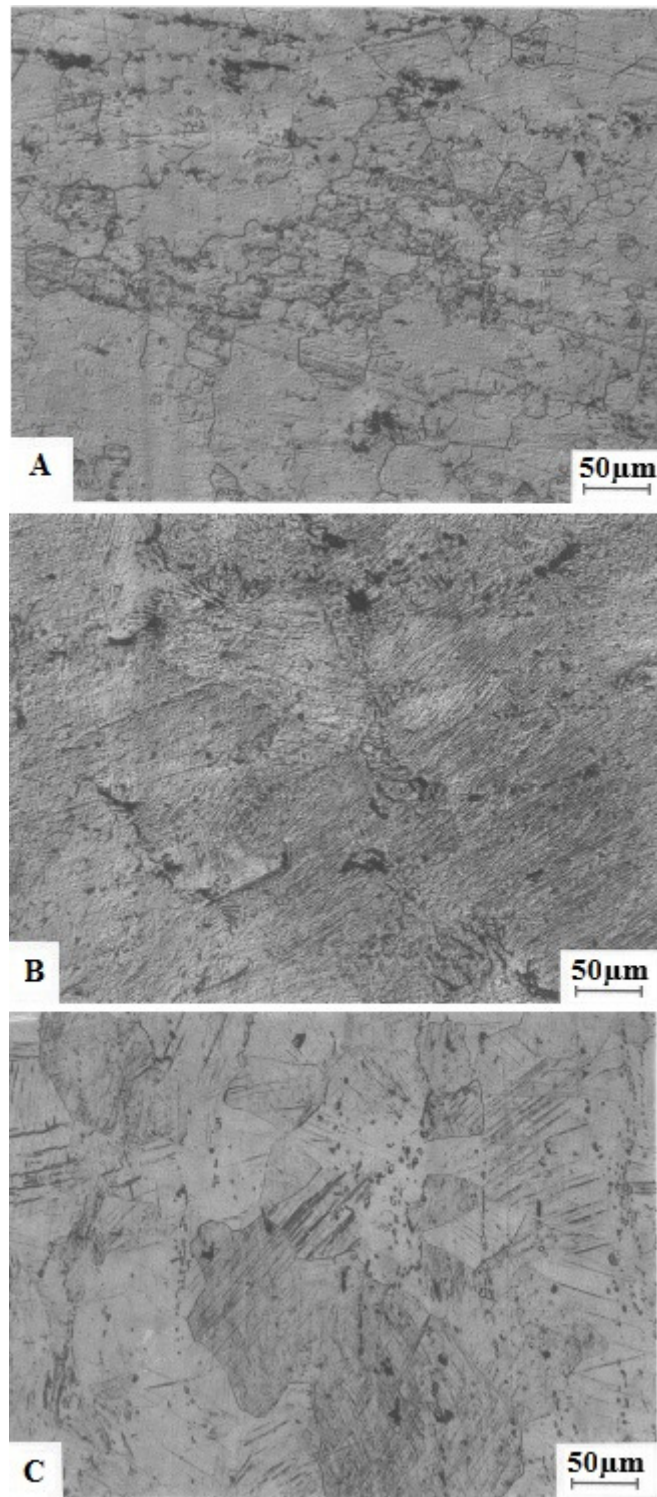


Figure 2.8: Microstructure of a NiTi specimen annealed to be in the (a) stable austenitic, (b) stable martensitic and (c) superelastic phase [Dauskardt *et al.*, 1989].

Chapter 3

Material Characterisation

3.1 Introduction

The overall aim of this thesis is to computationally investigate the effect of microstructural phase (i.e. austenitic and stress-induced martensitic NiTi) and grain orientation distribution (crystallographic texture) on NiTi's fundamental mechanical behaviour and overall fatigue performance to highlight concerns with current design procedures and protocols for NiTi biomedical self-expanding stent devices. In order to achieve this objective detailed material characterisation of suitable superelastic NiTi specimens were conducted, namely, a 'v-strut' stent subcomponent specimen and a micro-dogbone specimen. The characterisation of the fundamental material behaviour of both specimens provides input properties for the tensile computational models to be created in Chapters 4 and 5 in addition to the fatigue computational models of Chapters 6 and 7. Furthermore, through a direct comparison, the uniaxial tensile-compressive experimental data of this chapter also provides a means to validate the predicted macroscopic material response generated by the NiTi computational models used in the computational analyses of this thesis.

Firstly, a 'v-strut' stent subcomponent specimen, shown in Figure 3.1 and Figure 3.2, was custom fabricated by Admedes Schuessler GmbH. In the computational investigation which will be discussed in Chapter 4, this specimen is employed in the construction of a 3-D 'v-strut' model. This model allows for the computational analysis of the effect of microstructural phase, in particular SIM, on the specimen's macroscopic uniaxial tensile behaviour. In Chapter 5, the 'v-strut' specimen and corresponding support strut specimen (as shown in Figures 3.1-3.3) are employed in the construction of 2-D 'v-strut' and support strut models for the computational analysis into the microscale effect of texture on SIMT. In addition, the identification of critical discrete locations of potential fatigue failure initiation sites (i.e. stress concentrators) in the 'v-strut' biomedical stent subcomponent are analysed in Chapter 5. Details of the material characterisation experimental procedures, and generated results for direct input into the numerical models, are described in this chapter: the characterisation of the uniaxial material behaviour (Section 3.2.1), transformational

behaviour (Section 3.2.2) and full details of the microstructural imaging of the specimen (Section 3.2.3).

Secondly, a micro-dogbone specimen, as shown in the schematic of Figure 3.4, was also supplied by Admedes Schuessler GmbH. This specimen is employed in Chapter 5 to construct a rectangular 2-D numerical model which incorporates a realistic representation of the texture found in the NiTi specimen in order to investigate the effect of crystallographic texture on SIMT behaviour. This numerical model is specifically used to analyse the localised effect of individual grain orientations on the microscopic SIMT behaviour. In addition to this computational investigation, the evolution of grains in the micro-dogbone specimen during the stress-induced martensitic transformational process is also experimentally investigated by means of an *in situ* SEM uniaxial tensile test. Details of the material characterisation experimental procedures for input into the numerical models are described in this chapter: the characterisation of the uniaxial material behaviour (Section 3.3.1), transformational behaviour (Section 3.3.2), microstructural SEM imaging (Section 3.3.3), EBSD textural characterisation (Section 3.3.4) and individual grain orientation behaviour characterisation (Section 3.3.5).

3.2 ‘V-strut’ Stent Subcomponent

Excess materials at both ends of the ‘v-strut’ specimen, along with two support struts, were included in the design to provide precise alignment, structural stability and secure gripping during testing; as identified in the micrographs of Figure 3.1 and Figure 3.2. The ‘v-strut’ stent subcomponent used in this work is representative of a single strut of a NiTi self-expanding stent. The concept of exploiting a stent subcomponent, typically in the form of the ‘v-strut’ geometry or complete ‘diamond’ geometry, is commonly used for experimental and computational studies of biomedical stent devices, for example in the research of [Tolomeo *et al.*, 2000], [Pelton *et al.*, 2003], [Pelton *et al.*, 2008], [Harrison and Lin, 2000] and [Dordoni *et al.*, 2015], as previously discussed in Section 2.4.3.

3.2.1 Uniaxial Material Behaviour

To accurately characterise the material behaviour of the NiTi ‘v-strut’ stent subcomponent specimen, a uniaxial experimental tensile testing procedure was performed on the linear support strut of the custom manufactured specimen (as identified in the micrographs of Figures 3.1-3.2 and in the schematic of Figure 3.3). The strain in the specimen was measured using the standard strain equation of: $\varepsilon = \Delta l/l$, where l is the length. It is acknowledged, due to the specimen’s uniform rectangular geometry, a ‘stress concentration effect’ may occur at either end of the specimen during loading. This can be directly attributed to the absence of a smaller cross-sectional portion of material in the specimen’s gauge section which would allow for a controlled deformation at a given location and for more repeatability of results. In addition, as NiTi’s mechanical properties are highly temperature dependent, the experimental investigations were carried out at 37°C, i.e. body temperature, to accurately represent the material’s behaviour *in vivo*. This was achieved using the EnduraTEC ELF/3200 in conjunction with an environmental chamber with air-heating fan; the set-up for this experimental procedure can be seen in Figure 3.5. The exothermic stress-induced martensitic transformation (SIMT), and endothermic reverse transformation, has a considerable influence on the stress-strain response of NiTi. This can be attributed to the release of latent heat due to the exothermic nature of the transformation process as discussed in Section 2.4.2. Therefore, to ensure accuracy of data, the test temperature was strictly monitored and controlled at 37°C using an environmental chamber. The improved heat exchange between the specimen and the surrounding environment results in more accurate and repeatable results. In addition, due to the faster dissipation of heat from the specimen, it allows for the higher strain rate of 0.05mm/sec to be used. In this way, the time required for testing was also consequently reduced. The negligible impact of higher strain rates on the resulting tensile properties of superelastic NiTi was systematically demonstrated in the experimental investigations of [Johe, 2009].

Using the excess material at both ends, the specimen was placed in the EnduraTEC for testing using custom manufactured vice grips (Figure 3.5). Upon securing the specimen in the grips, the two ‘v-strut’ specimens along with the remaining support strut were cut such that one linear support strut alone would be tested. During the testing procedure, a visual inspection of the positioning of the specimen was performed to ensure no out-of-plane motion occurred during loading. Following the standard test procedure ASTM F2516-14 [ASTM, 2014], the NiTi support strut specimen (as shown in the micrograph of Figure 3.2 and schematic of Figure 3.3) was loaded to 6% global strain, unloaded to zero stress and subsequently loaded to failure. From the established tensile stress-strain curve, as shown in Figure 3.6, key material properties were extracted for input into the user defined UMAT/Nitinol integrated into the commercially available modelling platform ABAQUS™ 6.10 for computation analysis; as identified in Table 3.1. This material subroutine, based on model proposed by [Auricchio and Taylor, 1997], is discussed in greater detail in Section 4.2. To ensure the model accurately predicts the complex superelastic material behaviour of the specimen, validation of the generated computational model is achieved through comparison of the simulated macroscopic stress-strain response to that of the experimental stress-strain data; see Chapter 4 and Chapter 5 for further details of the validation procedure. In this work, the asymmetric tension-compression behaviour of superelastic NiTi has not been taken into account. The simulation of the ‘v-strut’ specimen’s compressive behaviour is instead simplified to behave symmetrically to the tensile behaviour by allocating a 0MPa to the value representing the stress at initiation of transformation during loading in compression (σ_{CL}^S) in the UMAT/Nitinol (as shown in Table 3.1).

3.2.2 Transformational Behaviour

To ensure a biomedical NiTi self-expanding stent device exhibits superelastic behaviour at human body temperature, it is necessary to control the transformational properties of the NiTi micro-tubing through thermo-mechanical processing during the production stage. Therefore to ensure the ‘v-strut’ stent subcomponent specimen used

in this work accurately represents the material behaviour of a superelastic stent material, the specimen was laser cut from 50.6Ni-49.4Ti at. % NiTi micro-tubing and underwent similar cold working and heat-treatment processing techniques to those performed on commercially available self-expanding NiTi endovascular stents to obtain final product dimensions with desired physical and mechanical properties. The specimen's austenite start, A_f , temperature was found to be $11.2\pm 2^\circ\text{C}$ using both the Bend-Free Recovery (BFR) and Differential Scanning Calorimetry (DSC) methods; thus confirming the specimen's suitability for use as it exhibits superelastic behaviour at body temperature, i.e. 37°C .

The BFR method determines the active austenite start, A_s , and austenite finish, A_f , temperatures of a NiTi specimen through the correlation of shape recovery with temperature. The experimental setup for BFR testing, following to the standard test procedure ASTM F2082-03 [ASTM, 2003], involves the immersion of a NiTi specimen in a temperature-controlled water bath. In this work, a support strut was carefully removed from the specimen for analysis. The specimen was initially placed in an ice-cold water-bath in the ductile martensitic microstructural phase. Upon cooling, the specimen was subsequently deformed 90° into an 'L'-shape. As the specimen was heated up, through increasing the temperature in the water-bath, it reverted back to the austenitic microstructural phase with the recovery of its original linear shape. The position of the specimen at a given temperature was therefore recorded at the point of initial shape recovery (A_s) and at final shape recovery (A_f). In this way, this process determines the component's behaviour in the range of the service temperature environment, i.e. around 37°C , for biomedical stent devices.

Unfortunately, results of BFR tests available in the literature occasionally exhibit low accuracy due to imprecise temperature control during the testing [Bartning and Simpson, 2003], or due to correlation of temperature and reverse deformation by only a small set of data points [Liu *et al.*, 1997] [Undisz *et al.*, 2009]. As a result, DSC methods were also used to confirm transformation temperatures of the specimen. Full transformational temperatures, namely, A_s , A_f , M_s , M_f , in addition to R_s and R_f if an

R-phase is present, can be determined by the thermo-analytical technique of DSC. This method measures the heat flow between the NiTi specimen and the environment as a function of temperature. Following the test standard ASTM F2004-05[ASTM, 2010] a small slug (3-5 μ g) of the specimen, along with a reference empty container, were placed into specified locations in the DSC equipment. The difference in the amount of heat required to change the temperature of the specimen compared to the reference, from -100°C to +100°C in this testing protocol, was measured as a function of temperature; both the specimen and reference were maintained at the same temperature through the experiment. The resulting DSC chart, with labelled transformation temperatures, is shown in Figure 3.7.

3.2.3 Microstructural Imaging

For the creation of realistic numerical models incorporating the granular structure of a polycrystalline superelastic NiTi specimen, used in the analysis described in Chapter 5, visual imaging of the microstructure of a suitable NiTi specimen is required. Consequently, the characterisation of the granular structure of the ‘v-strut’ specimen’s support strut was achieved using SEM techniques. The support strut, as identified in Figures 3.1-3.2 and in the schematic of Figure 3.3, was therefore carefully removed from the ‘v-strut’ specimen for individual analysis. The linear support strut was selected for analysis as it has the most uniform geometry, when compared to the curved nature of the ‘v-strut’. The rectangular support strut specimen was subsequently set in an epoxy resin for ease of handling. The specimen was manually polished to a finish of 0.06 μ m and chemically etched using a 1HF:4HNO₃:5H₂O solution to reveal the grain boundaries. Finally, the support strut specimen was viewed under SEM. Using the resulting SEM micrographs, the grain distribution and average grain size (20 \pm 2 μ m) was specifically identified in the specimen as demonstrated in Figure 3.8. Utilising the obtained micrographs, realistic numerical models incorporating the microstructure of the superelastic NiTi material can now be successfully created; further details of the construction of these computational models are discussed in Chapter 5.

3.3 Micro-Dogbone Specimen

The micro-dogbone specimen was laser cut from bulk 50.8Ni-49.2Ti at. % NiTi material and underwent precise thermomechanical heat-treatment procedures at Admedes Schuessler GmbH to ensure the material would be superelastic at room temperature, i.e. at $21\pm 2^\circ\text{C}$. This was completed as the uniaxial tensile test conducted in Chapter 5 was performed under *in situ* SEM at room temperature; this procedure will be discussed further in Section 3.3.1. The specimen also received an electro-polished finish to enhance surface quality, as is typical with commercially available endovascular stent components. The specimen was chosen to be of the standard dogbone geometry for ease of testing and for reliability of results. Two flat shoulders are present at either end of the specimen, with an elongated gauge section in between. The shoulders are relatively large to allow ease of gripping, whereas the gauge section has a smaller cross-section so that all deformation, and eventual failure, will only occur in this controlled section. This uniform design of the specimen ensures the elimination of a ‘stress concentration effect’ during loading; full dimensions are identified in the schematic of Figure 3.4.

3.3.1 Uniaxial Material Behaviour

To simultaneously characterise the micro- and macro-scale uniaxial stress-strain and SIMT behaviour of the micro-dogbone specimen, an *in situ* SEM tensile test was performed. The micro-dogbone specimen was securely placed in a Deben micro-stage rig for placement into the SEM equipment, as shown in Figure 3.9. Employing displacement-controlled deformation, the specimen was subjected to uniaxial tensile loading to 5% strain, unloading to its original position and subsequently loading to 10% strain before final unloading. The plot of Figure 3.10 shows the experimentally determined macroscopic uniaxial stress-strain response of the superelastic specimen under the aforementioned tensile loading procedure; this stress-strain plot displays the characteristic superelastic loading and unloading plateau stresses with the effects of residual strain removed between the two loading procedures. As identified in Figure 3.10 the residual strain in the first cycle of loading is typically relatively large while,

with continuous loading, the increment of residual strain is shown to dissipate rather rapidly as the number of cycles increase [Nemat-Nasser and Guo, 2006]. This residual strain represents the small volume of plastic deformation in the martensitic phase that can potentially have a detrimental effect on the overall fatigue behaviour through reducing the materials ability to undergo SIMT. Such residual strains could affect the fatigue behaviour of NiTi as the internal residual stresses constraining the martensitic phase may contribute to the externally applied load on the specimen. The required 15 material properties, identified in Table 3.2, are extracted from the uniaxial stress-strain curve shown in Figure 3.11 for input into the computational models of Chapter 5. As previously mentioned in Section 3.2.1, the asymmetric tension-compression behaviour of superelastic NiTi is not be taken into account in this work. As displayed in Table 3.2, the micro-dogbone's compressive behaviour is similarly simplified to behave symmetrically to its tensile behaviour.

In addition, during the tensile loading-unloading procedure to 10% strain, optical video of the specimen's surface was simultaneously recorded using the *in situ* SEM apparatus in order to analyse the microscopic response of the specimen under stress-induced phase transformational loading. In this way, the resulting recorded video was subsequently visually analysed in order to attempt to identify any notable evolution of the micro-dogbone specimen's surface in a chosen test area in the gauge section of the specimen during the SIMT process. Interestingly, no prominent changes to the surface of the specimen were identified during the transformation process in the chosen test area. Full details of results of this experimental investigation will be discussed in greater detail in Section 5.4. It should be noted, as the experimental procedure was performed within the SEM experimental apparatus, many restrictions arose relating to the set-up of testing. Specifically, no environmental chamber could be used to control the test temperature in order to improve the heat exchange between the specimen and its surrounding environment during testing. As a result, the experimental testing procedure was conducted at room temperature with no fan-cooling assistance. However, as referenced in the previous Section 3.2.1, the exothermic SIMT and endothermic reverse transformation has a considerable influence on the stress-strain

response of NiTi. Therefore, as no fan-cooling could be used to aid in the heat exchange between the specimen and its environment, the displacement-controlled testing procedure was completed at extremely low strain rates of 0.005mm/sec. This resulted in an extended test time, however it consequently kept the impact of the exothermic/endothermic phase transformation at a minimum and thus produced more accurate and repeatable results.

3.3.2 Transformational Behaviour

Precise heat treatment procedures were applied by Admedes Schuessler GmbH to ensure the specimen would be in the superelastic austenitic microstructural phase at room temperature. This was due to the fact that the specimen's aforementioned uniaxial tensile test was conducted under *in situ* SEM at room temperature. Full transformational temperatures, namely, A_s , A_f , M_s , M_f , were confirmed through the use of DSC techniques using the methodology previously outlined in Section 3.2.2. The resulting DSC chart for the micro-dogbone specimen can be seen in Figure 3.12. It should be noted the austenite finish, A_f , temperature is found to be 11.1°C which confirms the specimen will exhibit superelastic properties at room temperature, i.e. 21°C, during the experimental *in situ* SEM testing procedures..

3.3.3 Microstructural Imaging

To characterise key microstructural features of the micro-dogbone specimen for the creation of the accurate micro-mechanical models of Chapter 5, a sequence of mechanical polishing and chemical etching was carried out to reveal the grain structure present in the specimen. As with the experimental support strut specimens, as previously described in Section 3.2.3, the mechanical polishing procedure was completed on the micro-dogbone specimens to a 0.06µm roughness and the chemical etching procedure was performed using a 1HF:4HNO₃:5H₂O solution to reveal the grain boundaries. Subsequently, SEM imaging was carried out on the specimen in order to visualise the grain structure in a 200µm x 290µm rectangle test area at the edge of the gauge section of the specimen (as identified by the box in Figure 3.13).

This location for the test area was selected for analysis due to the ease at which it may be located under SEM for the numerous experimental tests completed, namely, the SEM microstructural analysis, the EBSD textural analysis and subsequently the *in situ* SEM tensile testing procedure. It is recognised, however, that the reduced constraint at the specimen edge may affect the local stress profile at this region. As shown in Figure 3.13, a total of 40 grains are identified in the resulting SEM micrograph of the selected test area; the average grain size in the test area was found to be $29.8 \pm 3.9 \mu\text{m}$ having an aspect ratio close to one. Furthermore, a number of inclusions, averaging in the size of $8.2 \pm 1.4 \mu\text{m}$, were also acknowledged to be present in the specimen; as identified as the dark regions of the SEM micrograph of Figure 3.13. Utilising Energy Dispersive X-ray Analysis (EDXA) techniques, integrated into the SEM equipment, these inclusions were positively identified as inherent TiC precipitates.

3.3.4 Texture Characterisation

Employing Electron Back-Scatter Diffraction (EBSD) analysis techniques, the grain orientation distribution in the selected $200 \mu\text{m} \times 290 \mu\text{m}$ test site of the micro-dogbone specimen (as identified in the box of Figure 3.13) was analysed. The highly polished specimen was placed in the SEM chamber of the Hitachi SU-70 apparatus at a 70° angle towards the diffraction detector. An operating voltage of 20kV and current of 28uA was selected for testing. A phosphor screen was also located within the specimen chamber of the SEM at an angle of 90° to the pole piece and was coupled to a compact lens which focuses the image from the phosphor screen onto the CCD (charged-coupled device) camera. The electron beam was focussed onto the surface of a polycrystalline specimen, in this way the electrons enter the specimen and some may backscatter. Escaping electrons exit near to the Bragg angle and diffract to form Kikuchi bands. The resulting Kikuchi pattern is characteristic of the crystal structure and orientation of the sample region from which it is generated [Kikuchi and Nishikawa, 1928]. Using these Kikuchi patterns, the diffraction patterns were related to the underlying crystal phase and orientation of the targeted grain. For example, an unlabelled and labelled Kikuchi patterns from a (111) orientated grain in the test site

are shown in Figure 3.14. The grain orientation of each grain in the test area of the specimen was subsequently identified and a grain orientation distribution map was generated, as shown in Figure 3.15. Errors in crystal orientation measurements from the Kikuchi diffraction pattern depend principally on the accuracy of the Kikuchi band position measurement and the system calibration. In this work the crystallographic orientation measurement, with respect to the chosen specimen axes for texture measurement, was accurate to within $\pm 2.0^\circ$.

The texture of the representative test region examined in the specimen was found to comprise mostly of (100), (110) and (111) orientated grains with the highest proportion being of (111) crystallographic orientation. Remarkably similar results were seen when comparing the grain orientation distribution of the micro-dogbone specimen in this work against an experimentally established crystallographic texture of a flattened NiTi micro-tube specimen by [Robertson *et al.*, 2006], in which the manufacturing and processing techniques used were consistent with those performed on commercially available stents. The average grain size in the tubing was reported as $25 \pm 3 \mu\text{m}$, as compared to $29 \pm 4 \mu\text{m}$ in this work and, similarly, the majority of grains present in the tubing had (100), (110) and (111) orientations with the highest proportion being the (111) orientation, thus confirming the texture of the NiTi specimen used in this work is similar to that reported in micro-tubing used in biomedical stent production.

3.3.5 Grain Orientation Behaviour

To experimentally characterise the material properties of individual grains of varying orientations in the micro-dogbone specimen, nano-indentation techniques were employed. This approach was selected as it allows for testing of small volumes of the test specimen, i.e. unique grains. Such nano-indentation techniques have been used by numerous researchers on NiTi materials, including [Crone *et al.*, 2003] and [Shastri and Ramamurty, 2013], to investigate the nanoscale mechanical behaviour of the shape memory effect. In the experimental work by [Pfetzing-Micklich *et al.*, 2013], the local mechanical properties of individual grains of crystallographic (001), (101)

and (111) orientations were specifically investigated. Using a Berkovich indenter, they found a clear and pronounced dependence of nano-indentation behaviour on the crystallographic grain orientation. Results obtained for the three orientations targeted fell into three distinct groups of load–displacement curves. In this way, local nano-indentation testing within each grain is particularly useful as varying grain orientations have been shown to exhibit local microstructural variations, most notably, in their Young’s moduli [Pfetzing-Micklich *et al.*, 2013] [Gall *et al.*, 1998] [Huang and Ramirez, 2011]. This, therefore, was the key parameter extracted from the obtained nano-indentation results used to characterise each grain orientation present in the selected 200 μm x 290 μm rectangle test area of the micro-dogbone specimen used in this work.

Utilising the generated grain orientation map, as previously described in Section 3.3.4 of this chapter, each grain in the selected test area of the specimen was individually targeted for testing. Grain identification was achieved through the use of a microscope attached to the nano-indentation apparatus. The Berkovich tip, to a maximum force of 100mN, was indented into the micro-dogbone specimen at room temperature. Two indentation points were used to test each grain; each subsequent indentation location was selected sufficiently far enough away from the previous indentation location as to avoid corruption of results. Unloading data, along with the examination of the shape of the unloading curve, are studied using the standard Oliver and Pharr technique for Young’s modulus measurement. Resulting averaged austenitic Young’s moduli for the (100), (110) and (111) grain orientations in the test site were found as $45.6\pm 1.0\text{GPa}$, $44.3\pm 0.5\text{GPa}$ and $49.1\pm 2.0\text{GPa}$, respectively. For a representative unloading curve for each grain orientation targeted in the test area of the micro-dogbone specimen, see Figure 3.16 for reference.

In addition to highlighting the anisotropic nature of individual grains in the specimen, this analysis was carried out in order to validate the suitability of single crystal data from literature [Gall *et al.*, 1998] for the creation of the computational models of Chapter 5 which aim to incorporate the crystallographic texture of the NiTi

specimen. As identified in Table 3.3, the Young's moduli reported in literature for the (100), (110) and (111) orientated grains were 46.6GPa, 43.3GPa and 48.8GPa, respectively. As similar results were found in the test specimen, as discussed above, of 45.6 ± 1 GPa, 44.3 ± 0.5 GPa and 49.1 ± 2 GPa, respectively, the single crystal data from literature was deemed suitable to represent the full granular transformational behaviour of the specimen in the model. The 15 required parameters extracted from the single crystal stress-strain curve for tensile loading conditions, as shown in Table 3.3, are subsequently assigned to each grain of corresponding orientation in the model; this is discussed in greater detail in Section 5.3.2. The unloading transformational data of the single crystals in this table are speculated values, based on the experimental stress-strain curves presented, by artificially removing the effects of residual strain. The figures stated for the start and end of transformation unloading (σ_U^S and σ_U^E , respectively) therefore simply offer an estimate of the experimental unloading behaviour of the single crystals as heating of the specimen would be required in order to accurately remove all effects of the residual strain. The TiC precipitates identified in the micro-dogbone specimen are assumed to behave as a typical engineering material with standard elastic-plastic behaviour. The Young's modulus assigned to the TiC precipitates (230GPa) in numerical models is extracted from an experimental nano-indentation study reported in literature [Saffari *et al.*, 2013].

3.4 Summary of Results

For the superelastic NiTi 'v-strut' stent subcomponent specimen, the uniaxial stress-strain behaviour of its linear support strut was employed for input into the computational model of Chapter 4. This model will be used to analyse the effect of individual microstructural phases on the uniaxial response of the superelastic NiTi specimen. In order to confirm the specimen would exhibit superelastic behaviour at the test temperature of 37°C, the transformational temperatures were initially inspected. Microstructural imaging of the granular structure of the support strut was also performed for the construction of micro-mechanical model which incorporated an idealised representation of a specimen's microstructure. This model is used in the

computational work of Chapter 5 in which the effect of crystallographic texture on the uniaxial response of the specimen is under investigation.

In a similar manner, the uniaxial stress-strain behaviour of the micro-dogbone specimen was characterised for input into a second computational micro-mechanical model in Chapter 5. The transformational temperatures were also inspected in order to confirm the specimen would exhibit superelastic behaviour at room temperature, for the *in situ* SEM tensile test of Chapter 5, to experimentally investigate the effect of texture on the specimen's uniaxial tensile behaviour. In order to construct the micro-mechanical model of Chapter 5, with a realistic representation of the specimen's microstructure, microstructural imaging and textural characterisation of the micro-dogbone specimen were performed. For the input of individual granular transformational behaviour into these models, suitable single crystal uniaxial stress-strain behaviour was extracted from the published work of [Gall *et al.*, 1998].

With regards to the fatigue modelling of Chapter 6, in which the effect of microstructural phase on the fatigue behaviour of NiTi is under investigation, all material properties for input to these models, such as the fatigue crack growth rate behaviour and the fatigue crack resistance properties, are extracted from various published works in the literature, namely, of [McKelvey and Ritchie, 2001], [Robertson and Ritchie, 2007] and [Holtz *et al.*, 1999]. This will be discussed further in Section 6.3. For the fatigue modelling of Chapter 7, in which the effect of crystallographic texture on the fatigue behaviour of NiTi is under investigation, the same input data is employed. However, in the work of Chapter 7, the fatigue modelling approach developed in Chapter 6 is combined with the micro-mechanical modelling approach developed in Chapter 5. In this way, the realistic granular structure and textural characterisation performed on the micro-dogbone specimen are used to advance the fatigue models of Chapter 6 to incorporate the granular transformational behaviour of the individual grains identified in the specimen employing the aforementioned single crystal material data of [Gall *et al.*, 1998].

3.5 References

ASTM International Standards, ASTM F2004-05 Standard Test Method for Transformation Temperature of Nickel-Titanium Alloys by Thermal Analysis, 2010.

ASTM International Standards, ASTM F2082-03 Standard Test Method for Determination of Transformation Temperature of Nickel-Titanium Shape Memory Alloys by Bend and Free Recovery, 2003.

ASTM International Standards, ASTM F2516-14 Test Method for Tension Testing of Nickel-Titanium Superelastic Materials, 2014.

Auricchio F. and Taylor R., Shape-Memory Alloys: Modelling and Numerical Simulations of the Finite-Strain Superelastic Behavior. *Computer Methods in Applied Mechanics and Engineering*, 1997, **143**, p 175 – 194.

Bartning M. and Simpson J., Design and Performance of a Non-Contact Af Tester, *Proceeding of the International Conference on Shape Memory and Superelastic Technologies*, 2003, p 53.

Crone W.C., Shaw G.A., Strone D.S., Johnson A.D. and Ellis A.B., Shape Recovery after Nanoindentation of NiTi Thin Films, *Proceeding of the Scanning Electron Microscopy Annual Conference*, 2003, p 1-6.

Dordoni, E., Petrini L., Wu W., Migliavacca F., Dubini G. and Pennati G., Computational Modeling to Predict Fatigue Behavior of NiTi Stents: What do we need?, *Journal of Functional Biomaterials*, 2015, **6(2)**, p 299-317.

Gall K., Sehitoglu H., Chumlyakov Y.I. and Kireeva I.V., Tension-Compression Asymmetry of the Stress-Strain Response in Aged Single Crystal and Polycrystalline NiTi, *Acta Metallurgica*, 1998, **47**, p 1203–1217.

Harrison W.J. and Lin Z.C., The Study of Nitinol Bending Fatigue, *Proceedings of the International Conference on Shape Memory and Superelastic Technologies*, 2000, p 391-396.

Holtz R.L., Sadananda K. and Imam M.A., Fatigue Thresholds of Ni-Ti alloys near the Shape Memory Transition Temperatures, *International Journal of Fatigue*, 1999, **21**, p 137-145.

Huang X. and Ramirez A.G., Crystal Orientation Effects on the Onset of Plasticity on Single-Crystal NiTi, *Scripta Materialia*, 2011, **65**, p 879-882.

Kikuchi S. and Nishikawa S., The Diffraction of Cathode Rays by Calcite, *Proceedings of the Imperial Academy of Japan*, 1928, **4**, p 475-477.

Liu Y.N., Chen X., and McCormick P.G., Effect of Low Temperature Ageing on the Transformation Behaviour of near-equiatomic NiTi, *Journal of Materials Science*, 1997, **32**, p 5979.

McKelvey A.L. and Ritchie R.O., Fatigue-Crack Growth Behavior in the Superelastic and Shape-Memory Alloy Nitinol, *Metallurgical and Material Transactions A*, 2001, **32**, p 731-743.

Nemat-Nasser, S. and Guo, W-G., Superelastic and Cyclic Response of NiTi SMA at various Strain rates and Temperatures, *Mechanics of Materials*, 2006, **38**, p 463–474.

Pelton A.R., Gong X.-Y. and Duerig T., Fatigue Testing of Diamond-Shaped Specimens, *Proceedings of the Materials and Processes for Medical Devices Conference*, 2003, p 199-204.

Pelton A.R., Schroder V., Mitchell M.R., Gong X.-Y., Barney M. and Robertson S.W., Fatigue and Durability of Nitinol Stents, *Journal of the Mechanical Behavior of Biomedical Materials*, 2008, **1**, p 153–164.

Pfetzinger-Micklich J., Somsen C., Dlouhy A., Begay C., Hartmaier A., Wagner M.F.-X. and Eggeler G., On the Crystallographic Anisotropy of Nanoindentation in Pseudoelastic NiTi, *Acta Materialia*, 2013, **61(1)**, p 602-616.

Robertson S.W., Gong X.-Y. and Ritchie R.O., Effect of Product Form and Heat Treatment on the Crystallographic Texture of Austenitic Nitinol, *Journal of Materials Science*, 2006, **41**, p 621–630.

Robertson S.W. and Ritchie R.O., In-vitro Fatigue–Crack Growth and Fracture Toughness Behavior of Thin-Walled Superelastic Nitinol Tube for Endovascular Stents: A Basis for Defining the Effect of Crack-like Defects, *Biomaterials*, 2007, **28**, p 700–709.

Saffari P., Senthilnathan K., Robertson S.W. and Pelton A.R., Influence of Inclusions on Localized Stress/Strain Distributions, *Proceedings of the International Conference of Shape Memory and Superelastic Technologies*, 2013, p 181-182.

Shastry V.V. and Ramamurty U., Simultaneous measurement of Mechanical and Electrical Contact Resistances during Nanoindentation of NiTi Shape Memory Alloys, *Acta Materialia*, 2013, **61(14)**, p 5119-5129.

Tolomeo D., Davidson S. and Santinoranout M., Cyclic Properties of Superelastic Nitinol: Design Implications, *Proceedings of the International Conference of Shape Memory and Superelastic Technologies*, 2000, p 409–417

Undisz A., Fink M. and Rettenmayr M., Determination of Transformation Properties of Thin Medical Grade Ni-Ti Wire by High-Resolution Bend and Free Recovery Testing, *Journal of Materials Engineering and Performance*, 2009, **18**, p 814-817.

Johe R., Tensile Testing of Nitinol Tubes and Wires with Higher Strain Rates, *Journal of Materials Engineering and Performance*, 2009, **18(5-6)**, p 836-842.

Table 3.1: Material properties extracted from the experimental uniaxial tensile testing procedure completed on the linear support strut specimen.

Material Properties	Value
E_A : Austenite Elasticity	11865.33 MPa
ν_A : Austenite Poissons Ratio	0.3
E_M : Martensite Elasticity	6638.86 MPa
ν_M : Martensite Poissons Ratio	0.3
ϵ^L : Transformation Strain	0.046
$(\frac{\delta\sigma}{\delta T})_L$: $\frac{\delta\sigma}{\delta T}$ Loading	0
σ_L^S : Start of Transformation Loading	252 MPa
σ_L^E : End of Transformation Loading	260 MPa
T_0 : Reference Temperature	37°C
$(\frac{\delta\sigma}{\delta T})_U$: $\frac{\delta\sigma}{\delta T}$ Unloading	0
σ_U^S : Start of Transformation Unloading	115 MPa
σ_U^E : End of Transformation Unloading	30 MPa
σ_{CL}^S : Start of Transformation Stress during loading in compression, as a positive value	0 MPa
ϵ_V^L : Volumetric Transformation Strain, If $\epsilon_V^L = \epsilon^L$, an associated algorithm us used, with ϵ_V^L computed based on σ_L^S and σ_{CL}^S	0.046
N_A : Number of annealings to be performed during the analysis	0

Table 3.2: Material properties extracted from experimental uniaxial tensile testing procedure completed on the micro-dogbone specimen.

Material Properties	Value
E_A : Austenite Elasticity	28600 MPa
ν_A : Austenite Poissons Ratio	0.3
E_M : Martensite Elasticity	27000 MPa
ν_M : Martensite Poissons Ratio	0.3
ϵ^L : Transformation Strain	0.033
$(\frac{\delta\sigma}{\delta T})_L$: $\frac{\delta\sigma}{\delta T}$ Loading	0
σ_L^S : Start of Transformation Loading	530 MPa
σ_L^E : End of Transformation Loading	550 MPa
T_0 : Reference Temperature	21°C
$(\frac{\delta\sigma}{\delta T})_U$: $\frac{\delta\sigma}{\delta T}$ Unloading	0
σ_U^S : Start of Transformation Unloading	340 MPa
σ_U^E : End of Transformation Unloading	160 MPa
σ_{CL}^S : Start of Transformation Stress during loading in compression, as a positive value	0 MPa
ϵ_V^L : Volumetric Transformation Strain, If $\epsilon_V^L = \epsilon^L$, an associated algorithm us used, with ϵ_V^L computed based on σ_L^S and σ_{CL}^S	0.033
N_A : Number of annealings to be performed during the analysis	0

Table 3.3: Material properties extracted from experimental tensile testing curves of NiTi single crystals with varying crystallographic orientation with respect to the loading direction [Gall *et al.*, 1998].

Material Properties	(100) Orientation	(110) Orientation	(111) Orientation
E_A : Austenite Elasticity	46600 MPa	43300 MPa	48800 MPa
ν_A : Austenite Poissons Ratio	0.3	0.3	0.3
E_M : Martensite Elasticity	26300 MPa	21100 MPa	10000 MPa
ν_M : Martensite Poissons Ratio	0.3	0.3	0.3
ϵ^L : Transformation Strain	0.05	0.065	0.073
$(\frac{\delta\sigma}{\delta T})_L$: $\frac{\delta\sigma}{\delta T}$ Loading	0	0	0
σ_L^S : Start of Transformation Loading	570 MPa	300 MPa	240 MPa
σ_L^E : End of Transformation Loading	580 MPa	380 MPa	340 MPa
T_0 : Reference Temperature	21.85°C	21.85°C	21.85°C
$(\frac{\delta\sigma}{\delta T})_U$: $\frac{\delta\sigma}{\delta T}$ Unloading	0	0	0
σ_U^S : Start of Transformation Unloading	575 MPa	340 MPa	290 MPa
σ_U^E : End of Transformation Unloading	180 MPa	270 MPa	160 MPa
σ_{CL}^S : Start of Transformation Stress during loading in compression, as a positive value	0 MPa	0 MPa	0 MPa
ϵ_V^L : Volumetric Transformation Strain, If $\epsilon_V^L = \epsilon^L$, an associated algorithm us used, with ϵ_V^L computed based on σ_L^S and σ_{CL}^S	0.05	0.065	0.073
N_A : Number of annealings to be performed during the analysis	0	0	0

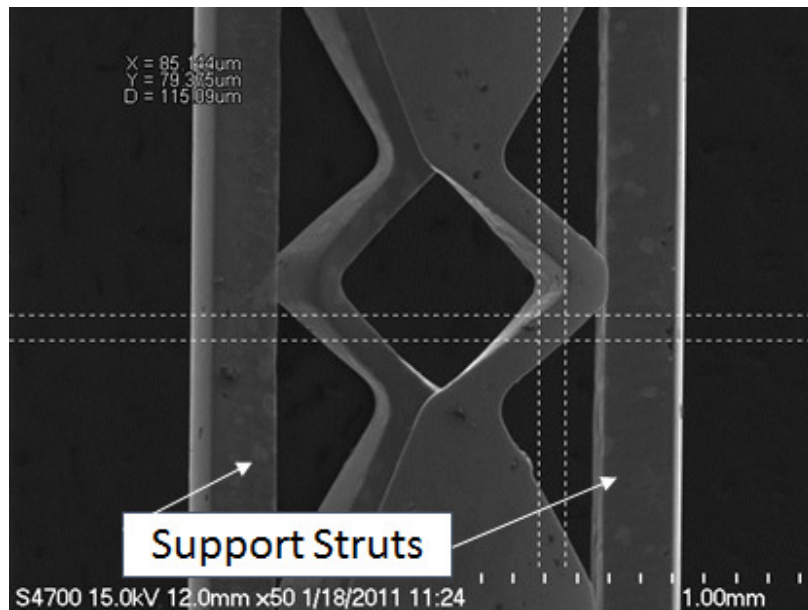


Figure 3.1: SEM micrograph of the superelastic NiTi ‘v-strut’ stent subcomponent specimen, strut width identified as approximately 85 μ m.

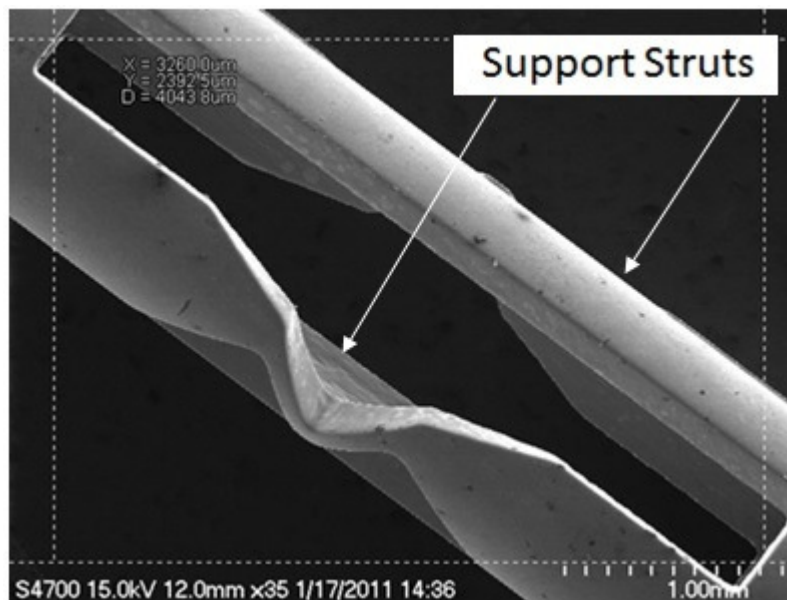


Figure 3.2: SEM micrograph of the superelastic NiTi ‘v-strut’ stent subcomponent specimen, total specimen length identified as 3260 μ m.

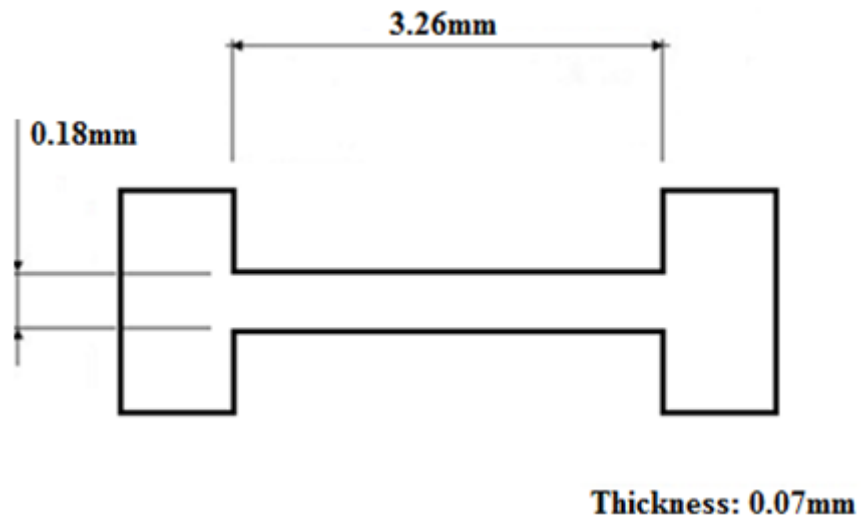


Figure 3.3: Schematic of the linear support strut test specimen (from the ‘v-strut’ stent subcomponent specimen) used in this work. All dimensions are in mm.

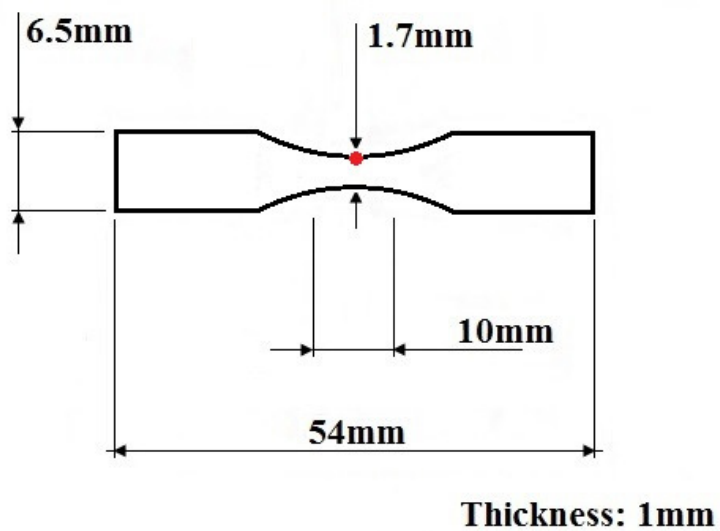


Figure 3.4: Schematic of micro-dogbone specimen used in this work. All dimensions are in mm.

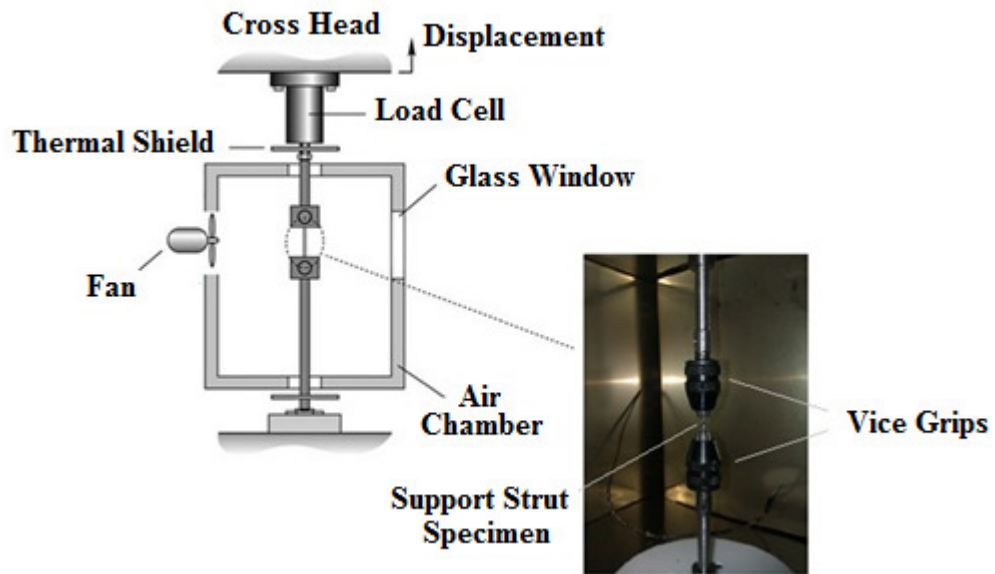


Figure 3.5: Experimental set-up of the EnduraTEC ELF/3200 with environmental chamber used in the uniaxial tension-compression testing of the linear support strut NiTi specimen.

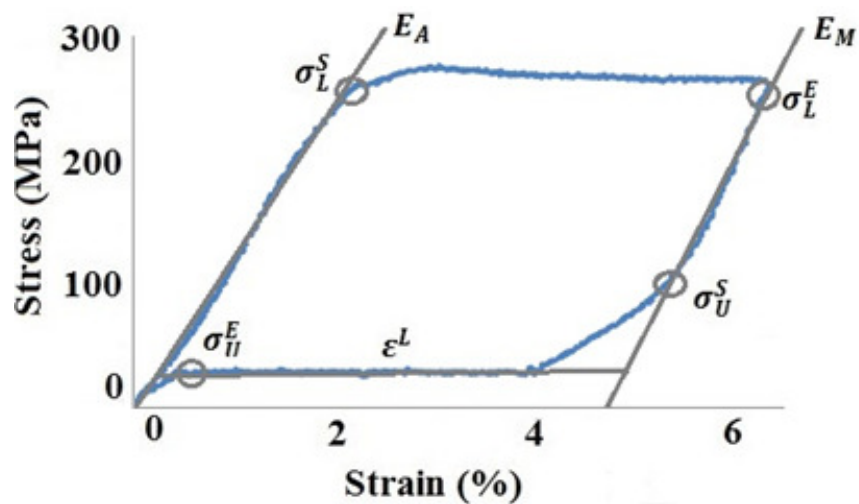


Figure 3.6: Experimental uniaxial tensile stress-strain response of the linear support strut specimen to 6% strain. Displayed are the extracted inputs for the computational modelling.

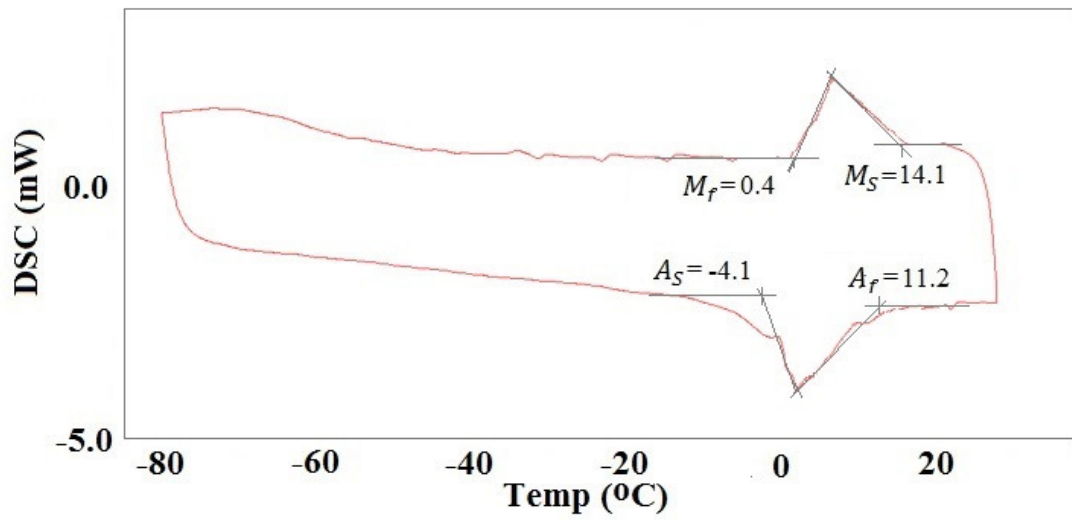


Figure 3.7: Resulting experimental DSC curve of the linear support strut specimen with all transformation temperatures labelled.

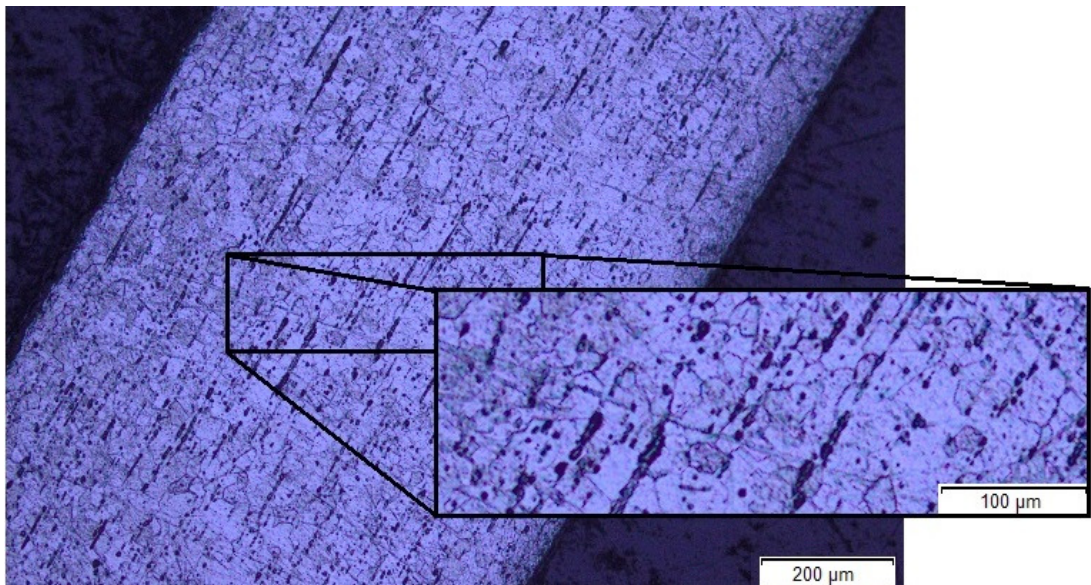


Figure 3.8: SEM micrograph of microstructure identified in the linear support strut of the 'v-strut' stent subcomponent specimen.

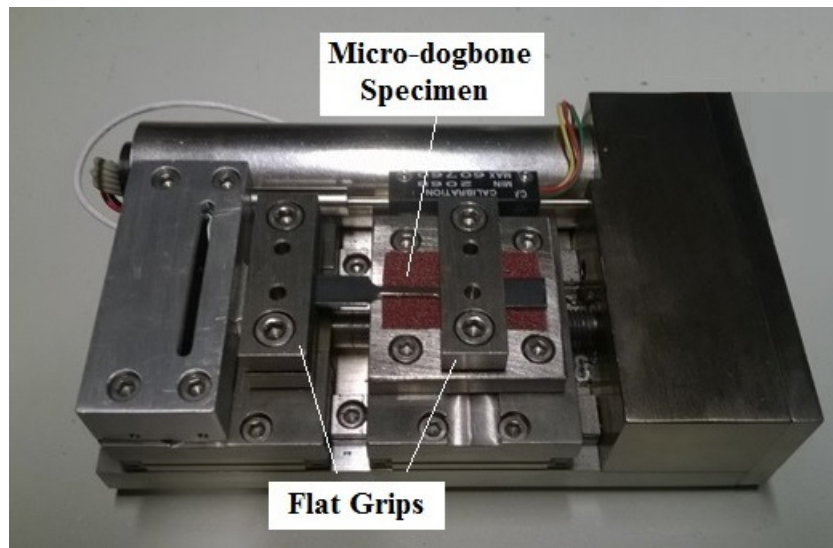


Figure 3.9: Experimental set-up of the Deben micro-stage tester used in the in situ SEM tensile test of the micro-dogbone NiTi specimen.

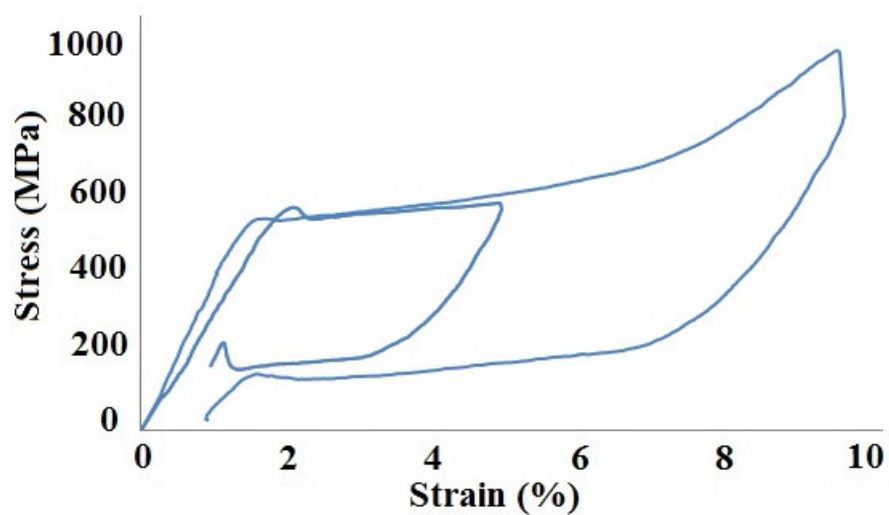


Figure 3.10: Experimental uniaxial stress-strain curve of the micro-dogbone specimen; loading to 5% strain, followed by unloading and subsequently loaded to 10% strain.

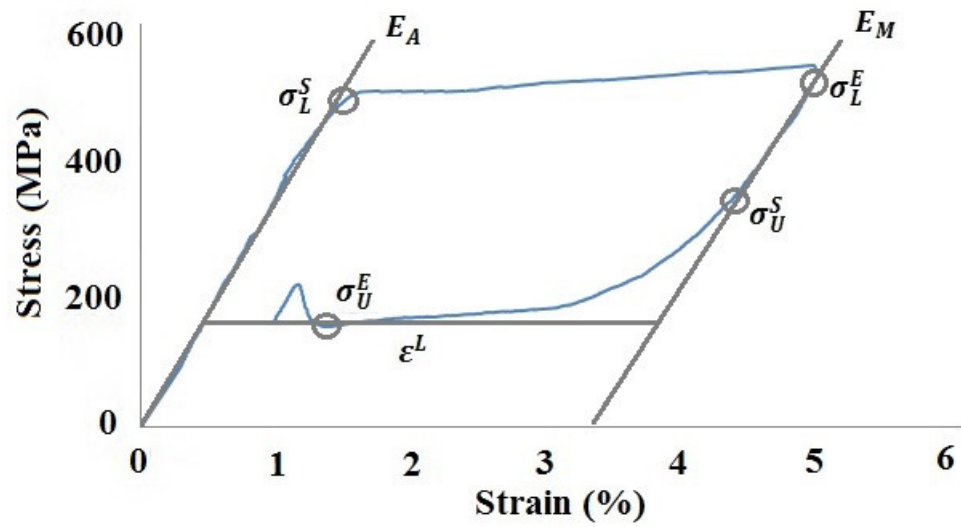


Figure 3.11: Experimental uniaxial tensile stress-strain response of the micro-dogbone specimen used in this work under 5% strain reversed loading displaying the extracted inputs for computational modelling.

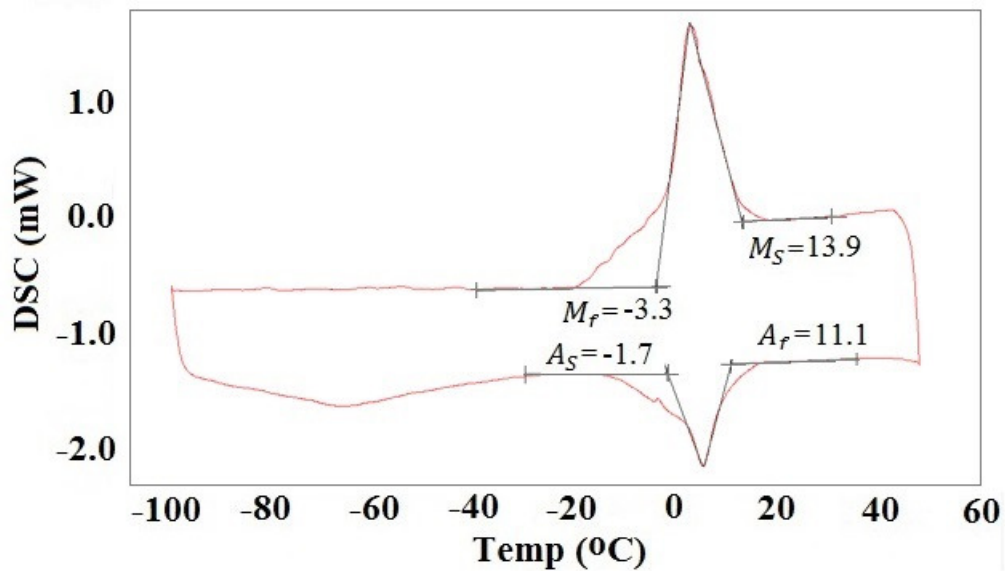


Figure 3.12: Resulting experimental DSC curve of the micro-dogbone specimen with all transformation temperatures labelled.

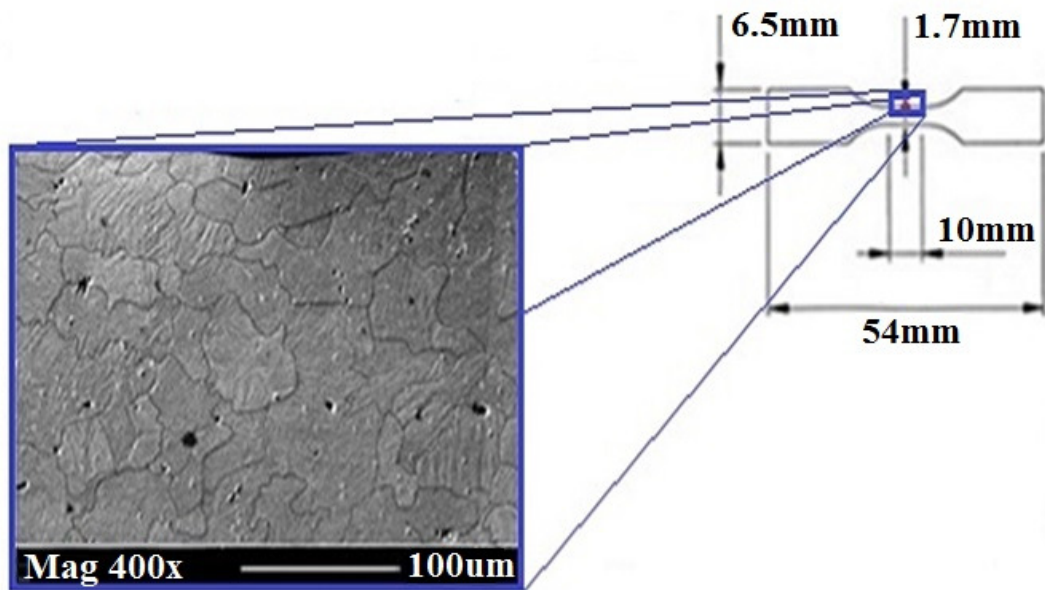


Figure 3.13: Schematic of dogbone specimen highlighting location of testing with corresponding SEM micrograph of the microstructure present in specimen.

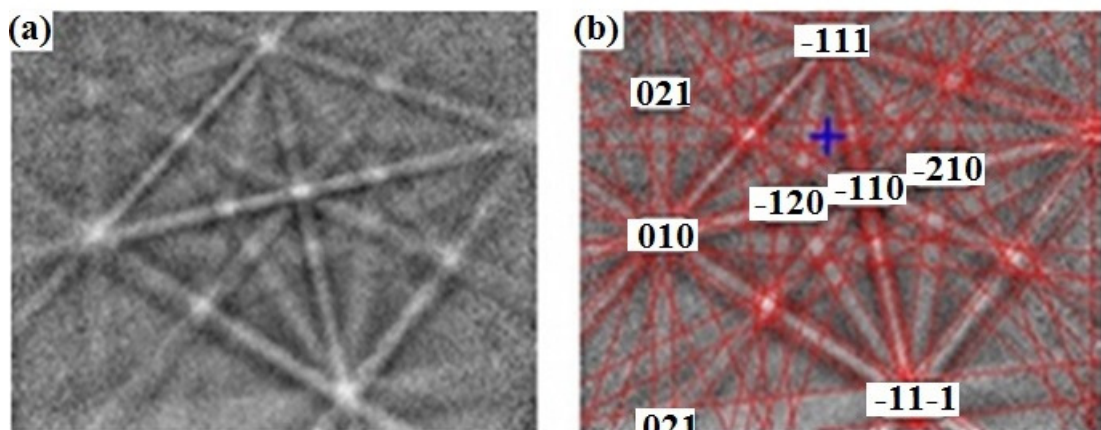


Figure 3.14: (a) Unlabeled and (b) labelled Kikuchi patterns for a (111) orientated grain identified under electron backscatter diffraction (EBSD) analysis in the test region of the micro-dogbone specimen.

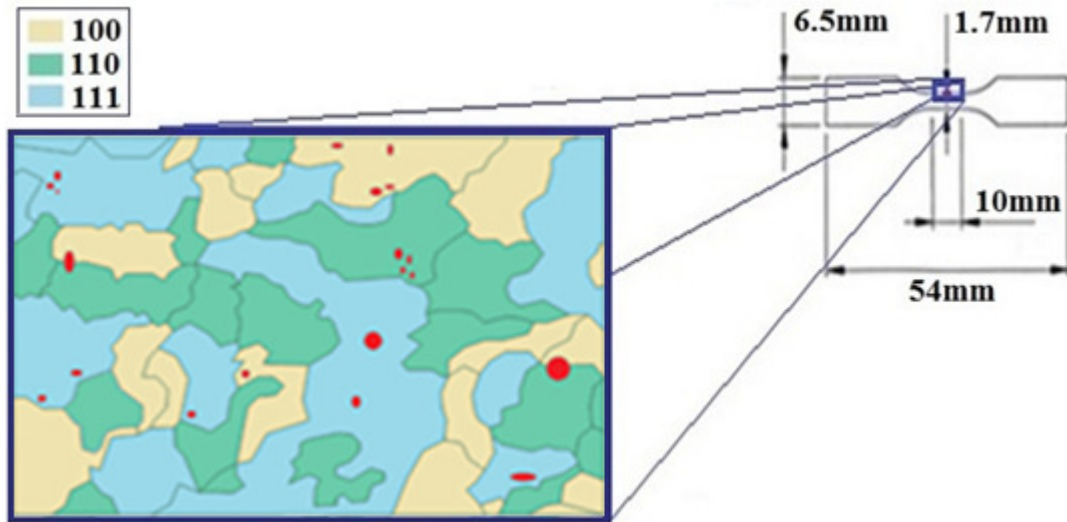


Figure 3.15: Grain orientation distribution map generated for the chosen test area of the micro-dogbone specimen using results from EBSD analysis. All crystallographic orientation plotted are with respect to loading direction.

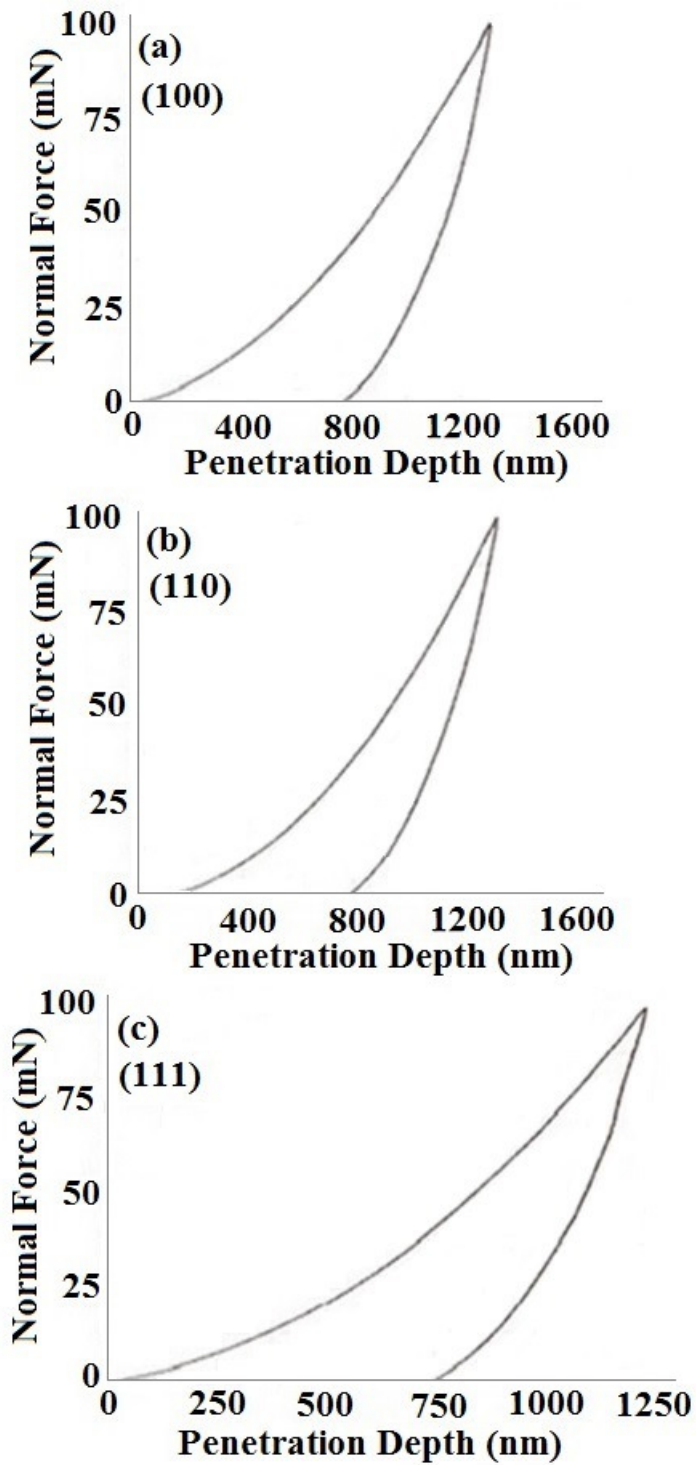


Figure 3.16: Sample nano-indentation unloading curves for (100), (110) and (111) orientated grain targeted in the chosen test area of the micro-dogbone specimen.

Chapter 4

Effect of Microstructural Phase on the Tensile Behaviour of NiTi

4.1 Introduction

In healthy human vasculature, arteries undergo diameter changes of approximately 3-10% when subject to typical 100mmHg pulse pressures [Pederson *et al.*, 1993]; these diameter changes being potentially lower with arterial stenosis. Therefore, due to the cardiac systolic-diastolic cycle, endovascular stents experience *in vivo* compressive strain amplitudes following deployment into target vessels. The mean (mid-pulse) strain has been determined to be the most significant when discussing the fatigue life of superelastic NiTi stent devices [Duerig *et al.*, 2000]. The standard operating mean strain range experienced by a self-expanding endovascular NiTi stent is approximately 1-2% strain [Gong *et al.*, 2003]. The level of mean strain experienced by a stent *in vivo* is dependent upon the level of over-sizing during design, the stenting location in addition to the tortuosity of the surrounding anatomy. Mean strain can be characterised by the balance between the exhibited inward radial resistance force (RRF) to crushing and the chronic outward force (COF) imposed by the stent against the vessel wall, termed ‘biased stiffness’ (Figure 1.2). Typical engineering materials will experience a decrease in fatigue life with increasing mean strain, however, superelastic NiTi has been experimentally shown to exhibit improved fatigue performance from approximately 1.5 to 6% mean strain levels by researchers such as [Tolomeo *et al.*, 2000], [Pelton *et al.*, 2003] and [Pelton *et al.*, 2008].

As discussed in Section 2.4.4, this unique behaviour was captured in an experimental study investigating the effect of mean strains and strain amplitudes on the cycles to failure (N_f) for fully processed superelastic NiTi stent subcomponents in the diamond configuration by [Tolomeo *et al.*, 2000]. It was noted, for a given strain amplitude, specimens that were subjected to 3% mean strain resulted in longest fatigue lives. In more recent studies, completed by [Pelton *et al.*, 2003] and [Pelton *et al.*, 2008] on superelastic NiTi diamond and dogbone specimens, complimentary results were reported. In those studies, specimens that were subjected to 4% mean strain were reported to result in the longest fatigue lives for a given applied strain amplitude. In these three experimental studies, the initial improvement of fatigue performance was

shown to occur at approximately 1.5-2% mean strain. As the operating mean strain range of self-expanding NiTi stents falls within the exhibited increased fatigue performance range, this confirms superelastic NiTi as an appealing material for self-expanding stent device manufacture.

However, clarification into the phenomenon of superelastic NiTi's increased fatigue performance with increasing mean strain still remains incomplete in the literature. In particular, insufficient knowledge exists to describe the influence of individual microstructural phases, namely austenite and SIM, on this advantageous macroscopic behaviour. Therefore, the aim of this chapter is to computationally investigate the potential influence of SIM microstructural phase on the observed macroscopic fatigue behaviour of superelastic NiTi. Employing a 3-D FEA model of a 'v-strut' stent subcomponent, this is achieved by identifying the volume fraction of SIM at critical locations in the stent subcomponent at various physiologically relevant levels of mean strain. The hypothesis presented in this chapter states that there is a strong connection relating SIM with the observed unusual fatigue behaviour of superelastic NiTi and, at sufficiently high mean strains, resulting stress levels induce stabilised SIM and this is what gives rise to NiTi's increased fatigue performance.

4.2 Computational Background

NiTi is a difficult material to characterise numerically due to its complex transformational behaviour. An approximation, capable of modelling the loading portion of the model, is hyperelasticity. Whilst other constitutive models have been proposed to address NiTi's behaviour, a thorough verification of these models is difficult due to the complex manufacturing requirements of NiTi. As a result, NiTi is typically available as relatively thin wires and tubes, for which the testing data available is mostly in the form of uniaxial data. It is moderately straightforward to produce a uniaxial model for NiTi; however, it is a greater challenge to produce a model that accurately represents the three-dimensional stress-strain behaviour of NiTi. Nevertheless, [Auricchio and Taylor, 1997] successfully developed a constitutive model capable of describing the superelastic and shape memory behaviour of this alloy

at finite strains. Following this constitutive model, an in-built user-defined material subroutine (UMAT/Nitinol) was successfully written for incorporation into the commercially available numerical FEA modelling platform, ABAQUS™, to capture the fundamental complex macro-scale material behaviour of transforming NiTi in three-dimensions. The theory proposed by [Auricchio and Taylor, 1997] is based on the concept of generalised plasticity and physical principles. The model is based on an additive strain decomposition, in which the total strain is divided into two parts, a purely linear elastic strain component, ε^{el} , and a transformational strain component, ε^{tr} :

$$\Delta\varepsilon = \Delta\varepsilon^{el} + \Delta\varepsilon^{tr}. \quad \text{EQ. 4.1}$$

The parent austenite to daughter martensite phase transformation, as described in Chapter 1, is driven by the resolution of Bain strain and shear forces and it takes place within a range of stress levels that are characteristic to the material:

$$\Delta\varepsilon^{tr} = \alpha\Delta\zeta \frac{\partial F}{\partial \sigma}, \quad \text{EQ. 4.2}$$

$$F^S \leq F \leq F^F, \quad \text{EQ. 4.3}$$

where ζ is the fraction of martensite, F is a transformation potential and α is a scaling parameter representing the maximum deformation obtainable by detwinning of the martensite. The same is true for the reverse transformation but at observed lower stress levels, i.e. along a hysteresis curve. The intensity of the transformation follows a stress potential law:

$$\Delta\zeta = f(\sigma, \zeta)\Delta F. \quad \text{EQ. 4.4}$$

During transformation, any change in externally applied stress levels produces a reorientation of the twinned martensite phase in a preferential direction with negligible additional effort due to the self-accommodating nature of twinned martensite. Due to the small volume change associated with the SIMT, less stress is required to induce the transformation in tension than in compression. Under tension, a flat stress-plateau occurs, while under compression, the material is quickly strain hardened such that no

flat stress-plateau is observed. TEM observations have confirmed that, under tension, martensite variants are reoriented via migration of variant interfaces with the formation of dislocation networks, with no significant plastic deformation observed. While, under compression, a high density of dislocations is generated in both the martensite twin bands and the variant accommodation area, however no significant martensite reorientation via variant interfacial migration is observed [Liu *et al.*, 1998]. Thus confirming that the deformation mechanism of superelastic NiTi is different under tension from compression. This behaviour is modelled by the UMAT/Nitinol using a linear Drucker-Prager approach for the transformation potential:

$$F = \bar{\sigma} - p \tan \beta + CT, \quad \text{EQ. 4.5}$$

with $\bar{\sigma}$ being the Mises equivalent stress, p the pressure stress, T the temperature and β and C the scaling constants.

The material data required by the UMAT/Nitinol, to fully capture the macro-scale superelastic behaviour of a phase transforming NiTi specimen, are obtained from straightforward observations of uniaxial tension-compression testing of a suitable specimen following the ASTM standard F2516-14 [ASTM, 2014]. The data characterises the start and end of the phase transformation during loading, unloading and reverse loading. The calibration of the resulting stress-strain curve consists of 15 material parameters, as demonstrated in Figure 4.1. A rule of mixtures is employed to implement the change in linear elasticity from austenitic to martensitic values. Whilst computing stresses and strains, the UMAT routine tracks variables specific to the model including, for example, the equivalent transformation strains, ε_{eq}^{tr} , ('SDV19') and the equivalent tensile stresses and strains, $\bar{\sigma}$ (MPa) and $\bar{\varepsilon}$, ('SDV22', 'SVD24'). In the computation investigation discussed in this chapter, the main focus is the explicit nodal output of the distribution of the volume fraction of SIM, ζ_i , ('SDV21') in order to investigate the influence of microstructural phase on NiTi's uniaxial response. A more in depth discussion and description of the model, in addition to further

information on how it is adapted to a three-dimensional case can be found in the work of [Auricchio and Taylor, 1997].

The UMAT/Nitinol subroutine has proven itself as a useful tool in the modelling of self-expanding NiTi's stents, in combination with *in vitro* testing, as part of a thorough design protocol. As with the approach taken in this work, the use of subcomponent FEA models have previously been used by many researchers; such as with the use of 'diamond' specimens by [Gong and Pelton, 2002] and 'v-strut' specimens by [Gong *et al.*, 2003] and [Pelton *et al.*, 2003]. Full stent models are employed for a complete analysis of stent behaviour, but with the associated additional computational time requirement. For example, [Perry *et al.*, 2002] employed a complete FEA stent model, incorporating the UMAT/Nitinol, to analyse the fatigue behaviour of the NiTi stent under cyclic loading while [Gong *et al.*, 2003] employed a similar model to analyse the stent's crush resistance. The residual stresses due to stent formation during production were examined using this approach of a complete stent model incorporating the UMAT/Nitinol by [Thériault *et al.*, 2006]. Repetitive unit cells and full stent models were employed by [Dordoni *et al.*, 2015] for an investigation into the validation of the UMAT/Nitinol for use in predicting the *in vivo* response of a NiTi stent in contact with an artery wall. Full deployment of NiTi stents for the analysis of the associated interaction with arteries, employing the UMAT/Nitinol, has become a growing topic in this research field [Prabhu *et al.*, 2004] [Wu *et al.*, 2007] [Conti *et al.*, 2010] [Auricchio *et al.*, 2010].

4.3 Computational Investigation

4.3.1 Finite Element Model Development

To investigate the effect of SIM on the fatigue behaviour of a self-expanding NiTi stent device, a 3-D homogenous 'v-strut' FEA model is created as displayed in Figure 4.2. The 'v-strut' is representative of a single strut subcomponent of a NiTi self-expanding stent laser cut from a cylindrical tube. In this way the transformational behaviour of a stent can be identified and analysed clearly in the FEA model, with the

economical use of computational time, eliminating the need to model the complete stent device. The dimensions of the FEA model are scaled to accurately represent the custom manufactured ‘v-strut’ subcomponent specimen; measurements of the ‘v-strut’ stent subcomponent are achieved using SEM imaging techniques as described in Chapter 3. As mentioned, the volume fraction of SIM is an explicit nodal output, entitled ‘SDV21’, of the in-built UMAT/Nitinol of the FEA platform ABAQUS™ 6.10. The percentage volume fraction of material transformed to SIM can therefore be extracted from the FEA model and subsequently analysed to identify its potential influence on the macroscopic response and, ultimately, on NiTi’s fatigue behaviour.

The 3-D FEA model is constructed with 27,138 eight-node hexahedral (C3D8) elements. To ensure the density of the mesh employed is sufficient, a converged solution for the maximum tensile stress, extracted from a node located on the outer apex of the ‘v-strut’ model, is achieved for a given applied displacement. In this way, the number of elements in the mesh is increased until the incremental difference between extracted results is shown to become negligible. To address the associated shear locking of 3-D elements, and to simultaneously increase computational efficiency, a reduced integration scheme is implemented in FEA codes. However, the reduced integration first order eight-noded C3D8 element used in this work also suffer from a numerical difficulty termed ‘hourglassing’ since they tend to be excessively flexible. Therefore, this must also be controlled through the selection of ‘relax stiffness’ hourglass behaviour in the user-defined UMAT/Nitinol material subroutine. Initial boundary conditions constrain the ‘bottom’ surface in all three directions ($U_x=U_y=U_z=0$); where U is the displacement. In addition, constraining boundary conditions are also placed on the nodes on the respective sides of the FEA model to prevent out-of-plane motion ($U_y=U_z=0$). In the first step of the FEA simulation, a boundary condition is employed to displace the ‘top’ surface of the 3-D model by a specified value to replicate a desired extension/compression of the ‘v-strut’ by a given global strain as illustrated in Figure 4.3. To ensure accuracy of results, it is of significant importance that the chosen simulated loading modes represent physiological conditions experienced by a stent *in vivo*. As displayed in the contour

plots of Figure 4.4, there is a considerable variation in the specimen's resulting stress profile when loaded in compression (Figure 4.4(a)) and in tension (Figure 4.4(b)). As a stent experiences *in vivo* compressive loading in a target vessel, defined by the biased stiffness, compressive loading procedures are performed on the 'v-strut' subcomponent model in the computational investigation described in this chapter.

4.3.2 Finite Element Model Inputs

As the manufacturing and processing techniques used on the custom manufactured 'v-strut' subcomponent specimen are consistent with those performed on commercially available NiTi self-expanding stents, the specimen exhibits superelastic behaviour at body temperature, 37°C. The austenite finish temperature, A_f , was determined using DSC methods to be $11.2\pm 2^\circ\text{C}$, as described in Section 3.2.2. For the characterisation of the specimen's *in vivo* superelastic material behaviour at body temperature, experimental uniaxial tensile tests are performed on the linear support struts of the specimen (as shown in Figure 3.3) at 37°C following the ASTM standard F2516-14 [ASTM, 2014], as previously described in Section 3.2.1. In the computational investigation described in this chapter, following standard design practice, the material behaviour of the 'v-strut' stent subcomponent is assumed to behave as a continuum. The 15 material parameters required by the UMAT/Nitinol to describe the specimen's homogenous behaviour are extracted from the tensile stress-strain curve of a linear support strut of the 'v-strut' stent subcomponent specimen (shown in Figure 3.6); as displayed in Table 3.1.

The material properties input into the UMAT/Nitinol to describe the elastic behaviour of the specimen's austenitic and martensitic NiTi phases, in addition to the transformational behaviour in forward and reverse loading, neglect plasticity in the investigation discussed in this chapter. Neglecting of plasticity was deemed applicable in this work as the highest value of localised strain imposed on the 3-D FEA 'v-strut' model was at a maximum of 6% strain. This level of maximum strain was evaluated in the FEA model at a node located on the outer apex of the 'v-strut' specimen for a given applied displacement, following the maximum principal strain vs axial

displacement curve presented in Figure 4.3. As the elastic limit of the superelastic NiTi ‘v-strut’ stent subcomponent specimen was experimentally shown to be greater than 6% strain (as illustrated in the stress-strain curve of Figure 3.6), no local plastic deformation would be experienced by the experimental specimen at the imposed maximum 6% strain level. Therefore, as there would be no volume of material in the ‘v-strut’ geometry experiencing a strain level exceeding the elastic limit of the specimen, neglecting of plasticity in the models was deemed applicable in this work.

4.3.3 Finite Element Model Results

There remain many unknowns associated with superelastic NiTi’s highly advantageous trait of exhibited increased fatigue performance with increasing mean strain. As a result, the potential influence of SIM on the observed macroscopic behaviour of superelastic NiTi is the main focus of investigation in this chapter. Employing a homogenous 3-D FEA ‘v-strut’ stent subcomponent model, the volume fraction of SIM was extracted and analysed during various levels of tensile and compressive loading conditions. For illustrative purposes the contour plots of the exhibited volume fraction of SIM for three various compressive strain levels, namely, 2.5%, 4% and 6% strain, are displayed in Figure 4.5. From these three images, it can be seen that the total volume fraction of SIM follows a trend of increasing value with increasing imposed compressive global strain. The region containing the largest volume fraction of SIM can be identified as the region of maximum induced compressive stress located at the inner apex of the ‘v-strut’ geometry. At high enough strains it is possible that stabilised SIM may occur in the specimen, such that a discrete area of the microstructure may no longer be able to transform back to austenite. This may be attributed to deformed martensite structures upon transformation resulting from defects, such as inherent precipitates, in the material; this will be discussed further in the discussion of Section 4.4.

The most significant location for quantitative analysis for the impact of SIM on fatigue behaviour is that of peak principal tensile stress as this stress concentration represents the potential site of fatigue crack initiation. Therefore when constructing

the plot of Figure 4.6 the volume fraction of SIM was extracted from the node exhibiting peak principal tensile stress, located on the outer apex of the ‘v-strut’, for both testing conditions of global tensile and compressive loading. As seen in Figure 4.6 and Figure 4.7, the percentage volume fraction of SIM extracted from this critical node was found to follow a relatively similar trend to that of the experimentally established constant life diagram for superelastic NiTi by [Pelton *et al.*, 2003] and [Pelton *et al.*, 2008]. Both plots are shown to exhibit an increasing trend (of volume fraction of SIM and fatigue performance, respectively) initiating at approximately the $\pm 1.5\text{-}2\%$ mean strain level. Under conditions of tensile loading, the increase in the volume fraction of SIM observed in the ‘v-strut’ specimen (Figure 4.6), along with the observed on-set of increased fatigue performance from literature (Figure 4.7), are also shown to correlate with the on-set of SIM under uniaxial tensile loading in the specimen at approximately the 2% strain level (Figure 3.6). This suggests there is a potential correlation between the SIM microstructural phase and the observed unusual fatigue behaviour of superelastic NiTi.

4.3.4 Computational Model Validation

In order to assess the use of the UMAT/Nitinol in the 3-D FEA model created for the computational investigation discussed in this chapter, the predicted stress-strain material response generated by a 3D single element FEA model was directly compared against the experimental uniaxial tensile test data performed on the support strut of the custom manufactured ‘v-strut’ specimen. As seen in Figure 4.8, a good agreement is achieved between the predicted uniaxial stress-strain curve of a 3-D single element FEA model employing the in-built UMAT/Nitinol and the experimental macroscopic uniaxial stress-strain response of the support strut specimen. In this way, the UMAT/Nitinol material subroutine is confirmed to be capable of capturing the complex transformational behaviour of the superelastic NiTi under uniaxial loading conditions. However, in order to validate the simulated response of the 3-D ‘v-strut’ FEA geometry, a comparison is required of the predicted load-displacement behaviour against an experimental load-displacement curve generated from the ‘v-strut’

experimental specimen. As seen in Figure 4.9 a relatively accurate agreement is observed for the load-displacement behaviour of the experimental specimen and the FEA model up to a 0.06mm axial displacement. However, it can be seen that the experimental data exhibits an unusual unstable behaviour with a high degree of residual strain upon unloading. This exhibited instability may be attributed to slippage in the grips under loading; as the experimental procedure was not viewed using a video extensometer, this cannot be stated for certain. Nevertheless, this model has been applied as a useful tool in analysing trend in the macroscopic transformational behaviour of the ‘v-strut’ stent subcomponent specimen under various uniaxial loading conditions experienced by a self-expanding NiTi stent *in vivo*. In this way, it can be used to aid with the objective of this work in the investigating into the potential correlation of SIM and superelastic NiTi’s exhibited fatigue behaviour.

4.4 Discussion

One remarkable trait exhibited by superelastic NiTi is the improvement of its fatigue performance with increasing mean strain. This is in stark contrast to typical engineering materials where a decrease in fatigue performance is expected with increasing mean strain. Therefore, the aim of this chapter is to establish a correlation between microstructural phases, in particular the volume fraction of SIM, and the overall macroscopic material response of superelastic NiTi. FEA models utilising the in-built material subroutine UMAT/Nitinol, proven to be capable of predicting the complex transformational behaviour of superelastic NiTi, are created to determine the influence of SIM on the quasi-static response of superelastic NiTi ‘v-strut’ stent subcomponents as a potential indicator of fatigue behaviour. The use of the detailed FEA simulation described in this chapter allows for the analysis of the evolutionary transformational behaviour of the NiTi stent subcomponent specimen at various imposed displacements; these being representative of various levels of physiologically relevant mean strains.

Through the computational work described in this chapter it has been established, as the strain levels in a ‘v-strut’ stent subcomponent specimen increase,

the volume fraction of SIM exhibited correspondingly increases. Interestingly, the percentage of the volume fraction of SIM at the critical location of fatigue failure, i.e. the location of peak principal tensile stress on the outer apex of the 'v-strut' specimen from which a fatigue crack would initiate, is shown to follow a relatively similar trend to that of the experimentally established constant life diagram for superelastic NiTi as generated by [Pelton *et al.*, 2003] and [Pelton *et al.*, 2008]. In particular, both curves are shown to display a trend of increased volume fraction of SIM and increased fatigue performance, respectively, in the compressive and tensile mean strain ranges initiating at approximately $\pm 1.5\text{-}2\%$ mean strain. Furthermore, the observed improvement of fatigue performance in the tensile loading conditions in the constant life diagram, from the works of [Pelton *et al.*, 2003] and [Pelton *et al.*, 2008], is shown to correlate with the on-set of SIM in uniaxial tensile loading procedure of the NiTi support strut specimen at approximately 2% mean strain (Figure 3.6). It can therefore be hypothesised, there is a potential connection relating SIM with the observed fatigue behaviour of superelastic NiTi, and that it may be the SIMT which underpins this unusual behaviour.

It has been experimentally demonstrated, through the Transmission Electron Microscopy (TEM) work by [Wang *et al.*, 2010], that deformed martensite structures and defects are hindered at critically high strain levels capable of inducing SIM. This altered microstructural behaviour ultimately leads to differing dominant de-twinning, reorientation modes and dislocation densities in a specimen's microstructure during SIMT [Wang *et al.*, 2010]. This may result in discrete areas of the microstructure no longer being able to transform back into austenite (i.e. stabilised SIM); on a microstructural scale the stress fields of the dislocations are high enough to prevent unloading, even if the material is macroscopically without load. Due to the presence of stabilised SIM, the material will locally behave as a standard metallic material accumulating plasticity during cyclic mechanical loading. Stabilised SIM results in localised strengthening of the superelastic NiTi by means of a proposed strain hardening effect [Brinson *et al.*, 2004]. Clarification into the effect of this process with regards to fatigue performance still remains relatively unexplored in literature.

Although it is acknowledged that stabilised SIM is not taken into account in the computational modelling work completed in this thesis, the theory of stabilised SIM may provide potential evidence towards the proposed hypothesis presented in this chapter which states that there is a potential correlation between SIM and the observed improved fatigue performance of NiTi with increased mean strain levels.

4.5 References

ASTM International Standards, ASTM F2516-14 Test Method for Tension Testing of Nickel-Titanium Superelastic Materials, 2014.

Auricchio F. and Taylor R., Shape-Memory Alloys: Modelling and Numerical Simulations of the Finite-Strain Superelastic Behavior. *Computer Methods in Applied Mechanics and Engineering*, 1997, **143**, p 175 – 194.

Auricchio F., Conti M., Morganti S. and Reali A., Shape Memory Alloy: From Constitutive Modeling to Finite Element Analysis of Stent Deployment, *Computer Modeling in Engineering and Sciences*, 2010, **57(3)**, p 225-243.

Brinson L., Stress-Induced Transformation Behavior of a Polycrystalline NiTi Shape Memory Alloy: Micro and Macromechanical Investigations via In-Situ Optical Microscopy. *Journal of the Mechanics and Physics of Solids*, 2004, **52(7)**, p 1549–1571.

Conti M., Auricchio F., De Santis G., De Beule M. and Verheghe B., Patient-specific Finite Element Analysis of Carotid Artery Stenting, *Proceedings of the ASME 2010 Summer Bioengineering Conference*, 2010, p 1-2.

Dordoni E., Petrini L., Wu W., Migliavacca F., Dubini G. and Pennati G., Computational Modeling to Predict Fatigue Behavior of NiTi Stents: What do we need?, *Journal of Functional Biomaterials*, 2015, **6**, p 299-317.

Duerig T., Tolomeo D.E. and Wholey M., An Overview of Superelastic Stent Design, *Minimally Invasive Therapy & Allied Technologies*, 2000, **9(3/4)**, p 235-246.

Gong X.-Y. and Pelton A.R., Finite Element Analysis on Nitinol Medical Applications, *Proceedings of the International Conference of Shape Memory and Superelastic Technologies*, 2002, p 443–451.

Gong X.-Y., Pelton A.R., Duerig T., Rebelo N. and Perry M., Finite Element Analysis and Experimental Evaluation of Superelastic Nitinol Stents, *Proceedings of the International Conference of Shape Memory and Superelastic Technologies*, 2003, p 453 – 462.

Liu Y., Xie Z., Van Humbeeck J. and Delaey L., Asymmetry of Stress-Strain Curves under Tension and Compression for NiTi Shape Memory Alloys, *Acta Materialia*, 1998, **12**, p 4325-4338.

Pederson O.M., Aslaksen A. and Vik-Mo H., Ultrasound Measurement of the Luminal Diameter of the Abdominal Aorta and Iliac Arteries in Patients without Vascular Disease, *Journal of Vascular Surgery*, 1993, p 596-601.

Pelton A.R., Gong X.-Y. and Duerig T., Fatigue Testing of Diamond-Shaped Specimens, *Proceedings of the Materials and Processes for Medical Devices Conference*, 2003, p 199-204.

Pelton A.R., Schroder V., Mitchell M.R., Gong X.-Y., Barney M. and Robertson S.W., Fatigue and Durability of Nitinol Stents, *Journal of the Mechanical Behavior of Biomedical Materials*, 2008, **1**, p 153–164.

Perry M., Oktay S. and Muskivitch J.C., Finite Element Analysis and Fatigue of Stents, *Minimally Invasive Therapy and Allied Technologies*, 2002 **11(4)**, p 165-171.

Prabhu S., Feezor C., Denison A., Rebelo N. and Serrar M., Deployment of a Self-expanding Stent in an Artery, *Proceedings of the ABAQUS Users' Conference*, 2004, p 541-550.

Thériault P., Terriault P., Brailovski V. and Gallo R., Finite Element Modeling of a Progressively Expanding Shape Memory Stent, *Journal of Biomechanics*, 2006, **39**, p 2837-2844.

Tolomeo D., Davidson S. and Santinoranout M., Cyclic Properties of Superelastic Nitinol: Design Implications, *Proceedings of the International Conference of Shape Memory and Superelastic Technologies*, 2000, p 409–417

Wang S., Tsuchiya K., Wang L. and Umemoto M., Deformation Mechanism and Stabilization of Martensite in TiNi Shape Memory Alloy, *Journal of Materials Science and Technology*, 2010, **26(10)**, p 936-940.

Wu W., Qi M., Liu X.-P., Yand D.-Z. and Wang W.-Q., Delivery and Release of Nitinol Stent in Carotid Artery and their Interactions: A Finite Element Analysis, *Journal of Biomechanics*, 2007, **40**, p 3034-3040.

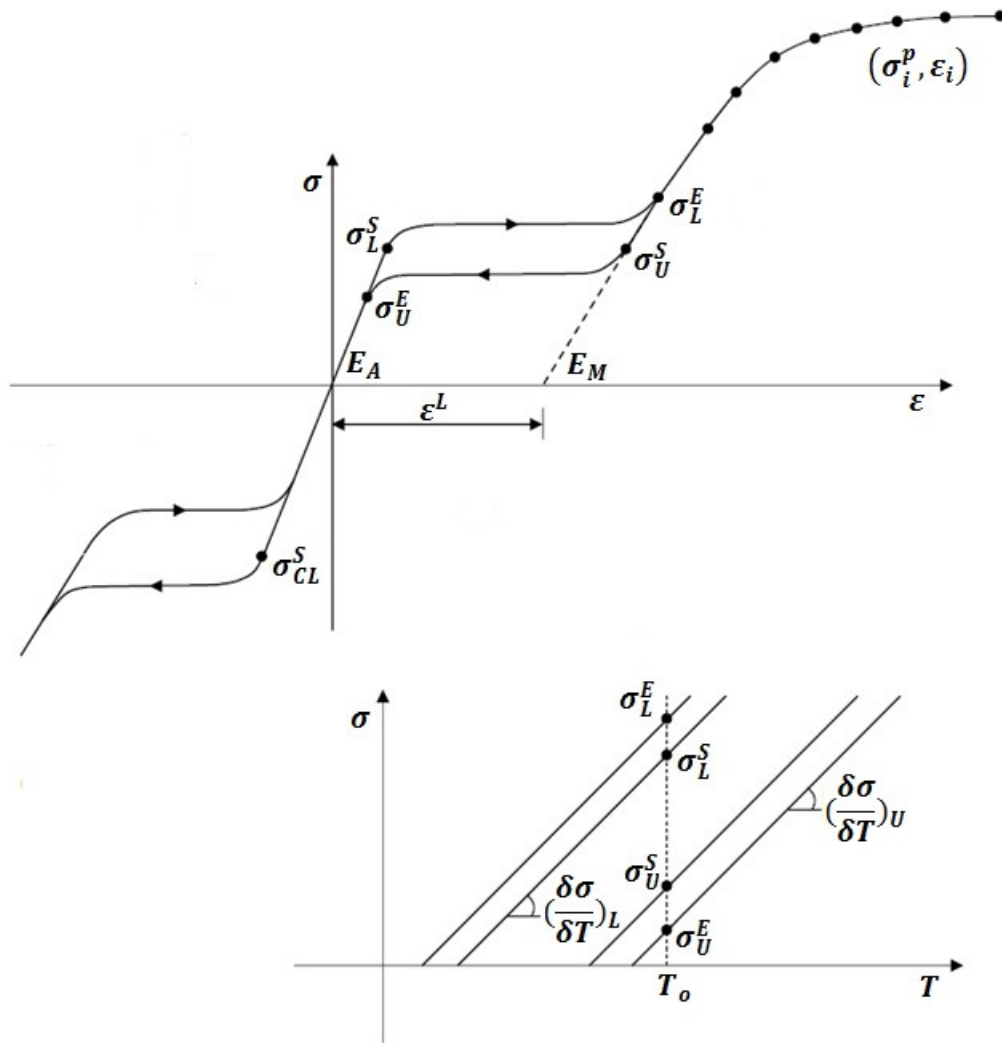


Figure 4.1: Calibration of material properties from uniaxial tension-compression testing curves for input into the in-built UMAT/Nitinol subroutine.

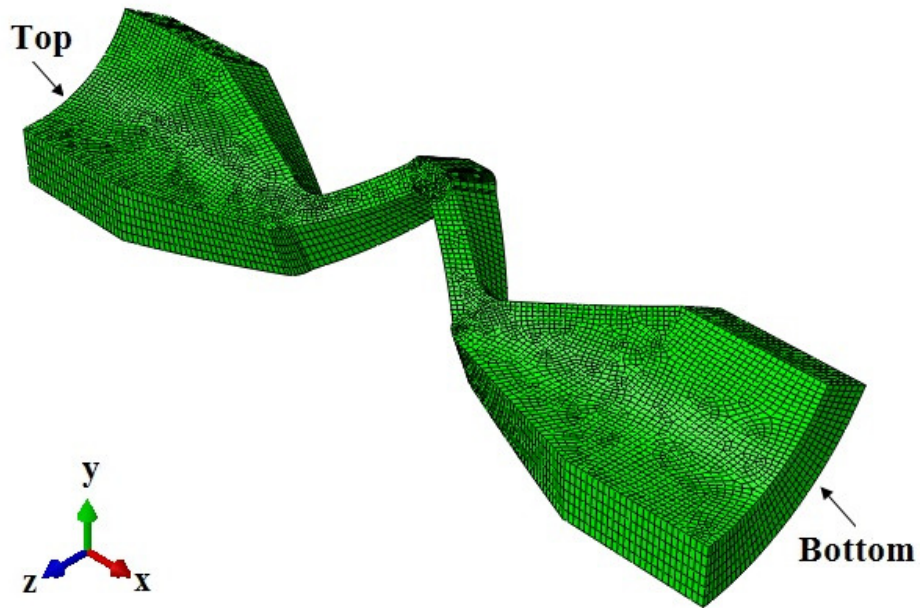


Figure 4.2: The homogenous 3-D FEA model of the ‘v-strut’ stent subcomponent specimen used in this work.

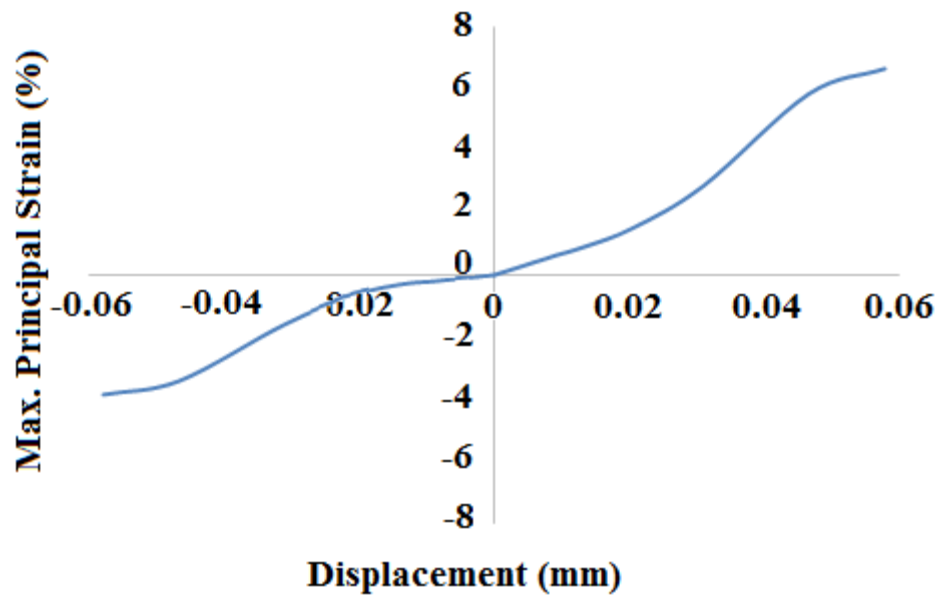


Figure 4.3: Maximum nodal principal strain in the 3-D ‘v-strut’ FEA model for various levels of axial displacement imposed, for the range of 6% to -4% strain levels.

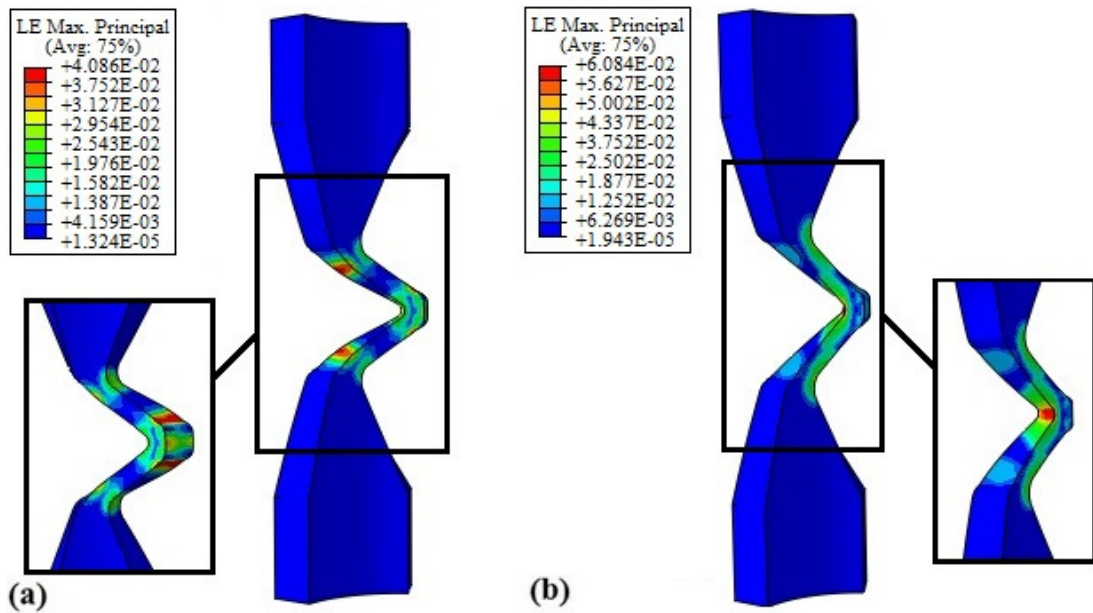


Figure 4.4: Maximum strain experienced in 'v-strut' stent subcomponent FEA model under (a) compressive loading and (b) tensile loading. Highlighting importance of correct loading procedure for physiologically relevant computational analysis.

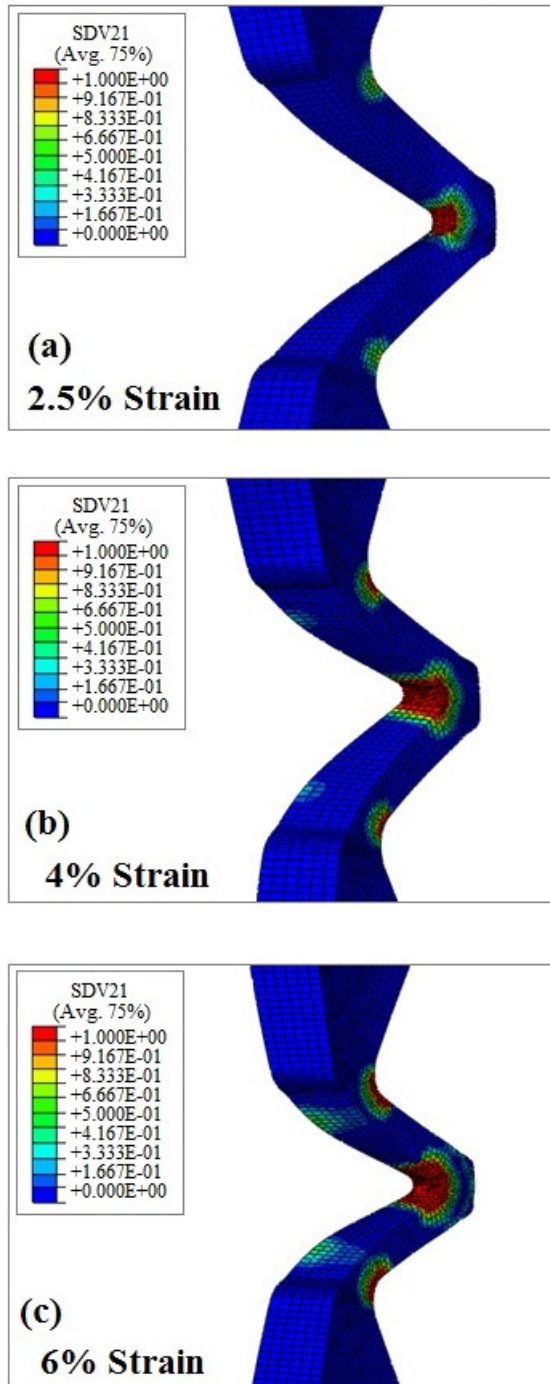


Figure 4.5: Contour plots of the 3-D 'v-strut' stent subcomponent FEA model displaying the volume fraction of SIM ('SDV21') present in the 'v-strut' geometry under (a) 2.5%, (b) 4% and (c) 6% compressive loading.

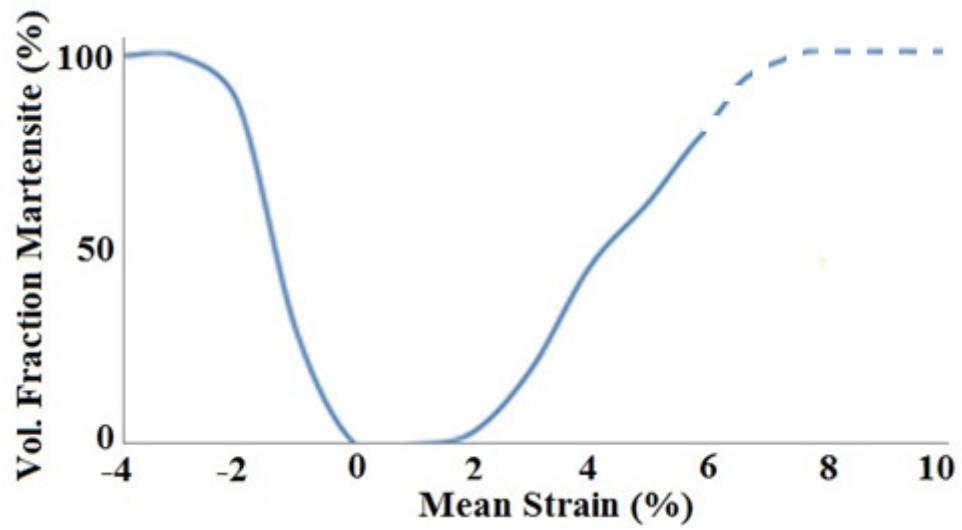


Figure 4.6: The percentage volume fraction of SIM extracted from the node exhibiting maximum tensile stress, located on the outer apex of the 3-D ‘v-strut’ FEA model, plotted against the imposed mean strain levels of -4% to +6%. Dotted line represents the predicted volume fraction of SIM up to levels of 10% mean strain.

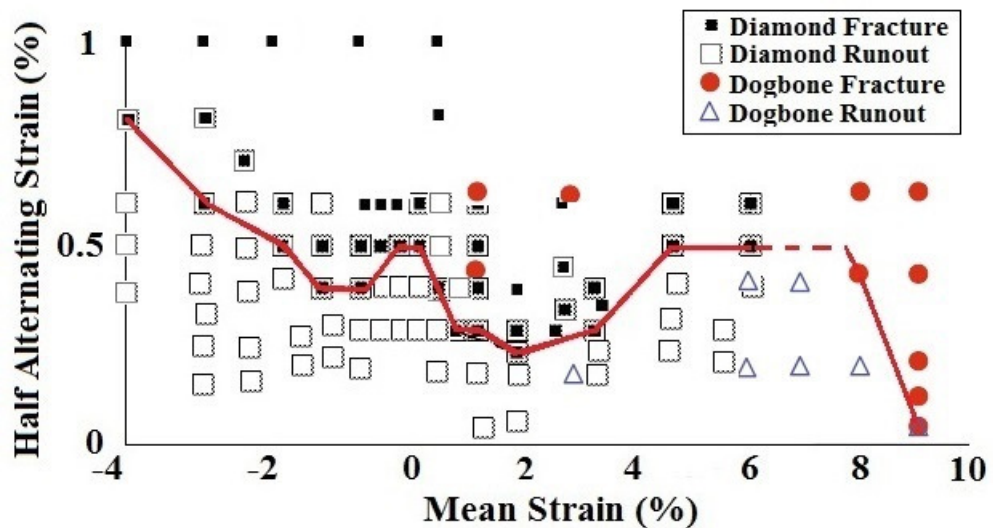


Figure 4.7: Experimental established constant life diagram of superelastic NiTi from the combined works of [Pelton *et al.*, 2003] and [Pelton *et al.*, 2008].

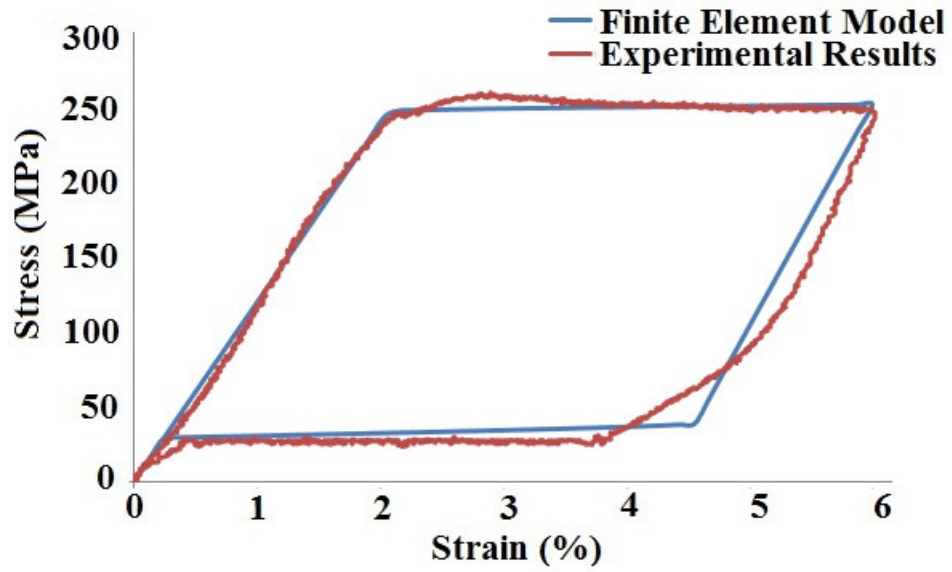


Figure 4.8: Comparison of the generated results from a 3-D single element FEA model, employing the UMAT/Nitinol subroutine, with the experimentally established stress-strain response of the linear support strut specimen.

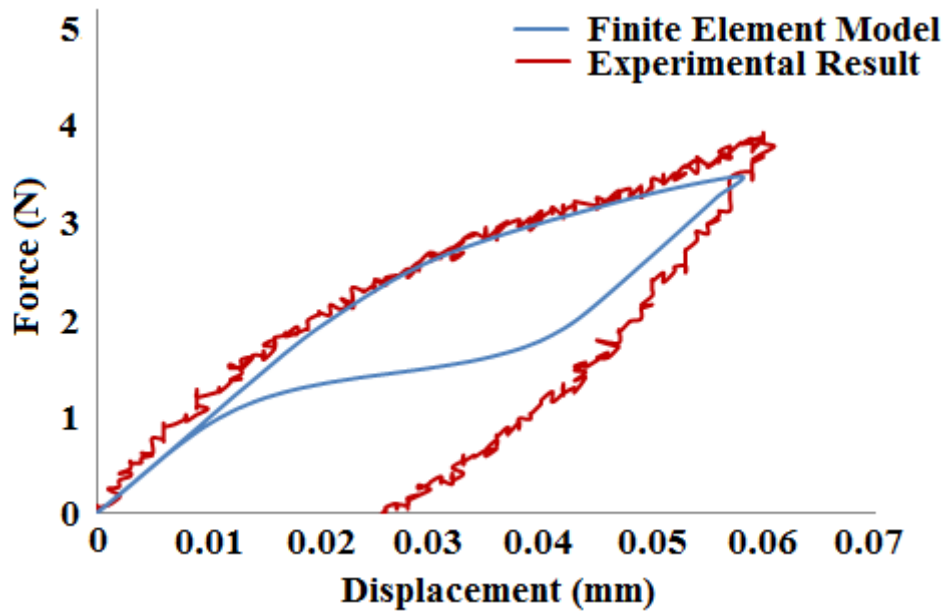


Figure 4.9: Comparison of the generated results from the 3-D 'v-strut' FEA model, employing the UMAT/Nitinol subroutine, with the experimentally established load-displacement curve of the 'v- strut' specimen.

Chapter 5

Effect of Crystallographic Texture on the Tensile Behaviour of NiTi

5.1 Introduction

Chapter 4 of this thesis examined the influence of microstructural phase, in particular the SIM phase, under tension-compression conditions as a potential indicator of the fatigue performance of superelastic NiTi. In the current chapter the influence of crystallographic texture on the tension-compression behaviour of NiTi is under investigation. The potential effect of texture on the fatigue behaviour of superelastic NiTi is targeted for computational examination as the micro-tubing in which NiTi self-expanding stent devices are manufactured from are inherently textured [Robertson *et al.*, 2006] [Gall and Sehitoglu, 1999]. The deformation behaviour of individual grains in a material is dependent upon the grain orientation with respect to the global loading direction [Huang and Ramirez, 2011]. In this way, due to texture, each grain deforms to a different extent at a local level when a specimen is subject to an externally applied mechanical load. In small engineering components, such as stent struts, individual grain behaviour is particularly significant due to the grain size to strut width ratio [Murphy *et al.*, 2003] [Donnelly, 2012]. As a result, texture may cause the material behaviour of a specimen to deviate significantly from the assumed bulk material behaviour. If such behaviour is to be captured within computational models, it is necessary to represent in some way the crystalline structure and the anisotropic behaviour of individual grains within the generated FEA models.

Despite the experimentally demonstrated dependence of mechanical properties on crystallographic texture, standard practice used in the computational design of biomedical stent devices assumes the material behaves as a continuum. Therefore, computational investigations described thus far in this thesis consider the material as a continuum, with bulk material homogenous properties assigned to the FEA model. However, when the grain size is of the order of the component size, i.e. in a biomedical stent strut, a more detailed approach must be taken. Therefore, this current chapter offers a micro-mechanical computational examination into the effect of texture on the microscopic SIMT behaviour, and ultimately on the overall macroscopic material response, of superelastic NiTi specimens subject to uniaxial tensile loading.

The numerical modelling software ABAQUS™ 6.10, along with the in-built material subroutine UMAT/Nitinol, is employed to simulate the complex transformational behaviour of the specimens on a micro-scale level. Two FEA investigations are described in this chapter, namely, a computational investigation into the effect of crystallographic texture on SIMT using FEA models incorporating (1) a realistic grain structure of a NiTi micro-dogbone specimen and, (2) an idealised, randomly generated texture based upon the grain structure of the support strut of the ‘v-strut’ stent subcomponent specimen. The localised effect of texture on the SIMT behaviour is analysed using a 2-D model with realistic grain structures, while its effect on NiTi’s macroscopic SIMT response is analysed using 2-D models employing multiple idealised, randomly generated textures. In addition, using a 2-D ‘v-strut’ model with an idealised grain structure, the identification and analyses of critical locations of potential fatigue crack initiation (i.e. peak tensile stresses) in the biomedical stent subcomponent is analysed. Finally, the evolution of phase transformation within the grains in the micro-dogbone specimen is experimentally investigated by means of an *in situ* SEM tensile test.

5.2 Computational Background

In the last four decades, constitutive modelling of superelastic materials has been an active research topic. The three main modelling methodologies used can be categorised as macro, micro or micro-macro scaled based approaches. Macro-scale approaches use averaged material behaviour extracted from experimental tension-compression testing procedures and, in general, are suitable to be used within numerical methods such as FEA. As discussed in Section 4.2 the most significant constitutive model, based on an internal variable formalism and the framework of generalised plasticity, was proposed by [Auricchio and Taylor, 1997]. This constitutive model was subsequently used in the formulation of the in-built UMAT/Nitinol material subroutine found in the commercially available FEA platform ABAQUS™. In this way, the fundamental material behaviour of transforming NiTi can be reproduced using an FEA model in a relatively efficient manner. This

formulation has been used by many researchers such as [Gong and Pelton, 2002], [Gong *et al.*, 2003], [Pelton *et al.*, 2003] and [Dordoni *et al.*, 2015], in conjunction with *in vitro* testing, to aid in the investigation into the safest and most efficient design of superelastic NiTi biomedical stent devices.

The description of micro-scale features is the main focus of micro models, for example a micro-scale constitutive model was proposed for martensitic reorientation and de-twinning in superelastic materials by [Thamburaja, 2005]. This model was further developed by [Pan *et al.*, 2007] to be capable of quantitatively predicting the experimental response of an initially textured and martensitic polycrystalline NiTi rod under a variety of uniaxial and multiaxial stress states. A 3-D micro-mechanical modelling approach was employed by [Sweeney *et al.*, 2012]. This work adopted an intricate combined kinematic–isotropic hardening crystal plasticity constitutive formulation to simulate the micro-scale behaviour of 316 L stainless steel materials. In a similar manner, the modelling work of [Mirzaeifar *et al.*, 2013] employed a 3-D micro-mechanical modelling approach to simulate the unique features exhibited by superelastic materials. The FEA models, which incorporated the crystallographic texture of a polycrystalline NiTi specimen, were created using the Voronoi tessellation methodology. Generalised coupled thermomechanical governing equations were determined using the first law of thermodynamics and the energy balance relation for the polycrystalline NiTi specimen. Such models have proven useful in developing a further understanding of fundamental phenomena occurring at the microscopic level, however, they are not easily applicable on the relatively larger biomedical device scale within numerical methods such as the FEA.

A micro–macro thermomechanical model was proposed by [Siredey *et al.*, 1999] to capture granular transformational behaviour in polycrystalline superelastic materials by using the average martensite fraction in each domain containing martensite plates as an internal variable. [Fischer *et al.*, 1997] suggested that the phase transformation in a micro-region is related to a critical value of the Gibbs free energy and obtained a description for the phase transformation in polycrystalline superelastic

materials by statistical methods. Such micro-macro studies combine micromechanics and macroscopic continuum mechanics to derive constitutive laws. In a similar way, microscale constitutive models have been created in recent years which aim to describe the anisotropic behaviour of individual grains with the computational efficiency of a macro-scale approach. [Donnelly, 2012] successfully combined the relevant elements of crystal plasticity for the micro-mechanical modelling of 316L stainless steel stents using the ‘Microstructural – J2’ macro-scale approach which was first developed by [Ilie, 2010]. This was achieved using crystal plasticity to generate stress-strain curves for all possible loading orientations of a single anisotropic grain subjected to a standard load. These material properties were subsequently assigned to each grain in a biomedical stent strut to give a global anisotropic material response.

A similar approach is taken in the computational investigation described in this chapter. Utilising the experimental uniaxial tensile stress-strain response of superelastic NiTi single crystals of varying orientations with respect to the loading direction [Gall *et al.*, 1998], as listed in Table 3.3, suitable material parameters are extracted for use in the inbuilt material subroutine UMAT/Nitinol in the FEA platform ABAQUS™ 6.10. Each grain is therefore assumed to have homogenous material behaviour which is dependent on the grain’s orientation with respect to the global loading direction. In this way, the anisotropic granular transformational behaviour of the polycrystalline specimens is captured in the FEA numerical models with the computational efficiency of a continuum mechanics approach. However, as the material behaviour of the individual grains are determined by the stress-strain data extracted from literature, the effect of plasticity cannot be taken into account in the FEA models as the single crystals were not experimentally loaded to sufficiently high strains for plasticity to occur [Gall *et al.*, 1998]. In addition, as the work in this thesis assumes that each grain has homogenous material behaviour which is dependent on the grain’s orientation with respect to the global loading direction, this continuum approach neglects the effect of other microstructural features. This is a limitation of this work as this simplification may affect the accuracy of the results as, for example, grain boundaries have been shown to affect the fatigue response of materials in acting

as barriers to continuous fatigue crack growth [Gall *et al.*, 2000]. Nevertheless, the overall anisotropic granular transformational behaviour of a polycrystalline NiTi specimen can be successfully captured in the micro-mechanical FEA models developed in this work. In this way, the evolution of local stresses and strain in the FEA models, in addition to the distribution of the volume fraction of SIM (as nodal output termed ‘SDV21’ from the UMAT/Nitinol), can therefore be analysed under various uniaxial loading conditions. Specifically, the effect of individual grain orientations on SIMT behaviour and, therefore, on the fundamental mechanical behaviour of the superelastic NiTi specimen can be evaluated.

5.3 Computational Investigation

5.3.1 Finite Element Model Development

For the first section of investigation discussed in this chapter, into the microscale effect of crystallographic texture on SIMT using the realistic grain structure of a NiTi micro-dogbone specimen, a geometrically representative 2-D generalised plane strain FEA model was created. This realistic granular structure is employed to analyse the microstructural evolutions of localised stresses and strains within a selected test area of the specimen. In addition, the distribution of the volume fraction of material which has undergone SIMT (output as ‘SDV21’ from the UMAT/Nitinol) can be explicitly identified in the FEA model on a microscale level. This allows for a targeted investigation into the individual effect of each grain orientation in the model on the SIMT evolutionary process. To accurately represent the realistic grain structure, grains present in a representative 200 μm x 290 μm test site located at the edge of the gauge section in the micro-dogbone specimen are identified using SEM. The orientation of each grain in the test site was identified using EBSD techniques. Details of all experimental work referenced can be found in Chapter 3.

The grain structure of the selected 200 μm x 290 μm test area is subsequently geometrically replicated in the FEA model, as shown in Figure 5.1(a) and Figure 5.1(b). In this way, the model incorporates each individual grain and TiC precipitate

identified under the SEM imaging. The FEA model is constructed with 10,332 eight-node quadrilateral generalised plane strain elements (CGPE8R). This number of elements was deemed necessary following a convergence study of the resulting maximum tensile stress extracted from the master node in the 2-D model for a given applied displacement. In this way, the number of elements in the generated mesh is increased until the incremental difference between the extracted resulting values is shown to become negligible. As shown in Figure 5.1(b), boundary conditions constrain the bottom surface in the y-direction ($U_y = 0$), and the left-hand-side surface in the x-direction ($U_x = 0$); where U is the displacement. The top surface is left free to represent the free edge of the gauge section of the micro-dogbone specimen. A displacement-controlled boundary condition is employed to displace the right-hand surface of the model shown in Figure 5.1(b) in the x-direction in order to replicate the experimental uniaxial tensile testing of the micro-dogbone specimen to 5% and 10% global strain.

For the second section of the investigation described in this chapter, to evaluate the macro-scale effect of crystallographic texture on SIMT using randomly generated idealised grain structures, a 2-D generalised plane strain rectangular FEA model is first created using Voronoi tessellation. As illustrated in Figure 5.2(a) and Figure 5.2(b), this micro-mechanical model is based on the obtained SEM micrograph of the support strut specimen of the custom manufactured ‘v-strut’ subcomponent described in Chapter 3 (as seen in Figure 3.1 and Figure 3.2). Voronoi tessellation involves the subdivision of a space into user-specified regions. These regions are called Voronoi cells which, in this investigation, represent an individual grain in the NiTi support strut specimen. In this way, the number of grains present in the given rectangular sub-section of the support strut specimen was identified under SEM (Figure 5.2(a)). The selected rectangular sizing, in addition to the number of grains present, are subsequently input into a user-defined script. Using the Voronoi tessellation method, given the number of sample points which represent grain nuclei, this code was employed to solve for grain geometry within the specified rectangular sub-section (Figure 5.2(b)). However, as the grains present in the support strut had an aspect ratio close to 1, the complex Voronoi tessellation models were deemed unnecessary in the

generation of multiple models for the investigation of randomly generated textures. A new model is therefore created in which each grain is represented by a simple hexagonal unit cell, as illustrated in Figure 5.2(c) and in more detail in Figure 5.3. However, as this idealised modelling approach assumes all grains in the specimen are of equal sizing, it neglects to include grains with above or below average dimensions. In this way the FEA micro-mechanical models used in this work assumes a more uniform polycrystalline textural behaviour than that which would not occur naturally. This simplification may result in an inaccurate prediction of material behaviour being simulated. This can be directly attributed to the differing micro-scale behaviour of a realistic polycrystalline NiTi specimen, compared to an idealised specimen, resulting in a material response which differs from the expect behaviour due to the more scattered stress and strain distributions caused by the varying grain sizes.

Due to the uniform construction of the model, the distribution of grain orientations within the material could be easily altered, in order to investigate the effect of varying randomly generated textures on the macroscopic material response of the NiTi specimen. Models are constructed using 7,600 eight-node quadrilateral generalised plane strain elements (CGPE8R), and with all boundary conditions being identical to that of the previously described rectangular model with realistic grain structure of Figure 5.1(b). In order to investigate the influence of crystallographic texture on the behaviour of a more representative stent subcomponent geometry, a 2-D ‘v-strut’ generalised plane strain FEA model with an idealised hexagonal grain structure is also created, as shown in Figure 5.4. The scaling of this micro-mechanical FEA model is based on the SEM imaging of the ‘v-strut’ stent subcomponent specimen, as previously described in Section 3.3.3. As identified in Figure 3.1 and Figure 3.2, the strut width is $85\pm 0.2\mu\text{m}$ and the total length of the specimen is $3260\mu\text{m}$ respectively. Following the methodology used thus far, each hexagonal unit cell in a micro-mechanical model represents an individual grain of the specimen. A uniform grain size (i.e. maximum grain length) of $20\mu\text{m}$ was chosen in the 2-D ‘v-strut’ model based on the average grain size typically found in NiTi stent devices, as previously established in Section 3.2.3. This 2-D ‘v-strut’ model is created using 15,972 eight-

node quadrilateral generalised plane strain elements (CGPE8R). For symmetry reasons, only one half of the ‘v-strut’ was necessary for modelling. As to maintain symmetry, the bottom surface is constrained to have zero displacement in the y-direction (vertical direction) $U_y=0$; where U is the displacement. In the first step, a displacement-controlled boundary condition is employed to displace the top surface by a specified value to replicate a desired strain level within the specimen. Simultaneously, constraining boundary conditions are placed on the nodes on the respective sides of the model to prevent out-of-plane motion ($U_y=0$).

It should be mentioned, common microstructures in NiTi stents feature grain sizes of approximately 20-25 μm with an ultrafine-grained microstructure sublayer in the order of 40–100nm [Robertson *et al.*, 2005]. In this investigation, however, only the larger grain geometries of 20 μm identified under SEM in the support strut specimen (as previously discussed in Section 3.2.3) are represented in the numerical models. In addition, the annealed NiTi single crystal properties used for input into the UMAT/Nitinol in this investigation [Gall *et al.*, 1998] would represent the behaviour of an average grain size of approximately 20 μm in a polycrystalline material. By eliminating the smaller nano-scaled grains present in NiTi stent devices, a ‘worst-case-scenario’ effect of texture on the behaviour of the ‘v-strut’ specimen can be investigated as these grains may allow crack growth to propagate through them along a single path before being affected by changes in slip directions (represented by changes in material properties in the model) at the grain boundaries. In this manner, the microscopic stress-strain and SIMT evolutionary behaviour can be analysed using the FEA model with realistic grain structures, while the effect on NiTi’s macroscopic response can be analysed using the FEA model with the idealised, multiple randomly generated textures. In addition, using the ‘v-strut’ FEA model, the identification and analyses of critical discrete locations of peak tensile stresses in the stent subcomponent can be analysed which may represent a potential fatigue failure initiation site in NiTi medical devices.

5.3.2 Finite Element Model Inputs

The modelling methodology used in this chapter seeks to describe single grain behaviour with the computational efficiency of continuum mechanics. This is achieved by assuming each grain has homogenous isotropic behaviour and material properties are dependent on the grain's orientation with respect to the global loading direction, as previously described in Section 5.2. In addition, grain boundaries are assumed to be perfectly bonded with no inter-granular slip. To accurately simulate the granular transformational behaviour the in-built subroutine UMAT/Nitinol is employed. The constitutive equations for these micro-scale models are established using uniaxial stress-strain curves obtained from single crystals of varying orientations with respect to the loading direction which are reported in literature [Gall *et al.*, 1998]; as listed in Table 3.3. From the Kikuchi patterns described in Section 3.3.4, the grain orientation of each grain, with respect to the loading direction, was identified in the test area and a grain orientation distribution map was generated. The texture of the test region examined in the specimen was found to comprise mostly of (100), (110) and (111) orientated grains with the highest proportion being of the (111) crystallographic orientation. Utilising this grain orientation distribution map, the appropriate material properties from the literature was assigned to the individual grains in the FEA micro-mechanical model for each corresponding grain orientation. In this way, the constitutive behaviour of NiTi on a micro-scale was achieved with a satisfactorily accurate representation of the global anisotropic material response.

The suitability of the single crystal data extracted from the literature is validated by comparing the reported Young's moduli against that achieved through nano-indentation testing; full details of the nano-indentation procedures completed can be found in Section 3.3.5. The Young's moduli reported in literature for the (100), (110) and (111) orientated grains were 46.6GPa, 43.3GPa and 48.8GPa, respectively. As similar results were found in the test specimen through nano-indentation of 45.6 ± 1.0 GPa, 44.3 ± 0.5 GPa and 49.1 ± 2.0 GPa, respectively, the single crystal data from literature was deemed suitable to represent the granular behaviour of the

specimen in the FEA model. The TiC precipitates included in the realistic micro-dogbone model (Figure 5.1(b)) are assumed to behave as typical engineering materials with standard elastic-plastic behaviour. The Young's modulus assigned to the TiC precipitates (of 230GPa) was extracted from an experimental nano-indentation study reported in the literature [Saffari *et al.*, 2013].

As in the computational investigation described in Chapter 4, the material properties input into the UMAT/Nitinol in this chapter to define the elastic behaviour of the specimen's austenitic and martensitic NiTi phases, in addition to the transformational behaviour in both forward and reverse loading, neglect plasticity. Neglecting of plasticity was deemed applicable in the 2-D FEA 'v-strut' stent subcomponent model (Figure 5.4) as the maximum localised strain imposed on this FEA model was 2.5% strain. As the elastic limit of the 'v-strut' stent subcomponent material was shown to exceed 6% strain (Figure 3.6), it was therefore assumed no material would experience plastic deformation at this maximum localised strain level. Neglecting of plasticity was also deemed applicable in the 2-D rectangular FEA models of the micro-dogbone specimen (Figure 5.1) and the support strut specimen (Figure 5.3). In these cases, the global strain imposed on both FEA models remained below a maximum of 6% strain. However, a very small volume of localised material is observed to exceed the elastic limits of the micro-dogbone and stent subcomponent materials (6% and 10% strain as shown in Figure 3.10 and Figure 3.6, respectively). Although the neglecting of plasticity in the FEA micro-mechanical models is acknowledged to be a limitation of the work completed, it was rationalised by the argument that the volume of material experiencing a strain level exceeding the elastic limit of the material would be extremely low and thus the impact on the overall strain profile will be at a minimum.

5.3.3 Finite Element Model Results

For the first section of the investigation, into the microscopic analysis of the transformational behaviour of NiTi, the FEA model with realistic granular structure based on the micro-dogbone specimen is employed. As described, the distribution of

the volume fraction of SIM is an explicit nodal output, entitled 'SDV21', of the in-built UMAT/Nitinol. A contour map displaying the percentage volume fraction of SIM ('SDV21') in the test area of the micro-dogbone specimen under 2.5% and 5% strain levels are shown in Figure 5.5(a) and Figure 5.5(b), respectively. By comparing the contour plot results of Figure 5.5(a) with grain orientation map established previously in Figure 5.1(b), it can be seen that the highest proportion of SIM can be identified in the regions containing (111) orientated grains while regions containing (100) orientated grains appear to have the smallest volume fraction of transformed SIM. This can be explained through the analysis of the individual granular transformational behaviour for each of the crystallographic orientations which are identified in Table 3.3. It is found that (111) orientated grains have a relatively low initiation stress for SIMT of only 240MPa, while (100) orientated grains have a relatively high initiation stress of 570MPa. It can therefore be confirmed that grains in the (111) orientation are shown to promote, while grains orientated in the (100) crystallographic direction inhibit SIMT [Robertson *et al.*, 2006] [Weafer and Bruzzi, 2014] [Weafer *et al.*, 2015].

Using this rectangular FEA model with realistic grain structure, the evolution of localised stresses and strains in the test area of the micro-dogbone specimen during the transformational process can be identified and analysed. As seen in the contour plot of Figure 5.5(a), areas of strain banding exist in the FEA model. The highest levels of strain are identified in regions containing (111) orientated grains, while the lowest level of strain can be identified in regions containing (100) orientated grains. Following from the discussion above, due to the transformational behaviour of the individual grains, material in the vicinity of the (111) orientated grains will transform to the softer, more compliant martensitic phase at a lower stress level (240MPa) and thus will be the dominant vicinity for strain accommodation. Meanwhile, (100) orientated grains will remain in the stiffer austenitic phase until the critically high stress level (570MPa) is reached. As seen in model (b), strain gradients are also identified between grain boundaries of varying grain orientation and regions containing the TiC precipitates. When discussing the fatigue performance of small biomedical components, such as stent struts, these non-uniform strain gradients

become significant in the identification of induced peak tensile stresses as locations of potential fatigue crack initiation in the component; this will be discussed following the discussion of analysis performed on the ‘v-strut’ specimen model.

The second section of the investigation described in this chapter involves the evaluation of the macroscopic effect of crystallographic texture on SIMT using the rectangular support strut FEA models with idealised hexagonal grain unit cells. Assuming a non-uniform distribution of grain orientations are present in the support strut specimen, ten variations of the textured rectangular idealised hexagonal unit cell model were created. A user-defined script was employed to generate a random number between one and three, each number representing one of the three grain orientations present in the support strut specimen [Robertson and Ritchie, 2007]. In this way, the granular properties are randomly assigned to each of the hexagonal unit cells in the FEA model. Upon applying a uniaxial tensile load to each of the ten variations of the rectangular idealised granular models the effect of varying crystallographic textures on the macroscopic stress-strain response of NiTi becomes apparent. The two models producing the most similar to, and the most extreme deviation from, an expected homogenous stress-strain response are shown in Figure 5.6(a) and Figure 5.6(b).

As the FEA models used in this work simply consider a small portion of the support strut, such models would not be expected to fully capture the precise global material response of the complete support strut experimental specimen. Instead, it is the aim of this work is to highlight the potential effect of varying crystallographic textures on NiTi’s macroscopic behaviour. The large level of scatter in the specimen’s response due to varying textures, identified in Figure 5.6, provides evidence towards the hypothesis that the observed scatter in experimental results can be attributed towards crystallographic texture. As stated, it was confirmed that grains orientated in the (100) crystallographic direction inhibit, while grains in the (111) orientations promote the SIMT [Robertson *et al.*, 2006] [Weafer and Bruzzi, 2014] [Weafer *et al.*, 2015]. This becomes particularly evident when comparing Figure 5.6(a) and Figure 5.6(b), in including a higher volume of (111) orientated grains in model (b) it can be

seen that notably lower stress values are reached along the loading plateau due to the lower stress values at which SIMT occurs in (111) grains (as displayed in Table 3.3). In this way, the model illustrated in Figure 5.6(b) will have a high volume fraction of grains transforming fully to martensite at a lower stress level resulting in a negative plateau. In addition, as the Young's modulus of the (111) orientated grains is the lowest of all three grain orientations simulated, this will also result in lower stress values being reached. This computational investigation, therefore, successfully demonstrates the potential effect crystallographic texture may have on the macroscopic material response of NiTi.

As demonstrated, the difference in transformational behaviour of the individual grains result in localised stress gradients over grain boundaries; these peak stresses become particularly important when discussing fatigue behaviour of biomedical stent devices. To further explore this, the influence of crystallographic texture is investigated in the 2-D 'v-strut' model incorporating the idealised hexagonal grain unit cells (as shown in Figure 5.4). The volume fraction distribution of grain orientations present in the 'v-strut' strut specimen, based on the experimental work of [Robertson and Ritchie, 2007], is illustrated in Figure 5.7. Using this experimental data, three variations of the texture present in the 2-D 'v-strut' specimen were created while still maintaining the same volume fraction distribution of each grain orientation. The critical location of peak principal tensile stress in the model, being important as the potential site of fatigue crack initiation, was identified in the homogenous model of Chapter 4 as a node located on the outer apex of the 'v-strut' geometry. To investigate the most potentially significant effect of crystallographic texture on the 'v-strut' geometry, the three FEA models were created such that a different grain orientation was located at this critical location of potential failure.

From the three cases examined, in allocating a (100), (110) or (111) orientated grain at this critical location in the 2-D 'v-strut' geometry, it is found the hindrance to the SIMT is at a maximum with the presence of a (100) orientated grain; as illustrated in Figure 5.8. The maximum principal strain contour plot generated for each of the

three cases, namely, in which (100) orientated grains, (110) orientated grains and (111) orientated grains are located at the critical location of peak tensile stress on the outer apex of the 'v-strut' as shown in Figure 5.8(a), Figure 5.8(b) and Figure 5.8(c), respectively. The non-uniform strain distribution, due to crystallographic texture, becomes particularly evident in Figure 5.8(c) in which a (111) orientated grain is assigned to the critical fatigue crack initial site on the outer apex. Such non-uniform contour plots illustrate the discrete locations of induced peak tensile strains which become significant as potential locations of peak tensile stresses and thus as potential fatigue failure initiation sites.

5.3.4 Finite Element Model Validation

As discussed in Section 4.3.4, in order to validate the simulated results generated by the FEA models used in this work, the predicted stress-strain response generated by the model is directly compared against the experimentally established stress-strain curve for the specimen. As previously seen in Figure 4.8 and Figure 4.9, the use of the UMAT/Nitinol material subroutine in the 3-D 'v-strut' FEA model was shown to be sufficiently capable of simulating NiTi's superelastic behaviour. In a similar manner, as identified in Figure 5.9, a relatively good agreement is achieved between the predicted response of the micro-dogbone specimen segment, using the realistic micro-mechanical model of Figure 5.1(b), and the experimentally established stress-strain behaviour of the specimen of Figure 3.11. The slight variations exhibited in the predicted material behaviour, namely in the critical stress for SIMT initiation and in the slope of the SIMT plateau, can be attributed to the simplifications made in the FEA model. For instance, only a small section of the micro-dogbone specimen was considered for computational analysis, thus making it difficult for the model to fully capture the global material response of the experimental specimen.

In addition, the experimental specimen's macroscopic material behaviour may not be fully captured by the FEA model due to the assumptions made in comparing the 3-D physical geometry of the experimental micro-dogbone specimen against a generalised plane strain 2-D numerical model. In this way, the grains identified on the

specimen's surface are assumed to be projected through the thickness of the model, however this assumption of the generalised plane strain model neglects the anisotropic textured behaviour of the specimen beneath the surface. Nevertheless, the micro-mechanical modelling methodology adopted in this work of using single crystal uniaxial data of individual grains is confirmed to be sufficiently capable of capturing the complex microstructural phase transformation behaviour of the polycrystalline NiTi specimens under uniaxial loading conditions. These models can therefore be warranted as useful tools in the analysis of the transformational behaviour of superelastic NiTi under suitable loading conditions experienced during experimental testing in addition to *in vivo* loading.

5.4 Experimental Investigation

The SIMT behaviour of the micro-dogbone specimen, used to create the model with a realistic granular structure, was also experimentally investigated by means of an *in-situ* SEM tensile test. Employing a Deben micro-stage rig, the specimen was loaded to 5% strain, unloaded and subsequently loaded to 10% strain before final unloading; as was described in greater detail in Section 3.3.1. The experimentally determined uniaxial stress-strain response of the superelastic micro-dogbone specimen can be seen in Figure 3.10, clearly displaying the characteristic superelastic loading and unloading plateau stresses. During loading, optical video of the specimen was simultaneously recorded in order to attempt to identify any notable evolution of the specimen's surface during the transformational process. Interestingly, no prominent changes to the surface of the specimen are identified during the transformational process; as seen in Figure 5.10(a) and Figure 5.10(b), under 0% and a maximum of 10% strain, respectively.

In a similar investigation carried out by [Brinson *et al.*, 2004], the use of an interference filter on the microscope enabled observation of martensitic plate formation and growth. It is therefore possible that no distinct variation in surface appearance is visible under SEM without the aid of such apparatus. In addition, as martensite was found to be inherently present in the specimen in the unstrained

configuration, as seen in the micrograph of Figure 5.11, it may also be possible that SIMT may not be visible in the 200 μm x 290 μm test area targeted. The presence of this trapped martensite (stabilised SIM) in the austenitic phase may act as a barrier to the phase transformation occurring as the coordinated atomic movements manifesting in the phase transformation are highly influenced by any significant alterations in the crystallographic configuration. As the FEA model with the realistic grain structure of the micro-dogbone specimen, as described in Section 5.3.1, assumes transformation from a pure austenitic to pure martensitic material, this offers an explanation as to why the transformation is present in the computational model but is not visible under the experimental SEM procedure as this is not the case experimentally. It is also possible that at the 10% maximum macroscopic global strain imposed on the micro-dogbone tensile specimen, significant deformation and phase transformation occurs in a region other than that examined during the *in situ* SEM test. This may be due to a local stress concentration effect [Gall *et al.*, 2000] or due to the presence of highly orientated crystallographic texture elsewhere in the specimen.

5.5 Discussion

When conventional engineering materials are mechanically loaded, they undergo typically less than 1% elastic deformation followed by permanent plastic deformation. Superelastic NiTi, however, responds differently; its elastic response is followed by a stress-induced phase transformation from a cubic austenitic NiTi phase to a monoclinic martensitic NiTi phase that can result in fully recoverable macroscopic strains up to 8-11%. However as this SIMT depends upon coordinated atomic movements, any significant alignment of the atomic planes, i.e., texturing, in the polycrystalline material can have a marked influence on the mechanical response of the material by either limiting, or promoting, SIMT. Standard computational design practice of biomedical devices simply relies on uniaxial homogenous material properties to fully describe the material behaviour. However, due to the grain size to strut width ratio in biomedical stent struts, texture has been shown to cause the material behaviour to deviate significantly from the assumed homogenous response. Therefore,

in order to highlight concerns with current design practice, this chapter offers a computational investigation into the effect of crystallographic texture on SIMT employing FEA models which incorporate a realistic and idealised representation of superelastic NiTi specimen's microstructure.

Firstly, a realistic granular FEA model capable of predicting the complex constitutive behaviour of NiTi was created to determine the microscopic influence of individual crystallographic grain orientations on the SIM transformational behaviour. This 2-D model was constructed based on the microstructure identified in a superelastic NiTi micro-dogbone specimen (as identified previously in Section 3.3.3). Secondly, idealised hexagonal unit granular models are created to investigate the effect of multiple randomly generated textures on the macroscopic stress-strain response of superelastic NiTi. These 2-D models are constructed based on the texture identified in a support strut of the custom manufactured 'v-strut' stent subcomponent specimen (as identified previously in Section 3.2.3). In addition, idealised hexagonal unit cell granular models are also created in the 'v-strut' geometry to represent the 'v-strut' stent subcomponent specimen. These 2-D model were used to investigate the effect of varying grain orientations at the critical location of fatigue crack initiation in the more complex 'v-strut' geometry to provide a possible explanation for observed unforeseen failures in biomedical devices.

The granular FEA models created in this study represented a grain size of $20\mu\text{m}$ in the polycrystalline NiTi specimens, meanwhile, typical grains sizes found in NiTi endovascular self-expanding stent devices are of the order $20\text{-}25\mu\text{m}$ with ultra-fine grains of $40\text{-}100\text{nm}$. For illustrative purposes, the micro-mechanical models generated in this work neglect the influence of nano-sized grains in the material and thus demonstrate the most severe impact of crystallographic texture on the superelastic NiTi specimen's material response. The modelling approach employed in this work assumes that the individual grains, represented in all three model configurations, have isotropic homogenous material behaviour with properties varying according to their crystallographic orientation with respect to the global loading direction; material

properties are extracted from uniaxial stress-strain curves of single crystals for each crystallographic orientation which are reported in the literature [Gall *et al.*, 1998]. In this way, a global anisotropic response is achieved and, subsequently, a quantitative study is offered into the effect of texture on SIMT in the micro- and macro-scale.

In applying a uniaxial tensile load on the rectangular FEA models with realistic grain structures, it is confirmed that grains orientated in the (100) direction inhibit, while grains in the (111) direction promote, SIMT. The non-uniform evolution of stresses and strains identified in the micro-mechanical model can be directly attributed to crystallographic texture. Due to the significant alteration in transformation behaviour triggered by varying grain orientations, resulting in localised stress gradients over grain boundaries, areas of peak tensile stresses are induced. These discrete locations of maximum tensile stress become significant as possible fatigue crack initiation sites. Employing a more complex 'v-strut' FEA model with idealised hexagonal unit cell structure it is clarified that altering grain orientations at this critical location of peak tensile stress, which can be identified on the outer apex of the 'v-strut' geometry, causes significant variations in the material's localised stress and strain profiles which, in turn, alters the SIMT evolutionary profile in the specimen. Varying crystallographic textures, in terms of varying grain orientations at this key location of peak tensile stress, are therefore demonstrated to potentially affect the fatigue life of the stent device. It is found that if a (100) orientated grain is located at the site of potential fatigue crack initiation, it results in greatest impact to the SIMT behaviour. In this manner, this grain orientation distribution would inhibit the SIMT and thus would result in the shortest fatigue life for a device. Therefore, in understanding the impact of local microstructural effects on global mechanical response, it leads to a much fuller understanding of the causes of deviation of the mechanical response from predictions and unforeseen fracture in NiTi biomedical devices.

5.6 References

Auricchio F. and Taylor R., Shape-Memory Alloys: Modelling and Numerical Simulations of the Finite-Strain Superelastic Behavior. *Computer Methods in Applied Mechanics and Engineering*, 1997, **143**, p 175 – 194.

Brinson L.C., Schmidt I. and Lammering R., Stress-induced Transformation Behavior of a Polycrystalline NiTi Shape Memory Alloy: Micro and Macromechanical Investigations via in-situ Optical Microscopy, *Journal of the Mechanics and Physics of Solids*, 2004, **52**, p 1549-1571.

Donnelly E.W., Ph.D. Thesis, *Mechanical and Biomedical Engineering, National University of Ireland, Galway, Ireland*, 2012

Fischer F.D., Oberaigner E.R. and Tanaka K., Micromechanical Approach to Constitutive Equations for Phase Changing Materials, *Computational Materials Science*, 1997, **9(1-2)**, p 56-63

Gall K., Sehitoglu H., Chumlyyakov Y.I. and Kireeva I.V., Tension-Compression Asymmetry of the Stress-Strain Response in Aged Single Crystal and Polycrystalline NiTi, *Acta Metallurgica*, 1998, **47**, p 1203–1217.

Gall K. and Sehitoglu H., The Role of Texture in Tension-Compression Asymmetry in Polycrystalline NiTi, *International Journal of Plasticity*, 1999, **15(1)**, p 69-72.

Gall K., Lim T.J., McDowell D.L., Sehitoglu H., and Chumlvakov Y.I, The Role of Intergranular Constraint on the Stress-induced Martensitic Transformation in Textured Polycrystalline NiTi, *International Journal of Plasticity*, 2000, **15(10-11)**, p 1189-1214.

Gall K., Sehitoglu H., Chumlyyakov Y.I. and Kireeva I.V., Tension-Compression Asymmetry of the Stress-Strain Response in Aged Single Crystal and Polycrystalline NiTi, *Acta Metallurgica*, 1998, **47**, p 1203–1217.

Gong X.-Y. and Pelton A.R., Finite Element Analysis on Nitinol Medical Applications, *Proceedings of the International Conference of Shape Memory and Superelastic Technologies*, 2002, p 443–451.

Gong X.Y., Pelton A.R., Duerig T.W., Rebelo N., and Perry K., Finite Element Analysis and Experimental Evaluation of Superelastic Nitinol Stent, *Proceedings of the International Conference of Shape Memory and Superelastic Technologies*, 2003, p 453 – 462.

Huang X. and Ramirez A.G., Crystal Orientation Effects on the Onset of Plasticity on Single-Crystal NiTi, *Scripta Materialia*, 2011, **65**, p 879-882.

Ilie D., Ph.D Thesis, *Mechanical and Biomedical Engineering, National University of Ireland, Galway, Ireland*, 2010

Lin H.C., Wu S.K. and Lin J.C., The Martensitic Transformation in Ti-rich TiNi Shape Memory Alloys, *Materials Chemistry and Physics*, 1994, **37(2)**, p184-190.

Liu Y., Xie Z.L., Van Humbeeck J. and Delaey L., Effect of Texture Orientation on the Martensite Deformation of NiTi Shape Memory Alloy Sheet, *Acta Materialia*, 1999, **47**, p 645–660.

Mirzaeifar R., Desroches R., Yavari A., and Gall K., A Micromechanical Analysis of the Coupled Thermomechanical Superelastic Response of Textured and Untextured Polycrystalline NiTi Shape Memory Alloys, *Acta Materialia*, 2013, **61(12)**, p 4542-4558.

Murphy B.P., Savage P., McHugh P.E. and Quinn D.F., The Stress-strain Behaviour of Coronary Stent Struts is Size Dependent, *Annals of Biomedical Engineering*, 2003, **31**, p 686-691.

Pan H., Thamburaja P. and Chau F.S., Multi-axial Behavior of Shape-Memory Alloys undergoing Martensitic Reorientation and Detwinning, *International Journal of Plasticity*, 2007, **23**, p 711-732

Pelton A.R., Gong X.-Y., and Duerig T., Fatigue Testing of Diamond-Shaped Specimens, *Proceedings of the Materials and Processes for Medical Devices Conference*, 2003, p 199–204

Robertson S.W., Stankiewicz J., Gong X.-Y. and Ritchie R.O., Cyclic Fatigue of Nitinol. *Proceedings of the International Conference of Shape Memory and Superelastic Technologies*, 2004, p 79–88.

Robertson S.W., Gong X.-Y. and Ritchie R.O., Effect of Product Form and Heat Treatment on the Crystallographic Texture of Austenitic Nitinol, *Journal of Materials Science*, 2006, **41**, p 621–630.

Saffari P., Senthilnathan K., Robertson S.W. and Pelton A.R., Influence of Inclusions on Localized Stress/Strain Distributions, *Proceedings of the International Conference of Shape Memory and Superelastic Technologies*, 2013, p 181-182.

Siredey N., Patoor E., Berveiller M. and Eberhardt A., Constitutive Equations for Polycrystalline Thermoelastic Shape Memory Alloys. Part I. Intragranular Interactions and Behavior of the Grain, *International Journal of Solids and Structures*, 1999, **36 (28)**, p 4289–4315

Sweeney C.A., McHugh P.E., McGarry J.P., Leen S.B., Micromechanical Methodology for Fatigue in Cardiovascular Stents, *International Journal of Fatigue*, 2012, **44**, p 202-216.

Thamburaja P., Constitutive Equations for Martensitic Reorientation and Detwinning in Shape-Memory Alloys, *Journal of the Mechanics and Physics of Solids*, 2005, **53**, p 825–856

Weafer F.M. and Bruzzi M.S., Influence of Microstructure on the Performance of Nitinol: A Computational Analysis, *Journal of Materials Engineering and Performance*, 2014, **23**, p 2539-2544.

Weafer F.M., Guo Y. and Bruzzi M.S., The Effect of Crystallographic Texture on Stress-induced Martensitic Transformation in NiTi: A Computational Analysis, *Journal of the Mechanical Behaviour of Biomedical Materials*, 2015, **53**, p 210-217.

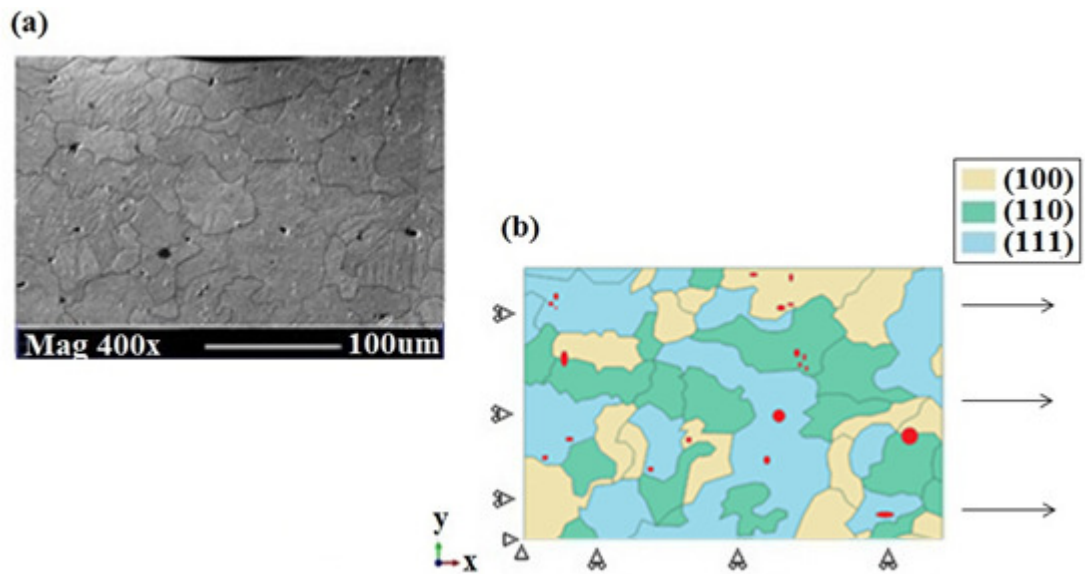


Figure 5.1: (a) SEM micrograph of the selected test area of the micro-dogbone NiTi specimen, and (b) the generated FEA micro-mechanical model based on the microstructure present in the micrograph with crystallographic grain orientations with respect to the loading direction included.

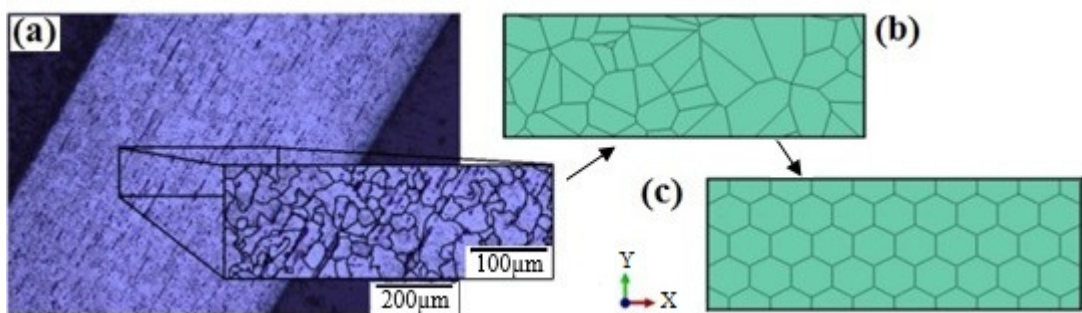


Figure 5.2: (a) SEM micrograph of the linear support strut of the 'v-strut' subcomponent specimen, and the two generated FEA micro-mechanical models based on the microstructure present in the micrograph using (b) Voronoi tessellation, and (c) idealised hexagonal unit cells.

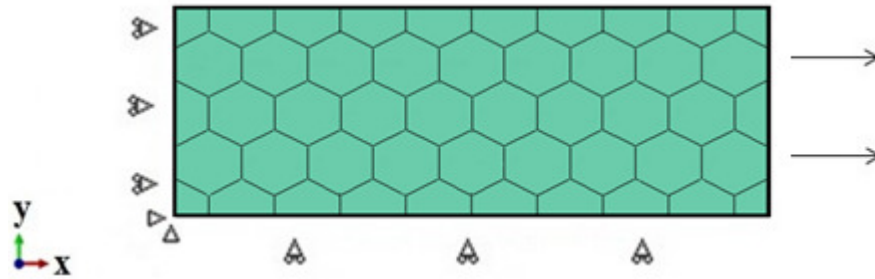


Figure 5.3: Rectangular FEA micro-mechanical model used in this work with an idealised representation of the specimen's granular structure employing hexagonal unit cells, also displaying boundary conditions used.

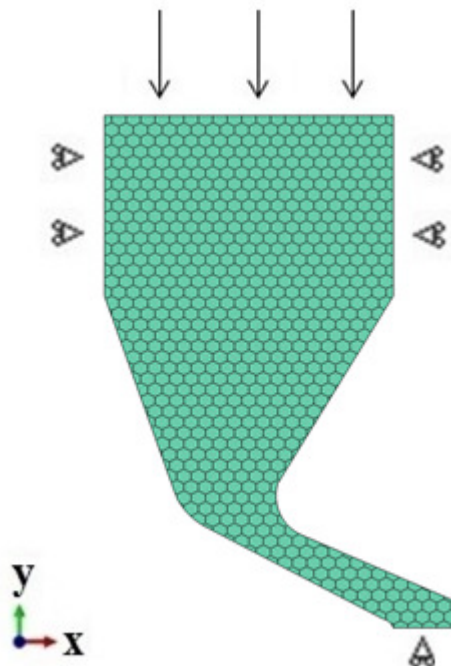


Figure 5.4: 'V-strut' FEA micro-mechanical model used in this work with an idealised representation of the specimen's granular structure employing hexagonal unit cells, also displaying boundary conditions used.

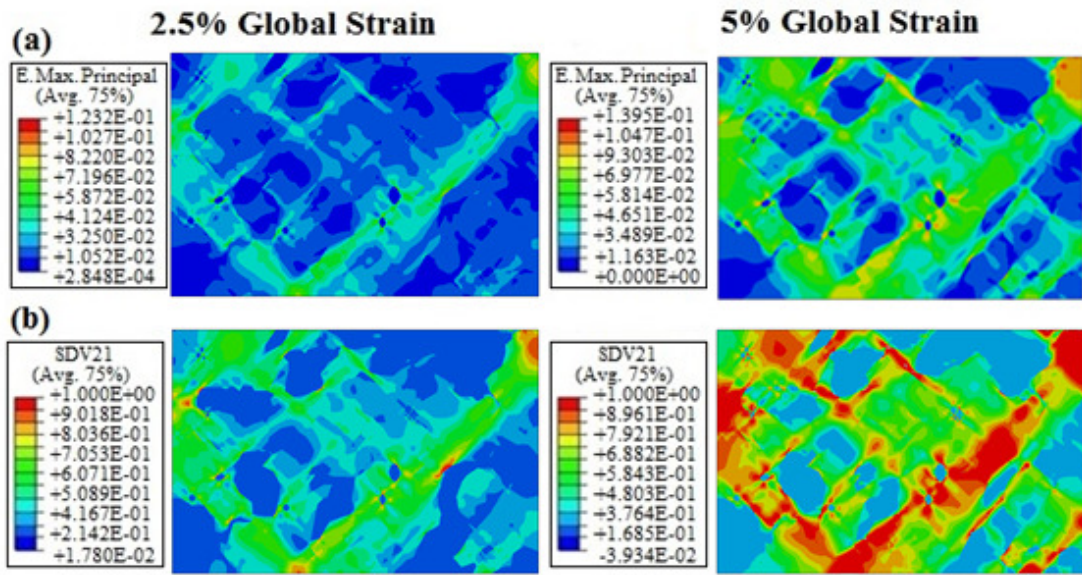


Figure 5.5: (a) Max. principal strain and (b) volume fraction of SIM ('SDV21') under a maximum of 2.5% and 5% localised tensile strain in the realistic FEA model.

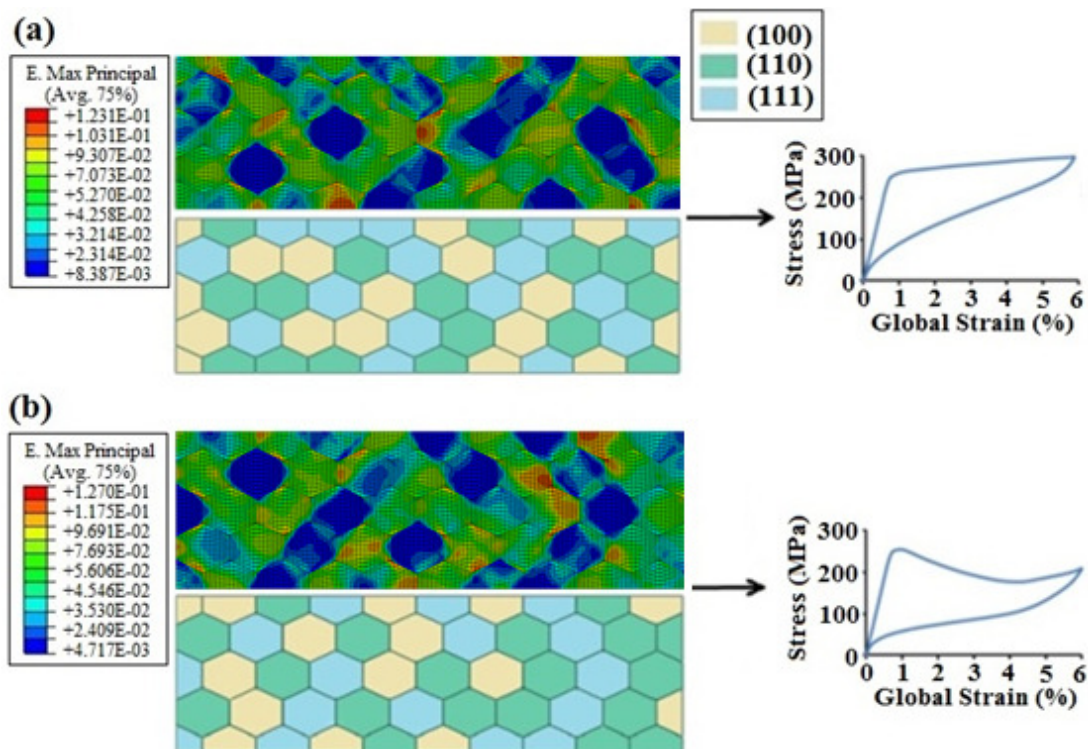


Figure 5.6: Max. principal strain evolution and uniaxial macroscopic material response due to varying textures, (a) and (b), in the idealised FEA model.

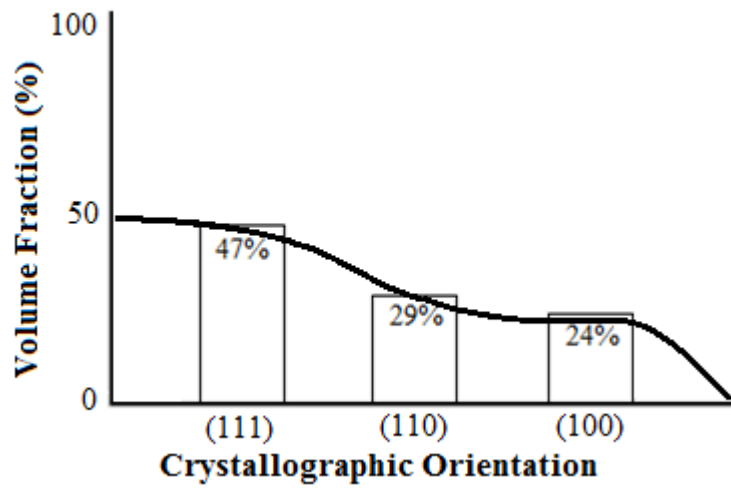


Figure 5.7: Distribution of grain orientations within the ‘v-strut’ micro-mechanical models, based on experimental textural results of [Robertson and Ritchie, 2007].

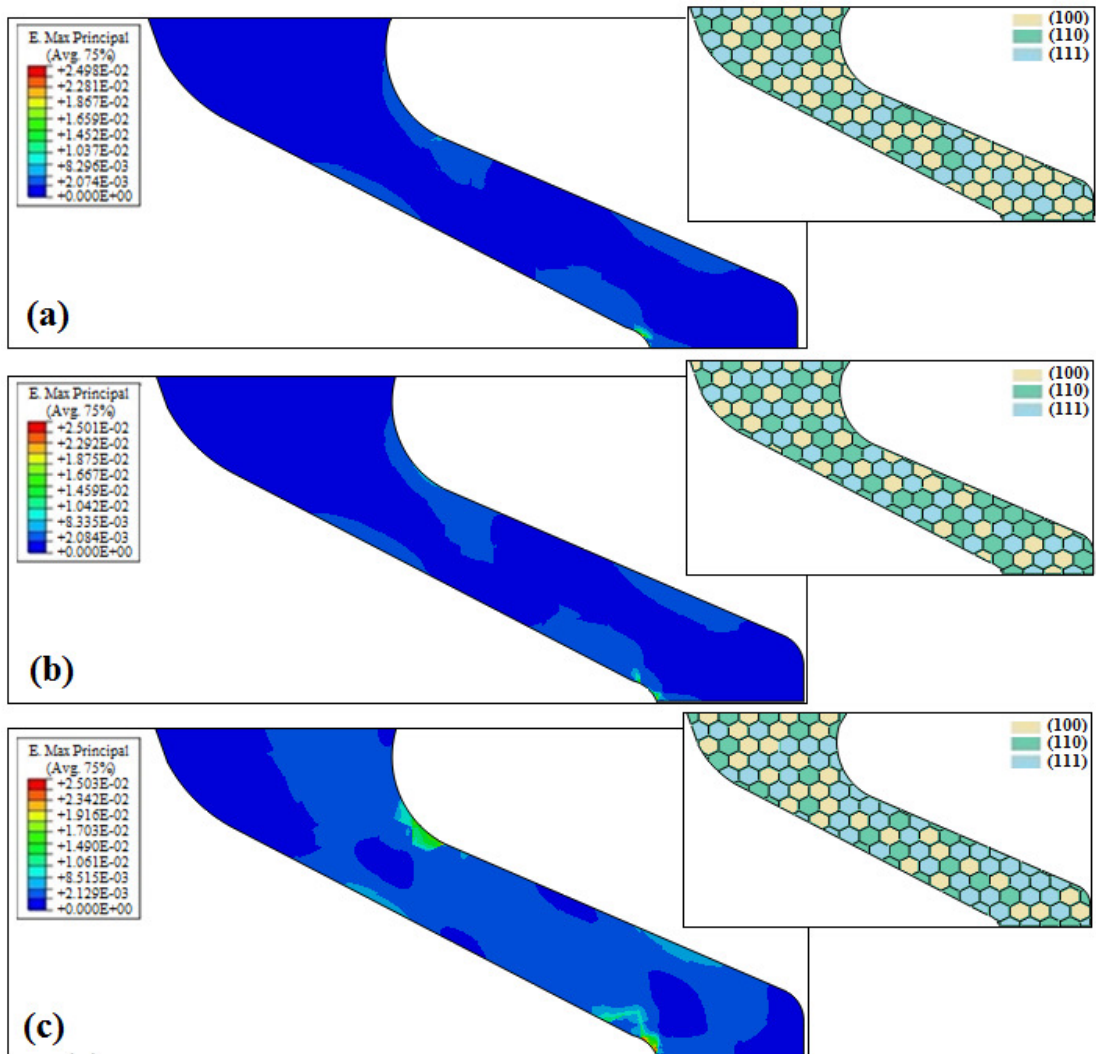


Figure 5.8: Resulting localised maximum principal strain evolution under 2.5% compressive strain in the ‘v-strut’ FEA micro-mechanical model with (a) a (100) orientated grain and (b) a (110) orientated grain, and (c) a (111) orientated grain at the critical location of peak tensile stress located on the outer apex of the ‘v-strut’.

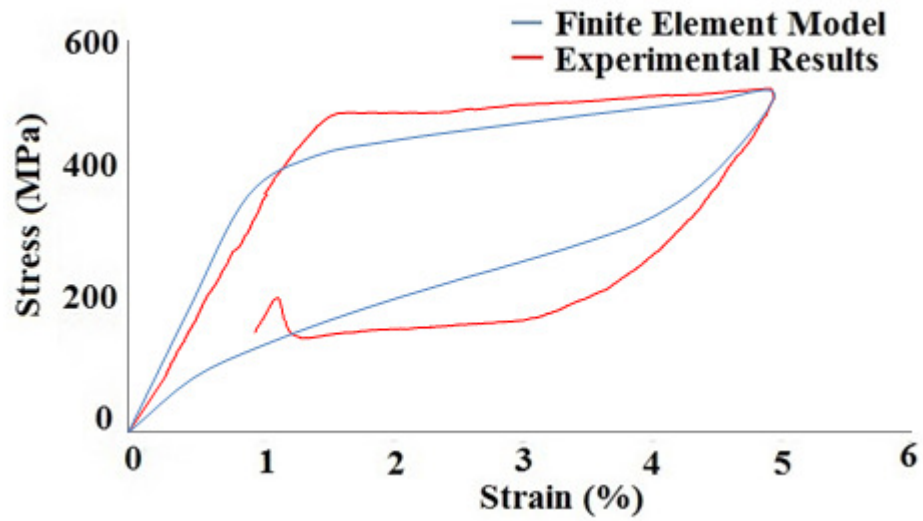


Figure 5.9: Validation of the UMAT/Nitinol subroutine used in this work through direct comparison of the generated results from the FEA micro-mechanical model, incorporating a realistic granular structure, against the experimentally established uniaxial stress-strain response of the micro-dogbone specimen.

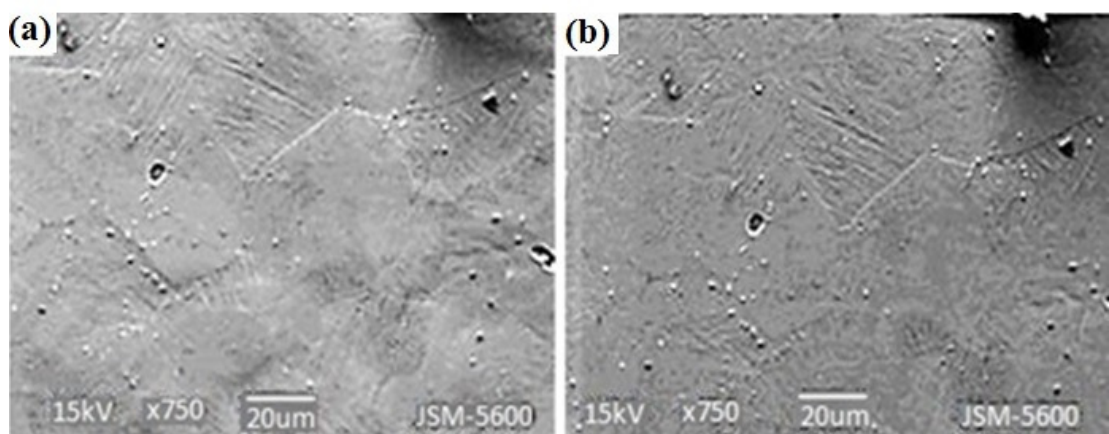


Figure 5.10: Micrographs of the micro-dogbone specimen under (a) 0% strain and (b) 10% strain taken during the in situ SEM tensile testing procedure.

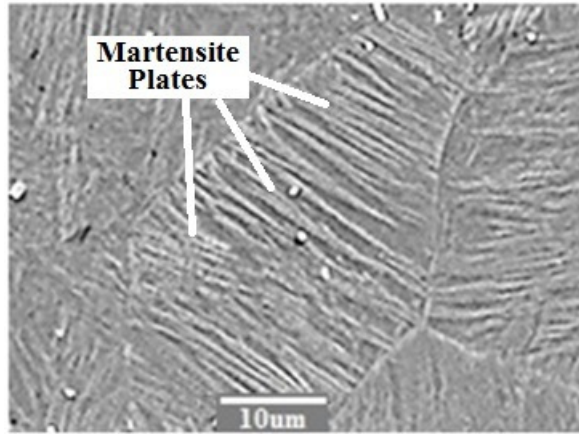


Figure 5.11: SEM micrograph of the micro-dogbone specimen used in this work which displays the presence of inherent martensite plates in the austenitic specimen.

Chapter 6

Effect of Microstructural Phase on the Fatigue Behaviour of NiTi

6.1 Introduction

Chapters 4 and 5 of this thesis focused on the quasi-static tension-compression modelling of NiTi. However, the greatest interest in this material for medical device applications is its fatigue response. For example, a biomedical endovascular stent device must survive 400 million loading cycles to be considered ‘safe for use’. Therefore, the objective of this chapter is to examine the fundamental fatigue behaviour of the individual microstructural phases of NiTi to offer further understanding to the unusual fatigue behaviour of NiTi of increasing fatigue performance with increasing mean strain. This work adopts a fatigue crack growth modelling methodology to predict the fatigue life of metallic specimens under a multitude of loading conditions following the defect tolerant approach to fatigue analysis. With a defect tolerant approach to understanding the fatigue behaviour of metals, previously discussed in Sections 2.2 and 2.3, it is the linear elastic fracture mechanics stress intensity factor range, ΔK , that is used to quantify the driving force for growth of a crack in a specimen under cyclic (fatigue) loading (EQ. 2.1). However, conditions exist in which the local stress intensity factor range at the crack tip varies significantly from the nominally applied stress intensity factor range which must be taken into account. This local ‘effective’ stress intensity factor range, ΔK_{eff} , represents the actual ‘driving force’ for fatigue crack growth.

The main mechanism responsible for this difference between the apparent and actual driving force for fatigue crack growth is crack closure, i.e. the premature closure of the opposing crack faces of a fatigue crack during unloading before the specimen as a whole has unloaded fully. The possibility that a fatigue crack can close, even under fully uniaxial far-field cyclic loading, was first proposed by [Elber, 1970] and [Elber, 1971] on the basis of experimental observations. As discussed in Section 2.3.3, Elber argued that a zone of residual tensile deformation is left in the wake of a fatigue crack tip which is characterised by the maximum applied stress intensity, K_{max} . As the crack advances, through fatigue crack growth, this permanently deformed zone is left in the wake of the advancing crack tip; this plastic zone manifests itself as a region of dilated

material on the crack fracture surfaces. This may result in the crack faces coming into contact during unloading, before the applied far-field stress has fully unloaded, such that the crack tip experiences only part of the applied stress range. In this way, the process of crack closure has been shown to lead to an apparent retardation of the fatigue crack growth and therefore enhances the material's resistance to fatigue crack growth. It was recognised that phase transformation at the crack tip can also lead to crack closure effects. This mechanism of 'transformation-induced plasticity' (TRIP) was first investigated by [Pineau and Pelloux, 1974] and [Hornbogen, 1978].

In the phase transforming superelastic NiTi material, TRIP is characterised by the stress-induced martensitic phase change (i.e. SIMT) at the crack tip leading to a net increase in the volume of the transforming region in the wake of the advancing crack. In the computational modelling of the fatigue behaviour of superelastic NiTi in this chapter, ΔK_{eff} is used to characterise the long crack growth behaviour and the initial growth of small cracks in place of the nominally applied stress intensity factor range, ΔK . However, as discussed in Section 2.4 in relation to small cracks, the near-tip plastic zone size can no longer be assumed to be negligible and as a result the elastic-plastic fracture mechanics parameter, ΔJ_{eff} , is used to provide a means of characterising the crack tip conditions (EQ. 2.10). This modelling approach was also successfully employed by [Bruzzi and McHugh, 2002] in the fatigue modelling of particulate reinforced metal matrix composites. Therefore, following his work, the aim of this chapter is to develop this methodology further in order to successfully predict the fatigue behaviour of stable austenitic, stable martensitic and superelastic NiTi specimens. Further insight can therefore be achieved into the particular contribution of microstructural phase, namely, austenitic and martensitic NiTi, on the unusual fatigue behaviour of superelastic NiTi. In this manner, additional quantitative evidence can be presented to further advance the theoretical explanation proposed in Chapter 4 which states that the SIMT underpins the exhibited increased fatigue performance of superelastic NiTi with increased mean strain [Weafer *et al.*, 2015].

6.2 Fatigue Modelling Methodology

The modelling methodology employed in this chapter assumes a defect tolerant approach. Conventional defect tolerant approaches to fatigue only consider the growth of a long fatigue crack, with a constant threshold for crack propagation, to a threshold for failure. However, as discussed in Section 2.3, the overall fatigue life of a micro-sized component such as a stent strut is significantly influenced by the initial small crack growth rate behaviour. Small cracks have been shown to grow at stress intensities lower than the experimentally measured stress intensities for long cracks. In addition, it has been experimentally demonstrated by [Suresh and Ritchie, 1984] and [Lankford *et al.*, 1982] that the crack growth rates of small cracks exceed those of long cracks at theoretically equivalent stress intensity ranges, ΔK . Small cracks are therefore intrinsically significant and should be included when modelling fatigue crack growth rate behaviour in microscale-sized specimens. If neglected, the accelerated sub-threshold crack growth rate of a small fatigue crack can lead to serious non-conservative life predictions for a biomedical stent device. As a result, it was concluded that a complete defect tolerant approach to fatigue would be employed in this work which would also include small crack effects. It is assumed that an initial flaw of length a_0 , free of crack closure, exists in the material and it is the propagation of this dominant initial small crack into a long crack, under cyclic loading, that is assumed to constitute the majority of the fatigue life of the material.

As mentioned, the modelling methodology presented in this chapter is based upon the modelling approach first developed by [Bruzzi and McHugh, 2002] to model the small crack fatigue behaviour of metallic matrix composite materials. This defect tolerant approach correlates local crack tip driving force conditions of an initial small crack with an experimental long crack growth rate curve, using crack closure. As mentioned in Section 2.3.4, ΔJ_{eff} , provides a means of characterising the crack tip conditions which is often given by [McClung *et al.*, 1997]:

$$\Delta J_{eff} = \frac{(U\Delta K)^2}{E'} \left\{ 1 + \frac{Y^2}{C_2} \left(\frac{n-1}{n+1} \right) \left[\frac{\left(\frac{\sigma_{\infty}^{max}}{\sigma_0} \right)^2}{1 + \left(\frac{\sigma_{\infty}^{max}}{\sigma_0} \right)^2} \right] \right\} + 4\alpha\sigma_0\varepsilon_0 ah_1 U \left(\frac{\Delta\sigma_{\infty}}{2\sigma_0} \right)^{n+1}, \text{EQ. 6.1}$$

where U is the effective stress range ratio given by:

$$U = \frac{\sigma_{max} - \sigma_{open}}{\sigma_{max} - \sigma_{min}} = \frac{\Delta K_{eff}}{\Delta K}, \text{EQ. 6.2}$$

and σ_{open} is the stress at which the crack surfaces become completely separated. C_2 for plane strain is 6, and Y is 1.2 and is defined as the collective geometry term in the elastic K expression $K = Y\sigma_{\infty}^{max}\sqrt{\pi a}$. The coefficients α , ε_0 and σ_0 , and the strain hardening exponent n are fitted to the experimental true tensile stress–logarithmic strain curve of the given metallic material under investigation. These coefficients represent parameters of the Ramberg–Osgood (power-law) constitutive relationship which takes the form:

$$\frac{\varepsilon}{\varepsilon_0} = \frac{\sigma}{\sigma_0} + \alpha \left(\frac{\sigma}{\sigma_0} \right)^n. \text{EQ. 6.3}$$

Once the crack tip conditions of a small fatigue crack are characterised for a nominally applied stress intensity range, ΔK , it is necessary to correlate ΔJ_{eff} with the rate at which the crack would grow if subjected to this driving force. This is achieved by correlating ΔJ_{eff} with the calculated effective crack growth rate curve ($\Delta K_{eff} - da/dN$ curve) for the material. The crack growth rate, da/dN , and the increment of crack extension for one cycle can therefore be obtained from the effective crack growth rate curve. The calculation of ΔJ_{eff} is repeated for the new crack length and the new level of fatigue crack closure, until the crack either arrests or propagates to failure. Using this cycle-by-cycle approach, the number of cycles to failure (N_f) is thus predicted for a given metallic material for a given stress amplitude.

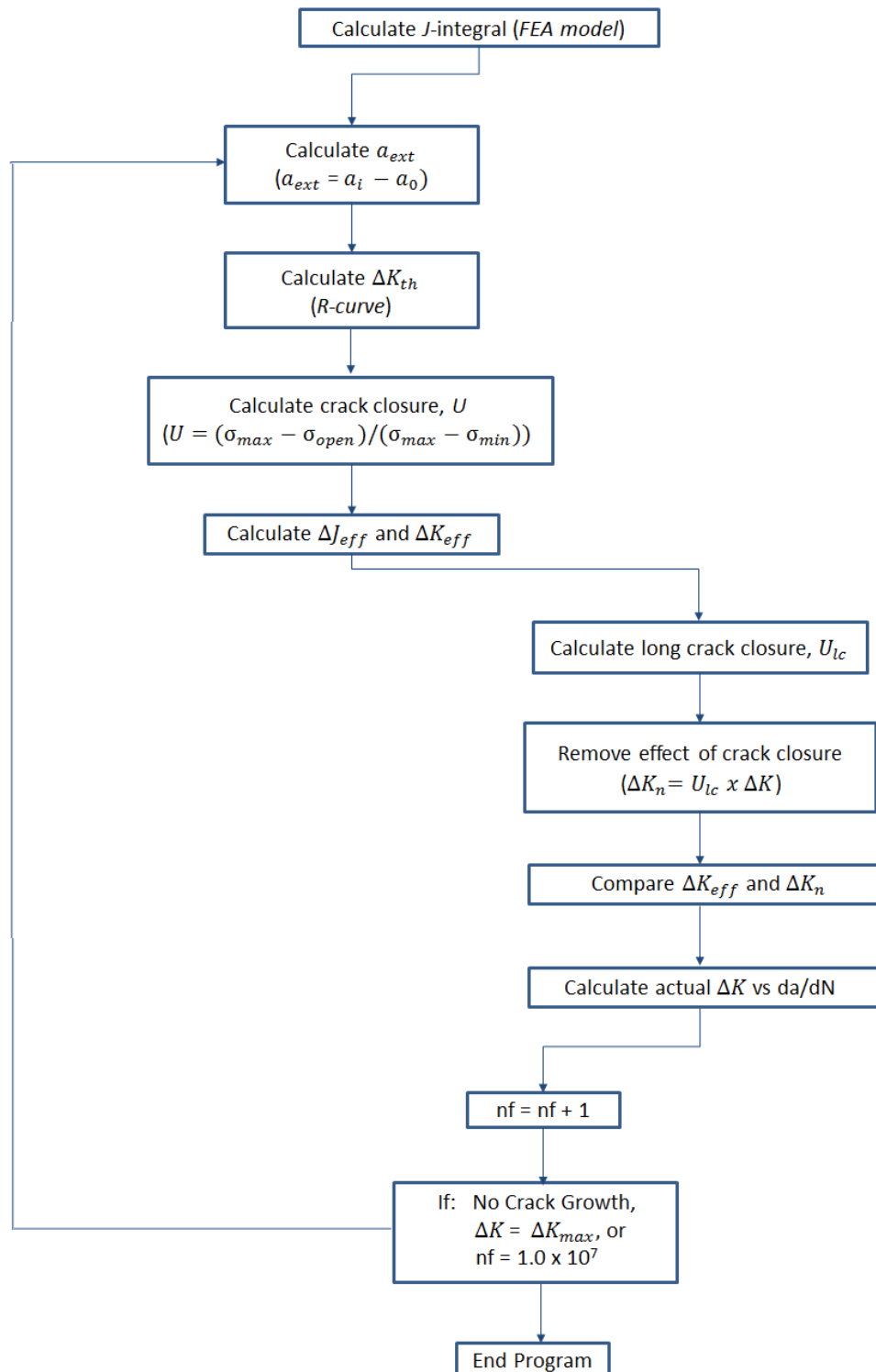


Figure 6.1: Flowchart detailing the main steps taken in the crack-closure based fatigue modelling procedure in this work.

6.3 Fatigue Model Inputs

The novelty of the work described in this chapter lies in the modification of the computational methodology developed by [Bruzzi and McHugh, 2002], briefly mentioned in Section 6.2, to incorporate the behaviour of a superelastic NiTi specimen. The main difficulties encountered can be attributed to the inherent complex transformational behaviour of superelastic NiTi and the associated issues in the incorporation of its dual-phase characteristics into the fatigue modelling methodology. As a result each loading condition, to which the superelastic NiTi compact tension specimen is subject to under the fatigue modelling procedure, is individually examined. Each case is evaluated to determine which of the two microstructural phases will be present, or combination thereof, in the specimen at each cycle for the given applied stress amplitude. For example, the specimen may be placed under a loading condition in which the phase transformation does not occur; such that the critical stress for SIMT initiation is not reached and therefore the specimen will remain in the austenitic NiTi phase. Alternatively, the specimen may be loaded to a critical stress which is high enough to stress-induce the martensitic NiTi phase and therefore the SIMT procedure will have to be taken into account during modelling through the selected inputs. See Appendix A for full details of the seven different possible cases of loading conditions examined in this work.

6.3.1 *J*-integral

The crack tip conditions of the compact tension specimen are modelled using FEA in order to calculate the elastic-plastic fracture mechanics parameter, ΔJ_{eff} , under various loading conditions (EQ. 6.1). A 2-D generalised plane strain analysis was performed with an initial flaw of a sharp crack, of length a_0 , initially free of crack closure in the specimen. Three identical models were created in order to separately investigate all three material phases, namely, stable austenitic, stable martensitic and superelastic NiTi. To accurately simulate the complex transformational behaviour of the superelastic NiTi specimen the UMAT/Nitinol, integrated into the commercially available numerical modelling platform ABAQUSTM 6.10, was employed; full details

of this material subroutine can be found in Section 4.2. To accurately characterise the uniaxial material behaviour of superelastic NiTi for input into the UMAT/Nitinol, the 15 required material properties are extracted from experimental stress-strain curve of the superelastic NiTi phase round-bar tensile specimen (Figure 6.2) published by [McKelvey and Ritchie, 2001] as listed in Table 6.1. In this work, the asymmetric tension-compression behaviour of superelastic NiTi has not be taken into account. As identified in Table 6.1, the compact tension specimen's compressive behaviour is simplified instead to behave symmetrically to its tensile behaviour by allocating a 0MPa to the value representing the initiation stress of transformation during loading in compression (σ_{CL}^S) in the UMAT/Nitinol. All required material properties to fully describe the stable austenitic and stable martensitic NiTi homogenous isotropic material behaviour in the FEA compact tension specimen model are also extracted from the experimentally established tensile stress-strain data of [McKelvey and Ritchie, 2001] (Figure 6.2). In particular, the Young's moduli of 64GPa and 21.3GPa were extracted for stable austenitic and stable martensitic NiTi behaviour, respectively, and the Poisson's ratio was assumed to be 0.3 for both. Material data for the superelastic NiTi was not extracted from the experimental specimens described in Chapter 3 as extracting all uniaxial mechanical and fatigue crack growth rate behaviour from the one complete experimental study aids in minimising the number of uncertainties in this work; this will be discussed further in Section 6.3.3.

The specimens modelled had a length 100 times greater than that of the crack as to remove boundary effects. For symmetry reasons, it was only necessary to model one-half of the specimens, as shown in Figure 6.3. The bottom edge, except the crack face, was constrained to have zero displacement in the y-direction (vertical direction) as to maintain symmetry. In total, 2,550 eight-node quadrilateral generalised plane strain elements (CGPE8R) are used to model the crack tip. This number of elements was deemed necessary following a convergence study of the resulting maximum tensile stress (σ_{22}) extracted from the node at the initial crack tip in the 2-D model for a given applied displacement. In this way, the number of elements in the generated mesh is increased until the incremental difference between the extracted resulting

values is shown to become negligible. A uniformly distributed tensile stress was applied in the vertical direction to the top surface of the model. Subsequently, the J -integral was extracted for a given applied maximum stress from a contour surrounding the crack tip. While the J -integral parameter is independent of the domain used, the J -integral estimates from different contours surrounding the crack tip may vary due to the approximate nature of the FEA solution. In this way, the J -integral values from the first few contours which are not approximately equal to the far-field values are discarded. It should also be noted that the strong variation among multiple far-field estimates of the J -integral typically indicate an error in the contour integral definition or that a finer mesh in the model is required. The characteristic J -integral curves employed in this algorithm for stable austenitic, stable martensitic and superelastic NiTi are given in Figure 6.4 for a specimen with an initial arbitrary defect size of $a_0=5\mu\text{m}$; this arbitrary value represents an initial flaw size which is approximately five times smaller than the typical length of one single grain in the material. Using this plot, the correct J -integral value could be extracted for use in the algorithm for a given maximum applied stress.

6.3.2 Ramberg-Osgood Parameters

The coefficients α , ε_0 and σ_0 , and the strain hardening exponent n of the ΔJ_{eff} formulation (EQ. 6.1) are fit to the true tensile stress–logarithmic strain curve from the aforementioned experimental work of [McKelvey and Ritchie, 2001] for input into the algorithm for the stable austenitic and stable martensitic NiTi models. These coefficients represent parameters of the Ramberg–Osgood (power-law) constitutive relationship which takes the form given in EQ. 6.3. These Ramberg-Osgood parameters, extracted from the stable austenitic and stable martensitic curves, are also used in the description of superelastic NiTi behaviour during the stress-induced phase transformation within the crack growth algorithm through combining the austenitic and martensitic parameters employing the rule of mixtures.

6.3.3 R-curves

In order to calculate the effective stress range ratio, U , (EQ. 6.2) crack growth resistance curves (R-curves) are employed. Ideally, fracture toughness tests should be performed on superelastic NiTi compact tension specimens using a crack-monitoring procedure outlined in the ASTM standard E99 [ASTM, 2005]. Specimens should first be pre-cracked prior to toughness testing at a low R-ratio, near-threshold the stress intensity (ΔK_{th}), to produce a nominally atomically sharp flaw. Initially, the crack-length to specimen-width ratio (a/W) should be approximately equal to 0.45. For superelastic NiTi specimens, displacement-controlled toughness tests should be conducted in a temperature-controlled environment using very slow crosshead displacement rates. Stable fatigue crack growth can subsequently be monitored from the initial a/W of 0.45 to a maximum of 0.60, in accordance with ASTM E399 [ASTM, 2005]. Corresponding measurements of the crack extension, Δa , as a function of the applied stress intensity, can then be used to determine the crack growth resistance of the specimen for the given applied R-ratio.

However for the computational fatigue investigation described in this chapter, investigating load ratios (R-ratios) $R=-1.0, 0.0$, and 0.1 to 0.7 , R-curves were generated through the combination of required data extracted from various experimental studies in the literature. Specifically, the required parameters of the effective threshold stress intensity range, $\Delta K_{th,eff}$, and the long crack threshold stress intensity range, $\Delta K_{th,lc}$, were extracted from the experimentally established crack growth rate curves and effective crack growth rate curves from the aforementioned work of [McKelvey and Ritchie, 2001] for load ratio $R=0.1, 0.5$ and 0.7 . The dependence of $\Delta K_{th,lc}$ on the R-ratio was extracted from the work of [Holtz *et al.*, 1999] for stable austenitic and stable martensitic NiTi for $R=0.0$ to 1.0 . The required value of $\Delta K_{th,lc}$ for $R=-1.0$, for both phases, was attained by means of extrapolation using the results from this study. The work of [Holtz *et al.*, 1999] was deemed as an appropriate source as similar results were reported for $R=0.1, 0.5$ and 0.7 when compared to the results generated by [McKelvey and Ritchie, 2001]. The effective threshold stress intensity range, $\Delta K_{th,eff}$,

meanwhile, remains constant for a given material regardless of the imposed R-ratio. Generated R-curves for stable austenitic and stable martensitic NiTi materials for load ratios $R=-1$ to $R=0.5$ are given for reference in Figure 6.5 and Figure 6.6, respectively.

As an assumption of the expected material behaviour, the trend of the generated R-curves were designed to follow that of an experimentally produced R-curve for flattened thin-walled superelastic NiTi tubing specimens reported by [Robertson and Ritchie, 2007]. It is acknowledged that it is not ideal to extract these numerous parameters from various studies; preferably they would all be taken from one experimental study using one batch of specimens to insure consistency in results. In extracting material data from multiple studies, employing a variety of experimental specimens, a level of uncertainty is introduced to the work with respect to the varying fundamental specimen dimensions, material processing techniques employed, and the resulting material microstructures of the specimens. Furthermore, the trend of the generated R-curve for austenitic and martensitic NiTi would be ideally based on an R-curve for the corresponding material behaviour, i.e. taken directly from austenitic and martensitic NiTi specimens. However, there is a limited number of relevant experimental studies in the literature relating to fracture mechanics-based approaches to fatigue in NiTi; furthermore, that which does exist invariably pertains to product forms that are not appropriate for stent manufacture, e.g., bulk NiTi bar and strip materials. Therefore, within the scope of the work completed as part of this investigation, this approach was deemed necessary.

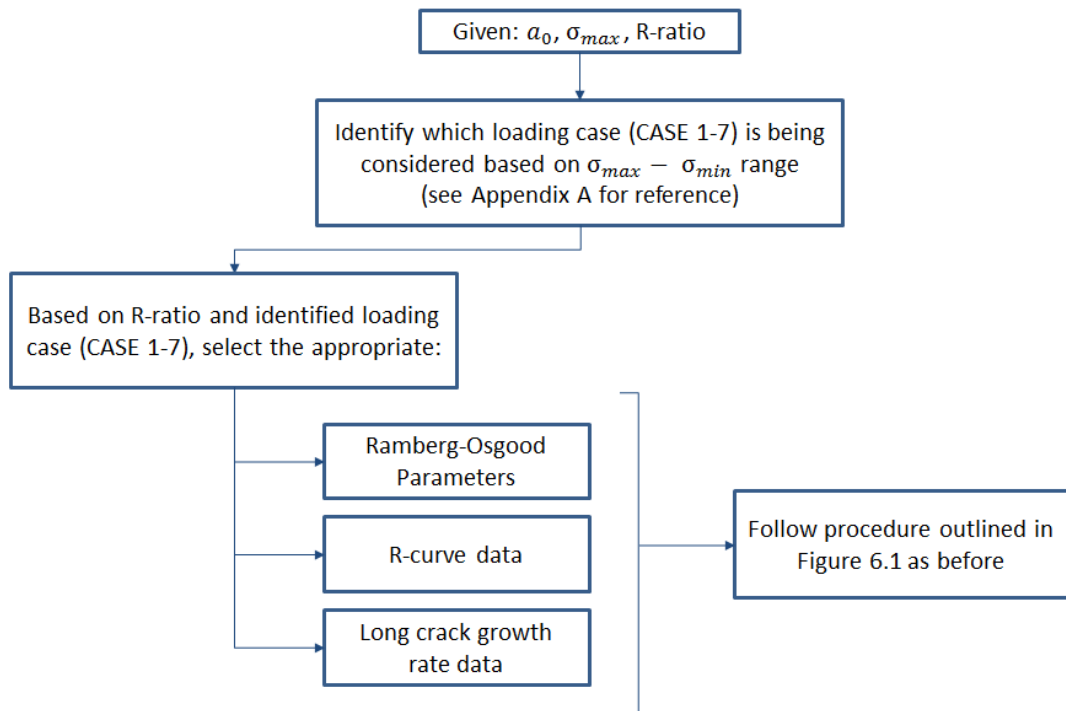


Figure 6.7: Flowchart detailing the main inputs for superelastic NiTi in the fatigue modelling procedure in this work.

As mentioned, during the cycle-by-cycle simulation, it was noted which material phase was present (or combination thereof) in the superelastic NiTi specimen, as shown in Appendix A. This procedure was implemented in order to accurately interpolate between the austenitic and martensitic NiTi R-curve data for input into the algorithm when modelling a superelastic NiTi specimen (refer to Figure 6.7 for further details). In this way, in the case of a simulated loading condition to high enough stresses to stress-induce the phase transformation from austenitic to martensitic NiTi (namely, cases 2, 3, 4, 5 and 7 of Appendix A), a combination of the characteristic austenitic and martensitic NiTi material behaviour will be present in the superelastic NiTi specimen. As a result, the rule of mixtures methodology was employed to determine the proportion of each of the two material phases, namely austenitic and martensitic NiTi, are present in the superelastic NiTi specimen under the selected

simulated loading procedure over the characteristic transforming stress range using the following formulation:

$$E_{SE} = fE_{aus} + (1 - f)E_{mar} \quad \text{EQ. 6.4}$$

where E_{se} , E_{aus} , and E_{mar} are the Young's modulus of the superelastic, austenitic and martensitic NiTi respectively, and f is the volume fraction of austenitic NiTi. Various combinations of the generated R-curve data, for the two material phases of austenitic and martensitic NiTi, are also therefore interpolated to accurately represent the complex material behaviour of the superelastic NiTi specimen during the SIMT procedure over the characteristic stress range.

6.3.4 Fatigue Crack Growth Rate Behaviour

The main focus in the work of [McKelvey and Ritchie, 2001] involved the investigation of the fatigue crack growth rate behaviour of stable austenitic, stable martensitic and superelastic NiTi materials, as previously discussed in Sections 1.1.4 and Section 2.3.1 of this thesis. Fatigue crack growth rate testing of the compact tension specimens performed on each microstructural phase was first completed neglecting, then subsequently including, fatigue crack closure effects in their work. This can be explicitly identified by the use of the elastic-plastic fracture mechanics stress intensity range parameter, ΔK , and the effective stress intensity range parameter, ΔK_{eff} , as shown in Figures 6.8-6.10 for stable martensitic, stable austenitic and superelastic NiTi, respectively. The fatigue crack growth rate curves from the experimental study of [McKelvey and Ritchie, 2001] are employed in this work to characterise the growth rate behaviour of each microstructural phase under the various R-ratios examined, namely, R=-1, 0 and 0.1 to 0.7. Subsequently, each curve was used to calculate the characteristic effective crack growth rate curve for a given material under a given loading condition through the incorporation of the specific level of crack closure experienced by the crack using the effective stress range ratio, U , extracted from the corresponding R-curve. Once calculated, ΔJ_{eff} is correlated with this effective crack growth rate curve as previously mentioned in Section 6.2. In this way, the rate

at which the fatigue crack would grow if subjected to this driving force is determined. Using this cycle-by-cycle approach, the number of cycles to failure can thus be predicted for stable austenitic, stable martensitic and superelastic NiTi material for a given applied far-field stress. As mentioned in Section 6.3.1, employing all input fatigue data to the algorithm from the same experimental study promotes confidence in the uniformity of resulting outputs, in that, all uniaxial mechanical and fatigue crack growth rate behaviour for input into the algorithm are extracted from the same collection of specimens used by [McKelvey and Ritchie, 2001].

6.4 Predicted Fatigue Behaviour

6.4.1 Small Crack Behaviour

The behaviour of small cracks can be explicitly identified through the output of the predicted effective crack growth rate curve. In this work the general trend of the small crack behaviour for stable austenitic, stable martensitic and superelastic NiTi specimens were shown to behave relatively similarly. For illustration purposes, individual crack growth rate curves for various applied maximum stresses, ' S_{max} ', for stable austenitic NiTi material with initial defect size $a_0=5\mu\text{m}$ and load ratio $R=0.1$ are plotted in Figure 6.11. For lower maximum stress values, for example $S_{max}=200\text{MPa}$ shown in Figure 6.11, the crack is shown to initially grow at rates corresponding with the effective crack growth rate curve, i.e. at crack growth rates higher and at lower thresholds than the long crack behaviour, after which the rates slow down due to increasing crack closure until this small crack behaviour arrests. With the increase of applied maximum stress, for example to $S_{max}=300\text{MPa}$ and $S_{max}=400\text{MPa}$ shown in Figure 6.11, the small crack growth rate behaviour is shown to initiate at the effective crack growth curve but subsequently slows in rate (due to increasing crack closure). This behaviour was observed until a point where the crack had grown sufficiently long such that the crack closure saturates (in reaching the R-curve plateau) and can be considered to behave as a long crack, and thus is observed to follow the traditional Paris law long crack growth rate behaviour.

It should be noted, for the analysis of the predicted effective small crack growth rate behaviour of superelastic NiTi specimens, the effective crack growth rate curve ($\Delta K_{eff} - da/dN$ curve) is that of the stable austenitic NiTi material behaviour and the long crack growth rate curve ($\Delta K - da/dN$ curve) is that of the stable martensitic NiTi material behaviour; as with the stable austenite and stable martensite analyses discussed above, both curves are extracted from the aforementioned experimental work of [McKelvey and Ritchie, 2001]. The fact that the small crack behaviour initiates at the effective stable austenitic curve can be attributed to the fact that the specimen is initially in the austenitic state prior to cyclic loading. Therefore the small crack, which is assumed to be inherently present in the material following the defect tolerant approach to fatigue, will initially propagate in the austenitic specimen and will thus follow the effective austenitic crack growth rate behaviour. Upon loading, the martensitic phase will be stress-induced in the specimen through SIMT and thus the crack behaviour will evolve to that of the conventional martensitic long crack growth rate behaviour. This is illustrated in the small crack growth rate curves of Figure 6.12 for a superelastic NiTi specimen with initial defect size $a_0=5\mu\text{m}$ and load ratio $R=0.1$.

6.4.2 Predicted Stable Austenitic and Martensitic Fatigue Behaviour

As described in Section 6.3, the predicted effective crack growth rate curve determines the propagation of a given small crack in a specimen to that of a long crack and subsequently to a length to induce catastrophic failure of the specimen. Such results can therefore be used to predict the number of cycles to reach failure, N_f , for a given metallic specimen under given loading conditions. In this way, using this cycle-by-cycle approach, stress-life curves (S-N curves) can be produced which display the predicted N_f for a given metallic material for a given applied stress amplitude for a particular load ratio, R-ratio (Figure 2.1). Such S-N curves are employed during the initial design process of commercial devices to inspect the endurance limit of a specimen for the evaluation of safe working load conditions. Example S-N curves generated using the modelling methodology described in this chapter, for stable austenitic and stable martensitic NiTi specimens with an initial defect size $a_0=5\mu\text{m}$

and load ratio $R=0.1$, are displayed in Figure 6.13. From these two plots the endurance limits can therefore be reported as 276MPa for stable austenitic NiTi, and 416MPa for stable martensitic NiTi, for a load ratio of $R=0.1$.

Compiling the S-N curves generated for the various R-ratios allows for the creation of the fatigue life evaluation tool referred to as the 'constant life diagram'. The constant life diagram is utilised following a fail/no-fail approach in the design of commercial devices (Figure 2.3). Since NiTi is typically presented using a strain-based methodology due to associated superelastic plateau, all endurance limits reported from S-N curves generated in this chapter are converted to the strain equivalent using the experimentally established tensile stress-strain curve for each material phase from the published work of [McKelvey and Ritchie, 2001]. Both the stable austenitic and stable martensitic constant life diagrams, as shown in Figure 6.14, represent conventional engineering fatigue behaviour of decreased fatigue life with increasing mean strain. From this figure, it should be noted that the stable martensitic NiTi phase is predicted as having superior fatigue performance when compared to the stable austenitic NiTi phase which is in agreement with published literature.

6.4.3 Predicted Superelastic NiTi Fatigue Behaviour

The fatigue behaviour of superelastic NiTi was successfully predicted for a multitude of loading conditions and defect sizes using the computational methodology outlined in this chapter. For illustrative purposes, the resulting constant life diagram for a superelastic NiTi specimen with initial defect size of $a_0=5\mu\text{m}$ is shown in Figure 6.15. The predicted curves of stable austenitic and stable martensitic NiTi phases, with the same initial defect size of $a_0=5\mu\text{m}$, are also included in this figure for reference. It is clearly identifiable that the stable austenitic and stable martensitic NiTi fatigue curves represent typical engineering material behaviour of decreasing fatigue life with increasing mean strain while the superelastic NiTi fatigue curve demonstrates the unusual behaviour of increasing fatigue performance with increasing mean strain. From the direct comparison of the fatigue behaviour of stable austenitic, stable martensitic and superelastic NiTi in this figure, it appears to show that the increase in

fatigue performance with increasing mean strain can be attributed to the shift from the austenitic to martensitic NiTi fatigue behaviour.

From the uniaxial tensile stress-strain curves for all the superelastic NiTi specimens investigated in this work, as illustrated in Figure 3.6, Figure 3.11 and Figure 6.2 [McKelvey and Ritchie, 2001], it can be seen that SIM appears to typically initiate at approximately 1-2% strain. When comparing this to the experimentally established constant life diagram for superelastic NiTi (Figure 4.7) [Pelton *et al.*, 2003] [Pelton *et al.*, 2008], in addition to the predicted constant life diagram for superelastic NiTi (Figure 6.15), it is noted that the increase in fatigue performance occurs at approximately 1-2% mean strain also. Therefore, it can be suggested that there exists a potential connection between the SIM microstructural phase and the observed improvement of fatigue performance of superelastic NiTi, as first suggested in Chapter 4. As it has been experimentally demonstrated by [McKelvey and Ritchie, 2001] and [Holtz *et al.*, 1999] that martensitic NiTi has a superior fatigue resistance when compared to austenitic NiTi, it follows that an increase in observed fatigue performance could be due to the transformation from the inferior austenitic NiTi to superior martensitic NiTi fatigue behaviour (as illustrated in Figure 6.15). Therefore, the computational work of this chapter provides further indications towards the validity of the theory, first discussed in Chapter 4, which proposes that it is the transformation from austenitic to martensitic NiTi material phases, i.e. SIMT, which underpins NiTi's unusual fatigue behaviour of increasing fatigue performance with increasing mean strain [Weafer and Bruzzi, 2014] [Weafer *et al.*, 2015].

6.4.4 Comparison to Experimental Data

In order to attempt to validate the resulting fatigue life predictions generated in this chapter, predicted results are directly compared against experimental data published in the literature. Firstly, as shown in Figure 6.16 and Figure 6.17, the predicted S-N curves for stable austenitic and martensitic NiTi are compared to published experimental S-N fatigue data. Taking two stress-based fatigue studies performed using stable austenite and stable martensite specimens, completed by

[Miyazaki *et al.*, 1988] and [Melton and Mercier, 1979], respectively, the predicted S-N behaviour can be directly compared against experimental data using the same initial defect size of $a_0=5\mu\text{m}$ and for an equivalent load ratio, namely, $R=0$ for stable austenitic and $R=-1$ for stable martensitic NiTi data. As seen in Figure 6.16 and Figure 6.17, a reasonable correlation is found between the experimentally produced S-N fatigue data and the computationally generated curves for both phases. Therefore, despite the number of simplifications applied in this investigation, the computational methodology employed in the work described in this chapter is confirmed to have the ability to predict relatively realistic solutions for fatigue life for typical engineering materials such as stable austenitic and stable martensitic NiTi specimens.

Secondly, the computationally predicted constant life diagram for superelastic NiTi of Figure 6.15 is shown to replicate the trend reported in the literature of increased fatigue life with increasing mean strain. When directly compared to the combined work of [Pelton *et al.*, 2003] and [Pelton *et al.*, 2008] in Figure 6.18 a good correlation of the overall trend is shown; thus confirming the success of the adapted modelling methodology described in this chapter in capturing the complex fatigue behaviour of superelastic NiTi. Investigation into the variation of fatigue behaviour (shifting of the constant life diagram) with initial defect size is also illustrated in Figure 6.18, in which initial defect sizes of 5, 10, 15, $25\mu\text{m}$ were investigated. As reported thus far, $a_0=5\mu\text{m}$ has been selected as the arbitrary initial defect size to illustrate the trends in the generated results. This defect size is shown to represent the best match when compared to experimental stress-strain and S-N data. However, the plot of Figure 6.18 demonstrates that a $25\mu\text{m}$ defect size is shown to be the best match when compared against the combined experimental works of Pelton *et al.*. Unfortunately, the grain size of the experimental specimens of Pelton *et al.* was not stated in their work; nevertheless, the use of the selected $25\mu\text{m}$ defect size in this chapter represents a length of the average grain size found in a typical NiTi stent material as investigated by [Robertson *et al.*, 2005]. In a small strut device such as a biomedical stent it is possible that a grain itself could act as the characteristic length that an initial flaw could propagate towards to cause failure, as previously discussed in Chapter 5.

Understandably this represents a significant crack length for a stent specimen. However, as inherent obstacles to continuous crack growth such as grain boundaries have not been included within the model (only the stress level changes from one grain to the next), cracks below 25 μ m may indeed grow and arrest at the grain boundaries in the material. In this context, the characteristic length associated with grain size may indeed be a more important measure of fatigue behaviour than the ‘initial defect size’.

6.5 Discussion

In this chapter, computational FEA models capable of predicting the constitutive fatigue behaviour of stable austenitic, stable martensitic and superelastic NiTi specimens are successfully created. Computationally derived predictions of fatigue behaviour are subsequently achieved for a multitude of loading conditions and initial defect sizes for a given specimen using the modelling methodology first developed by [Bruzzi and McHugh, 2002] and extracting suitable parameters from various experimental studies reported in published literature. These parameters include the uniaxial tension-compression data, fatigue crack growth rate data from the work of [McKelvey and Ritchie, 2001] and fatigue crack growth resistance curve (R-curve) data from the works of [Robertson and Ritchie, 2007] and [Holtz *et al.*, 1999]. Combining the individual effects of the stable austenite and stable martensite microstructural phases, in addition to modifying the methodology of [Bruzzi and McHugh, 2002] to include the rule of mixtures, the fatigue behaviour of superelastic NiTi was also successfully investigated. It was hypothesised that the transformation from the austenitic to martensitic NiTi fatigue behaviour, i.e. the SIMT, underpins superelastic NiTi’s unique behaviour of increasing fatigue performance with increasing mean strain [Weafer and Bruzzi, 2016].

Through the construction of computationally generated constant life diagrams for stable austenitic and stable martensitic NiTi specimens, it was confirmed that these microstructural material phases represent typical engineering material behaviour of decreasing fatigue life with increasing mean strain. Meanwhile, the computationally generated constant life diagram for superelastic NiTi specimens successfully

demonstrates the reported unusual behaviour of increasing fatigue performance with increasing mean strain. It was identified that the observed initiation of the improvement of fatigue performance of the superelastic NiTi specimen, at approximately 1-2% mean strain, correlates with the on-set of SIM in the specimen identified in its experimental uniaxial stress-strain curve. It can therefore be hypothesised, as suggested previously in Chapter 4, that there exists a potential association between SIM and the observed fatigue behaviour of superelastic NiTi. Specifically, it appears to be the shift from the individual austenitic to martensitic NiTi fatigue behaviour that results in the increased fatigue performance of superelastic NiTi. As the stable martensitic NiTi microstructural phase was shown to have a superior fatigue performance, with an approximate 700% improvement in predicted endurance limit compared to austenitic NiTi microstructural phase, it follows that the transformation from an inferior austenitic to superior martensitic fatigue behaviour would present a possible explanation for the observed increased fatigue performance of superelastic NiTi with increased mean strain.

It is acknowledged, however, that further experimental investigations are required to comprehensively validate this theory. In particular, fatigue testing on ‘v-strut’ or ‘diamond’ shaped austenitic, martensitic and superelastic NiTi specimens would be required at various combinations of mean strain and strain amplitudes in order to generate the experimentally established constant life diagram. Ideally, to limit the number of uncertainties in the work, all material data gathered for input into the fatigue modelling algorithm would also be extracted from the same batch of experimental specimens. In this way it ensures a fair comparison is made between the experimental data and the computational predictions by eliminating uncertainties such as those introduced by material processing methods used and the associated resulting material microstructures of the varying specimens. Therefore a uniaxial tensile test would also be required, using a suitable dogbone geometry, for all three material phases in order to extract the valid Ramberg-Osgood parameters for each phase for input into the algorithm. In addition, the fatigue crack growth rate and fracture toughness testing would also be ideally completed using the same batch of specimens

in the form of compact tension specimens. The R-curve data for all three material phases, generated from the results of the fracture toughness testing, may be achieved using the methodology outlined previously in Section 6.3.3.

The generated constant life diagram curves of superelastic NiTi in this work appear to marginally over-predict the material's fatigue performance when compared to experimentally generated constant life diagram data of [Pelton *et al.*, 2003] and [Pelton *et al.*, 2008]. This could be attributed to the fact that key elements are neglected in the modelling procedure such as crystallographic texture, plasticity, volume expansion and the influence of latent heat released during SIMT on mechanical properties. In addition, the selection of initial defect size, a_0 , has a significant impact on the predicted quantitative results in this computational work as the modelling methodology employed does not capture the initiation of fatigue crack growth. The initial crack itself could be derived from an inherent surface flaw, precipitate, or grain, which was not specified in this work. Indeed the individual grain boundaries, which have also been neglected in the FEA model, could potentially act as barriers to continuous crack growth in a specimen and thus improving its fatigue performance; as experimentally shown by [Gall *et al.*, 2000]. In addition, due to the limited data available in the field of stable austenitic and martensitic NiTi material behaviour, many assumptions were made in generating the input data for the fatigue algorithm. Ideally, as previously discussed, all uniaxial tension-compression data, R-curve data and fatigue crack growth rate data would be extracted from the same batch of specimens however this was not possible within the scope of this work.

As a result the experimental data from the combined work of [Pelton *et al.*, 2003] and [Pelton *et al.*, 2008], by which the predicted data was validated, did not use the same specimens as the source of the tension-compression and fatigue crack growth rate data (extracted from [McKelvey and Ritchie, 2001]) or the R-curve data (extracted as a combination of parameters from [McKelvey and Ritchie, 2001], [Robertson and Ritchie, 2007] and [Holtz *et al.*, 1999]) used in the fatigue modelling. Nevertheless, by employing the rule of mixtures methodology to successfully blend the austenitic

and martensitic NiTi mechanical and fatigue behaviour in this computational investigation, the complex fatigue behaviour of the phase-transforming superelastic NiTi material was accurately predicted. The quantitative trends predicted by the generated results follow those of experimental data thus providing confidence in the accuracy of the development modelling methodology. In this way the main objective of this work, following the initial quasi-static investigation of Chapter 4, was successfully achieved in the individual examination of the microstructural phases of NiTi in order to relate their characteristic fatigue behaviour to the unusual fatigue behaviour of superelastic NiTi. From the results generated, it is proposed to be the shift from the inferior fatigue behaviour of austenitic NiTi to the superior fatigue behaviour of martensitic NiTi which results in the observed increase in fatigue performance of superelastic NiTi with increasing mean strain.

6.6 References

ASTM International Standards, ASTM E99 Standard Test Method for Measurement of the Plane Strain Fracture Toughness in Metallic Materials, 2005.

Bruzzi M.S. and McHugh P.E., Methodology for Modelling the Small Crack Fatigue Behaviour of Aluminium Alloys, *International Journal of Fatigue*, 2002, **24**, p 1071–1078.

Elber W., Fatigue Crack Closure under Cyclic Tension, *Engineering Fracture Mechanics*, 1970, **2**, p 37-45.

Elber W., The Significant of Fatigue Crack Closure, *Damage Tolerance in Aircraft Structures*, 1971, Special Technical Publication **486**, p 230-242.

Gall K., Lim T.J., McDowell D.L., Sehitoglu H., and Chumlvakov Y.I, The Role of Intergranular Constraint on the Stress-induced Martensitic Transformation in Textured Polycrystalline NiTi, *International Journal of Plasticity*, 2000, **15(10-11)**, p 1189-1214.

Holtz R.L., Sadananda K., Imam M.A., Fatigue Thresholds of Ni-Ti Alloy near the Shape Memory Transition Temperature, *International Journal of Fatigue*, 1999, **21**, p 137–145.

Hornbogen E., Martensitic Transformation at a Propagating Crack, *Acta Metallurgica*, 1978, **26(1)**, p 147-152.

Iacoviello, F., Di Cocco V., Natali S. and Maletta C., Microstructural Influences on Crack Initiation and Growth in an Equiatomic NiTi PE Alloy, *Proceeding of the International Conference on Crack Paths*, 2012, **4**, p 319-326.

Lankford J., The Growth of Small Fatigue Cracks in 7075-T6 Aluminium, *Fatigue and Fracture of Engineering Materials and Structures*, 1982, **5**, p 233–248.

McClung R.C., Chell G.G., Russel D.A. and Orient G.E., A Practical Methodology for Elastic-Plastic Fatigue Crack Growth, *Fatigue and Fracture Mechanics*, 1997, **27**, p 317-337.

McKelvey A.L. and Ritchie R.O., Fatigue-Crack Growth Behavior in the Superelastic and Shape-Memory Alloy Nitinol, *Metallurgical and Material Transactions A*, 2001, **32**, p 731-743.

Melton K.N., Mercier O., Fatigue of NiTi Thermoelastic Martensites, *Acta Metallurgica*, 1979, **27**, p 137-144.

Miyazaki S., Sugaya Y., Otsuka K., Effects of Various Factors on Fatigue Life of Ti-Ni Alloys, *Proceeding of the International Meeting on Advanced Materials*, 1988, **9**, p 251-256.

Pelton A.R., Gong X.-Y., and Duerig T., Fatigue Testing of Diamond-Shaped Specimens, *Proceedings of the Materials and Processes for Medical Devices Conference*, 2003, p 199–204

Pelton A.R., Schroder V., Mitchell M.R., Gong X.-Y., Barney M., and Robertson S.W., Fatigue and Durability of Nitinol Stents, *Journal of the Mechanical Behavior of Biomedical Materials*, 2008, **1**, p 153–164.

Pineau, A.G. and Pelloux R.M., Influence of Strain-induced Martensitic Transformations on Fatigue Crack Growth Rates in Stainless Steels, *Metallurgical Transactions*, 1974, **5(5)**, p 1103-1112.

Robertson S.W., Imbeni V., Wenk H.-R., and Ritchie R.O., Crystallographic Texture for Tube and Plate of the Superelastic/Shape-Memory Alloy Nitinol used for Endovascular Stents, *Journal of Biomedical Materials Research Part A*, 2005, **72(2)**, p 190-199.

Robertson S.W., Ritchie R.O., In-vitro Fatigue–Crack Growth and Fracture Toughness Behavior of Thin-Walled Superelastic Nitinol Tube for Endovascular

Stents: A Basis for Defining the Effect of Crack-like Defects, *Biomaterials*, 2007, **28**, p 700–709.

Suresh S., Ritchie R.O., Propagation of Short Fatigue Cracks, *International Metals Reviews*, 1984, **29**, p 445–76.

Tolomeo D., Davidson S. and Santinoranout M., Cyclic Properties of Superelastic Nitinol: Design Implications, *Proceedings of the International Conference of Shape Memory and Superelastic Technologies*, 2000, p 409–417.

Weafer F.M. and Bruzzi M.S., Influence of Microstructure on the Performance of Nitinol: A Computational Analysis, *Journal of Materials Engineering and Performance*, 2014, **23**, p 2539-2544.

Weafer F.M., Guo Y. and Bruzzi M.S., The Effect of Crystallographic Texture on Stress-induced Martensitic Transformation in NiTi: A Computational Analysis, *Journal of the Mechanical Behaviour of Biomedical Materials*, 2015, **53**, p 210-217.

Weafer F.M. and Bruzzi M.S., ‘Crack-closure based Method for Modelling the Fatigue Behavior of Superelastic Nitinol’, *International Journal of Fatigue*, 2016, **82**, p 730-736.

Table 6.1: Material properties extracted from the experimental uniaxial tensile testing procedure completed on the superelastic NiTi round-bar tensile specimens reported in literature [McKelvey and Ritchie, 2001].

Material Properties	Value
E_A : Austenite Elasticity	64000 MPa
ν_A : Austenite Poissons Ratio	0.3
E_M : Martensite Elasticity	21333 MPa
ν_M : Martensite Poissons Ratio	0.3
ϵ^L : Transformation Strain	0.0328
$(\frac{\delta\sigma}{\delta T})_L$: $\frac{\delta\sigma}{\delta T}$ Loading	0
σ_L^S : Start of Transformation Loading	390 MPa
σ_L^E : End of Transformation Loading	410 MPa
T_0 : Reference Temperature	37°C
$(\frac{\delta\sigma}{\delta T})_U$: $\frac{\delta\sigma}{\delta T}$ Unloading	0
σ_U^S : Start of Transformation Unloading	200 MPa
σ_U^E : End of Transformation Unloading	155 MPa
σ_{CL}^S : Start of Transformation Stress during loading in compression, as a positive value	0 MPa
ϵ_V^L : Volumetric Transformation Strain, If $\epsilon_V^L = \epsilon^L$, an associated algorithm us used, with ϵ_V^L computed based on σ_L^S and σ_{CL}^S	0.0328
N_A : Number of annealings to be performed during the analysis	0

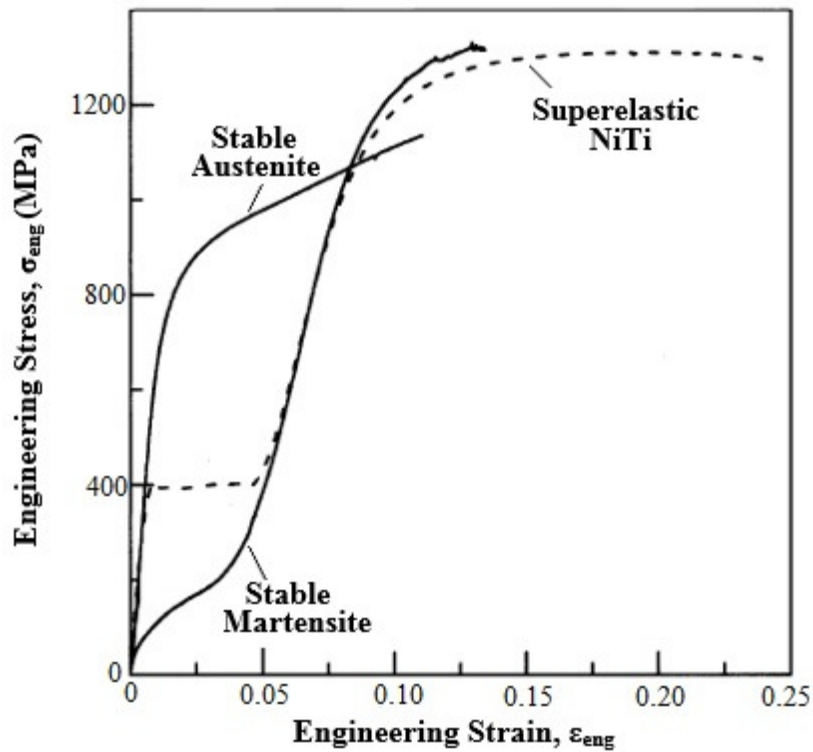


Figure 6.2: Uniaxial stress-strain behaviour of the stable austenitic, stable martensitic and superelastic NiTi materials used as input to the FEA model, adapted from [McKelvey and Ritchie, 2001].

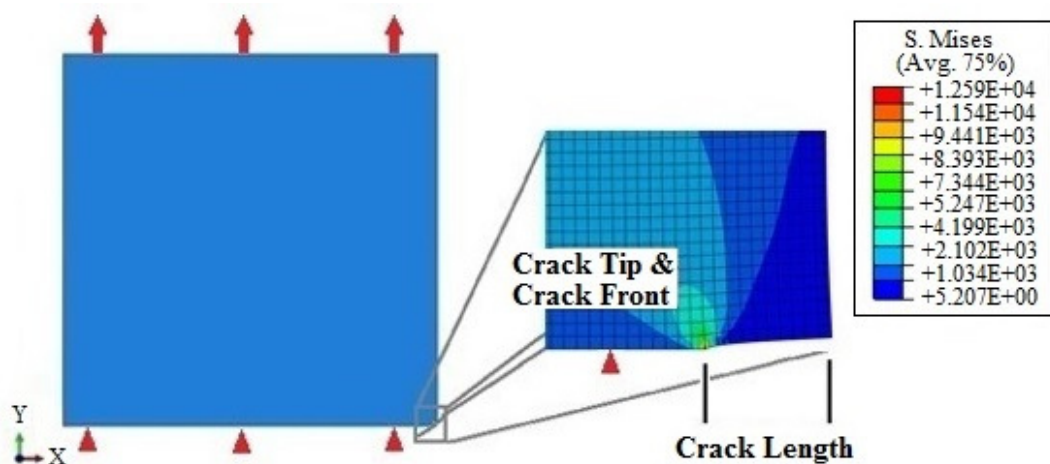


Figure 6.3: J -integral calculated through FEA modelling of the crack tip, J -integral extracted from the model upon loading to a maximum applied tensile stress.

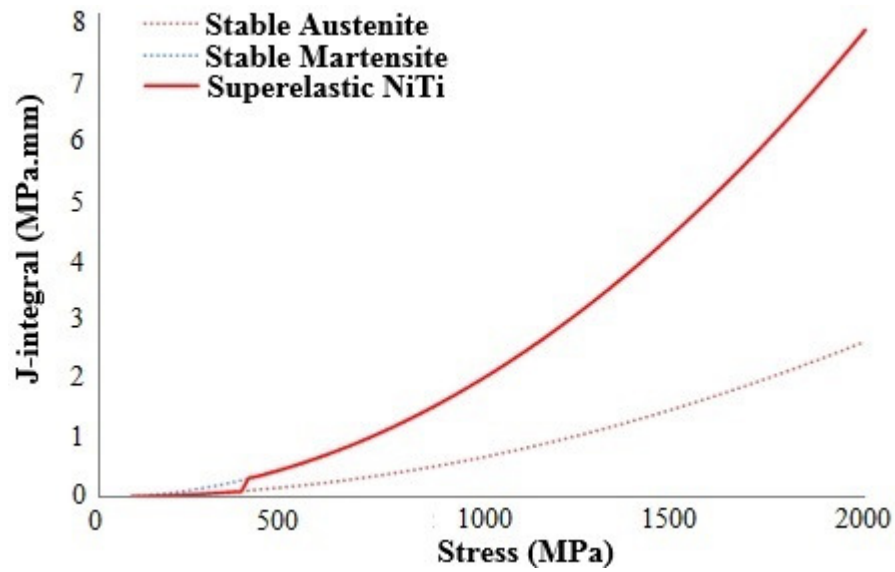


Figure 6.4: J -integral data extracted from the FEA model with an initial defect size, a_0 , of $5\mu\text{m}$ using stable austenitic, stable martensitic and superelastic NiTi material data, respectively.

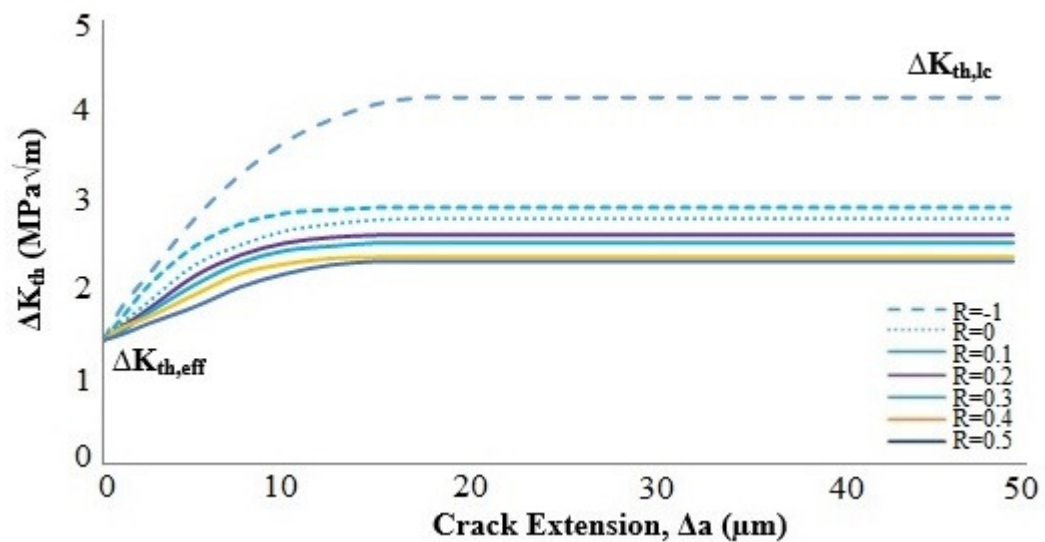


Figure 6.5: Crack growth resistance curves, R-curves, for stable austenitic NiTi for load ratios, $R=-1$ to $R=0.5$. Data adapted from [McKelvey and Ritchie, 2001], [Holtz *et al.*, 1999] and [Robertson and Ritchie, 2007].

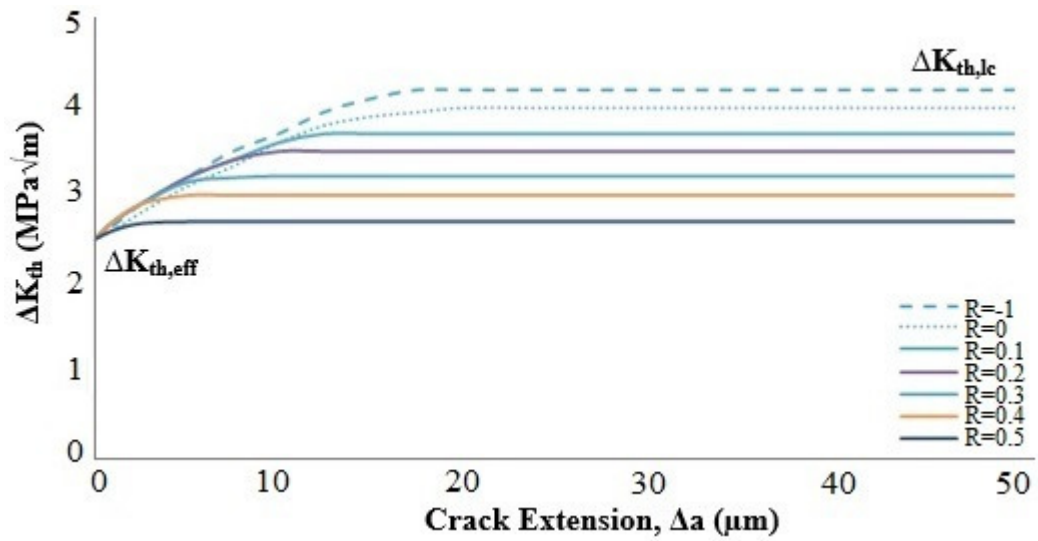


Figure 6.6: Crack growth resistance curves, R-curves, for stable martensitic NiTi for load ratios, R=-1 to R=0.5. Data adapted from [McKelvey and Ritchie, 2001], [Holtz *et al.*, 1999] and [Robertson and Ritchie, 2007].

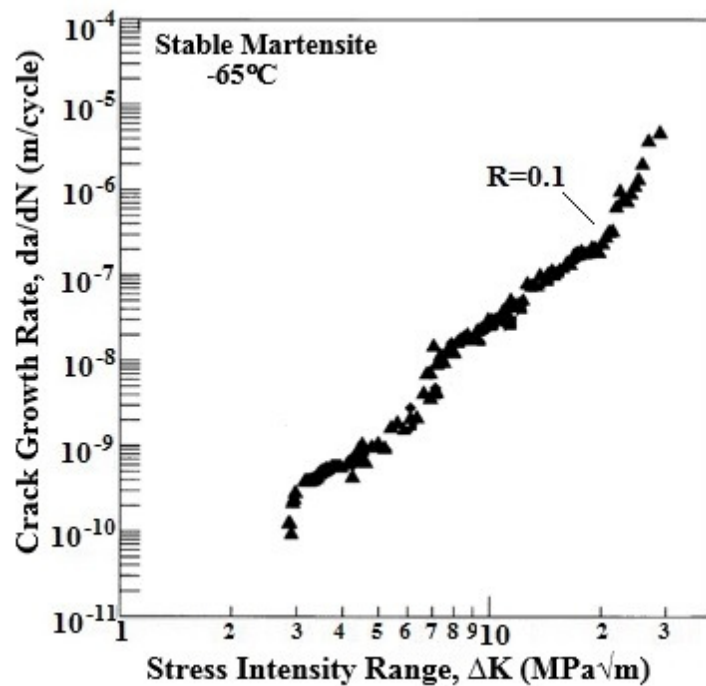


Figure 6.8: Fatigue crack growth rate behaviour for stable martensitic NiTi with load ratio, R=0.1. Tested at -65°C. Adapted from [McKelvey and Ritchie, 2001].

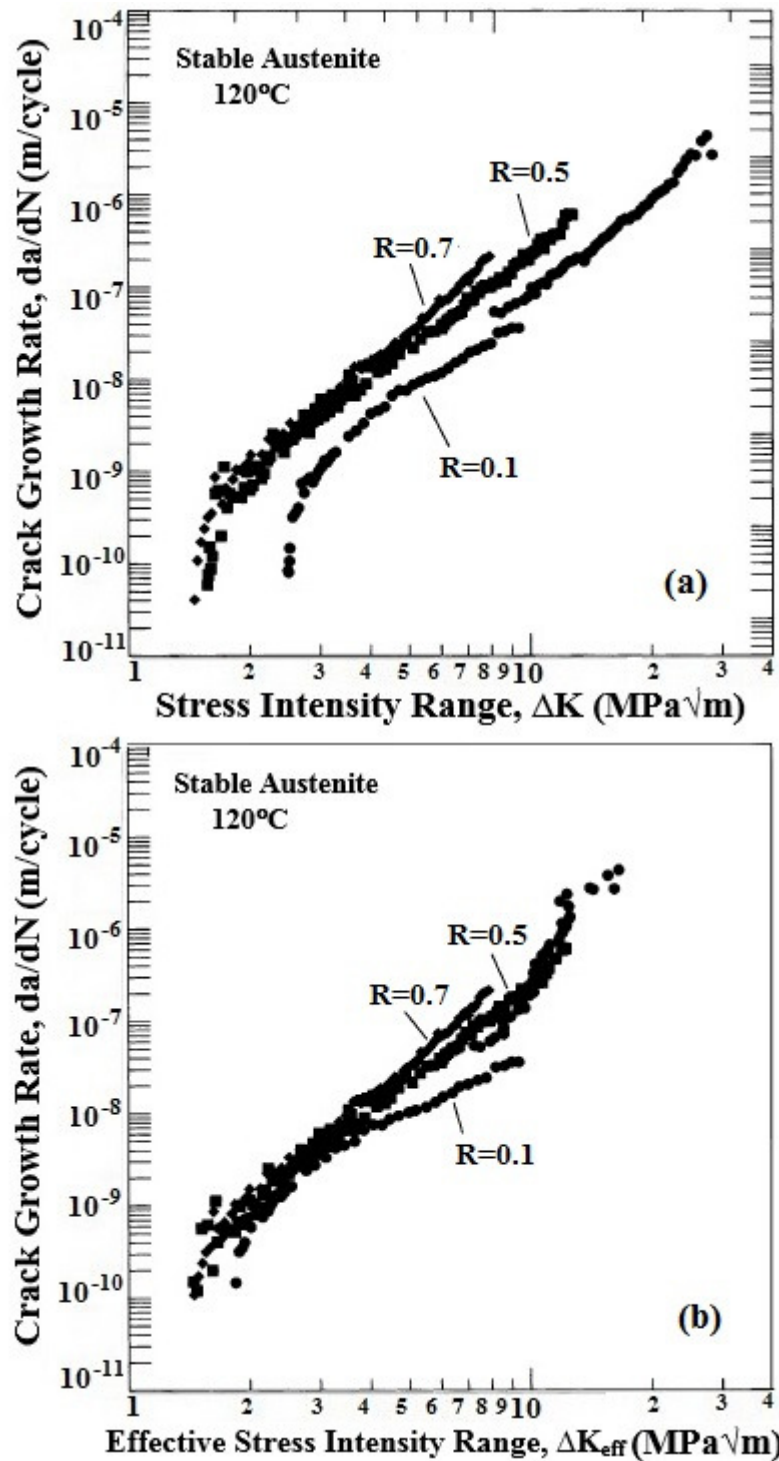


Figure 6.9: Fatigue crack growth rate behaviour for stable austenitic NiTi (a) neglecting, and (b) including crack closure, with load ratio, $R=0.1$, 0.5 and 0.7 . Tested at $120^\circ C$. Adapted from [McKelvey and Ritchie, 2001].

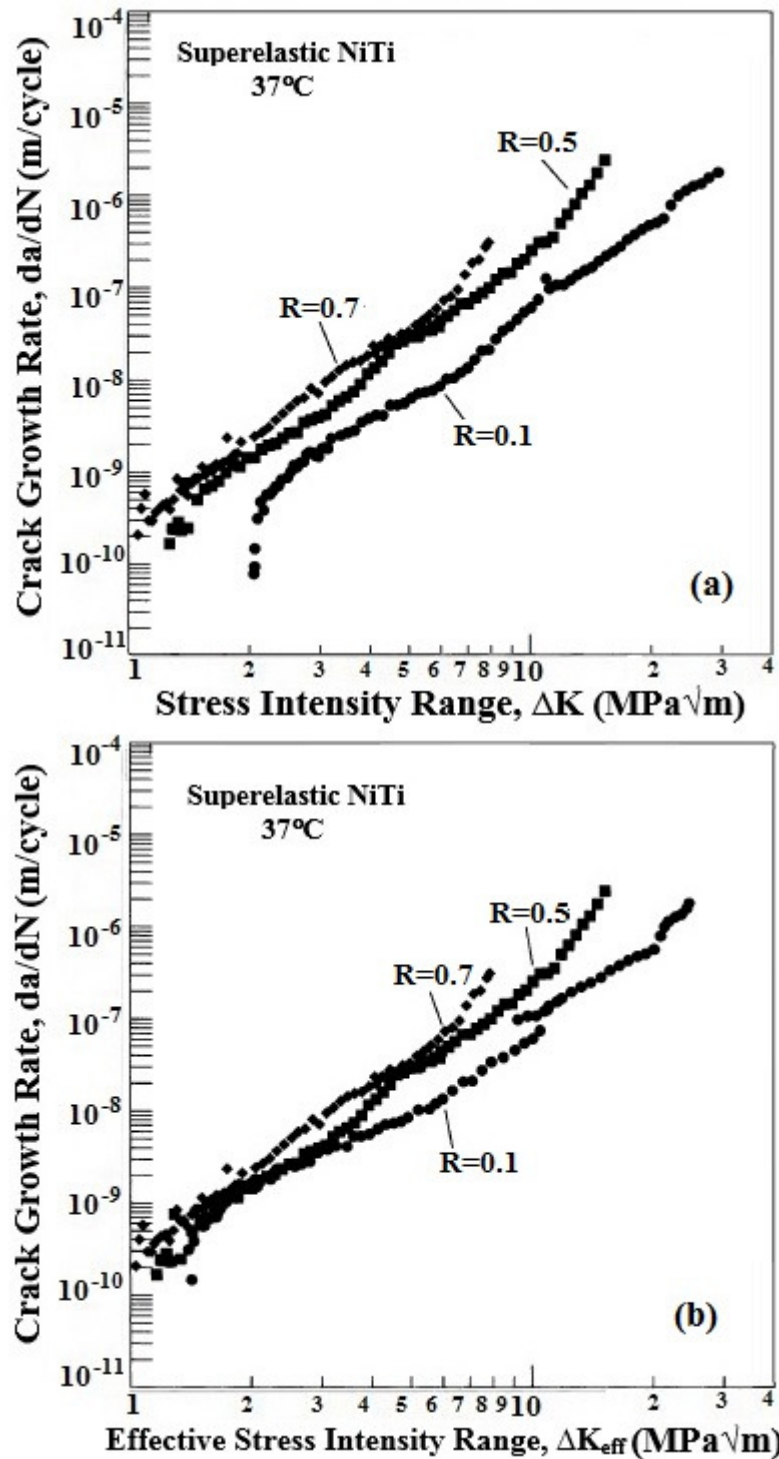


Figure 6.10: Fatigue crack growth rate behaviour for superelastic NiTi (a) neglecting, and (b) including crack closure, with load ratio, $R=0.1$, 0.5 and 0.7 . Tested at 37°C . Adapted from [McKelvey and Ritchie, 2001].

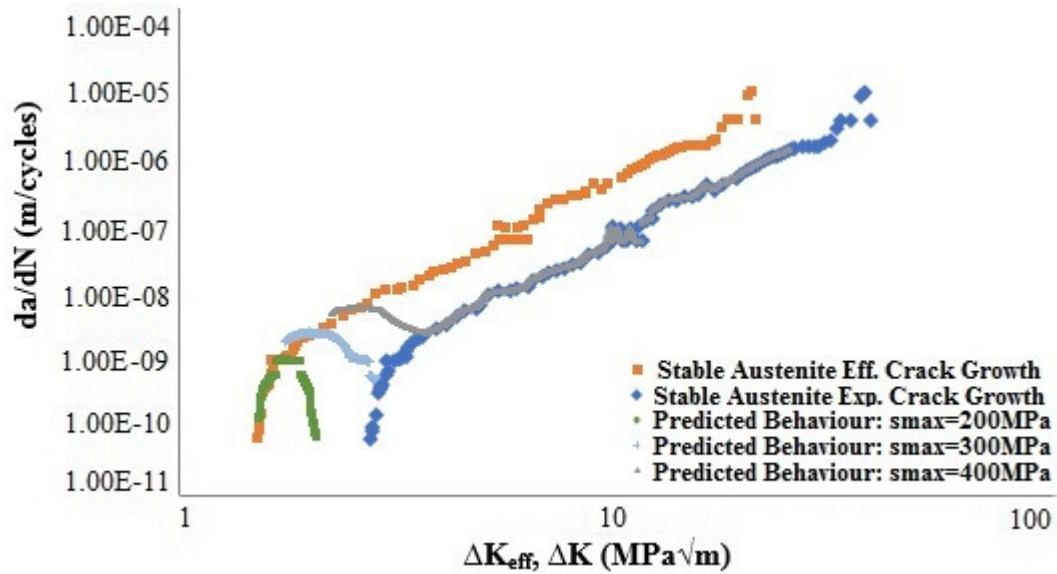


Figure 6.11: Predicted fatigue crack growth rate behaviour of a stable austenitic NiTi specimen with an initial defect size, a_0 , of $5\mu\text{m}$ for various applied maximum stress values.

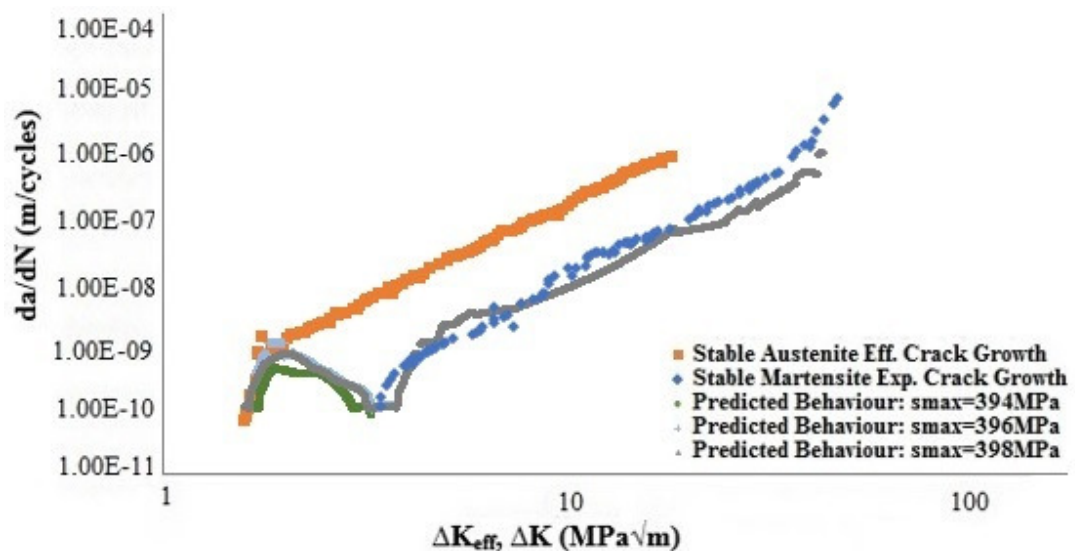


Figure 6.12: Predicted fatigue crack growth rate behaviour of a superelastic NiTi specimen with an initial defect size, a_0 , of $5\mu\text{m}$ for various applied maximum stress values.

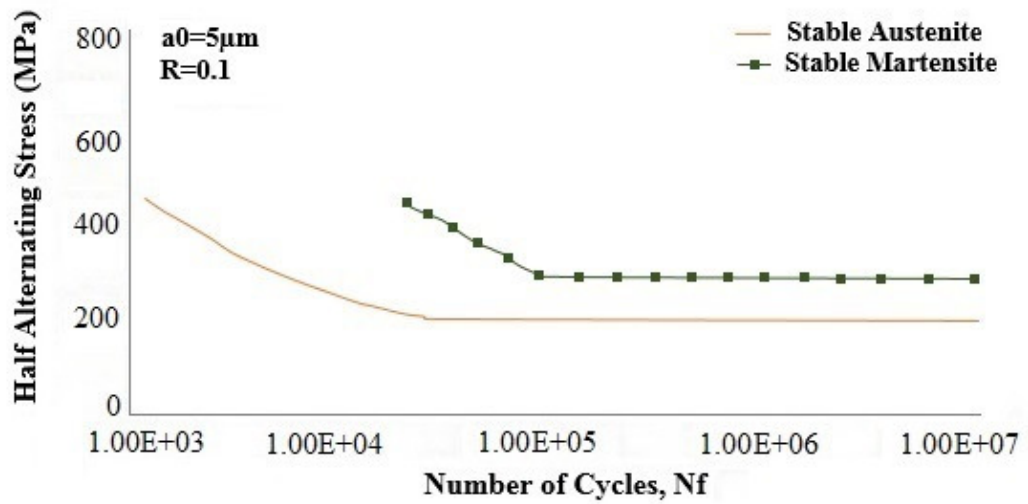


Figure 6.13: Predicted S-N curves for stable austenitic and stable martensitic NiTi specimens with initial defect size $a_0=5\mu\text{m}$ and load ratio $R=0.1$.

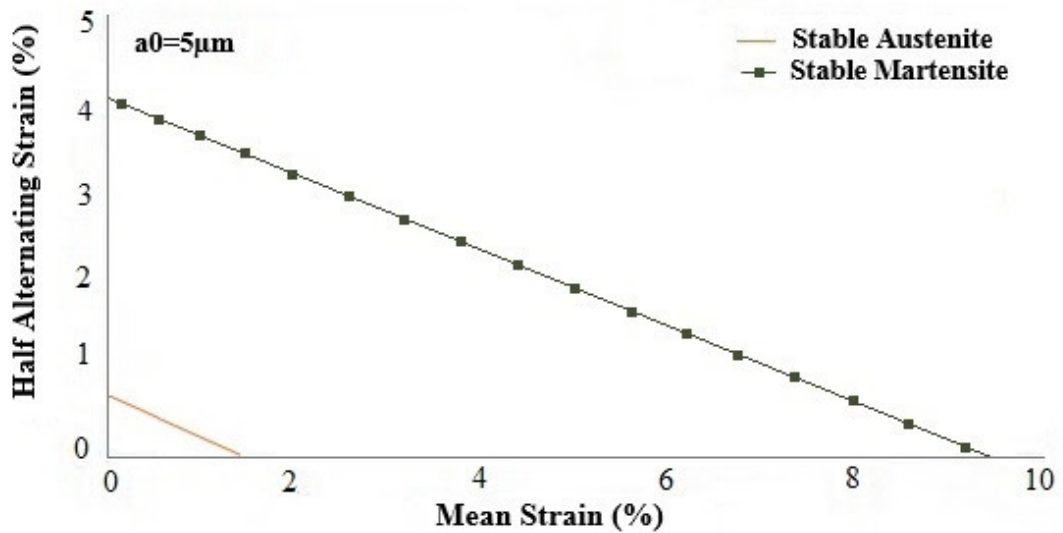


Figure 6.14: Predicted constant life diagram for stable austenitic and stable martensitic NiTi specimens with initial defect size $a_0=5\mu\text{m}$

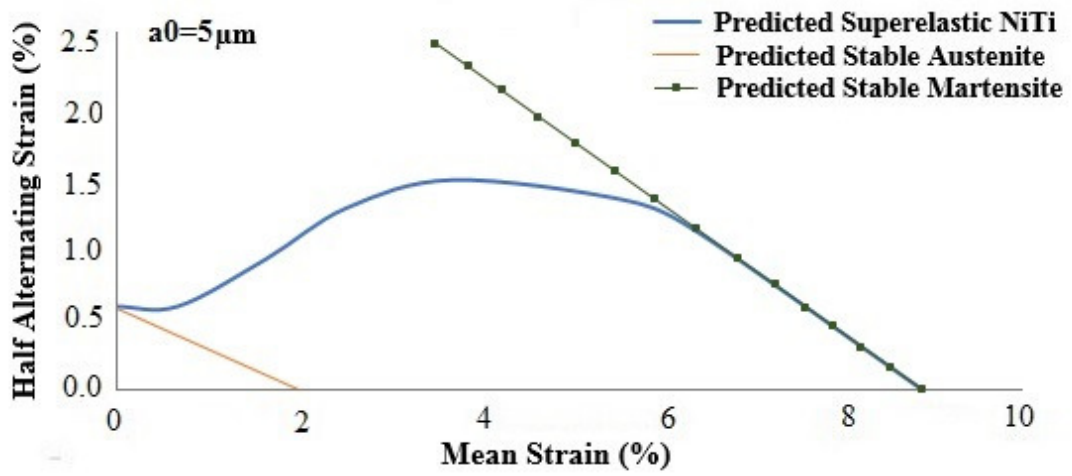


Figure 6.15: Predicted constant life diagram for stable austenitic, stable martensitic and superelastic NiTi specimens with initial defect size $a_0 = 5 \mu\text{m}$.

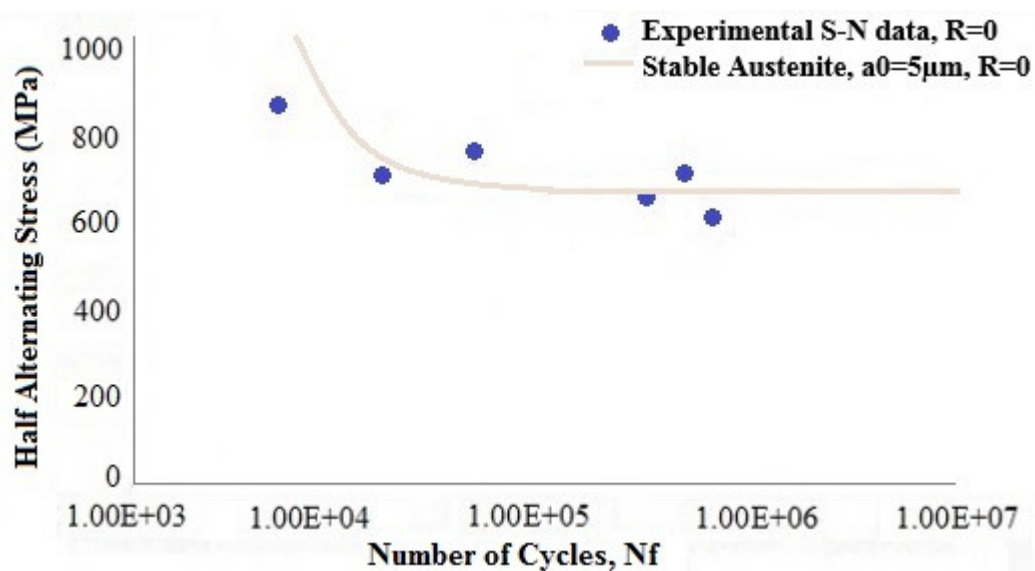


Figure 6.16: Predicted S-N curve for a stable austenitic specimen with initial defect size $a_0 = 5 \mu\text{m}$ and load ratio $R = 0$ compared against experimental S-N data taken from [Miyazaki *et al.*, 1988].

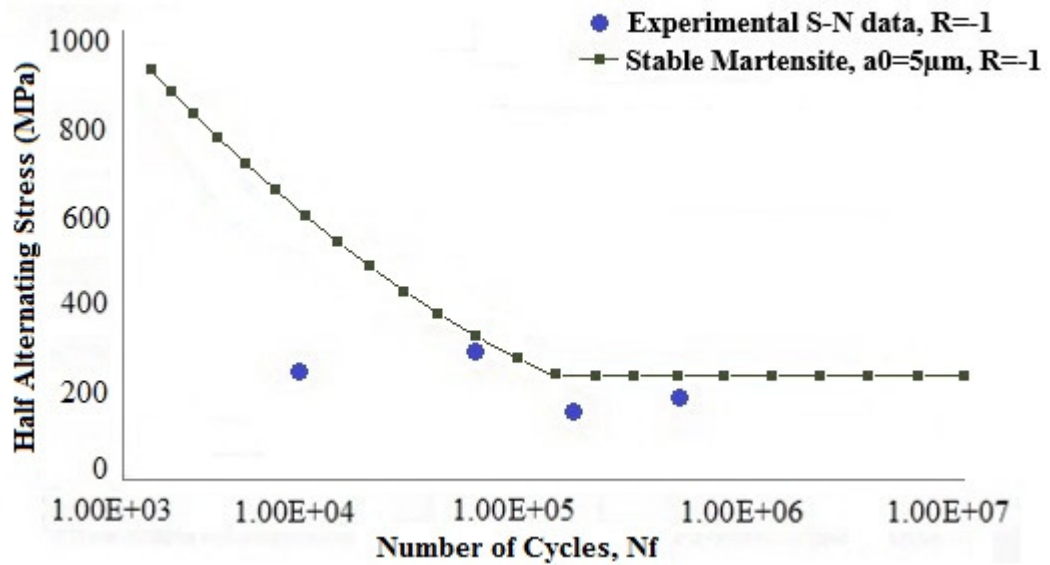


Figure 6.17: Predicted S-N curve for a stable martensitic specimen with initial defect size $a_0=5\mu\text{m}$ and load ratio $R=-1$ compared against experimental S-N data taken from [Melton and Mercier, 1979].

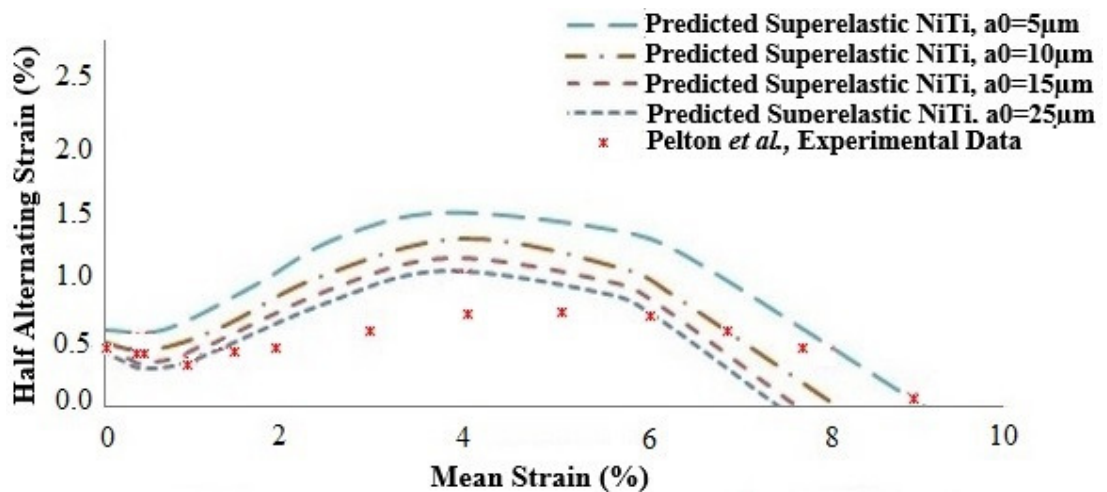


Figure 6.18: Comparison of the predicted constant life diagram to the experimental works of [Pelton et al., 2003] and [Pelton et al., 2008] for NiTi specimens with initial defect sizes, a_0 , of 5, 10, 15 and $25\mu\text{m}$.

Chapter 7

Effect of Crystallographic Texture on the Fatigue Behaviour of NiTi

7.1 Introduction

Standard computational design procedures for biomedical stent devices relies on the use of uniaxial homogenous material properties (which assumes continuum material behaviour) to fully describe material response despite the well documented dependence of material behaviour on texture. While the computational investigations described in Chapter 5 were solely concerned with highlighting the effect of texture on the uniaxial tension-compression behaviour of superelastic NiTi specimens, this current chapter computationally investigates the effect of texture on superelastic NiTi's fundamental fatigue behaviour. The computational methodology first developed by [Bruzzi and McHugh, 2002] to characterise the fatigue behaviour of metallic materials, which was modified for use with superelastic NiTi in Chapter 6, is therefore further adapted in this chapter to include the effects of crystallographic texture. In this way, the fatigue life predictions described in Chapter 6 for superelastic NiTi can be directly compared against the generated fatigue life predictions generated in this chapter in order to demonstrate the non-conservative approximations which can occur as a result of neglecting microstructural effects.

The computationally derived predictions of the crack growth rate behaviour, overall fatigue life (N_f), endurance limits and generated constant life diagrams are compared for superelastic NiTi specimens. These consider the material as (1) a continuum material with homogenous behaviour using the results of Chapter 6, and (2) a polycrystalline textured material with anisotropic granular behaviour. Both realistic and idealised representations of the specimen's microstructure are used in the analysis of this current chapter. In this manner, further insight can be achieved into the effect of crystallographic texture on the fatigue behaviour of superelastic NiTi which highlights the concerns with current design rules that neglect microstructural textural effects during standard numerical modelling procedures. In addition, the investigation described in this chapter offers a quantitative explanation towards the observed scatter in experimental fatigue data of NiTi specimens due to the inherently textured nature of experimental fatigue specimens.

7.2 Incorporation of Texture

7.2.1 *J*-integral

As described in Section 6.3, crack tip conditions are modelled using a 2-D generalised plane strain homogenous FEA model to calculate the elastic-plastic fracture mechanics parameter, ΔJ_{eff} . In this chapter, two 2-D generalised plane strain models which incorporate a realistic (Figure 7.1) and an idealised (Figure 7.2) representation of NiTi's microstructure are used. The microstructural features incorporated into the two models, to represent the microstructure of a compact tension specimen, are based on the microstructure of the NiTi micro-dogbone specimen (identified in Section 3.3) respecting the same volume fraction of the varying grain orientations identified in the test area through EBSD. The idealised model consisted of hexagonal unit cells which represent a grain size of 20 μ m following the modelling approach of Chapter 5. As with the continuum model of Chapter 6, it was only necessary to model one-half of the specimens due to symmetry effects. Both models, incorporating the realistic and idealised granular structures, include an initial flaw of a sharp crack free of crack closure of a given length, a_0 .

Specimens modelled had a length 100 times greater than that of the crack as to remove boundary effects. The bottom edge, except the crack face, was constrained to have zero displacement in the y-direction as to maintain symmetry. A total of 2,250 eight-node quadrilateral generalised plane strain elements (CGPE8R) were used in this model; this number of elements was deemed necessary following a convergence study of the resulting maximum tensile stress (σ_{22}) extracted from the node at the initial crack tip in the 2-D model for a given applied displacement. In this way, the number of elements in the generated mesh is increased until the incremental difference between the extracted resulting values is shown to become negligible. Following the methodology outlined in Chapter 6, a uniformly distributed tensile stress was applied in the y-direction to the top surface and thus the *J*-integral was subsequently extracted from the model for a given applied far-field stress. As the *J*-integral is dependent upon material behaviour it was noted which grain orientation, and subsequently what

microstructural phase, was present along the crack path for the given local stress conditions in order to assign the appropriate value for the J -integral for a given crack extension. This was necessary as the varying grain orientations located along the crack path will undergo phase transformation at different magnitudes of stress, as identified in Table 3.3, as thus will experience varying fatigue crack growth rate behaviour.

Following the micro-mechanical modelling methodology outlined in Section 5.3.2, grain boundaries in both models are assumed to be perfectly bonded with no inter-granular slip. The properties of each grain are assumed to be isotropic and dependent on its orientation with respect to the global loading direction. To accurately simulate the granular transformational behaviour of the specimen, the in-built material subroutine UMAT/Nitinol (integrated into the commercially available numerical modelling platform ABAQUS™ 6.10) was employed; full details of this material subroutine can be found in Section 4.2. Following the methodology outlined in Chapter 5, the constitutive equations for these micro-scale models were established using individual single crystal tension-compression data for varying crystallographic orientations from the published work of [Gall *et al.*, 1998]. The 15 material properties extracted from the uniaxial tensile stress-strain curves for each of the crystallographic orientations identified in the specimen are identified in Table 3.3. It should be noted that the values for ΔK_{eff} used in this work for austenitic, martensitic and superelastic NiTi (Figures 6.8-6.10) are extracted from the works of [McKelvey and Ritchie, 2001] which investigates the fatigue crack growth rate behaviour of bulk compact tension specimens. However, in this investigation, these values are assumed to be applicable to the single crystal behaviour also. It is acknowledged this is not ideal, as ΔK_{eff} is dependent upon the material tested, however this assumption was deemed necessary within the scope of this work.

When comparing the macroscopic material response predicted by the two micro-mechanical models, incorporating the realistic and idealised microstructure of the compact tension specimen as shown in Figure 7.1 and Figure 7.2, with an initial defect size of 5 μ m and an applied maximum far-field stress of 600MPa very similar results

are demonstrated, as illustrated in the plot of Figure 7.3. Therefore, the complex realistic micro-mechanical model was considered not necessary to capture the overall macroscopic behaviour of a polycrystalline superelastic NiTi specimen. As a result, and to reduce the computational time required, the idealised hexagonal unit cell micro-mechanical model was preferentially selected for use in the computational investigation described in this chapter. In the plot of Figure 7.3, the predicted uniaxial behaviour of the micro-mechanical models are also compared with the macroscopic material response generated from the continuum model created for the investigations of Chapter 6 in which uniaxial homogenous continuum material properties are employed. The high level of agreement which is demonstrated between the micro-mechanical and continuum models supports the use of the granular micro-mechanical FEA models as being suitable to accurately simulate the overall macroscopic material response of the NiTi specimen. As a result the FEA model, with the idealised microstructure (as shown in Figure 7.2), is considered to effectively represent the behaviour of a polycrystalline NiTi specimen with anisotropic granular behaviour for the extraction of the J -integral for calculation of ΔJ_{eff} (EQ. 6.1). Therefore, as the J -integral is dependent on material behaviour, it is extracted from a contour within the grain containing the crack tip for a given crack extension along the crack path. Once calculated, ΔJ_{eff} is correlated with the calculated effective crack growth rate curve ($\Delta K_{eff} - da/dN$ curve), as previously discussed in the homogenous fatigue modelling of Chapter 6. This then determines the rate at which the crack would grow if subjected to this driving force. Using this cycle-by-cycle approach, the number of cycles to failure (N_f) is thus predicted for the complex anisotropic granular phase transforming superelastic NiTi material for a given applied far-field stress.

7.2.2 R-curves

In order to calculate the effective stress range ratio, U , (EQ. 6.2) crack growth resistance curves (R-curves) were employed. As described in Section 6.3.2, the required R-curves for use in the computational investigations of this thesis were successfully generated through the combination of various previously published

experimental data, namely, from the works of [McKelvey and Ritchie, 2001], [Robertson and Ritchie, 2007] and [Holtz *et al.*, 1999]. However this computational investigation has identified that, with the incorporation of NiTi's crystallographic texture, the maximum stress (σ_{22}) experienced by the propagating crack tip deviates from the applied far-field stress due to the varying uniaxial stress-strain material responses of the different grain orientations along the crack path. This effect can be explicitly seen in Figure 7.4 which displays the variation of maximum stress (σ_{22}) experienced along the crack path for a nominally applied far-field stress of 600MPa; only the first 350 μm of the crack extension are displayed for illustrative purposes. In this way, even though a constant far-field stress of 600MPa is being applied to the compact tension specimen, the advancing crack tip will experience varying levels of maximum stress along the crack path. This can be attributed to the imposed granular constraints in the model which force each neighbouring grain to deform to the same extent. Therefore, due to the varying material behaviour of each of the grains along the crack path (as illustrated in Table 3.3), each grain will experience a different level of stress for a given strain.

With altering maximum stress experienced by the crack tip along the crack path, the stress intensity factor range, ΔK , therefore also correspondingly varies with crack extension, Δa . As a result of varying ΔK , the R-ratio correspondingly alters with crack extension as shown in Figure 7.5; as before, only the first 350 μm of crack extension was examined for the aforementioned case of an applied far-field stress of 600MPa. R-curves employed in the investigation described in this chapter must therefore be modified to reflect this fluctuating R-ratio with crack extension. In addition, due to the varying stress amplitudes experienced by the crack tip as a result of texture, the experienced peak tensile stress amplitudes may act as stress overloads during the cyclic loading procedure. Overloads can slow down or even arrest a long fatigue crack due to the significant change they induce on the level of crack closure in the wake of the crack tip [Bruzzi *et al.*, 2004]. A single peak stress overload has been shown by [von Euw *et al.*, 1971] to affect the fatigue crack growth rate for one quarter of the plastic zone size. In this investigation a legacy effect is therefore also included in the R-curve

used in the fatigue algorithm, as demonstrated in Figure 7.6 for the aforementioned case which examined the first 350 μm of crack extension which had an applied far-field stress of 600MPa. In this way a single peak tensile stress overload is assumed to affect the fatigue crack growth rate for one quarter the total length of a grain, i.e. the effect of a single peak stress overload was assumed to have dissipated after 5 μm of propagating crack growth in the FEA model incorporating the idealised hexagonal granular 20 μm unit cell structure in this chapter. It is acknowledged that while the plastic zone size and grain size in the specimen are not equivalent, this approach was adopted as it represents a simplified method to include the legacy effect in the R-curve. An example of a modified R-curve for a superelastic NiTi specimen with load ratio $R=0.1$ is shown in Figure 7.7. The R-curves used in this work were generated through the interpolation of previously established R-curves which were generated for the analysis discussed in Chapter 6 for varying R-ratios along the crack path following the varying experienced ΔK values.

7.3 Predicted Fatigue Behaviour

7.3.1 Small Fatigue Behaviour

As illustrated in Figure 7.8, the predicted crack growth rate curve generated by the model incorporating an idealised hexagonal unit cell representation of the NiTi specimen's microstructure, with a (100) orientated grain located at the initial crack tip, was compared to the predicted crack growth rate curve generated by the continuum model from Chapter 6 using homogenous material properties. To ensure that a fair comparison was made, both models include an initial defect size of 5 μm , an imposed applied far-field tensile stress of 600MPa and a load ratio of $R=0.1$. Nevertheless, the two models are shown to predict different crack growth rate behaviours which can be attributed to the varying maximum stress levels experienced by the advancing crack tip along the crack path. This deviation in stress observed in the model was attributed to the varying grain orientations located along the crack path in the FEA model which incorporated the texture of the superelastic NiTi specimen, thus giving a different material response than that of the continuum model for the same applied stress. This

differing material response of various grain orientations along the crack path is illustrated in Figure 7.9 for the first 350 μm of the crack path. For reference, see Table 3.3 and Table 6.1 for details of the varying material behaviour parameters for the homogenous material and the individual grain orientations, respectively.

From the extracted single crystal material properties used for input into the UMAT/Nitinol of Table 3.3, the (100) orientated grain located at the initial crack tip is identified as having a relatively high SIMT initiation stress of 570MPa [Gall *et al.*, 1998]. Therefore, the material surrounding the initial crack tip in the textured model will have just begun initiation of the phase transform from the austenitic to SIM phase at the maximum stress of 600MPa. Meanwhile, in the model employing homogenous continuum properties, the initiation stress for SIMT is at a lower stress value of 390MPa, as extracted from the uniaxial stress-strain curve of the superelastic NiTi specimen of Table 6.1. As a result, in the continuum model the material surrounding the initial crack tip will have fully transformed to the softer and more compliant SIM phase at the maximum experienced stress level of 600MPa. As martensite is shown to have a superior fatigue crack growth resistance [McKelvey and Ritchie, 2001] when compared to austenite, it follows that the crack growth in the continuum model may grow at a slower rate than that in the model incorporating texture. This differing transformational behaviour, between the homogenous and textured model, will continue along the crack path due to the varying stress levels experienced by the advancing crack tip.

In this manner, the NiTi specimen represented in the continuum model was predicted to have a longer number of cycles to failure, N_f of 16,952 cycles with a corresponding marginally longer crack length at failure of 1127.831 μm , as compared to the NiTi specimen represented by the model incorporating texture which has a predicted N_f of only 15,501 cycles with a crack length at failure of 1127.568 μm ; both crack lengths at failure represent a crack that would propagate through approximately 56 grains of a typical grain size 20 μm . From such results it can be identified that a serious non-conservative prediction of fatigue life is presented when employing

material models which neglect microstructural textural effects and which simply rely on the homogenous bulk material properties to fully describe material behaviour, as is standard practice in the current computational design of biomedical devices. However, it is acknowledged many assumptions are made in this work which subsequently affect the accuracy of predicted results; as previously discussed in Section 6.3.6. Therefore the degree of predicted scatter in the fatigue behaviour, assumed to be attributed to the effects of crystallographic texture, may not precisely portray the genuine scatter seen experimentally. This is a recognised limitation of this work due to the uncertainties introduced in the fatigue modelling procedures, for example, through extracting the required input material data from multiple studies reported in literature. In addition, a ‘worst-case-scenario’ approach is employed in the textural analyses completed in this work which result in the most conservative prediction of fatigue life being produced. Nevertheless, the profound effect of crystallographic texture on the fundamental material behaviour of NiTi has been demonstrated in this work; in particular, in terms of the non-homogenous material behaviour in a fatigue specimen due to the localised variation in maximum stress experienced by the advancing crack tip for a given applied far-field stress.

7.3.2 Effect of Grain Orientation at Crack Tip

A comprehensive investigation into the effect of different grain orientations at the crack tip can be achieved through the simple alteration of the grain orientation assigned to the idealised hexagonal unit cell located at the initial crack tip in the FEA model described in Section 7.2.1 (Figure 7.2). As illustrated in Figure 7.9(b), varying evolutionary stress profiles are presented which are dependent on the material properties assigned to the individual grains identified in Figure 7.9(a). This non-uniform response is attributed to the deviation of stress level from the applied far-field stress due to the varying characteristic transformational behaviours of each of the grain orientations (as listed in Table 3.3). Varying levels of maximum stress experienced by the crack tip, as shown in Figure 7.9(c), result in different stress intensity ranges, ΔK , at the crack tip with crack extension which ultimately alters the driving force for

fatigue crack growth. As a result, changing the characteristic granular material properties assigned to the grain located at the initial crack tip results in the variation of predicted crack growth rate behaviour as illustrated in Figure 7.10. From this image it can be identified that the FEA models with the (110) and (111) orientated grains located at crack tip behave relatively similarly while the model with the (100) orientated grain located at the crack tip shows most variation in small fatigue crack growth rate behaviour for the specimen with initial defect size, a_0 , of $5\mu\text{m}$, load ratio, R , of 0.1 and an applied far-field stress of 600MPa.

This behaviour can be clarified through the analysis of the transformational behaviour assigned to the individual grains, as outlined in Table 3.3. For example, the (110) and (111) orientated grains initiate SIMT at the relatively low stress levels of 330MPa and 240MPa, respectively, while the (100) orientated grains initiate the SIMT at the relatively higher stress level of 570MPa. Therefore, as the martensitic NiTi phase has been experimentally shown to have a superior fatigue performance than the austenitic NiTi phase [McKelvey and Ritchie, 2001] it follows that, localised stress conditions which promote the SIMT should result in the longest predicted fatigue lives. Specifically, it was found that N_f for the models with (100), (110) and (111) orientated grains at the crack tip were predicted to be 15,501, 16,896 and 17,151 cycles, respectively. These results suggest that for the specific circumstance in which a (100) orientated grain was present at the crack tip (due to the highest initiation stress for SIMT), transformation to the superior fatigue resistant martensitic phase was inhibited; therefore this results in the shortest predicted fatigue life of the three conditions investigated. This conclusion is in agreement with the discussion of Chapter 4 on the effects of individual grain orientations on SIMT [Weafer and Bruzzi, 2014] [Weafer *et al.*, 2015]. Since the overall fatigue performance of the specimen was demonstrated to be dependent on the particular grain orientation present at the crack tip this offers an explanation towards the observed scatter in experimental testing due to the inherently textured nature of the experimental specimens.

7.3.3 Predicted Endurance Limits

From the generated fatigue life results discussed in this chapter, it is demonstrated that the computational continuum models of Chapter 6 may result in an over-estimation of the fatigue life of the superelastic NiTi specimens. This is hypothesised to be attributed to the omission of microstructural textural effects in the models developed in Chapter 6 as they simply consider the material to behave as a continuum. The computational investigation described in this chapter therefore highlights the weakness in current standard computational design rules of biomedical commercial devices which simply employ uniaxial homogenous isotropic material properties to fully describe the complex material behaviour. This was particularly noticeable in the prediction of the superelastic NiTi specimen's fatigue endurance limit using both the continuum model of Chapter 6 and the model incorporating texture described in this chapter. For example, the endurance limit previously predicted using the continuum model in the investigation of Chapter 6 for a superelastic NiTi specimen with initial defect size of $5\mu\text{m}$, using homogenous material properties, was identified as 397MPa for $R=0.1$ (as shown in Figure 7.11). However, following the modification of the fatigue modelling methodology in this chapter to include the effects of crystallographic texture, the predicted endurance limit for the same superelastic NiTi specimen with a (100) grain at the initial crack tip was identified as being a much lower 340MPa for $R=0.1$ (as shown in Figure 7.11). This, as a result, may lead to serious non-conservative designs of commercial biomedical devices through the construction of inaccurate constant life diagrams.

It should be noted, the mechanical and fatigue behaviour of superelastic NiTi is typically expressed in terms of a strain-dominated approach due to the characteristic plateau associated with the stress-induced martensitic transformation (Figure 1.2). As a direct result of this SIMT, the superelastic material can experience large changes in strain within a relatively small stress range thus creating a challenge in determining the material behaviour in terms of a stress-dominated approach. In this way the fatigue behaviour of superelastic NiTi is typically expressed employing a strain-life (ϵ -N), in

place of a stress-life (S-N), curve; as previously discussed in Section 2.4. However, the traditional fracture mechanics methodology to characterise the fatigue life of metallic materials is a stress-dominated approach. As a result, the fatigue modelling methodology used in this work also adapts a stress-based approach in order to calculate the nominal crack growth in a specimen with respect to an effective local stress intensity range (ΔK_{eff}) experienced by the advancing crack tip. The predicted number of cycles to failure (N_f) for the specimen is therefore generated as a function of the applied alternating and mean stresses. Using this S-N curve, the endurance limit of the specimen can be calculated for the given loading conditions (Figure 7.11). In this work, these stress-based endurance limits are subsequently converted to the more relevant equivalent strain-based endurance limits, employing the material's uniaxial stress-strain curve, to express the fatigue behaviour of the superelastic NiTi specimen in terms of alternating and mean strains in the form of a constant life diagram.

7.3.4 Predicted Constant Life Diagram

Using the resulting endurance limits predicted by the model incorporating texture for various load ratios (R-ratios), a constant life diagram was constructed for the polycrystalline superelastic NiTi specimen. Figure 7.12 shows, for a specimen with initial defect size of 25 μ m, a vast difference is demonstrated between the constant life diagrams incorporating textural effects and that which was constructed in using the continuum model of Chapter 6, as previously described in Section 6.4.3. It was determined that the N_f for the continuum model was predicted to be 16,952 cycles, meanwhile, the N_f for the textured model with (100), (110) and (111) orientated grains at the crack tip was 15,501, 16,896 and 17,151 cycles, respectively. As a result it is identified that the standard continuum model may over-predict the useful fatigue life of a polycrystalline specimen. Utilising a fail/no-fail approach, constant life diagrams are employed as a guide in the safe design of biomedical stent devices. In this way, with the omission of crystallographic textural effects in the micro-mechanical fatigue modelling methodology, the over-prediction of such endurance limits may result in severely inaccurate designs of commercial biomedical devices. This may lead to

reduced device performance and, in worst case scenario, may lead to unanticipated device failure *in vivo* with potential injury, or even death, occurring to the patient.

7.4 Discussion

Standard computational design rules for commercial biomedical stent devices simply calls for the use of homogenous isotropic material properties, extracted from experimental uniaxial tensile testing, to fully describe material behaviour for analysis of the durability of a stent device design. Using this approach the material is assumed to behave as a continuum with bulk material properties. However, in small engineering components such as stent struts, the behaviour of varying grain orientations in the component becomes significant. At size scales in which the grain and component size are of the same order, the orientations of individual grains are shown to have a significant effect on the macroscopic component behaviour. Crystallographic texture, therefore, results in the material behaviour of stent struts to deviate significantly from the expected bulk material response and, thus, rendering the current continuum material model inaccurate for the computational prediction of small biomedical devices such as stents. If such a deviation in behaviour is to be captured within computational models for the accurate design of biomedical stent devices, it is necessary to amend the current material model to order to include a representation of the crystalline structure of the metal, and the anisotropic behaviour of individual grains, within the computational models.

In the investigation described in this chapter the methodology first developed by [Bruzzi and McHugh, 2002], and adapted in Chapter 6 to predict the fatigue behaviour of the complex phase transforming superelastic NiTi material, was further modified in this chapter to include the effects of grain orientation distribution (i.e. crystallographic texture). This was achieved through the incorporation of a realistic and idealised representation of a polycrystalline superelastic NiTi specimen's microstructural features in the FEA model used to simulate crack tip conditions of the compact tension specimen. A comparative study was subsequently performed in this chapter on the computationally derived predictions of fatigue life for a superelastic NiTi specimen,

considering the material as (1) a continuum material with homogenous behaviour using the results of Chapter 6, and (2) a textured polycrystalline material with anisotropic granular behaviour using the results generated in this chapter.

The dependence of NiTi fatigue performance on crystallographic texture was successfully demonstrated, focusing in particular on its effect on fatigue crack growth rate behaviour and, thus, the overall number of cycles to propagate this dominant crack to failure. Crystallographic texture was determined to cause a scatter of approximately 23% in the predicted fatigue endurance limits of a superelastic NiTi specimen when compared to that predicted simply employing homogeneous material properties. It was deduced that if a (100) orientated grain was present at the crack tip in a superelastic NiTi specimen the SIMT was inhibited due to its characteristically high SIMT initiation stress. In addition, the presence of a (100) orientated grain at the crack was shown to result in an overall reduced predicted fatigue life for the specimen when compared to a scenario that a (110) or (111) orientated grain is located at the crack tip. As the fatigue performance was shown to be dependent on the particular grain orientation present at the crack tip, this investigation offers an explanation to the observed scatter in experimental fatigue data due to the inherently textured nature of experimental specimens. It can be concluded that, through the comparative analysis of predicted endurance limits and generated constant life diagrams, the standard continuum model of Chapter 6, which simply employ uniaxial homogenous material properties, may result in an over-estimation of the fatigue life of superelastic NiTi. In this way, it was demonstrated that such simplified material models may lead to potentially inaccurate device design which may offer an explanation towards the reported unforeseen *in vivo* device failure.

7.5 References

Bruzzi M.S. and McHugh P.E., Methodology for Modelling the Small Crack Fatigue Behaviour of Aluminium Alloys, *International Journal of Fatigue*, 2002, **24**, p 1071–1078.

Bruzzi M.S. and McHugh P.E., Micromechanical investigation of the Fatigue Crack Growth Behaviour of Al-SiC MMCs, *International Journal of Fatigue*, 2004, **26**, p 795-804.

Gall K., Sehitoglu H., Chumlyakov Y.I. and Kireeva I.V., Tension-Compression Asymmetry of the Stress-Strain Response in Aged Single Crystal and Polycrystalline NiTi, *Acta Metallurgica*, 1998, **47**, p 1203–1217.

Holtz R.L., Sadananda K., Imam M.A., Fatigue Thresholds of Ni-Ti Alloy near the Shape Memory Transition Temperature, *International Journal of Fatigue*, 1999, **21**, p 137–145.

McKelvey A.L. and Ritchie R.O., Fatigue-Crack Growth Behavior in the Superelastic and Shape-Memory Alloy Nitinol, *Metallurgical and Materials Transactions A*, 2001, **32**, p 731-743.

Robertson S.W., Ritchie R.O., In-vitro Fatigue–Crack Growth and Fracture Toughness Behavior of Thin-Walled Superelastic Nitinol Tube for Endovascular Stents: A Basis for Defining the Effect of Crack-like Defects, *Biomaterials*, 2007, **28**, p 700–709.

von Euw E.F.J., Hertzberg R.W. and Roberts R., Delay Effects in Fatigue Crack Propagation, *Proceedings of the 1971 National Symposium on Fracture Mechanics*, 1971, p 230-259.

Weafer F.M. and Bruzzi M.S., Influence of Microstructure on the Performance of Nitinol: A Computational Analysis, *Journal of Materials Engineering and Performance*, 2014, **23**, p 2539-2544.

Weafer F.M., Guo Y. and Bruzzi M.S., The Effect of Crystallographic Texture on Stress-induced Martensitic Transformation in NiTi: A Computational Analysis, *Journal of the Mechanical Behaviour of Biomedical Materials*, 2015, **53**, p 210-217.

Weafer F.M. and Bruzzi M.S., 'Micromechanical Investigation into the Effect of Texture on the Fatigue Behaviour of Superelastic Nitinol', *International Journal of Fatigue*, Under Review (2016).

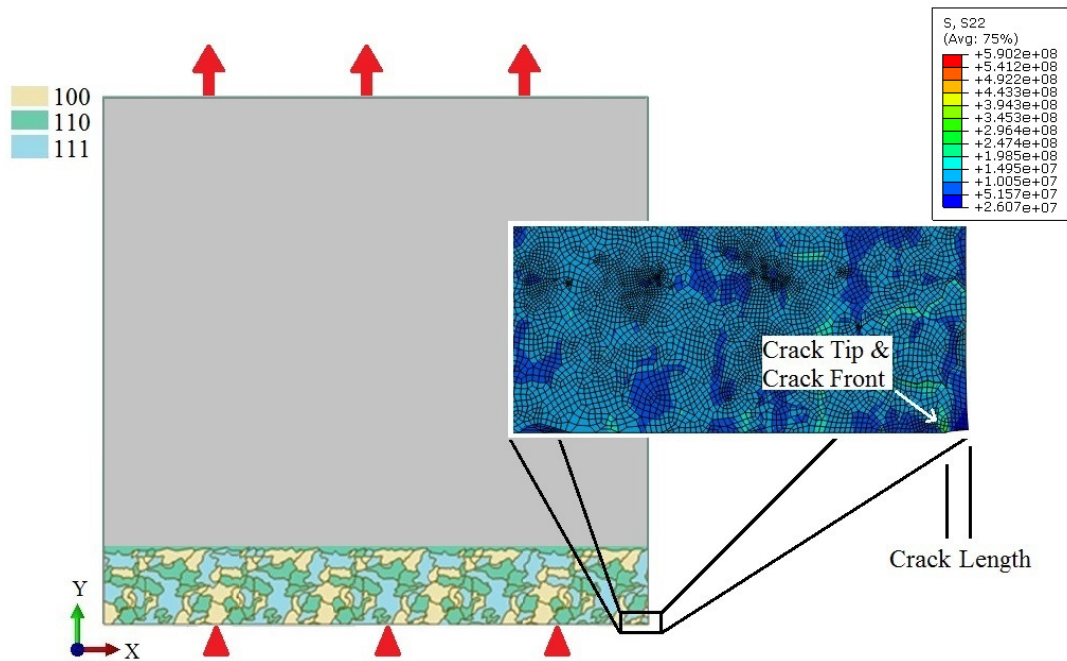


Figure 7.1: J -integral calculated through FEA modelling of the crack tip using a realistic representation of the specimen's microstructure. J -integral extracted from the model upon loading to a maximum applied tensile stress.

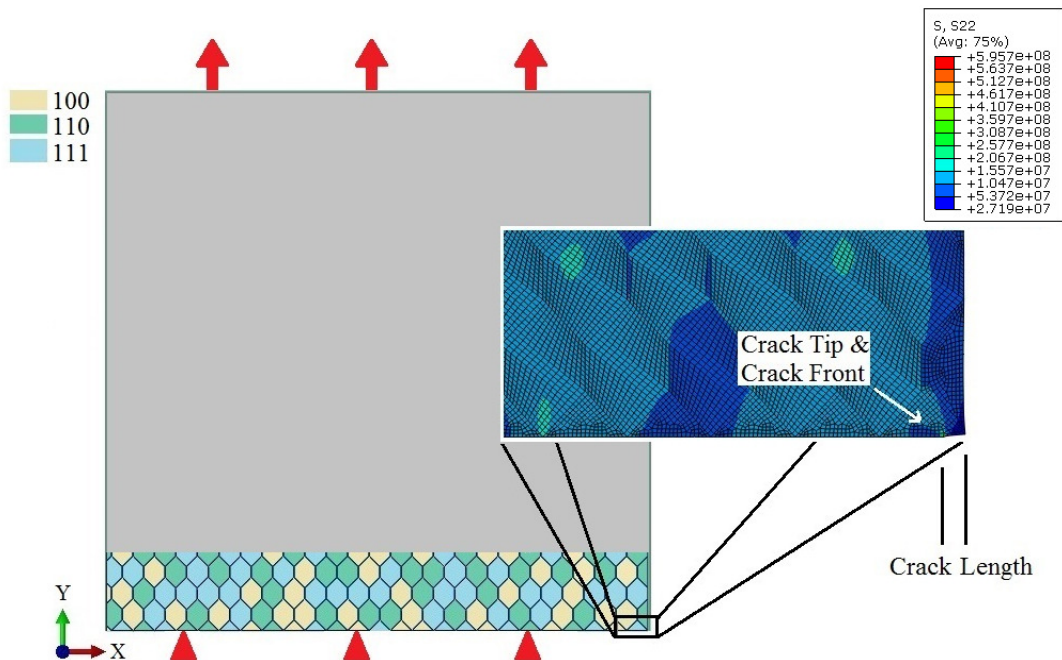


Figure 7.2: J -integral calculated through FEA modelling of the crack tip using an idealised representation of the specimen's microstructure. J -integral extracted from the model upon loading to a maximum applied tensile stress.

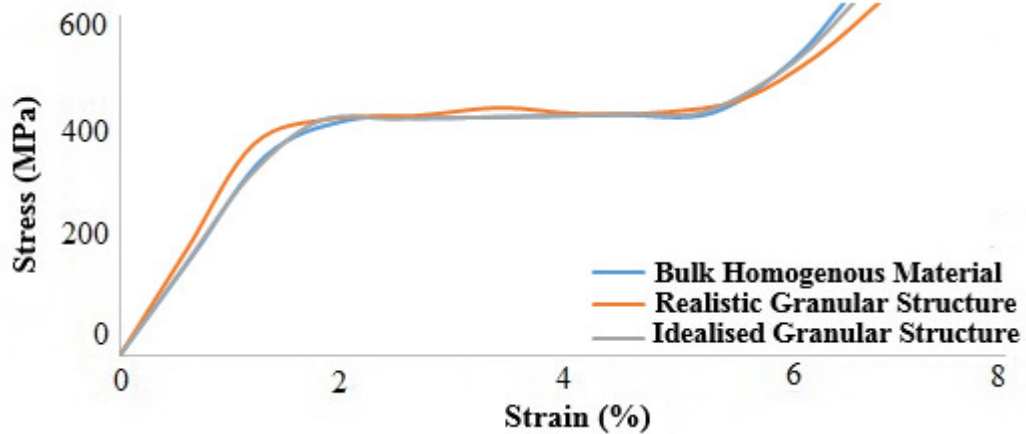


Figure 7.3: Predicted stress-strain response of a NiTi specimen generated by FEA models using a realistic and idealised representation microstructure compared against the predicted response using a continuum model.

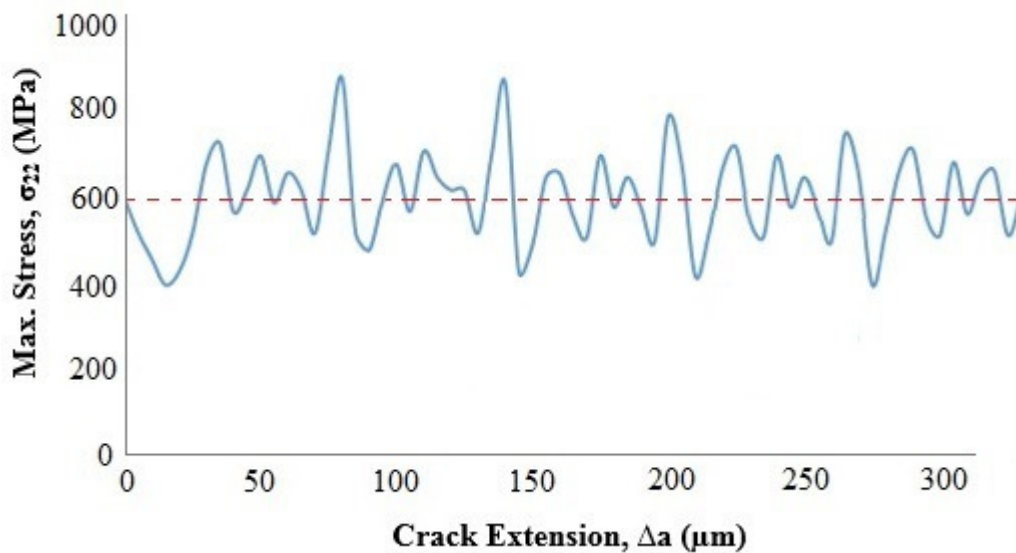


Figure 7.4: Maximum stress experienced by the crack tip along the crack length extracted from the FEA model incorporating an idealised representation of the specimen's microstructure and a (100) orientated grain located at the crack tip with an applied far-field stress of 600MPa.

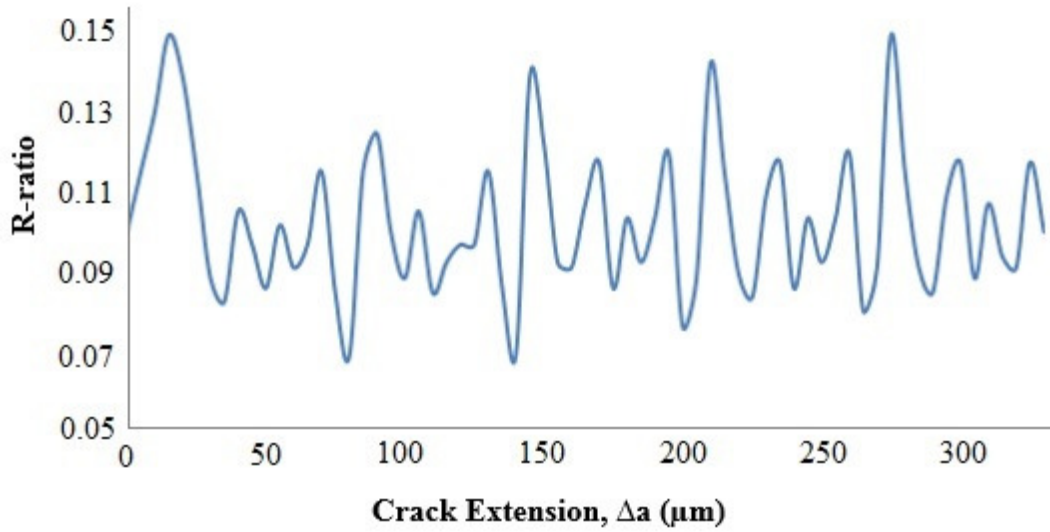


Figure 7.5: Altering R-ratio with crack extension due to shifting maximum stress experienced by the crack tip along the crack path path in the textured model for a specimen with initial defect size $5\mu\text{m}$ and an applied far field stress of 600MPa .

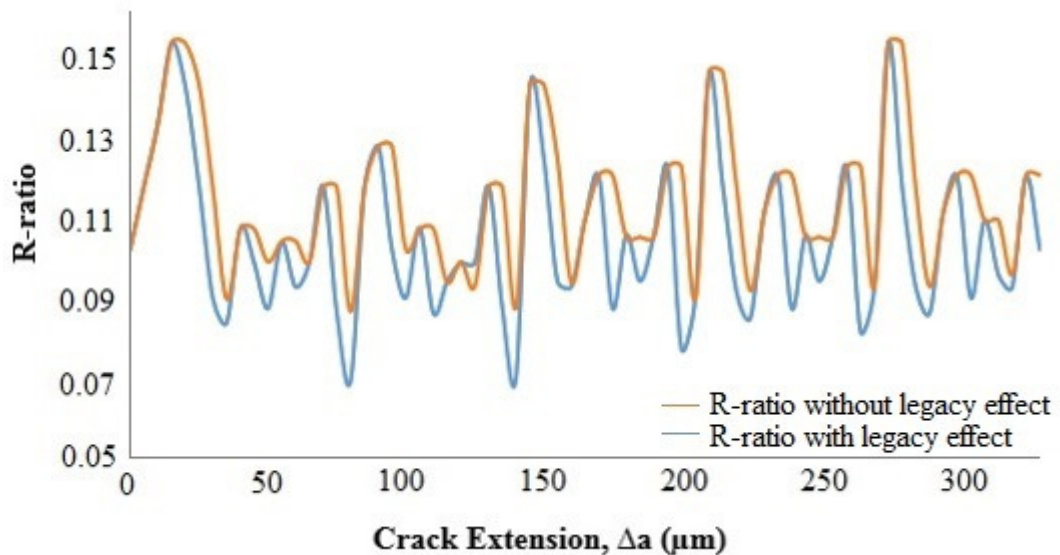


Figure 7.6: R-ratio with added legacy effect to account for the stress overload effects experienced by the crack tip in the textured model along the crack path for a specimen with initial defect size $5\mu\text{m}$ and an applied far field stress of 600MPa .

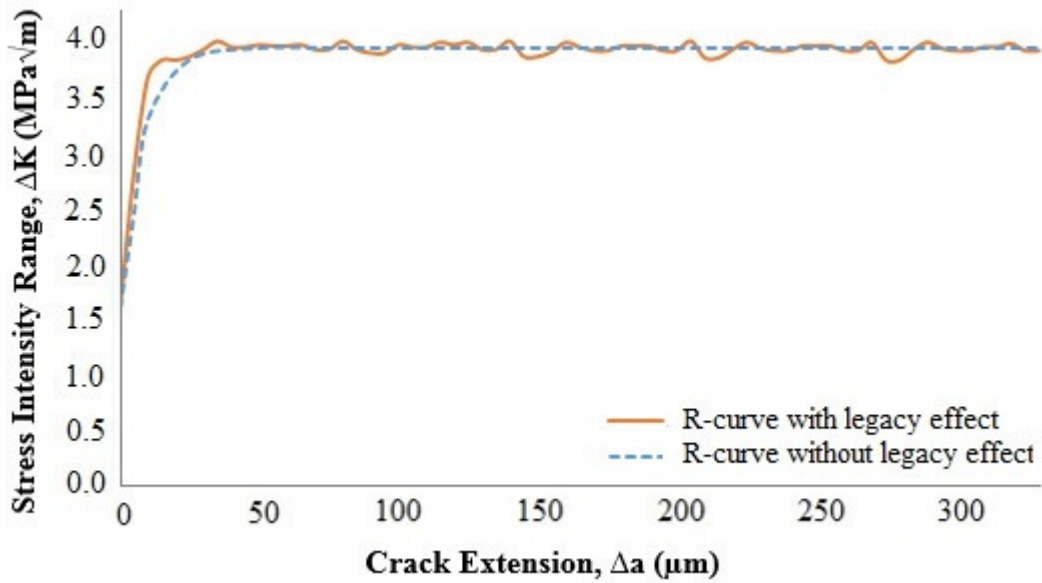


Figure 7.7: Crack growth resistance curve, R-curve, for a superelastic NiTi specimen with an applied load ratio $R=0.1$. Displaying altering stress intensity range, ΔK , with crack extension due to the shifting maximum stress experienced by the crack tip along the crack path in the textured model.

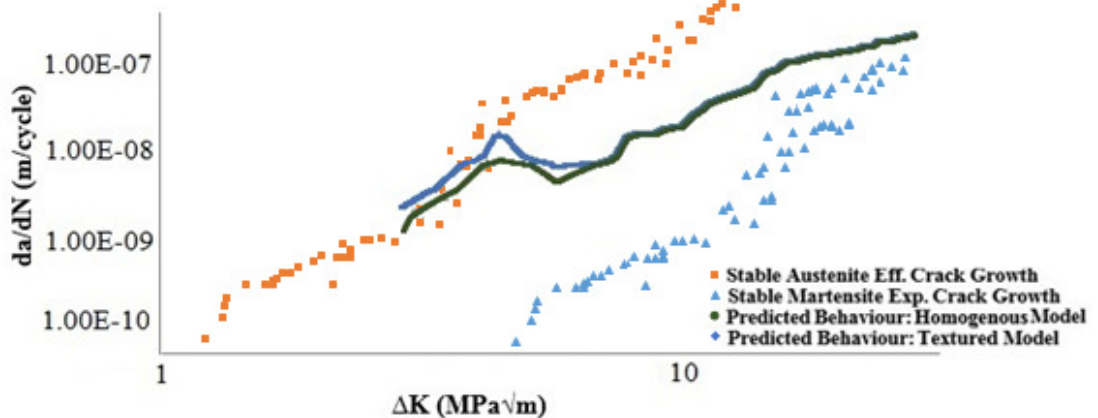


Figure 7.8: Predicted crack fatigue growth rate behaviour generated from FEA models with, and without, textural effects. Both models having an initial defect size $a_0=5\mu\text{m}$, load ratio $R=0.1$ and 600MPa applied far-field stress.

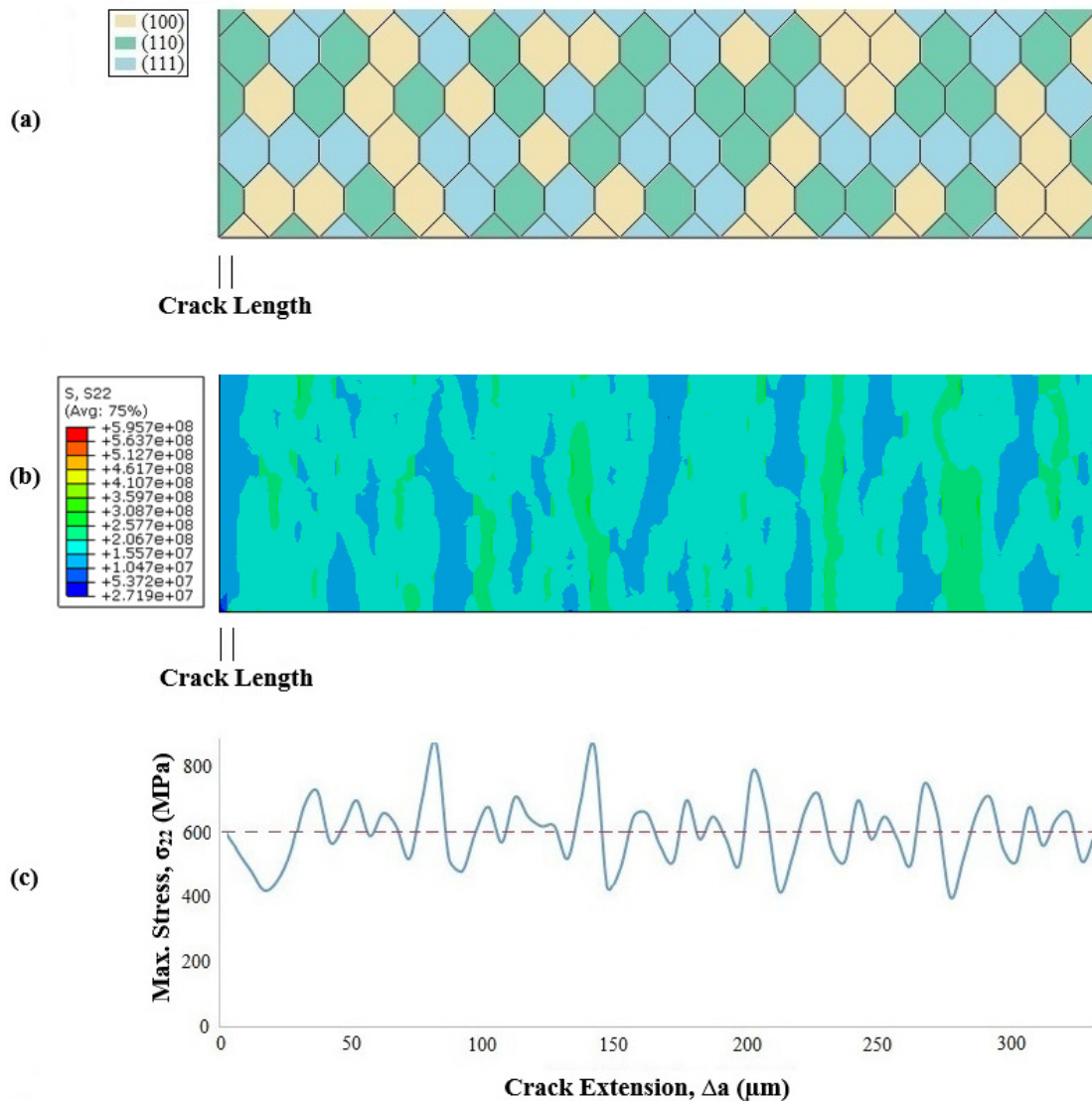


Figure 7.9: Altering material response with varying grain orientation along the crack path for an applied far-field stress of 600MPa: (a) the grain orientations present in the first 350 μm of the crack path displaying a (100) orientated grain at the crack tip, (b) the stress contour plot displaying the non-uniform evolution of the maximum stress (σ_{22}) in the FEA model of the compact tension specimen, and (c) the maximum stress (σ_{22}) extracted along the crack path of the FEA model.

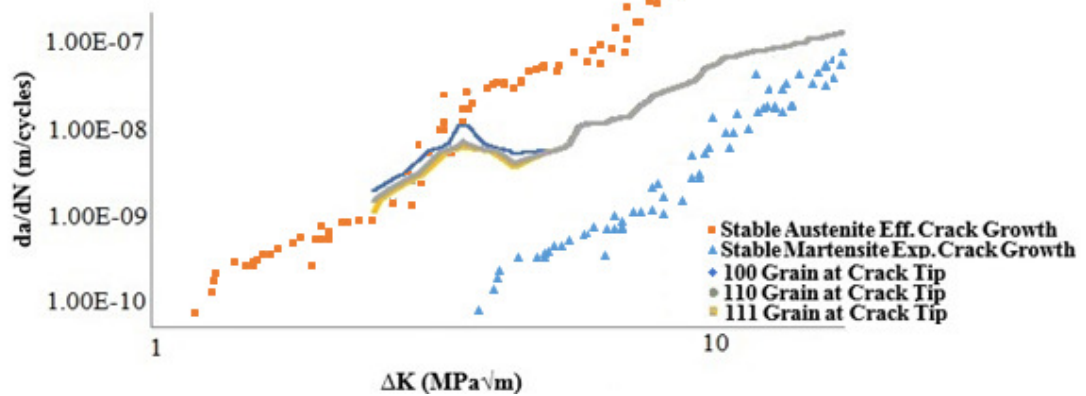


Figure 7.10: Predicted fatigue crack growth rate behaviour generated from FEA model with varying grain orientations at the crack tip. All models have an initial defect size $a_0=5\mu\text{m}$, load ratio $R=0.1$ and 600MPa applied far-field stress.

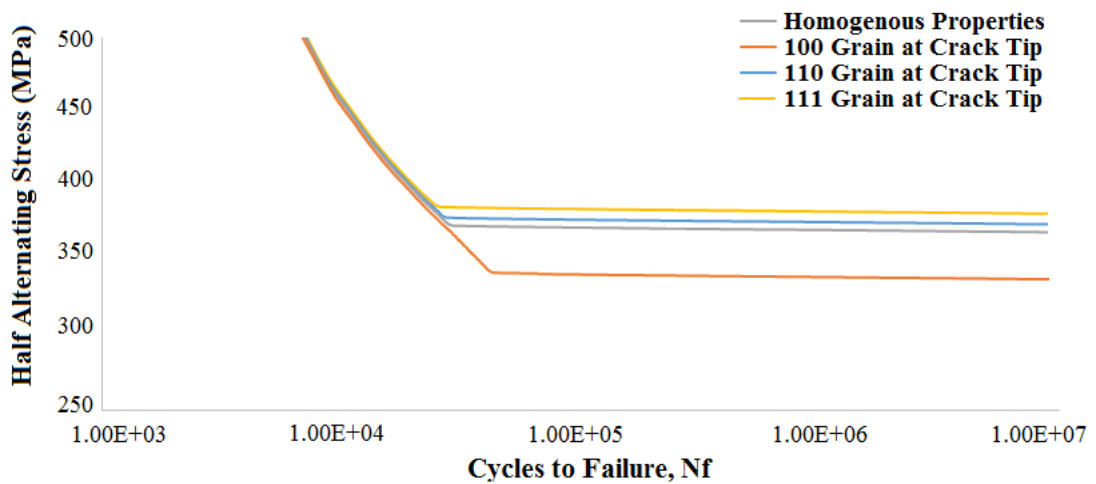


Figure 7.11: Predicted S-N curves generated from FEA models with a (100), (110) and (111) orientated grain at the crack tip, respectively, compared against the predicted S-N curve generated using a continuum model.

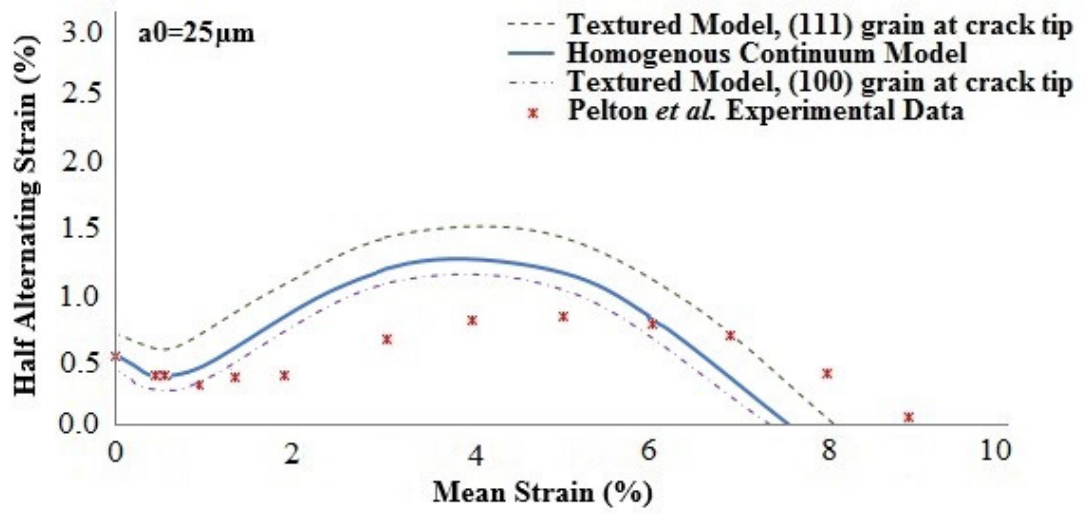


Figure 7.12: Predicted constant life diagram of a superelastic NiTi specimen with an initial defect size $a_0=25\mu\text{m}$, with and without the incorporation of textural effects, compared against the experimental works of [Pelton *et al.*, 2003] and [Pelton *et al.*, 2008].

Chapter 8

Summary of Results and Concluding Remarks

8.1 Objectives of Thesis

The development of computational models to predict the mechanical and fatigue response of superelastic NiTi specimens was presented in this thesis. This work was motivated by the alarming number of NiTi stent device failures reported in literature [Schlager *et al.*, 2005] [Scheinert *et al.*, 2005]. Therefore, the objective of this thesis was to computationally investigate the two major microstructural impacts on NiTi's fundamental mechanical behaviour and overall fatigue performance, namely, microstructural phase (i.e. austenitic and martensitic NiTi) and the grain orientation distribution in a polycrystalline material (i.e. crystallographic texture). Concerns with the current design procedures and protocols that utilise a homogenised material model were highlighted through the comparison of results generated from standard continuum models against those generated from models which incorporated these microstructural features. The overall aim of this work was to provide further understanding into the impact of local microstructural effects on the global mechanical response of superelastic NiTi, which can ultimately lead to a much fuller appreciation of the causes of deviation in the mechanical response from predictions and, thus, of unforeseen failures in NiTi biomedical self-expanding stent devices.

In this thesis, the influence of the individual microstructural phases of NiTi, in addition to its crystallographic texture, were first examined under uniaxial quasi-static tension-compression conditions as a potential indicator of superelastic NiTi's fatigue performance. The influence of the individual microstructural phases of NiTi and its crystallographic texture were subsequently computationally examined with respect to their distinct effect on the fatigue behaviour of superelastic NiTi. A summary of the modelling methodologies employed in this thesis, accompanied by the computational results gathered, are presented in this chapter. To begin with, a discussion is offered in Section 8.2 on the quasi-static tension-compression modelling performed as part of this work. Following this, a discussion is offered in Section 8.3 on the fatigue modelling performed as part of this work. Finally, concluding remarks are offered in

Section 8.4 of this chapter as a closing statement discussing the impact and novelty of the work performed as part of this thesis in the NiTi research field.

8.2 Tensile Modelling

8.2.1 Tensile Modelling Approach

Following conventional computational design practice, the commercially available Finite Element Analysis (FEA) platform ABAQUS™ 6.10 was employed for the computational modelling of NiTi as described in Chapters 4 and 5 of this thesis. To capture the complex phase transformational behaviour of superelastic NiTi, the in-built subroutine UMAT/Nitinol was employed. The experimental procedures performed on suitable superelastic NiTi specimens for the extraction of required input data into the FEA models were described in detail in Chapter 3 of this thesis. As an introduction to the tensile modelling investigations of Chapters 4 and 5, a brief discussion is offered on the basic theories and concepts behind the UMAT/Nitinol in Chapter 4. However for the computational micro-mechanical modelling of Chapter 5, which incorporates the microstructural textural features of the NiTi specimens, a modification of the adopted modelling methodology was necessary. Utilising experimental observations of the stress-strain response of superelastic NiTi single crystals by [Gall *et al.* 1998], the 15 required material parameters were successfully extracted for use in the in-built UMAT/Nitinol for various crystallographic grain orientations. Following this, each grain in the FEA models of Chapter 5 was assumed to have homogenous material behaviour which was dependent on the grain's orientation with respect to the global loading direction. In this way, the anisotropic granular transformational behaviour of the NiTi specimen was effectively captured in the model with the computational efficiency of continuum mechanics.

8.2.2 Effect of Microstructural Phase on NiTi's Tensile Behaviour

Chapter 4 of this thesis computationally examined the influence of the individual microstructural phases of NiTi, in particular stress-induced martensite (SIM), under quasi-static compressive conditions as a potential indicator of the fatigue performance

of superelastic NiTi. The aim of this chapter was to establish a correlation between the volume fraction of SIM in a ‘v-strut’ stent subcomponent specimen and its overall macroscopic material response. The use of a 3-D continuum model incorporating the UMAT/Nitinol in this chapter allows for the analysis of the evolutionary transformational behaviour of the NiTi specimen at various imposed displacements; those being representative of physiologically relevant strains. It was established, as the imposed compressive strain levels in the ‘v-strut’ stent subcomponent increase, the volume fraction of SIM exhibited correspondingly increases. The percentage volume fraction of SIM extracted from the critical location of potential fatigue failure, i.e. the peak principal tensile stress located on the outer apex of the ‘v-strut’ specimen, was shown to follow a similar trend to that of the experimentally established constant life diagram for superelastic NiTi. As with the observed increasing fatigue performance, the extracted volume fraction of SIM was shown to increase in value within the approximate 2-6% mean strain range. Furthermore, the observed improvement of fatigue performance observed in the experimentally established constant life diagram was shown to correlate with the on-set of SIM in the tensile stress-strain curve of the NiTi support strut of the ‘v-strut’ stent subcomponent specimen at approximately the 2% mean strain level. It was therefore hypothesised that there was a strong connection relating SIM and the unusual fatigue behaviour of superelastic NiTi.

8.2.3 Effect of Crystallographic Texture on NiTi’s Tensile Behaviour

Chapter 5 of this thesis examined the influence of crystallographic texture on the quasi-static tensile behaviour of superelastic NiTi specimens. The aim of this chapter was to highlight concerns with the current design practice of simply utilising a continuum model (as adopted in Chapter 4) through the development of a more complex micro-mechanical model which incorporated the effects of texture. Firstly, a 2-D rectangular model incorporating a realistic representation of the microstructure identified in a superelastic NiTi micro-dogbone specimen was created to determine the microscopic influence of individual crystallographic grain orientations on NiTi’s transformational behaviour. Secondly, 2-D rectangular and ‘v-strut’ models

incorporating an idealised hexagonal unit cell representation of the microstructure identified in the support strut of the ‘v-strut’ stent subcomponent specimen were created to investigate the effect of multiple randomly generated textures on the macroscopic stress-strain response of superelastic NiTi. Crystallographic texture was confirmed to have a marked influence on the mechanical response of NiTi by either limiting or promoting the phase transformation. Due to the varying granular transformational behaviour for each of the crystallographic orientations, in addition to the inherent precipitates found in the specimen, strain gradients and areas of strain banding were captured in the model results. It was confirmed, through the combined analysis of stress/strain contours and the volume fraction of SIM, that grains orientated in the (100) direction inhibit the stress-induced martensite transformation (SIMT) while grains in the (111) direction promote the SIMT. The resulting non-uniform evolution of stresses in the specimen was shown to induce discrete locations of peak tensile stresses which were identified as possible locations of failure in the ‘v-strut’ specimen. It was clarified that altering the grain orientation at this critical location in the ‘v-strut’ model results in significant variations to the SIMT evolutionary profile and thus has a potentially substantial effect on the fatigue life of a stent device. The largest deviation from the expected material behaviour was due to the presence of a (100) orientated grain at the identified critical site for fatigue failure; when compared to the presence of a (110) or (111) orientated grain. Crystallographic texture, therefore, was confirmed to cause material behaviour of the superelastic NiTi material to deviate significantly from the expected material behaviour. This scatter in material response, which can be attributed to the varying crystallographic textures, provides a possible explanation for the observed scatter in experimental fatigue testing due to the inherently textured nature of the specimens.

8.3 Fatigue Modelling

8.3.1 Fatigue Modelling Approach

Before details were offered with respect to the development of a computational model to predict the fatigue behaviour of superelastic NiTi, a review of the fatigue of

metals was first presented in Chapter 2. Only aspects relating to a defect tolerant approach to fatigue analysis were discussed, in that, it is assumed that engineering components are inherently flawed and the useful fatigue life of a component is defined as the number of cycles to propagate an initial dominant flaw in the material to failure. The characterisation of the stress-state ahead of this dominant crack in a body subject to an applied far-field stress was discussed using linear elastic fracture mechanics (LEFM) and elastic-plastic fracture mechanics (EPFM). The concept of fatigue crack closure was also introduced in this chapter with an outline of the mechanics of plasticity-induced and transformation-induced crack closure. Phase transformation-induced plasticity (TRIP) crack closure was discussed as this is the dominant closure mechanism in the phase transforming superelastic NiTi material. The quantification of fatigue crack closure by the R-curve method was offered and, finally, a discussion on the ‘small crack problem’ and the ability of crack closure to explain the so-called anomalous growth behaviour of a small crack was presented. It was concluded that, for the most accurate prediction of NiTi’s fatigue life, a complete defect tolerant approach to fatigue modelling employed in this work should include small crack effects and the evolution of fatigue crack closure. The stable austenitic and martensitic NiTi materials were assumed to behave as typical engineering materials with conventional elastic-plastic behaviour. All tensile and fatigue material properties such as the uniaxial tension-compression curves, fatigue crack growth rate behaviours and fatigue crack resistance properties were extracted from previously published studies completed in the literature, namely, from the works of [McKelvey and Ritchie, 2001], [Robertson and Ritchie, 2007] and [Holtz *et al.*, 1999].

8.3.2 Effect of Microstructural Phase on NiTi’s Fatigue Behaviour

The development of a fatigue modelling methodology using a defect tolerant approach, based on the work of [Bruzzi and McHugh, 2002], was described in Chapter 6. The methodology involved the incremental modelling of the growth behaviour of an initial small crack propagating to a threshold for failure with evolving crack closure. The crack tip driving force conditions were characterised for each crack length through

the use of the elastic-plastic fracture mechanics (EPFM) parameter, ΔJ_{eff} , which was calculated through a combination of an analytical and FEA modelling approach. Fatigue crack closure was quantified through the use of the stress range ratio, U , and the appropriate generated R-curve for a given loading condition. Once calculated, ΔJ_{eff} was then correlated with a calculated effective crack growth rate curve to give the crack growth increment per cycle, da/dN . Utilising the characteristic parameters of the two microstructural phases of NiTi, and modifying the methodology of Bruzzi *et al.* to include the rule of mixtures, the fatigue behaviour of superelastic NiTi was also successfully investigated. The objective of this chapter was to examine the fatigue behaviour of the two microstructural phases of NiTi individually, i.e. stable austenitic and stable martensitic NiTi, in order to present a possible explanation towards the unusual fatigue behaviour of superelastic NiTi of increasing fatigue performance with increasing mean strain which is in stark contrast to the fatigue behaviour of typical engineering materials.

Crack growth rate curves for initial small crack sizes ranging from 5 to 25 μ m were predicted for stable austenitic, martensitic and superelastic NiTi specimens for different nominally applied stress ranges. The general trend of the crack growth behaviour for the three microstructural phases were shown to be relatively similar. For varying applied stress ranges, the small crack was shown to either arrest (due to increasing levels of crack closure) or propagate to failure. Subsequently, the number of cycles for a small crack to propagate to failure was calculated for a given initial defect size at different stress levels for an R-ratio of -1, 0 and 0.1-0.7 for each of the material microstructural phases. The generated S-N curve trend of stable austenite and martensite was shown to offer a good prediction to the limited published experimental S-N behaviour in the literature for an appropriate choice of 5 μ m initial defect size. The endurance limit extracted from S-N curves are correlated to the propagation or non-propagation of the initial crack to failure and, in compiling the endurance limits generated for various R-ratios, it allows for the construction of the constant life diagram. This constant life diagram is employed during the design process of a biomedical stent device using a fail/no-fail approach based on the propagation/non-

propagation of a crack to failure within, typically, 400 million cycles to ensure a safe device design is achieved. Examining the generated constant life diagrams for stable austenitic, stable martensitic and superelastic NiTi for a 5 μ m defect size, it appears to be the shift from the austenitic to martensitic fatigue behaviour that results in the increased fatigue performance of superelastic NiTi. It was hypothesised that the transformation from the austenitic to martensitic NiTi fatigue behaviour, i.e. SIMT, underpins superelastic NiTi's unique behaviour of increasing fatigue performance with increasing mean strain.

8.3.3 Effect of Crystallographic Texture on NiTi's Fatigue Behaviour

As it is the fatigue response of inherently textured materials that is of greatest interest for medical device applications, Chapter 7 of this thesis explicitly examined the influence of crystallographic texture on the fatigue behaviour of polycrystalline superelastic NiTi specimens. The aim of this chapter was to further develop the fatigue modelling methodology of Chapter 6 to incorporate the effects of texture in order to highlight the necessity of including such fundamental micro-mechanical effects in a material model for the most accurate prediction of fatigue behaviour. This was achieved through the incorporation of a realistic and idealised representation of NiTi's microstructural features in the FEA model used to simulate the crack tip conditions for the calculation of the EPFM parameter, ΔJ_{eff} , for the superelastic NiTi compact tension specimen under given loading conditions. Following the modelling methodology of Chapter 5, and the experimental stress-strain curves for individual grains of varying crystallographic orientations of [Gall *et al.*, 1998], the macro-scale anisotropic granular behaviour of the polycrystalline material was effectively captured in the models. A comparative study was subsequently performed on the computationally derived predictions of fatigue life for a superelastic NiTi specimen, considering the material as (1) a continuum material with homogenous behaviour using the results of Chapter 6, and (2) a textured polycrystalline material with anisotropic granular behaviour using the results generated in Chapter 7.

In comparing the fatigue crack growth behaviour predicted by the continuum model and the textured model, with an idealised representation of the specimen's microstructure for a superelastic NiTi specimen, both with an initial defect size of $a_0=5\mu\text{m}$, an applied far-field stress of 600MPa and a load ratio of $R=0.1$, different results were identified. This was attributed to the varying grain orientations located along the crack path in the textured model thus having a different material response to that of the continuum model for the same applied stress. The resulting varying levels of maximum stress experienced by the crack tip with crack extension result in different stress intensity ranges, ΔK , at the advancing crack tip which ultimately alters the driving force for fatigue crack growth. Furthermore, in allocating a different grain orientation at the initial crack tip in the textured model for the same specimen and loading conditions, the resulting fatigue crack growth rate behaviour was shown to be significantly altered. It was found that the number of cycles for failure, N_f , using the continuum model and the textured models with (100), (110) and (111) orientated grains at the crack tip were predicted as 16,952, 15,501, 16,896 and 17,151 cycles, respectively, for the aforementioned specimen and loading conditions. The largest deviation from the expected behaviour predicted by the continuum model was illustrated to be due to the presence of a (100) orientated grain at the crack tip which, in Chapter 5, was shown to inhibit SIMT. As martensite is shown to have a superior fatigue crack growth resistance compared to austenite [McKelvey and Ritchie, 2001], it confirms the trend suggested by the generated results of this chapter which illustrated that the fatigue crack growth rate behaviour was dependent on the microstructural phase surrounding the crack tip and that longest fatigue lives were demonstrated in situations where the martensite phase was stress-induced at the crack tip. As the fatigue performance of the superelastic NiTi specimen was shown to be dependent on the particular grain orientation present at the crack tip, this work offers an explanation to the observed scatter in fatigue data due to the inherently textured nature of experimental specimens.

In this way, it was confirmed that a potentially non-conservative prediction of fatigue life may result from material models which neglect microstructural effects.

This may have serious consequences with respect to the prediction of endurance limits and therefore in the construction of the material's characteristic constant life diagram for the safe design of biomedical stent devices. For example, the endurance limit predicted using the continuum model in Chapter 6 was identified as 397MPa for a superelastic NiTi specimen with initial defect size of 5 μ m, load ratio of R=0.1 and an applied far-field stress of 600MPa, while the predicted endurance limit using the textured model with a (100) grain at the crack tip for the same conditions was identified as a much lower 340MPa. This, as a result, may lead to serious non-conservative decisions begin made during the design process of commercial devices such as NiTi self-expanding stents due to the construction of inaccurate constant life diagrams. This was explicitly demonstrated in the comparison of the constant life diagrams generated using the continuum model of Chapter 6 and the textural models of this chapter with either a (100) or (111) orientated grains located at the crack tip for a specimen with a 25 μ m initial defect size. It was confirmed that the continuum model of Chapter 6 may result in non-conservative predictions of safe working loads and thus may explain unanticipated device failures observed *in vivo* with potential injury, or even death, occurring to the patient as a result.

8.4 Concluding Remarks

Superelastic NiTi self-expanding stents push the boundaries of our current knowledge and understanding of material behaviour which ultimately influences the design of biomedical devices. In particular, the influence of microstructure on the fatigue behaviour of NiTi is not well understood in published literature available to date. Therefore, the objective of this thesis was to computationally investigate the effect of the two major microstructural influences on NiTi's fundamental mechanical behaviour and fatigue performance, namely, the microstructural phases of NiTi and its inherent crystallographic texture. This was achieved through computational modelling using the commercially available FEA platform ABAQUS™, using geometrically relevant specimens, and physiologically applicable stresses and strains. The influence of microstructural phase and crystallographic texture was first examined under quasi-

static tensile-compression conditions as a potential indicator of superelastic NiTi's fatigue performance. Subsequently, the fatigue behaviour of superelastic NiTi was examined using fatigue modelling methodologies incorporating the microstructural effects introduced by varying microstructural phases and crystallographic texture.

The computational studies performed as part of this research successfully achieve the objectives set out in this thesis. Through the individual examination of the behaviour of both austenitic and martensitic NiTi, a potential explanation towards the unusual fatigue behaviour of superelastic NiTi was offered. It was confirmed there exists a strong association between the SIM phase and the observed fatigue behaviour of superelastic NiTi. It was determined that the strain at which the SIM initiates in a stent subcomponent specimen corresponds with the observed initiation of increased fatigue behaviour of superelastic NiTi at 2% mean strain. Furthermore, the trend of increasing volume fraction of SIM found in the specimen follows that of the trend of increasing fatigue behaviour of superelastic NiTi in the 2-6% mean strain range. It was also established that martensitic NiTi has a superior fatigue performance when compared to austenitic NiTi; an approximate 700% increase in the endurance limit was predicted for a given specimen when modelled using martensitic NiTi material data compared to austenitic NiTi data. It was therefore proposed that the shift from the austenitic to martensitic NiTi fatigue behaviour, attributed to SIMT, results in the unusual characteristic increased fatigue performance behaviour of superelastic NiTi with increasing mean strain. From this research, a much fuller understanding of the local microstructural effects of individual phases on the global mechanical response of superelastic NiTi was successfully obtained.

The second objective of this thesis involved explicitly examining the effect of crystallographic texture on the fundamental fatigue behaviour of superelastic NiTi to highlight concerns with current design procedures for biomedical stent devices. The novelty of this work lies in the development of a mechanical and fatigue modelling approach to fully capture the complex anisotropic granular transformational behaviour of the polycrystalline superelastic NiTi specimen with the computational efficiency of

a continuum mechanics approach. Crystallographic texture was determined to cause a scatter of approximately 23% in the predicted fatigue endurance limits of a superelastic NiTi specimen, employing a 'worst-case-scenario' approach, when compared to that predicted simply using homogeneous material properties. From this research, it is proposed that the conventional use of continuum homogenous material properties alone prove inadequate to fully describe the complex material behaviour of superelastic NiTi. In order to avoid inaccurate fatigue behaviour assumptions, which may lead to potentially detrimental stent device designs, it is suggested that current design protocols in the biomedical device industry are amended. At this time, it is standard practice to complete computational numerical modelling analysis in combination with *in vitro* experimental testing to determine the safe design of a biomedical stent device. However from the results generated in this research it is suggested that the traditional computational numerical material models, which assume homogenous continuum material behaviour, are amended to incorporate a 'worst-case-scenario' effect of microstructural features such as crystallographic texture. In this way, for stent devices which typically have specimen dimensions less than 500 μm , the true potential effect of the specimen's microstructure can be taken into account. It is suggested that a more conservative approach is adopted to the computational analysis portion of the design procedure for the continued safe use of NiTi biomedical devices.

8.5 References

Bruzzi M.S. and McHugh P.E., Methodology for Modelling the Small Crack Fatigue Behaviour of Aluminium Alloys, *International Journal of Fatigue*, 2002, **24**, p 1071–1078.

Gall K., Sehitoglu H., Chumlyyakov Y.I. and Kireeva I.V., Tension-Compression Asymmetry of the Stress-Strain Response in Aged Single Crystal and Polycrystalline NiTi, *Acta Metallurgica*, 1998, **47**, p 1203–1217.

Holtz R.L., Sadananda K. and Imam M.A., Fatigue Thresholds of Ni-Ti alloys near the Shape Memory Transition Temperatures, *International Journal of Fatigue*, 1999, **21**, p 137-145.

McKelvey A.L. and Ritchie R.O., Fatigue-Crack Growth Behavior in the Superelastic and Shape-Memory Alloy Nitinol, *Metallurgical and Material Transactions A*, 2001, **32**, p 731-743.

Robertson S.W. and Ritchie R.O., In-vitro Fatigue–Crack Growth and Fracture Toughness Behavior of Thin-Walled Superelastic Nitinol Tube for Endovascular Stents: A Basis for Defining the Effect of Crack-like Defects, *Biomaterials*, 2007, **28**, p 700–709.

Schlager O., Dick P., Sabeti S., Amighi J., Mlekusch W., Minar E. and Schillinger M., Long-segment SFA Stenting - The dark sides: In-stent Restenosis, Clinical Deterioration, and Stent Fractures, *Journal of Endovascular Therapy*, 2005, **12**, p 676-684.

Scheinert D., Scheinert S., Sax. J., Piorkowski C., Braunlich S., Ulrich M., Biamino G. and Schmidt A., Prevalence and Clinical Impact of Stent Fractures after Femoropopliteal Stenting. *Journal of the American College of Cardiology*, 2005, **45**, p 312–315.

Appendix A

Case 1: Austenite Load-Unloading

$$0 \leq \sigma < \sigma_L^S \text{ to } 0 \leq \sigma \leq \sigma_L^S$$

Table A.1: Identification of Case 1 loading condition (Austenite).

R-ratio	Max. Stress Range
-1	100-390 MPa
0	100-390 MPa
0.1	100-390 MPa
0.2	100-390 MPa
0.3	100-390 MPa
0.4	100-390 MPa
0.5	100-390 MPa
0.6	100-390 MPa
0.7	100-390 MPa

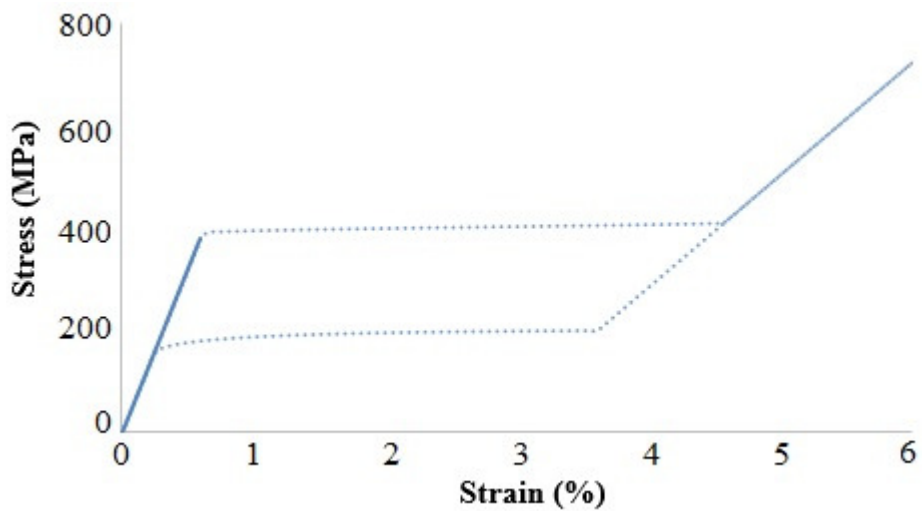


Figure A.1: Identification of Case 1 loading condition (Austenite).

Case 2: Austenite-to-Plateau Load-Unloading

$$0 \leq \sigma < \sigma_{UL}^E \text{ to } \sigma_L^s < \sigma < \sigma_L^E$$

Table A.2: Identification of Case 2 loading condition (Austenite-to-Plateau).

R-ratio	Max. Stress Range
-1	391-409 MPa
0	391-409 MPa
0.1	391-409 MPa
0.2	391-409 MPa
0.3	391-409 MPa
0.4	x
0.5	x
0.6	x
0.7	x

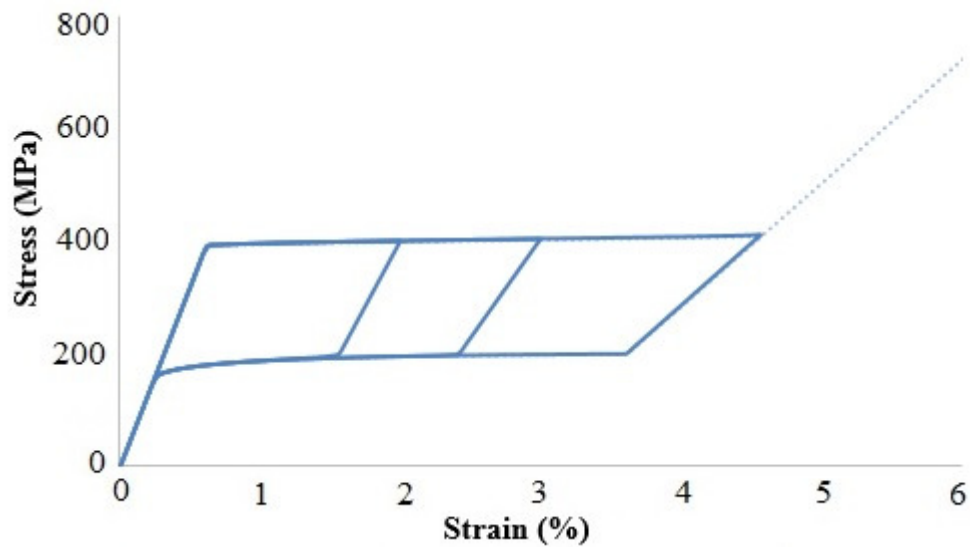


Figure A.2: Identification of Case 2 loading condition (Austenite-to-Plateau).

Case 3: Plateau Load-Unloading

$$\sigma_{UL}^E < \sigma < \sigma_{UL}^S \text{ to } \sigma_L^S < \sigma < \sigma_L^E$$

Table A.3: Identification of Case 3 loading condition (Plateau).

R-ratio	Max. Stress Range
-1	x
0	x
0.1	x
0.2	x
0.3	x
0.4	391 – 409 MPa
0.5	391 – 399 MPa
0.6	x
0.7	x

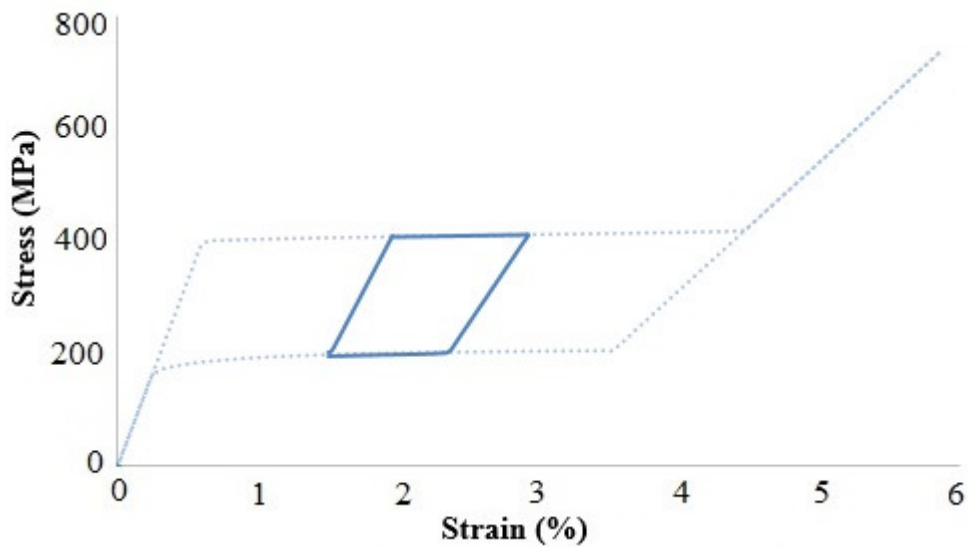


Figure A.3: Identification of Case 3 loading condition (Plateau).

Case 4: Plateau Load-Unloading

$$0 \leq \sigma < \sigma_L^E \text{ to } \sigma_{UL}^S < \sigma < \sigma_L^E$$

Table A.4: Identification of Case 4 loading condition (Plateau).

R-ratio	Max. Stress Range
-1	x
0	x
0.1	x
0.2	x
0.3	x
0.4	x
0.5	400 – 409 MPa
0.6	391 – 409 MPa
0.7	391 – 409 MPa

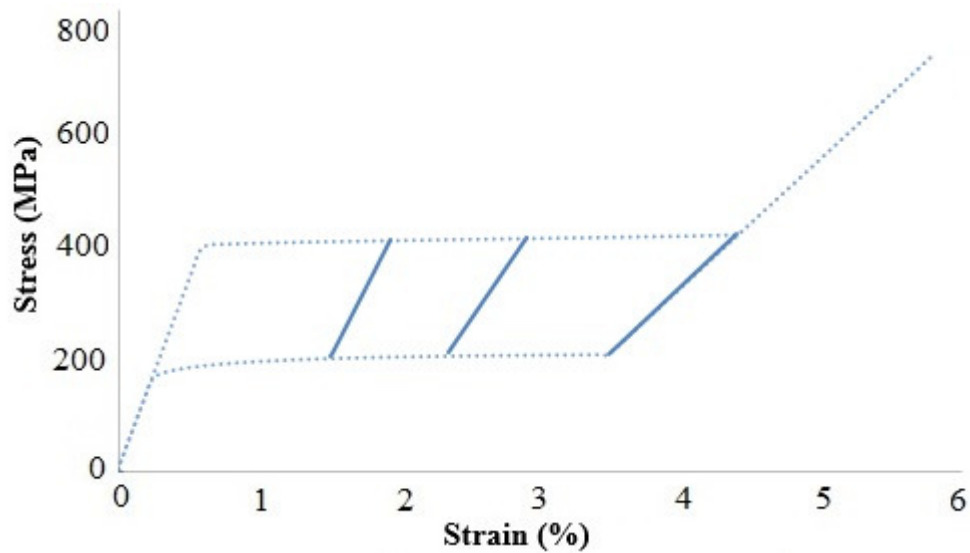


Figure A.4: Identification of Case 4 loading condition (Plateau).

Case 5: Plateau-to-Martensite Load-Unloading

$$\sigma_L^S \leq \sigma \leq \sigma_{UL}^S \text{ to } \sigma_L^E < \sigma$$

Table A.5: Identification of Case 5 loading condition (Plateau-to-Martensite).

R-ratio	Max. Stress Range
-1	x
0	x
0.1	x
0.2	780 – 990 MPa
0.3	520 – 660 MPa
0.4	410 – 490 MPa
0.5	x
0.6	x
0.7	x

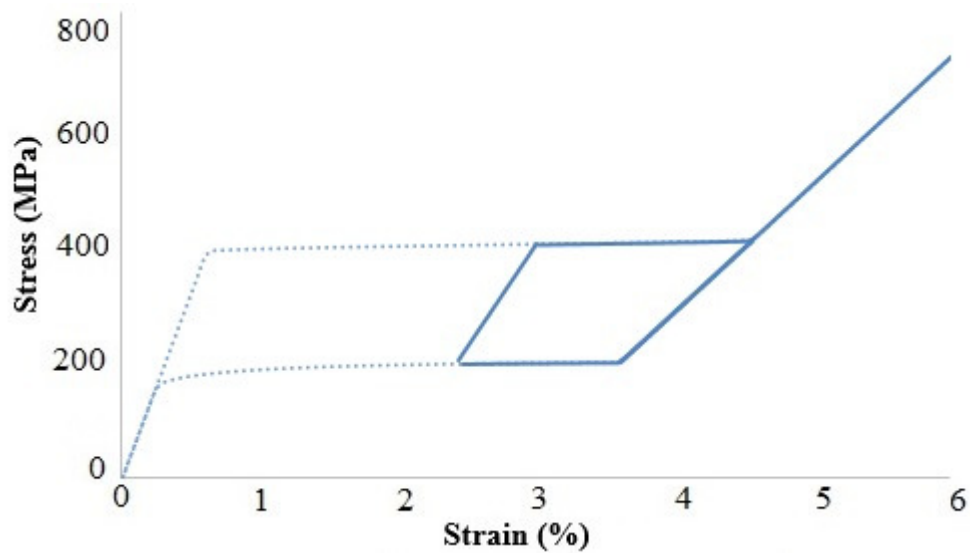


Figure A.5: Identification of Case 5 loading condition (Plateau-to-Martensite).

Case 6: Martenite Load-Unloading

$$\sigma_{UL}^S < \sigma \text{ to } \sigma_L^E < \sigma$$

Table A.6: Identification of Case 6 loading condition (Martensite).

R-ratio	Max. Stress Range
-1	x
0	x
0.1	x
0.2	1000 – 1500 MPa
0.3	670 – 1500 MPa
0.4	500 – 1500 MPa
0.5	410 – 1500 MPa
0.6	410 – 1500 MPa
0.7	410 – 1500 MPa

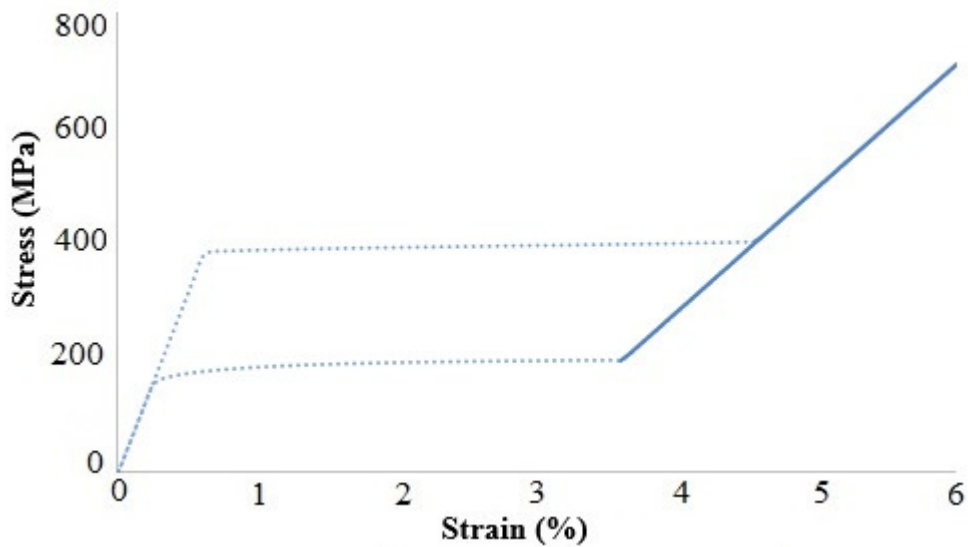


Figure A.6: Identification of Case 6 loading condition (Martensite).

Case 7: Austenite-to-Martensite Load-Unloading

$$0 \leq \sigma < \sigma_L^S \text{ to } \sigma_L^E < \sigma$$

Table A.7: Identification of Case 7 loading condition (Austenite-to-Martensite).

R-ratio	Max. Stress Range
-1	410 – 1500 MPa
0	410 – 1500 MPa
0.1	410 – 1500 MPa
0.2	410 – 770 MPa
0.3	410 – 510 MPa
0.4	x
0.5	x
0.6	x
0.7	x

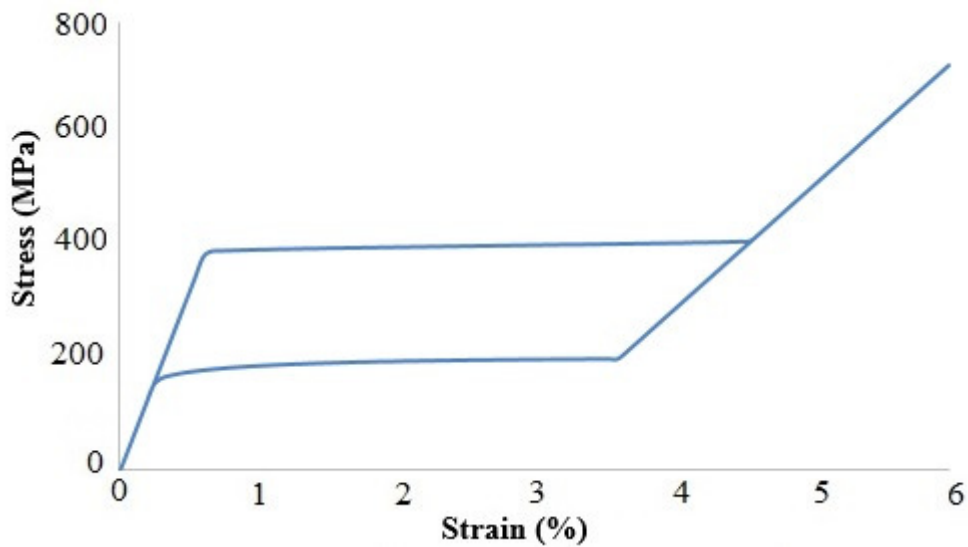


Figure A.7: Identification of Case 7 loading condition (Austenite-to-Martensite).

Appendix B

! Program for calculating the stress-life of austenitic or martensitic NiTi using crack closure

Program AusteniticNiTi_R=0

Implicit None

Real :: p1, p2, p3, h1, pi, E, mew, n, sra, alpha, s0, e0, a0, &

& sth, scl, b1, b3, dkeff, dJeff, da, aext, ai, dkmax, U, dkth, &

& smax, smin, ds, st, sthlc, scllc, Ulc, d, dan, deltak, splot, Jmax

Real, Dimension (191) :: stress, J

Real, Dimension (102) :: a, dk0

Real, Dimension (113) :: dk, dadn, dkn

Integer :: i, nf

! Opening files, reading in data (s0 and E in Pa)

Open(10, file='parameters.txt')

Read(10,*) alpha, n, s0, e0, E, mew

! Defining starting defect size and R-ratio (a0 in m), defining pi

a0 = 5.0E-06

pi = 4*atan(1.0)

! Opening and reading J integral data

Open(20, file='stress-jintegral5.txt')

Do 21 i=1,191

 Read(20,*) stress(i), J(i)

21 Continue

! Opening and reading da-dk0 data (in m and Pa.m^{1/2})

Open(30, file='da-dk0R0.txt')

Do 22 i=1,102

Read(30,*) a(i), dk0(i)

22 Continue

! Opening and reading growth rate curve data (in Pa.m^{1/2} and m/cycle)

Open(40, file='long-crackR0.txt')

Do 23 i=1,113

Read(40,*) dk(i), dadn(i)

23 Continue

Open(unit=18, file='S-N a0=5um R=0.txt', status='unknown')

Do 100

st=1000.0, 100.0, -5.0

! Converting the stresses to MPa

smax = st*1.0E+06

smin = 0.0

sra = (smax/s0)

ds = smax – smin

! Finding correct J for corresponding maximum stress

Do 24 i=1,191

 If (stress(i)==smax) then

 Jmax = J(i)

 End if

24 Continue

! Initialising parameters

 da = 0.0

 dan = 0.0

 nf = 0

 ai = a0

! Calculating new Crack Extension

7 ai = ai + da

 aext = ai - a0

! Calculating J-integral to find h1 constant

 p1 = (1.12*smax*sqrt(pi))**2/(E/(1-mew**2))

 p2 = 1+((1.12**2)*(n-1)*(sra**2))/(6.0*(n+1)*(1+sra**2))

 p3 = alpha*s0*e0*(sra**(n+1))

 h1 = (Jmax - p1*p2)/p3

! Calculating Stress Intensity Threshold, dkth

Do 25 i=1,102

If ((aext > a(i)).AND.(aext < a(i+1))) Then

dkth = dk0(i)+((aext-a(i))/(a(i+1)-a(i)))*(dk0(i+1)-dk0(i))

End if

25 Continue

! Calculating U

sth = dkth/(1.12*sqrt(pi*ai)*(1-(smin/smax)))

scl = sth - dk0(1)/(1.12*sqrt(pi*ai))

U = (sth - scl)/(sth - (smin/smax)*sth)

! Calculating dJeff and dKeff

b1 = ((U*1.12*ds*sqrt(pi*ai))**2)/(E/(1-mew**2))

b3 = alpha*s0*e0*ai*h1*U*((ds/(2*s0))**(n+1))

dJeff = b1*p2 + b3

dkeff = sqrt(dJeff*E/(1-mew**2))

! Calculating U

sthlc = dk0(102)/(1.12*sqrt(pi*ai)*(1-(smin/smax)))

scllc = sthlc - dk0(1)/(1.12*sqrt(pi*ai))

Ulc = (sthlc - scllc)/(sthlc - (smin/smax)*sthlc)

! Factor out crack closure, and plot if no growth or reached max

Do 26 i=1,113

 dkn(i) = dk(i)*Ulc

26 Continue

Do 27 i=1,113

 If ((dkeff > dkn(i)).AND.(dkeff < dkn(i+1))) then

 d = (dkeff-dkn(i))/(dkn(i+1)-dkn(i))

 dan = 10**(log10(dadn(i))+d*(log10(dadn(i+1))-log10(dadn(i))))

 goto 28

 elseif (dkeff < dkn(1)) then

 dan = dadn(1)

 End if

27 Continue

! Convert back to MPa valves for Dk

28 deltak = 1.12*ds*sqrt(pi*ai)*1.0E-6

Open(unit=14, file='dadn vs dk curve a0=5um R=0.txt', status='unknown')

Write(14,*) deltak, dan

! Convert back to MPa/mm values

 splot = smax*1.0E-6

 da = dan

 dkmax = dk(113)*1.0E-6

! Calculating Nf and plotting results

 If (dan == dadn(1)) then

 nf = 1.0E+7

 Print *, "NO CRACK GROWTH"

 Goto 35

 Elseif (deltak > dkmax) then

 Print *, "REACHED MAX"

 Goto 30

 End if

nf = nf + 1

Print *, "nf = ",nf

Goto 7

30 If (nf > 1.0E+7) then

 Print *, "REACHED RUNOUT"

 Goto 35

 End if

100 Write(18,*) "for stress max, nf = ", st, nf

Continue

35 EndProgram AusteniticNiTi_R=0

Appendix C

! Program for calculating the stress-life of superelastic NiTi using crack closure for Case 7 loading-unloading (austenite-to-martensite)

Program SE_CASE7

Implicit None

Real :: p1, p2, p3, h1, pi, E, mew, n, sra, alpha, s0, e0, a0, &

& sth, scl, b1, b3, dkeff, dJeff, da, aext, ai, dkmax, U, dkth, &

& smax, smin, ds, st, sthlc, scllc, Ulc, d, dan, deltak, splot, Jmax

Real, Dimension (191) :: stress, J

Real, Dimension (98) :: a, dk0

Real, Dimension (102) :: dk, dadn, dkn

Integer :: i, nf

! Defining starting defect size and R-ratio (a0 in m), defining pi

a0 = 5.0E-06

pi = 4*atan(1.0)

! Initialising parameters

da = 0.0

dan = 0.0

nf = 0

ai = a0

! Opening and reading J integral data

Open(20, file='stress-jintegral5.txt')

```
Do 21 i=1,191
```

```
    Read(20,*) stress(i), J(i)
```

```
21    Continue
```

```
Open(unit=18, file='S-N a0=5um R=0.3 CASE7 410-510MPa.txt', status='unknown')
```

```
Do 100 st=410.0, 510.0, 5.0
```

```
! Converting the stresses to MPa
```

```
    smax = st*1.0E+06
```

```
    smin = 0.3*st*1.0E+06
```

```
! Testing for CASE 7
```

```
    If (smax >= 410.0E+06 .AND. smin <= 155.0E+06) Then
```

```
        Print *, "CASE 7"
```

```
! Finding correct J for corresponding stress
```

```
Do 24 i=1,191
```

```
    If (stress(i)==smax) then
```

```
        Jmax = J(i)
```

```
    End if
```

```
24    Continue
```

```
!Opening files, reading in input data
```

```
Open(30, file='da-dK0R03.txt')
```

```
Do 32 i=1,98
```

```

        Read(30,*) a(i), dk0(i)
32    Continue

Open(40, file='long-crackR03.txt')
Do 33 i=1,102
        Read(40,*) dk(i), dadn(i)
33    Continue

Open(10, file='parametersMAR.txt')
Read(10,*) alpha, n, s0, e0, E, mew
        da = 1.711472E-09
        dan = da
        End if

sra = (smax/s0)
ds = smax - smin

! Calculating new crack extension
7    ai = ai + da
        aext = ai - a0

! Calculating J-integral to find h1 constant
        p1 = (1.12*smax*sqrt(pi))**2/(E/(1-mew**2))
        p2 = 1+((1.12**2)*(n-1)*(sra**2))/(6.0*(n+1)*(1+sra**2))

```

$$p3 = \alpha * s0 * e0 * (sra ** (n+1))$$

$$h1 = (Jmax - p1 * p2) / p3$$

! Calculating Stress Intensity Threshold, dkth

Do 25 i=1,98

If ((aext > a(i)).AND.(aext < a(i+1))) Then

$$dkth = dk0(i) + ((aext - a(i)) / (a(i+1) - a(i))) * (dk0(i+1) - dk0(i))$$

End if

25 Continue

! Calculating U

$$sth = dkth / (1.12 * \sqrt{\pi * ai} * (1 - (smin / smax)))$$

$$scl = sth - dk0(1) / (1.12 * \sqrt{\pi * ai})$$

$$U = (sth - scl) / (sth - (smin / smax) * sth)$$

! Calculating dJeff and dKeff

$$b1 = ((U * 1.12 * ds * \sqrt{\pi * ai}) ** 2) / (E / (1 - mew ** 2))$$

$$b3 = \alpha * s0 * e0 * ai * h1 * U * ((ds / (2 * s0)) ** (n+1))$$

$$dJeff = b1 * p2 + b3$$

$$dkeff = \sqrt{dJeff * E / (1 - mew ** 2)}$$

! Calculating U

$$sthlc = dk0(98) / (1.12 * \sqrt{\pi * ai} * (1 - (smin / smax)))$$

$$scllc = sthlc - dk0(1) / (1.12 * \sqrt{\pi * ai})$$

$$Ulc = (sthlc - scllc) / (sthlc - (smin / smax) * sthlc)$$

! Factor out crack closure, and plot if no growth or reached max

Do 26 i=1,102

 dkn(i) = dk(i)*Ulc

26 Continue

Do 27 i=1,102

 If ((dkeff > dkn(i)).AND.(dkeff < dkn(i+1))) then

 d = (dkeff-dkn(i))/(dkn(i+1)-dkn(i))

 dan = 10**(log10(dadn(i))+d*(log10(dadn(i+1))-log10(dadn(i))))

 Goto 28

 Elseif (dkeff < dkn(1)) then

 dan = dadn(1)

 End if

27 Continue

! Convert back to MPa valves for Dk

28 deltak = 1.12*ds*sqrt(pi*ai)*1.0E-6

Open(unit=14, file='dadn vs dk curve R=0.3 410-510MPa.txt', status='unknown')

Write(14,*) deltak, dan

! Convert back to MPa/mm values

 splot = smax*1.0E-6

 da = dan

dkmax = dk(102)*1.0E-6

! Calculating Nf and plotting results

If (dan == dadn(1)) then

nf = 1.0E+7

Print *, "NO CRACK GROWTH"

Goto 35

Else if (deltak > dkmax) then

Print *, "REACHED MAX"

Goto 30

End if

nf = nf + 1

Print *, "nf = ",nf

Goto 7

30 If (nf > 1.0E+7) then

Print *, "REACHED RUNOUT"

Goto 35

End if

100 Write(18,*) "for stress max, nf = ", st, nf

35 EndProgram SE_CASE7